Correlated Effective Field Theory Truncation Errors: From Neutron-Proton Scattering Amplitudes to Observables

Master's thesis in Physics

LUCAS I. G. B. ABRAHAMSSON

DEPARTMENT OF PHYSICS
CHALMERS UNIVERSITY OF TECHNOLOGY
Gothenburg, Sweden 2025
www.chalmers.se

Master's thesis 2025

Correlated Effective Field Theory Truncation Errors: From Neutron-Proton Scattering Amplitudes to Observables

Lucas I. G. B. Abrahamsson

CHALMERS
UNIVERSITY OF TECHNOLOGY

Department of Physics
Division of Subatomic, High Energy and Plasma Physics
Theoretical Subatomic Physics
Chalmers University of Technology
Gothenburg, Sweden 2025

Correlated Effective Field Theory Truncation Errors: From Neutron-Proton Scattering Amplitudes to Observables

Lucas I. G. B. Abrahamsson

© Lucas I. G. B. Abrahamsson, 2025.

Supervisor: Christian Forssén and Oliver Thim, Department of Physics
Examiner: Christian Forssén, Department of Physics

Master's Thesis 2025
Department of Physics
Division of Subatomic, High Energy and Plasma Physics
Theoretical Subatomic Physics
Chalmers University of Technology
SE-412 96 Gothenburg
Telephone +46 31 772 1000

Cover: detail of Raphael's *Scuola di Atene* (The School of Athens), fresco, Stanza della Segnatura, Apostolic Palace, Vatican Museums, Vatican City, 1509–1511.

Typeset in LaTeX
Printed by Chalmers Reproservice
Gothenburg, Sweden 2025

Correlated Effective Field Theory Truncation Errors: From Neutron-Proton Scattering Amplitudes to Observables

Lucas I. G. B. Abrahamsson
Department of Physics
Chalmers University of Technology

Abstract

The strong force governing *Nucleon-Nucleon* (NN) scattering can be modelled with an *Effective Field Theory* (EFT) of low-energy quantum chromodynamics. The Feynman diagrams contributing to this force are considered order-by-order in an expansion with decreasing importance. NN scattering observables can then be predicted by considering all contributions up to some finite order, while neglected orders result in predictable truncation errors. Contrary to previous studies, the EFT truncation errors of different NN observable types should not be considered independent since all of them depend on only five complex so-called scattering amplitudes. Instead, truncation errors must be correlated not only across energies and scattering angles but also across different observable types. In this thesis, we modelled and investigated such correlations between the uncertainties of different neutron-proton scattering observables resulting from a truncation of the chiral EFT guided by Weinberg power counting.

We applied a Bayesian uncertainty-quantification model, consisting of a fixed-kernel Gaussian process, on the leading order chiral EFT truncation errors of the neutron-proton scattering amplitudes. The resulting errors were then propagated to errors of various observables. We considered both Saclay and helicity conventions for the NN scattering amplitudes with their specific angular boundary constraints. Firstly, we found that the symmetry constraints of amplitudes propagate to observables, resulting in angle- and energy-dependent uncertainties. Secondly, we observed strong angle-dependent correlations and rigid inequalities between different observable types, cutting the joint posteriors into characteristic shapes traced back to their amplitude dependencies. Finally, we examined the extent to which our error model violates the unitarity constraint of the scattering operator by comparing the optical-theorem and integrated total cross section. There was little to no correlation between the uncertainties of these theoretically identical expressions. While we successfully incorporated unitarity on average, future studies are necessary to explicitly implement unitarity constraints into the error model.

This work is an important step in a larger effort to understand correlated EFT truncation errors, considering rigorously the correlation between different NN scattering observable types. The resulting error model could enhance the physical robustness of EFT parameter inference and the reliability of theoretical predictions for nuclear observables.

Keywords: nuclear physics, chiral effective field theory, nucleon-nucleon scattering, scattering amplitudes, scattering observables, Bayesian uncertainty quantification, effective field theory truncation error, Gaussian-process modelling.

Acknowledgements

First and foremost, I would like to thank my precious supervisors, Christian Forssén and Oliver Thim, for guiding me throughout this master's project.

I would also like to thank my colleagues, who have provided many helpful discussions. Without their feedback and insights, this project would not have been what it is now.

On a more general note, I would like to thank my family and friends for their support and companionship, both during my studies and the times in between.

Lucas I. G. B. Abrahamsson, Gothenburg, June 2025

List of Acronyms

Below is the list of acronyms that have been used throughout this thesis, listed in alphabetical order:

1PE	One-Pion Exchange
2PE	Two-Pion Exchange
BUQ	Bayesian Uncertainty Quantification
χEFT	Chiral Effective Field Theory
ChPT	Chiral Perturbation Theory
c.m.	center-of-mass
EFT	Effective Field Theory
ETI	Equal-Tailed Interval
GP	Gaussian Process
GL	Gauss-Legendre
i.i.d	independent and identically distributed
jPWS	total angular momentum Partial-Wave States
LECs	Low-Energy Constants
LO	Leading Order
LS	Lippmann–Schwinger
NN	Nucleon-Nucleon
np	neutron-proton
πN	pion-Nucleon
$\pi\pi$	pion-pion
PWA	Partial-Wave Analysis
PWS	Partial Wave State
QCD	Quantum Chromodynamics
RRMSE	Relative Root Mean Squared Error
StD	Standard Deviation
WPC	Weinberg Power Counting

Terminology

Below is special terminology that has been used throughout this thesis, listed in alphabetical order:

a priori *adj. (also adv.)* (Latin, meaning "from what is earlier") Pertaining to arguments, principles, or knowledge justified independently of sensory experience.

e.g. *adv.* Abbreviation of the Latin *exempli gratia*, meaning "for example".

et al. *phr.* Abbreviation of the Latin *et alia*, meaning "and others".

i.e. *adv.* Abbreviation of the Latin *id est*, meaning "that is".

interamplitudinal *adj.* Pertaining to comparative relations, systematic patterns, or structural dependencies between separate amplitudes, especially in scattering processes or wave-function components.

interobservabial *adj.* Pertaining to relationships, correlations, or structural linkages between distinct physical observables within a theoretical framework.

Nomenclature

Below is the nomenclature of operators and variables that have been used throughout this thesis.

All transformation operators are given in hatted script-style, *e.g.* $\hat{\mathscr{P}}$, $\hat{\mathscr{T}}$, and $\hat{\mathscr{C}}$, except for the permutation operator denoted as $\hat{\Pi}$.

All three-dimensional vectors are denoted as bold math symbols, *e.g.* $\boldsymbol{p}$, and the magnitude of the vector is generally defined as $p \equiv |\boldsymbol{p}|$ (note that not all bold math symbols are three-dimensional vectors).

Operators

H	Full Hamiltonian.
H_0	Free Hamiltonian.
V	Potentials.
$G(z)$	Full Greens operator.
$G_0(z)$	Free Greens operator.
S	Scattering operator.
T	Transition operator.
$\boldsymbol{\sigma}$	Pauli spin operators.
$\boldsymbol{\tau}$	Pauli isospin operators.
$\boldsymbol{S}$, s, and m_s	Spin operators, quantum number, and projection.
$\boldsymbol{T}$, t, and m_t	Isospin operators, quantum number, and projection.
$\boldsymbol{L}$, ℓ, and m_ℓ	Orbital angular momentum operators, quantum number, and projection.
$\boldsymbol{J}$, j, and m_j	Total angular momentum operators, quantum number, and projection.

Variables

$\boldsymbol{p}$, $\boldsymbol{k}$, and $\boldsymbol{q}$	Relative momentum vectors. In general, this thesis uses $\boldsymbol{k}$ for on-shell relative momenta and $\boldsymbol{q}$ for intermediate (integrated over) relative momenta. Outgoing relative momenta are generally denoted with a prime.
μ	Reduced mass
$\boldsymbol{K}$	Momentum transfer.
$\boldsymbol{P}$	Momentum average.
$\boldsymbol{N}$	Normal vector of the $\boldsymbol{PK}$-plane (the scattering plain).
T_{lab}	Laboratory kinetic energy.
ϑ	Centre-of-mass polar scattering angle.
Q	Chiral effective field theory expansion parameter.

Effective Field Theory related

$\mathcal{L}$	Lagrangians.
Λ_π	Soft scale of chiral effective field theory.
Λ_χ	Hard scale (chiral-symmetry breaking scale) of chiral effective field theory.
N	Heavy-baryon nucleon field.
$\boldsymbol{\pi}$	Pion fields.

Scattering Theory related

These are generally functions of T_{lab} (or equivalently relative momenta) and ϑ.

$\mathbf{M}$	Scattering amplitude matrix in the uncoupled spin basis.
$\{A_i\}_{i=1}^5$	Nucleon-nucleon Lucas scattering amplitudes.
$\{M_i\}_{i=1}^5$	Nucleon-nucleon helicity scattering amplitudes.
$\{a, b, c, d, e\}$	Nucleon-nucleon Saclay scattering amplitudes.

Table of Contents

List of Acronyms **ix**

Terminology **xi**

Nomenclature **xiii**

1 Introduction **1**

I Theory **5**

2 Effective Field Theory of Nuclear Physics **7**
2.1 Symmetries of Low-Energy QCD 8
2.1.1 Approximate Chiral Symmetry 9
2.1.2 Approximate Isospin Symmetry 10
2.1.3 Parity, Time Reversal, and Charge Conjugation 11
2.2 The Chiral Effective Field Theory Lagrangian 12
2.2.1 The Pion-Pion Lagrangian 13
2.2.2 The Pion-Nucleon Lagrangian 14
2.2.3 Two-Nucleon Contact Lagrangian 15
2.3 The Nuclear Interaction Potential 15
2.3.1 Two-Nucleon Interaction potential 15
2.3.2 Regularisation 19

3 Scattering Theory **23**
3.1 Scattering Theory in Operators 23
3.1.1 The Lippmann-Schwinger Operator Equation 25
3.2 Two-Particle Scattering 27
3.2.1 States for Two Particles with Spin and Isospin 28
3.3 Nucleon-Nucleon Scattering 31
3.3.1 Nucleon-Nucleon States 31
3.3.2 Symmetries 35
3.3.3 The Lippmann-Schwinger Equation for NN Scattering 41
3.3.4 The Scattering Matrix 42
3.4 Relativistic Nucleon-Nucleon Scattering 44

4 Nucleon-Nucleon Scattering Amplitudes and Observables 47
4.1 NN Scattering Amplitudes . . . 47
4.1.1 Constraint from Unitarity of S Operator . . . 51
4.2 Nucleon-Nucleon Scattering Observables . . . 51
4.2.1 Differential scattering observables . . . 52
4.2.2 Total cross sections . . . 54

II Methods and Implementation 59

5 Bayesian Effective Field Theory Truncation Errors 61
5.1 EFT Truncation Errors . . . 61
5.2 Bayesian Uncertainty Quantification . . . 63
5.2.1 Gaussian Process Error Model . . . 63

6 Numerical Solution of the Nucleon-Nucleon Scattering Problem 65
6.1 Solver for the Lippmann-Schwinger Equation . . . 65

7 Project-Specific Implementation 69
7.1 Leading Order Interaction Potential . . . 69
7.2 Numerical Predictions of Scattering Amplitudes and Observables . . . 70
7.3 Bayesian Uncertainty Quantification Model . . . 72
7.3.1 Propagation of Uncertenties . . . 74

III Results and Discussion 77

8 Results 79
8.1 Neutron-Proton Scattering Amplitudes . . . 79
8.2 Error Propagation: Differential Observables . . . 80
8.2.1 Correlated Errors: Differential Observables . . . 86
8.3 Unitarity and Total Cross Section . . . 89

9 Conclusion and Outlook 97

References 99

A Scattering with Generally Normalised States I
A.1 The Scattering Amplitude Matrix . . . II
A.2 The S Matrix . . . III
A.3 Application for Particles with Spin and Isospin . . . IV

B Variances of Differential Observables VII

C Additional Results XI
C.1 Energy and Angle Dependence of LO Predictions of Scattering amplitudes . . . XI
C.2 Differential Observable . . . XI

C.3 Total cross sections XII

1

Introduction

Understanding the strong nuclear force remains one of the central challenges in modern theoretical physics. The lineage of theoretical efforts to formally describe this force traces back to 1935 and H. Yukawa's meson theory [1]. His work paved the way to the first field-theoretic attempts to derive the *Nucleon-Nucleon* (NN) interaction in the 1950s. The *One-Pion Exchange* (1PE) model successfully reproduced low-energy scattering data; however, the attempts to extend this framework to multiple pions suffered from serious ambiguities. As a result, the so-called "pion theories" of the 1950s were generally regarded as failures and were abandoned in favour of the one-boson exchange models of the 1960s. We now recognise that these failures are linked to the fact that pion dynamics are constrained by chiral symmetry, which was not understood at that time [2].

However, the "pion theories" were resurrected with the discovery of *Quantum Chromodynamics* (QCD) in the 1980s. While QCD provided solutions to some of the issues faced by earlier approaches, it also introduced new challenges. The problem with deriving nuclear forces from QCD is that this theory is non-perturbative in the low-energy regime, making direct solutions difficult. The final breakthrough occurred with the discovery of *Effective Field Theory* (EFT), which was applied to low-energy QCD [2]. The recipe for constructing EFTs was outlined by S. Weinberg [3] as writing down the most general Lagrangian consistent with the assumed symmetry principles of the underlying theory. The *Chiral Effective Field Theory* (χEFT), initially proposed by Weinberg [4, 5], considers in particular the (approximate) chiral symmetry of QCD. It effectively describes low-energy nuclear forces, using pions (Goldstone bosons of the broken chiral symmetry) and nucleons as the effective degrees of freedom.

The most general Lagrangian consistent with the (broken) chiral symmetry will contain an infinite number of terms. To assess the importance of each term, the χEFT Lagrangian is systematically handled as an expansion in powers of an expansion parameter Q. The nuclear interaction potential is then similarly considered on an order-by-order basis, by including contributions from the Feynman diagrams of that order. However, there is always a next order to consider, which means that the theory must be truncated at some level of accuracy. The neglected orders subsequently

lead to unavoidable truncation errors, propagating to all physically observable quantities. The systematic order-by-order convergence of a well-constructed EFT does, however, provide not only increasingly accurate predictions but also quantitative guidance for modelling these residual truncation uncertainties [6, 7].

The quest of constructing an error model that provides as much information as possible about the EFT truncation errors is thus a fundamental part of increasing our understanding of nuclear physics. Considerable efforts have been made to incorporate the *a priori* knowledge from the truncated prediction into *Bayesian Uncertainty Quantification* (BUQ) models of the residual truncation errors [6, 8], in the context of NN scattering and many-body observables[9–11]. These error models have, over time, evolved to consider an increasing amount of physics knowledge about the NN observables on which the models are applied [9, 10]. The consequent models consider the scattering observables to be correlated with themselves across energies and angles, but independent of other observable types.

The NN scattering system is constrained by various symmetries and invariance principles, which constrain the number of independent scattering quantities. There are only five complex so-called NN scattering amplitudes from which all observables can be determined [12]. This quantity bottleneck presents an excellent opportunity to further evolve the BUQ models of correlated EFT truncation errors by also considering the correlations between different observable types. The primary idea behind this expansion is that applying the BUQ model independently on the five scattering amplitudes enables the propagation of uncertainties across all observables. This approach should result in correlations between various observable types, thereby capturing the underlying physics at a more fundamental level.

A recent article by B. McClung *et al.* [13] applied a BUQ model onto scattering amplitudes. The space carved out for this project is thus to further extend the model by propagating the truncation errors of the scattering amplitudes to observables and investigating the correlations across energies, scattering angles, and, most significantly, the correlations between different observable types.

Aim and Structure

The primary objectives of this thesis are to:

- Implement a BUQ model for χEFT truncation errors at the level of NN scattering amplitudes.

- Propagate the errors from the amplitudes to various NN observables and investigate the correlations between the resulting truncation errors of different observable types.

- Examine the implications of the unitarity of the scattering operator on the scattering amplitudes and to what extent the constructed error model violates this implicit constraint.

The study is limited to only considering *neutron-proton* (*np*) scattering and the *Leading Order* (LO) *Weinberg Power Counting* (WPC) χEFT potential. The hyperparameters implemented in the BUQ model were thus not independently determined. The project does, however, consider both the helicity and Saclay conventions of the *np* scattering amplitudes, which significantly increases the nuance of the discussion of the new results of this thesis.

The thesis is divided into three parts. In Part I, the underlying theory behind the project implementation is presented. The general concept of construction of a EFT and the implemented χEFT potential is presented in chapter 2. The quantum mechanical theory of non-relativistic scattering is introduced in chapter 3. This chapter also takes a detailed look at the symmetries and invariance principles utilised to define the NN scattering amplitudes and observables in chapter 4. Part II presents the general methods used, *i.e.* the general BUQ model (chapter 5) and the numerical solution to the *Lippmann–Schwinger* (LS) equation (chapter 6). The exact project-specific implementation used is then presented and motivated in chapter 7. The last part, Part III, presents and discusses the acquired results. Chapter 8 consists of three sections, one for the results relating to each of the three primary objectives of the thesis. The closing chapter of the thesis (chapter 9) concludes the results and presents an outlook for future studies.

The frequently used acronyms, considered nomenclature, and special terminology are presented in the front matter. Note also that natural units ($\hbar = c = 1$) are used in all theoretical expressions throughout the thesis. The results are presented in units of MeV (energies), fm (amplitudes), and fm^2 (cross sections), linked to the natural units through the factor $\hbar c \approx 197.327\,\text{MeVfm}$.

Part I

Theory

2

Effective Field Theory of Nuclear Physics

Nuclear forces are governed by low-energy QCD, which is the theory of strong interactions. QCD is a non-Abelian gauge field theory[1], based on the colour $SU(3)$ gauge group. The degrees of freedom of the theory are the "coloured" quarks (fermionic fields) and gluons (gauge fields). The non-Abelian nature of the gauge group $SU(3)$ implies that QCD, which has six fermion fields (the six quark flavours), is asymptotically free. The "strong" force governing the strong interaction of coloured objects is, therefore, weak at high energies (or short distances), allowing for perturbative treatment of high-energy QCD. The strong force is, however, strong for low energies (or long distances), leading to the confinement of quarks into colourless hadrons. Low-energy QCD is, therefore, highly non-perturbative, making direct solutions in nuclear physics very difficult [15].

The efficient approach to treat problems in nuclear physics, like the NN scattering problem, which is of interest in this project, is to construct a EFT consistent with low-energy QCD. The recipe for constructing an EFT from an underlying field theory can be summarised as [2]:

1. Identify the soft and hard scales, and the effective degrees of freedom appropriate for the system in question.

2. Identify the relevant (exact and approximate) symmetries and symmetry breakings of the underlying theory.

3. Construct the most general Lagrangian, in terms of the effective degrees of freedom, consistent with the symmetries and symmetry breakings of the underlying theory.

[1] a non-Abelian gauge field theory is a field theory of which the Lagrangian is invariant under local (space-time dependent) transformations (of a gauge group) associated with a Lie algebra with non-commuting generators [14].

4. Distinguish between more and less important terms in the Lagrangian, by considering the Lagrangian as an expansion in terms of the soft scale over the hard scale, where some systematic power counting scheme determines the expansion order of each term.

5. Calculating Feynman diagrams for the problem in question using the effective Lagrangian truncated at some order in the expansion factor.

In low-energy QCD, where nuclear physics resides, the coloured quarks are confined in colourless hadrons, meaning that quarks and gluons are ineffective degrees of freedom for a nuclear physics EFT. It is thus more appropriate to consider the hadrons as the effective degrees of freedom. In the hadron spectrum, a large gap between the masses of the pions[2], m_π, and the masses of the vector mesons[3], $m_\rho \sim 1\,\text{GeV}$, can be identified. It is thus reasonable to consider the soft scale to be set by the scale of the pion masses, $\Lambda_\pi \sim m_\pi$, and the hard scale to be set by the scale of the vector meson masses, $\Lambda_\chi \sim m_\rho$, also known as the chiral-symmetry breaking scale. The relevant degrees of freedom for nuclear physics are thus considered to be given by nucleons and pions [2].

With the hard and soft scales established, the remaining points on the EFT recipe checklist will be covered in the upcoming sections. The relevant symmetries of QCD are identified in section 2.1. The most general χEFT Lagrangian is then considered and distinguished based on importance in section 2.2. Section 2.3 asserts the Feynman diagrams for two-nucleon interactions and presents the WPC scheme and the LO χEFT potential.

2.1 Symmetries of Low-Energy QCD

The gauge invariant QCD Lagrangian is given by

$$\mathcal{L}_{\text{QCD}} = -\frac{1}{4}F^a_{\mu\nu}F^{a\mu\nu} + \sum_f \bar{\psi}_f(i\gamma^\mu D_\mu - m_f)\psi_f \tag{2.1}$$

where ψ_f are the quark Dirac fields (of flavour $f = \text{u}, \text{d}, \text{s}, \text{c}, \text{b}, \text{t}$), m_f are the quark masses, $F^a_{\mu\nu}$ is the gluon field strength tensor (with colour index $a = 1, 2, \ldots, 8$ and space-time indices $\mu, \nu = 0, 1, 2, 3$), D_μ is the covariant derivative, and γ^μ are the gamma matrices. The gluon field strength tensor is given by

$$F^a_{\mu\nu} = \partial_\mu A^a_\nu - \partial_\nu A^a_\mu + g f^{abc} A^b_\mu A^c_\nu, \tag{2.2}$$

g is the strong coupling constant, A^a_μ are the gluon fields, and f^{abc} are the structure constants of the $SU(3)_{\text{colour}}$ Lie algebra. The covariant derivative is given by

$$D_\mu = \partial_\mu - igA^a_\mu T^a, \tag{2.3}$$

[2]The charged pions have masses $m_{\pi^\pm} = 139.57039 \pm 0.00018\,\text{MeV}$ and the neutral pion has mass $m_{\pi^0} = 134.9768 \pm 0.0005\,\text{MeV}$ [16].

[3]The $\rho(770)$ is the lightest vector meson with a mass of $m_\rho = 775.26 \pm 0.23\,\text{MeV}$ [16].

where T^a are the generators of the $SU(3)_{\text{colour}}$ Lie algebra .

There are six quark flavours: *up* (u), *down* (d), *strange* (s), *charm* (c), *bottom* (b), and *top* (t). The up, down, and strange quarks have masses

$$m_{\text{u}} = 2.16 \pm 0.07\,\text{MeV}, \quad m_{\text{d}} = 4.70 \pm 0.07\,\text{MeV}, \quad m_{\text{s}} = 93.5 \pm 0.8\,\text{MeV}, \tag{2.4}$$

and the charm, bottom, and top quarks have masses[4] over 1 GeV [16]. For the energy scale relevant for nuclear physics, *i.e.* $\Lambda_\chi \sim 1\,\text{GeV}$, only the up and down quark flavours are considered[5] [17].

2.1.1 Approximate Chiral Symmetry

Given that the masses of the up and down quarks are much smaller than the energy scale relevant for nuclear physics, the massless quark approximation is good. Under these approximations, the low-energy QCD Lagrangian becomes

$$\mathcal{L}^0_{\text{QCD}} = -\frac{1}{4}F^a_{\mu\nu}F^{a\mu\nu} + \bar{\psi}i\gamma^\mu D_\mu\psi, \quad \psi \equiv \begin{pmatrix}\psi_{\text{u}} \\ \psi_{\text{d},}\end{pmatrix} \tag{2.5}$$

where ψ is a composite spinor of the up and down quark Dirac fields. This composite spinor can be separated into *Left-handed* (L) and *Right-handed* (R) projections as

$$\psi = \psi_{\text{L}} + \psi_{\text{R}}, \quad \psi_{\text{L}} = P_{\text{L}}\psi, \quad \psi_{\text{R}} = P_{\text{R}}\psi. \tag{2.6}$$

The operators P_{L} and P_{R} are the so-called chiral projection operators and are defined as

$$P_{\text{L}} = \frac{1}{2}(1-\gamma^5), \quad P_{\text{R}} = \frac{1}{2}(1+\gamma^5), \tag{2.7}$$

where $\gamma^5 \equiv i\gamma^0\gamma^1\gamma^2\gamma^3$ is the "fifth" gamma matrix. The massless quarks low-energy QCD Lagrangian can then be expressed as

$$\mathcal{L}^0_{\text{QCD}} = -\frac{1}{4}F^a_{\mu\nu}F^{a\mu\nu} + \bar{\psi}_{\text{L}}i\gamma^\mu D_\mu\psi_{\text{L}} + \bar{\psi}_{\text{R}}i\gamma^\mu D_\mu\psi_{\text{R}}, \tag{2.8}$$

which does not mix left- and right-handed quark fields. It is apparent that this Lagrangian is invariant under the global transformations

$$\psi_{\text{L}} \longrightarrow g_{\text{L}}\psi_{\text{L}} = e^{-i\Theta_{\text{L},i}\frac{\tau_i}{2}}\psi_{\text{L}}, \quad \psi_{\text{R}} \longrightarrow g_{\text{R}}\psi_{\text{R}} = e^{-i\Theta_{\text{R},i}\frac{\tau_i}{2}}\psi_{\text{R}}, \tag{2.9}$$

where $g_{\text{L}} \in SU(2)_{\text{L}}$, $g_{\text{R}} \in SU(2)_{\text{R}}$, and τ_i $(i = 1,2,3)$ are the generators of $SU(2)_{\text{flavour}}$ with the commutation relation $[\tau_i, \tau_j] = 2i\epsilon_{ijk}\tau_k$. This

$$G_\chi \equiv SU(2)_{\text{L}} \times SU(2)_{\text{R}} = \{(g_{\text{L}}, g_{\text{R}}) \mid g_{\text{L}} \in SU(2)_{\text{L}},\ g_{\text{R}} \in SU(2)_{\text{R}}\} \tag{2.10}$$

symmetry is known as *chiral symmetry* [2].

[4]The charm, bottom, and top quarks have masses $m_{\text{c}} = 1.2730 \pm 0.0046\,\text{GeV}$, $m_{\text{b}} = 4.183 \pm 0.007\,\text{GeV}$, and $m_{\text{t}} = 172.57 \pm 0.29\,\text{GeV}$, respectively [16].

[5]The strange quark is not considered since the neutron, proton, and pions are hadrons of up and down quarks.

Even if the massless quarks approximation is good for nuclear physics, the up and down quarks do indeed have a mass and the true low-energy QCD Lagrangian is

$$\mathcal{L}_{\text{QCD}} = -\frac{1}{4}F^a_{\mu\nu}F^{a\mu\nu} + \bar{\psi}_{\text{L}}(i\gamma^\mu D_\mu - m)\psi_{\text{L}} + \bar{\psi}_{\text{R}}(i\gamma^\mu D_\mu - m)\psi_{\text{R}} - \bar{\psi}_{\text{L}}m\psi_{\text{R}} - \bar{\psi}_{\text{R}}m\psi_{\text{L}}, \tag{2.11}$$

where $m = \text{diag}(m_{\text{u}}, m_{\text{d}})$ is the diagonal (up and down) quark masses matrix. It is clear that the $\bar{\psi}_{\text{L}}m\psi_{\text{R}}$ and $\bar{\psi}_{\text{R}}m\psi_{\text{L}}$ terms explicitly break the chiral symmetry for non-zero quark masses. The up and down quark masses are, however, very small in relation to the energy scale of nuclear physics, meaning that the explicit breaking of the chiral symmetry is very small. Low-energy QCD is thus said to have an *approximate chiral symmetry*. In addition, there is evidence that the approximate chiral symmetry of low-energy QCD is spontaneously broken to an approximate $SU(2)_V$ symmetry. The three spontaneously broken generators result in three pseudo-Goldstone bosons, namely the three (barely) massive pions (π^0, π^+, π^-) [15]. In the so-called chiral limit, where $m_{\text{d}}, m_{\text{u}} \to 0$, the pions become massless Goldstone bosons.

2.1.2 Approximate Isospin Symmetry

Noether's theorem implies that the chiral symmetry carries six conserved currents

$$L^\mu_i = \bar{\psi}_{\text{L}}\gamma^\mu\frac{\tau_i}{2}\psi_{\text{L}}, \quad R^\mu_i = \bar{\psi}_{\text{R}}\gamma^\mu\frac{\tau_i}{2}\psi_{\text{R}}, \tag{2.12}$$

with $\partial_\mu L^\mu_i = 0$ and $\partial_\mu R^\mu_i = 0$. Three conserved vector currents, V^μ_i, and three conserved axial-vector currents, A^μ_i, can then be identified as

$$V^\mu_i = R^\mu_i + L^\mu_i = \bar{\psi}\gamma^\mu\frac{\tau_i}{2}\psi, \quad A^\mu_i = R^\mu_i - L^\mu_i = \bar{\psi}\gamma^\mu\gamma^5\frac{\tau_i}{2}\psi. \tag{2.13}$$

The vector transformations are given as

$$\psi \longrightarrow U_{\text{V}}\psi = e^{-i\Theta_{\text{V},i}\frac{\tau_i}{2}}\psi, \tag{2.14}$$

which can be recognised as isospin rotations $U_{\text{V}} \in SU(2)_{\text{V}}$. The invariance under vector transformations can, therefore, be identified as *isospin symmetry* [2].

The quark mass term in the low-energy QCD Lagrangian can be expressed as

$$\bar{\psi}m\psi = \bar{\psi}\begin{pmatrix} m_{\text{u}} & 0 \\ 0 & m_{\text{d}} \end{pmatrix}\psi = \frac{m_{\text{u}} + m_{\text{d}}}{2}\bar{\psi}\psi + \frac{m_{\text{u}} - m_{\text{d}}}{2}\bar{\psi}\tau_3\psi, \tag{2.15}$$

where τ_3 is the third Pauli matrix (third generator of $SU(2)_{\text{flavour}}$). It is clear that the quark mass term only is invariant under the vector transformations if $m_{\text{u}} = m_{\text{d}}$. Given that $|m_{\text{u}} - m_{\text{d}}| \approx 2.54\,\text{MeV} \ll 1\,\text{GeV}$, the low-energy QCD exhibit an *approximate isospin symmetry* for energy scales relevant for nuclear physics.

2.1.3 Parity, Time Reversal, and Charge Conjugation

The parity, time-reversal, and charge-conjugation transformation properties of the various bilinears are summarised in table 2.1. The details of the transformations are presented in the remaining part of this subsection.

Table 2.1: Transformation properties of the five Dirac field bilinears (and the partial space derivative and gauge fields) under parity (P), time-reversal (T), and charge-conjugation (C) transformations. γ^μ are the four gamma matrices, $\gamma^5 \equiv i\gamma^0\gamma^1\gamma^2\gamma^3$ is the "fifth" gamma matrix, and $\sigma^{\mu\nu} \equiv -\frac{i}{2}[\gamma^\mu, \gamma^\nu]$. In this table $(-1)^\mu \equiv 1$ for $\mu = 0$ and $(-1)^\mu \equiv -1$ for $\mu = 1, 2, 3$ [18].

	$\bar{\psi}\psi$	$i\bar{\psi}\gamma^5\psi$	$\bar{\psi}\gamma^\mu\psi$	$\bar{\psi}\gamma^\mu\gamma^5\psi$	$\bar{\psi}\sigma^{\mu\nu}\psi$	∂_μ and A^a_μ
P	$+1$	-1	$(-1)^\mu$	$-(-1)^\mu$	$(-1)^\mu(-1)^\nu$	$(-1)^\mu$
T	$+1$	-1	$(-1)^\mu$	$(-1)^\mu$	$-(-1)^\mu(-1)^\nu$	$-(-1)^\mu$
C	$+1$	$+1$	-1	$+1$	-1	$+1$

The parity transformation reverses the momentum of a particle without changing its spin, *i.e.*

$$\boldsymbol{p} \longrightarrow \hat{\mathscr{P}}\boldsymbol{p}\hat{\mathscr{P}} = -\boldsymbol{p}, \tag{2.16}$$

where $\hat{\mathscr{P}}$ is the unitary and Hermitian parity operator and $\boldsymbol{p}$ is the momentum three-vector [18]. Dirac spinors transform under parity as

$$\psi(t, \boldsymbol{x}) \longrightarrow \hat{\mathscr{P}}\psi(t, \boldsymbol{x})\hat{\mathscr{P}} = \eta_a\gamma^0\psi(t, -\boldsymbol{x}), \tag{2.17}$$

where η_a is a possible phase obeying $\eta_a^*\eta_a = 1$. Gauge fields transform under parity as

$$A^a_\mu(t, \boldsymbol{x}) \longrightarrow \hat{\mathscr{P}}A^a_\mu(t, \boldsymbol{x})\hat{\mathscr{P}} = \begin{cases} A^a_\mu(t, -\boldsymbol{x}) & \text{for } \mu = 0, \\ -A^a_\mu(t, -\boldsymbol{x}) & \text{for } \mu = 1, 2, 3. \end{cases} \tag{2.18}$$

It is with these transformations and the defining anticommutator relations of the gamma matrices $\{\gamma^\mu, \gamma^\nu\} = 2\eta^{\mu\nu}\mathbb{1}$ easy to show that the QCD Lagrangian (2.1) is parity invariant [14, 15].

The time-reversal transformation changes the direction of particle momentum and reverses the time coordinate, *i.e.*

$$\boldsymbol{p} \longrightarrow \hat{\mathscr{T}}\boldsymbol{p}\hat{\mathscr{T}}^\dagger = -\boldsymbol{p}, \quad (t, \boldsymbol{x}) \longrightarrow \hat{\mathscr{T}}(t, \boldsymbol{x})\hat{\mathscr{T}}^\dagger = (-t, \boldsymbol{x}) \tag{2.19}$$

where $\hat{\mathscr{T}}$ is the antiunitary[6] time-reversal operator, $\boldsymbol{p}$ is the momentum three-vector and $x = (t, \boldsymbol{x})$ is the space-time coordinate [18]. Dirac spinors transform under time reversal as

$$\psi(t, \boldsymbol{x}) \longrightarrow \hat{\mathscr{T}}\psi(t, \boldsymbol{x})\hat{\mathscr{T}}^\dagger = -\gamma^1\gamma^3\psi(-t, \boldsymbol{x}). \tag{2.20}$$

[6] $T^\dagger T = 1$ and $TA = A^*T$, where A is a general mathematical object.

Gauge fields transform under time reversal as

$$A^a_\mu(t,\boldsymbol{x}) \longrightarrow \hat{\mathscr{T}} A^a_\mu(t,\boldsymbol{x})\hat{\mathscr{T}}^\dagger = \begin{cases} -A^a_\mu(-t,\boldsymbol{x}) & \text{for } \mu = 0, \\ A^a_\mu(-t,\boldsymbol{x}) & \text{for } \mu = 1,2,3. \end{cases} \tag{2.21}$$

These transformations in combination with the antiunitarity of $\hat{\mathscr{T}}$ and the properties of the gamma matrices can be used to show that the QCD Lagrangian (2.1) is invariant under time reversal [14, 15].

The charge-conjugation transformation changes a fermion with a given spin orientation into its antifermion with the same spin orientation, *i.e.*

$$a^s_{\boldsymbol{p}} \longrightarrow \hat{\mathscr{C}} a^s_{\boldsymbol{p}} \hat{\mathscr{C}} = b^s_{\boldsymbol{p}}, \quad b^s_{\boldsymbol{p}} \longrightarrow \hat{\mathscr{C}} b^s_{\boldsymbol{p}} \hat{\mathscr{C}} = a^s_{\boldsymbol{p}}, \tag{2.22}$$

where $\hat{\mathscr{C}} = \hat{\mathscr{C}}^\dagger$ is the unitary and Hermitian charge-conjugation operator and $a^s_{\boldsymbol{p}}$ ($b^s_{\boldsymbol{p}}$) is the annihilation operator of a fermion (anti-fermion) with momentum $\boldsymbol{p}$ and spin s [18]. Dirac spinors transform under charge conjugation as

$$\psi(x) \longrightarrow \hat{\mathscr{C}}\psi(x)\hat{\mathscr{C}} = -i[\bar{\psi}(x)\gamma^0\gamma^2]^T, \tag{2.23}$$

where $x = (t, \boldsymbol{x})$ is the space-time coordinate. Gauge fields transform under charge conjugation as

$$A^a_\mu(x) \longrightarrow \hat{\mathscr{C}} A^a_\mu(x) \hat{\mathscr{C}} = A^a_\mu(x). \tag{2.24}$$

Although not as easy as for parity, the properties of the gamma matrices can then be employed together with the charge-conjugation transformations of the fields to show that the QCD Lagrangian (2.1) is invariant under charge-conjugation [14, 15].

2.2 The Chiral Effective Field Theory Lagrangian

The EFT used in the context of nuclear physics is called χEFT, given that it, besides parity, charge conjugation, and time reversal invariance, considers the approximate chiral symmetry of low-energy QCD. The relevant degrees of freedom in χEFT are pions (pseudo Goldstone bosons) and nucleons (baryons), and the effective Lagrangian used to derive nuclear forces of a system of $2, 3, 4, \ldots, n$ nucleons is given by

$$\mathcal{L}^{\mathrm{2N}}_{\mathrm{eff}} = \mathcal{L}_{\pi\pi} + \mathcal{L}_{\pi N} + \mathcal{L}_{NN} \tag{2.25}$$

$$\mathcal{L}^{\mathrm{3N}}_{\mathrm{eff}} = \mathcal{L}^{\mathrm{2N}}_{\mathrm{eff}} + \mathcal{L}_{\pi NN} + \mathcal{L}_{NNN} \tag{2.26}$$

$$\mathcal{L}^{\mathrm{4N}}_{\mathrm{eff}} = \mathcal{L}^{\mathrm{3N}}_{\mathrm{eff}} + \mathcal{L}_{\pi NNN} + \mathcal{L}_{NNNN} \tag{2.27}$$

$$\vdots \tag{2.28}$$

$$\mathcal{L}^{n\mathrm{N}}_{\mathrm{eff}} = \mathcal{L}^{(n-1)\mathrm{N}}_{\mathrm{eff}} + \mathcal{L}_{\pi N^{n-1}} + \mathcal{L}_{N^n} \tag{2.29}$$

where $\mathcal{L}_{\pi\pi}$ describes the dynamics among pions, $\mathcal{L}_{\pi N^{n-1}}$ describes the interaction between pions and $n-1$ nucleons, and $\mathcal{L}_{N^n}$ deals with the n-nucleon contact interaction. The interaction of Goldstone bosons must vanish at zero momentum transfer,

and in the chiral limit ($m_\pi \to 0$), the low-energy expansion of the Lagrangian is arranged in powers of derivatives and pion masses. In *Chiral Perturbation Theory* (ChPT), the expansion is considered in powers of $Q = \Lambda_\pi/\Lambda_\chi$, where Λ_π is the soft scale given by a small momentum or pion mass and $\Lambda_\chi \sim 1\,\text{GeV}$ is the chiral symmetry breaking scale (the hard scale). Each of the terms in the effective Lagrangian is organised as

$$\begin{aligned}
\mathcal{L}_{\boldsymbol{\pi\pi}} &= \mathcal{L}^{(2)}_{\boldsymbol{\pi\pi}} + \mathcal{L}^{(4)}_{\boldsymbol{\pi\pi}} + \mathcal{L}^{(6)}_{\boldsymbol{\pi\pi}} + \dots, \\
\mathcal{L}_{\boldsymbol{\pi}N^{n-1}} &= \mathcal{L}^{(1)}_{\boldsymbol{\pi}N^{n-1}} + \mathcal{L}^{(2)}_{\boldsymbol{\pi}N^{n-1}} + \mathcal{L}^{(3)}_{\boldsymbol{\pi}N^{n-1}} + \mathcal{L}^{(4)}_{\boldsymbol{\pi}N^{n-1}} + \mathcal{L}^{(5)}_{\boldsymbol{\pi}N^{n-1}} + \dots, \\
\mathcal{L}_{N^n} &= \mathcal{L}^{(0)}_{N^n} + \mathcal{L}^{(2)}_{N^n} + \mathcal{L}^{(4)}_{N^n} + \dots,
\end{aligned} \tag{2.30}$$

where the superscripts indicate the number of derivatives or pion masses, d, in each term. Only terms with even d contributes to $\mathcal{L}_{\boldsymbol{\pi\pi}}$ due to Lorentz invariance, and the LO contribution consists of two derivatives given that Goldstone bosons only can interact if they carry momentum, *i.e.* the interaction between pions comes in powers of derivatives. Similarly, only terms with even d contribute to $\mathcal{L}_{N^n}$ due to parity and time reversal invariance [2].

In this project, only two-nucleon interactions will be investigated, meaning that the relevant Lagrangian is given by

$$\mathcal{L}_{\text{eff}} = \mathcal{L}_{\boldsymbol{\pi\pi}} + \mathcal{L}_{\boldsymbol{\pi}N} + \mathcal{L}_{NN}. \tag{2.31}$$

2.2.1 The Pion-Pion Lagrangian

To construct the chiral Lagrangian, the matrix $\Pi \in SU(2)_{\text{flavour}}$ is introduced to collect the pseudo-Goldstone pions $\boldsymbol{\pi}$ as

$$\Pi = \mathbb{1} + \frac{i}{f_\pi}(\boldsymbol{\tau}\cdot\boldsymbol{\pi}) - \frac{\boldsymbol{\pi}^2}{2f_\pi^2}\mathbb{1} - \frac{i\alpha}{f_\pi^3}(\boldsymbol{\tau}\cdot\boldsymbol{\pi})^3 + \frac{(8\alpha-1)\boldsymbol{\pi}^4}{8f_\pi^4}\mathbb{1} + \dots, \tag{2.32}$$

where f_π is the pion decay constant and $\boldsymbol{\tau} = (\tau_1, \tau_2, \tau_3)^T$ are the generators of the $SU(2)_{\text{flavour}}$ Lie algebra (isospin operators). The coefficient of the term which is linear in the pion fields is fixed such that the correct kinetic term is produced in the $\boldsymbol{\pi\pi}$ Lagrangian. The coefficient α is arbitrary due to the freedom of choice for the interpolating pion fields[7] [2]. An appropriate choise of the coefficient is $\alpha = 1/6$, for which (2.32) can be written as

$$\Pi = e^{i(\boldsymbol{\tau}\cdot\boldsymbol{\pi})/f_\pi}, \tag{2.33}$$

which is obvious when noting that $(\boldsymbol{\tau}\cdot\boldsymbol{\pi})^{2n} = \boldsymbol{\pi}^{2n}$ for all $n \in \mathbb{Z}$.

The LO $\boldsymbol{\pi\pi}$ Lagrangian can be expressed in terms of the matrix $\Pi \in SU(2)_{\text{flavour}}$ as

$$\mathcal{L}^{(2)}_{\boldsymbol{\pi\pi}} = \frac{f_\pi^2}{4}\text{Tr}\Big\{\partial_\mu\Pi\partial^\mu\Pi^\dagger + m_\pi^2(\Pi + \Pi^\dagger)\Big\}, \tag{2.34}$$

[7]Note that on-shell observables must be independent of the choice of the pion fields, *i.e.* must be independent of α.

where m_π is the pion mass. The *bifundamental field*[8] Π transfrom under global chiral rotations, the group G_χ as defined in (2.10), as

$$\Pi \longrightarrow g_{\mathrm{L}} \Pi g_{\mathrm{R}}^\dagger. \tag{2.35}$$

It is then, with the use of the unitarity and space-time independence of the global transformation matrices $g_{\mathrm{L/R}} \in SU(2)_{\mathrm{L/R}}$ and the cyclic property of the trace, trivial that the first term of (2.34) is chiral invariant. Equally trivial, the second term is not chiral invariant and breaks the chiral symmetry explicitly. This explicit breaking of the chiral symmetry is intentionally consistent with low-energy QCD such that the correct mass term for the pions are reproduced.

2.2.2 The Pion-Nucleon Lagrangian

Baryon fields can be incorporated into the EFT in a chirally consistent manner. The LO $\boldsymbol{\pi}N$ Lagrangian can be derived relativistically (see *e.g.* [19]) as

$$\mathcal{L}_{\boldsymbol{\pi}N}^{(1)} = \bar{\Psi}\Big[i\gamma^\mu D_\mu - M_{\mathrm{N}} + \frac{g_{\mathrm{A}}}{2}\gamma^\mu\gamma^5 u_\mu\Big]\Psi, \quad D_\mu = \partial_\mu + \Gamma_\mu, \tag{2.36}$$

where Ψ is the baryon field, M_{N} is the nucleon mass, D_μ is the chirally covarient derivative, and g_{A} is the axial-vector coupling constant. The chiral connection Γ_μ and the axial vector u_μ can be expressed as[9]

$$\Gamma_\mu = \frac{1}{2}[\xi^\dagger, \partial_\mu \xi] = \frac{1}{2}\Big(\xi^\dagger\partial_\mu\xi + \xi\partial_\mu\xi^\dagger\Big), \quad u_\mu = i\{\xi^\dagger, \partial_\mu\xi\} = i\Big(\xi^\dagger\partial_\mu\xi - \xi\partial_\mu\xi^\dagger\Big), \tag{2.37}$$

where

$$\xi \equiv \sqrt{\Pi} = \mathbb{1} + \frac{i}{2f_\pi}(\boldsymbol{\tau}\cdot\boldsymbol{\pi}) - \frac{\boldsymbol{\pi}^2}{8f_\pi^2}\mathbb{1} - \frac{i(8\alpha-1)}{16f_\pi^3}(\boldsymbol{\tau}\cdot\boldsymbol{\pi})^3 + \ldots. \tag{2.38}$$

It can then be understood that the term $\propto \bar{\Psi}\gamma^\mu\Gamma_\mu\Psi$ describes interactions between a baryon and an even number of pions, and the term $\propto \bar{\Psi}\gamma^\mu\gamma^5 u_\mu\Psi$ describes interactions between a baryon and an odd number of pions [2].

This relativistic treatment of baryons in ChPT leads to problems as the resulting Lagrangian contains time derivatives of the baryon fields and nucleon masses, which are not small compared to the chiral symmetry breaking scale and do not vanish in the chiral limit. The solution to this problem is to treat the baryons as heavy static sources (non-relativistic limit) such that the momentum transfer between baryons by pion exchange is small compared to the baryon mass. The expansion is then performed in terms of these small momenta over the baryon mass and is known as heavy-baryon ChPT. The LO $\boldsymbol{\pi}N$ Lagrangian, in this heavy-baryon formalism, is given by

$$\widehat{\mathcal{L}}_{\boldsymbol{\pi}N}^{(1)} = \bar{N}\Big[iD_0 - \frac{g_{\mathrm{A}}}{2}(\boldsymbol{\sigma}\cdot\vec{u})\Big]N, \tag{2.39}$$

[8]That Π is a bifundamental field implies (in this context) that Π transform linearly in the bifundamental representation $(\mathbf{2}_{\mathrm{L}}, \bar{\mathbf{2}}_{\mathrm{R}})$ of G_χ, *i.e.* $[\Pi]^a{}_{\dot{b}} \to [g_{\mathrm{L}}]^a{}_c [g_{\mathrm{R}}^\dagger]^{\dot{d}}{}_{\dot{b}} [\Pi]^c{}_{\dot{d}}$.

[9]Note that the unitarity of $\Pi \in SU(2)_{\mathrm{flavour}}$ implies that $\xi\xi^\dagger = 1$, and thus that $\partial_\mu(\xi\xi^\dagger) = (\partial_\mu\xi)\xi^\dagger + \xi\partial_\mu\xi^\dagger = 0$, *i.e.* $(\partial_\mu\xi)\xi^\dagger = -\xi\partial_\mu\xi^\dagger$.

where N is the heavy-baryon nucleon field (upper components of the baryon field) and $\boldsymbol{\sigma}$ is the vector of the three Pauli matrices (spin operators).

2.2.3 Two-Nucleon Contact Lagrangian

Two-nucleon contact interactions consist of four nucleon fields and no pions. These terms are necessary to renormalise loop integrals, to make the results independent of regulators, and to parameterise the unresolved low-energy dynamics of the nuclear force. The LO two-nucleon contact Lagrangian is given by

$$\mathcal{L}_{NN}^{(0)} = -\frac{1}{2}C_{\mathrm{S}}\bar{N}N\bar{N}N - \frac{1}{2}C_{\mathrm{T}}(\bar{N}\boldsymbol{\sigma}N)\cdot(\bar{N}\boldsymbol{\sigma}N), \tag{2.40}$$

where N is the heavy-baryon nucleon field and $\{C_{\mathrm{S}}, C_{\mathrm{T}}\}$ are unknown *Low-Energy Constants* (LECs) which can be determined from nucleon-nucleon interaction data [2].

2.3 The Nuclear Interaction Potential

As understood in the previous section, there are an infinite number of terms in the EFT Lagrangian, allowing for an infinite number of Feynman diagrams for the nuclear interactions. The importance of each of these Feynman diagrams is thus determined, in accordance with ChPT, by the corresponding power of $Q^\nu = (\Lambda_\pi/\Lambda_\chi)^\nu$. The determination of the power (chiral order) ν is known as *power counting*. In this project, WPC is employed, where the chiral order of a given Feynman diagram is given by

$$\nu = -2 + 2A - 2C + 2L + \sum_i \Delta_i, \quad \Delta_i \equiv d_i + \frac{n_i}{2} - 2, \tag{2.41}$$

where A is the number of nucleons in the interaction, C is the number of separately connected pieces, and L is the number of loops in the diagram. Δ_i is the interaction index of vertex i, determined by the number of derivatives or pion masses d_i and the number of nucleon fields n_i in the vertex. The Feynman diagrams for two-nucleon, three-nucleon, and four-nucleon interactions at different orders are shown in table 2.2. The benefit of ChPT, as can be concluded from the above-mentioned table, is that there exists only a finite number of diagrams that contribute at a given order ν [2].

2.3.1 Two-Nucleon Interaction potential

The covariant Bethe-Salpeter equation describing two-nucleon scattering is, in operator notation, given by

$$\mathcal{T} = \mathcal{V} + \mathcal{V}\mathcal{G}\mathcal{T}, \tag{2.42}$$

where $\mathcal{T}$ is the invariant amplitude, $\mathcal{V}$ is the sum of all connected irreducible diagrams, and $\mathcal{G}$ is the relativistic two-nucleon propagator. The Bethe-Salpeter equation can also be understood in terms of diagrams as shown in figure 2.1. The three-dimensional reduction of this equation is given by the coupled equations

$$T = V + VGT, \quad V = \mathcal{V} + \mathcal{V}(\mathcal{G} - G)V, \tag{2.43}$$

Table 2.2: The Feynman diagrams for the two-, three-, and four-nucleon forces at different orders. The solid lines are nucleons, and the dashed lines are pions. The black dots, blue rhombi, red squares, and green pentagon denote vertices of interaction index $\Delta = 0$, 1, 2, and 4, respectively. Note that there are various loop diagrams of order $\nu > 0$ that renormalise diagrams of lower orders, which are not included in this table [20].

	Nucleon Contact	One-Pion Exchange	Two-Pion Exchange	Three-Pion Exchange	Four-Pion Exchange
Two-Nucleon force					
LO ($\nu = 0$)					
NLO ($\nu = 2$)			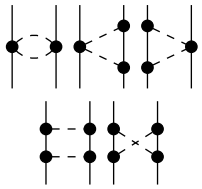		
N^{2}LO ($\nu = 3$)			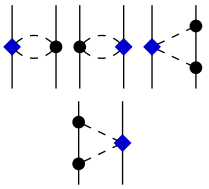		
N^{3}LO ($\nu = 4$)			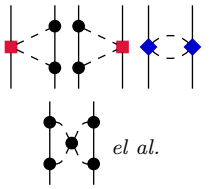 *el al.*	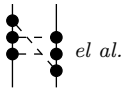 *el al.*	
Three-Nucleon force					
N^{2}LO ($\nu = 3$)		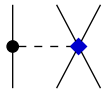	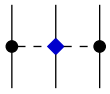		
N^{3}LO ($\nu = 4$)			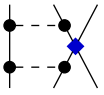 *el al.*	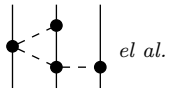 *el al.*	
Four-Nucleon force					
N^{3}LO ($\nu = 4$)		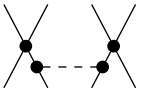 *el al.*	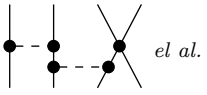 *el al.*	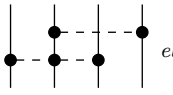 *el al.*	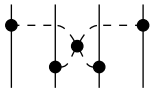

where G is a covariant three-dimensional propagator which preserves relativistic elastic unitarity [2].

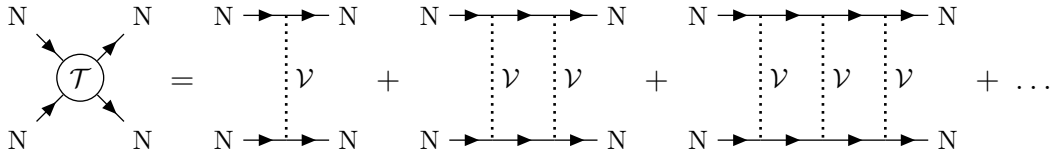

Figure 2.1: The Bethe-Salpeter equation, (2.42), relating the invariant NN scattering amplitude $\mathcal{T}$ to the sum of all connected irreducible diagrams and the relativistic two-nucleon propagator, $\mathcal{G}$.

The LO, *Next-to-Leading Order* (NLO), and *Next-to-Next-to-Leading Order* (N^{2}LO) Feynman diagrams for two-nucleon scattering can be divided into two-nucleon contact, 1PE, and *Two-Pion Exchange* (2PE) diagrams, see table 2.2. For two-nucleon scattering up to N^{2}LO, $\mathcal{V}$ can thus be expressed as

$$\mathcal{V} = \mathcal{V}_{1\pi} + \mathcal{V}_{2\pi} + \mathcal{V}_{\text{ct}}, \tag{2.44}$$

where $\mathcal{V}_{1\pi}$ is the relativistic 1PE, $\mathcal{V}_{2\pi}$ is the sum of all irreducible 2PE diagrams[10], and $\mathcal{V}_{\text{ct}}$ is the sum of all irreducible two-nucleon contact diagrams[11]. The two-nucleon potential V, as given in (2.43), then becomes

$$V = \mathcal{V}_{1\pi} + \mathcal{V}_{2\pi} + \mathcal{V}_{\text{ct}} + (\mathcal{V}_{1\pi} + \mathcal{V}_{\text{ct}})(\mathcal{G} - G)(\mathcal{V}_{1\pi} + \mathcal{V}_{\text{ct}}) = V_{1\pi} + V_{2\pi} + V_{\text{ct}} + V_{\pi\text{ct}}, \tag{2.45}$$

where terms that only contribute at *Next-to-Next-to-Next-to-Leading Order* (N^{3}LO) or higher orders ($\nu \geq 4$) have been omitted. As can be seen in table 2.3, $V_{1\pi}$ is the on-shell 1PE potential, $V_{2\pi}$ is the irreducible 2PE potential, V_{ct} is the irreducible two-nucleon contact potential, and $V_{\pi\text{ct}}$ is the potential considering irreducible parts of diagrams with pion exchange and two-nucleon contact.

The on-shell 1PE potantial can be expanded, in accordance with ChPT, as

$$V_{1\pi} = V_{1\pi}^{(0)} + V_{1\pi}^{(2)} + V_{1\pi}^{(3)} + \ldots, \tag{2.46}$$

where the superscripts indicate the chiral order ν of the expansion term. The LO 1PE potential is, in the relative momentum basis, given by[12]

$$V_{1\pi}^{(0)}(\boldsymbol{p}', \boldsymbol{p}) = -\frac{g_{\text{A}}^2}{4f_\pi^2}[\boldsymbol{\tau}^{(1)} \cdot \boldsymbol{\tau}^{(2)}]\frac{[\boldsymbol{\sigma}^{(1)} \cdot \boldsymbol{K}][\boldsymbol{\sigma}^{(2)} \cdot \boldsymbol{K}]}{|\boldsymbol{K}|^2 + m_\pi^2}, \tag{2.47}$$

where $\boldsymbol{p}$ and $\boldsymbol{p}'$ are the ingoing and outgoing relative momenta, respectively, $\boldsymbol{K} \equiv \boldsymbol{p}' - \boldsymbol{p}$ is the momentum transfer, and $\boldsymbol{\tau}^{(n)}$ and $\boldsymbol{\sigma}^{(n)}$ are the isospin operator and

[10] Note that all 2PE diagrams shown table 2.2 are irreducible except for the planar box.

[11] All irreducible two-nucleon contact diagrams are shown in table 2.2.

[12] Note that the operators $\{\boldsymbol{\sigma}^{(1)}, \boldsymbol{\sigma}^{(2)}, \boldsymbol{\tau}^{(1)}, \boldsymbol{\tau}^{(2)}\}$ act in different spaces. The operator dependence of the 1PE potential is more formally identified as $[\boldsymbol{\tau}^{(1)} \cdot \boldsymbol{\tau}^{(2)}][\boldsymbol{\sigma}^{(1)} \cdot \boldsymbol{K}][\boldsymbol{\sigma}^{(2)} \cdot \boldsymbol{K}] \equiv ([\boldsymbol{\tau}^{(1)} \otimes \mathbb{1}_{\text{isospin}}^{(2)}] \cdot [\mathbb{1}_{\text{isospin}}^{(1)} \otimes \boldsymbol{\tau}^{(2)}]) \otimes [\boldsymbol{\sigma}^{(1)} \cdot \boldsymbol{K}] \otimes [\boldsymbol{\sigma}^{(2)} \cdot \boldsymbol{K}]$.

spin operator, respectively, of nucleon $n = 1, 2$ [2]. The higher order terms $\{V_{1\pi}^{(\nu)}\}_{\nu>0}$ correspond to contributions that renormalisation the LO 1PE diagram. These potential does not provide any new momentum dependence, but instead renormalise the constants[13] in (2.47) [20].

The two-nucleon irreducible 2PE potential considers all 2PE diagrams except for the planar box diagrams, for which it only contains the non-iterative contribution, see figure 2.2. The leading contribution from 2PE appears at NLO ($\nu = 2$) and the

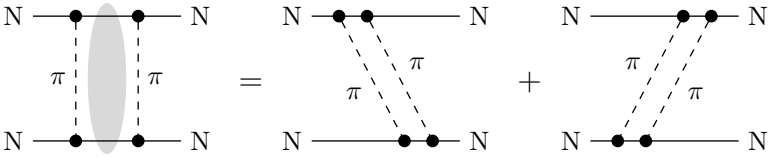

Figure 2.2: The irreducable part of the 2PE planar box Feynman diagram. The two diagrams in the last equality are time-ordered graphs [20].

irreducible 2PE potential can be expanded as

$$V_{2\pi} = V_{2\pi}^{(2)} + V_{2\pi}^{(3)} + V_{2\pi}^{(4)} + \dots . \tag{2.48}$$

The two-nucleon contact potential can be expanded, in accordance with the expansion (2.30) of the governing Lagrangian $\mathcal{L}_{NN}$, as

$$V_{\text{ct}} = V_{\text{ct}}^{(0)} + V_{\text{ct}}^{(2)} + V_{\text{ct}}^{(4)} + \dots . \tag{2.49}$$

The LO contribution, in the relative momentum basis, is given by[14]

$$V_{\text{ct}}^{(0)}(\boldsymbol{p}', \boldsymbol{p}) = C_{\text{S}} + C_{\text{T}}[\boldsymbol{\sigma}^{(1)} \cdot \boldsymbol{\sigma}^{(2)}], \tag{2.50}$$

where C_{S} and C_{T} are the LECs appearing in (2.40) [2]. The NLO contubution, $V_{\text{ct}}^{(2)}$, contains the term $\mathcal{V}_{\text{ct}}(\mathcal{G} - G)\mathcal{V}_{\text{ct}}$, which is shown in figure 2.3. The contribution from $\mathcal{V}_{\text{ct}}(\mathcal{G} - G)\mathcal{V}_{\text{ct}}$ is, however, zero since the intermediate state only contains nucleons and is thus completely reducible [20].

The $V_{\pi\text{ct}}$ potential can be expanded as

$$V_{\pi\text{ct}} = V_{\pi\text{ct}}^{(2)} + V_{\pi\text{ct}}^{(4)} + V_{\pi\text{ct}}^{(5)} + V_{\pi\text{ct}}^{(6)} + \dots , \tag{2.51}$$

and are the contributions from the irreducible parts of diagrams containing both two-nucleon contacts and pion exchanges. The leading diagrams of that kind are shown in figure 2.4. The $V_{\pi\text{ct}}$ potential only leads to pion-mass-dependent shifts of the LECs in V_{ct} and will thus not produce any new momentum dependence [20].

[13] The renormalisation of the 1PE potential is solved by using the empirical values for g_{A}, f_π, m_π, and M_{N} and adding an shift to g_{A} known as the *Goldberger-Treiman discrepancy*. This project only considers the LO NN interaction potential and will thus not dissect the details of the 1PE renormalisation and instead refer interested readers to [20, 21].

[14] The two terms in two-nucleon potential are more formally identified as $C_{\text{S}} \equiv C_{\text{S}}[\mathbb{1}_{\text{spin}}^{(1)} \otimes \mathbb{1}_{\text{spin}}^{(2)} \otimes \mathbb{1}_{\text{isospin}}^{(1)} \otimes \mathbb{1}_{\text{isospin}}^{(2)}]$ and $C_{\text{T}}[\boldsymbol{\sigma}^{(1)} \cdot \boldsymbol{\sigma}^{(2)}] \equiv C_{\text{T}}[([\boldsymbol{\sigma}^{(1)} \otimes \mathbb{1}_{\text{spin}}^{(2)}] \cdot [\mathbb{1}_{\text{spin}}^{(1)} \otimes \boldsymbol{\sigma}^{(2)}]) \otimes \mathbb{1}_{\text{isospin}}^{(1)} \otimes \mathbb{1}_{\text{isospin}}^{(2)}]$.

$$\mathcal{V}_{\rm ct}(\mathcal{G}-G)\mathcal{V}_{\rm ct} \;=\;$$ 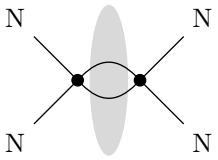

$$\;=\;0$$

Figure 2.3: The (zero) contribution to $V_{\rm ct}^{(2)}$ from the $\mathcal{V}_{\rm ct}(\mathcal{G}-G)\mathcal{V}_{\rm ct}$ diagram.

$$\mathcal{V}_{1\pi}(\mathcal{G}-G)\mathcal{V}_{\rm ct}+\mathcal{V}_{\rm ct}(\mathcal{G}-G)\mathcal{V}_{1\pi} \;=\;$$ 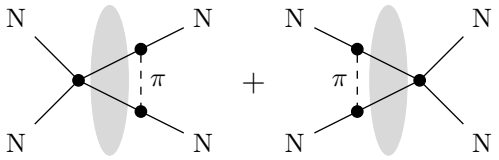

Figure 2.4: The leading contribution to the $V_{\pi{\rm ct}}$ potential.

The NN interaction potential at LO, NLO, and N^{2}LO is thus given by

$$V_{\rm NN}^{\rm LO}=V_{1\pi}^{(0)}+V_{\rm ct}^{(0)}, \tag{2.52}$$

$$V_{\rm NN}^{\rm NLO}=\tilde{V}_{\rm NN}^{\rm LO}+V_{2\pi}^{(2)}+V_{\rm ct}^{(2)}, \tag{2.53}$$

$$V_{\rm NN}^{\rm N^2LO}=\tilde{V}_{\rm NN}^{\rm NLO}+V_{2\pi}^{(3)}, \tag{2.54}$$

where the tilde implies that the potential constants have been appropriately renormalised and shifted. A summary of the diagrams that contribute to these potentials can be seen in Table 2.3. Of particular interest in this project is the LO NN interaction potential, which in the relative momentum basis is given by

$$V_{\rm NN}^{\rm LO}(\boldsymbol{p}',\boldsymbol{p})=-\frac{g_A^2}{4f_\pi^2}[\boldsymbol{\tau}^{(1)}\cdot\boldsymbol{\tau}^{(2)}]\frac{[\boldsymbol{\sigma}^{(1)}\cdot\boldsymbol{K}][\boldsymbol{\sigma}^{(2)}\cdot\boldsymbol{K}]}{|\boldsymbol{K}|^2+m_\pi^2}+C_{\rm S}+C_{\rm T}[\boldsymbol{\sigma}^{(1)}\cdot\boldsymbol{\sigma}^{(2)}]. \tag{2.55}$$

2.3.2 Regularisation

The nucleon-nucleon interaction potential was, in the previous subsection, constructed with ChPT, which is a low-momentum expansion, and is thus only valid for ingoing and outgoing relative momenta much smaller than the chiral symmetry breaking scale, *i.e.* $|\boldsymbol{p}|,|\boldsymbol{p}'|\ll\Lambda_\chi\sim 1\,\text{GeV}$. The interaction potential is, therefore, regularised by including the factor

$$f_\Lambda(\boldsymbol{p}',\boldsymbol{p})=e^{-\left[\frac{|\boldsymbol{p}'|}{\Lambda}\right]^{2n}}e^{-\left[\frac{|\boldsymbol{p}|}{\Lambda}\right]^{2n}}, \tag{2.56}$$

where Λ is the momentum cutoff and n determines the sharpness of the cutoff. The regularisation effectively dampens the potential for ingoing and outgoing relative momenta larger than the cutoff Λ. The regularised potential is then given by

$$V_{\rm NN}(\boldsymbol{p}',\boldsymbol{p})=V_{\rm NN}^{\rm LO}(\boldsymbol{p}',\boldsymbol{p})f_\Lambda(\boldsymbol{p}',\boldsymbol{p}). \tag{2.57}$$

The LECs $\{C_{\rm S},C_{\rm T}\}$ appearing in the two-nucleon contact potential can be determined by fitting quantities predicted with the potential to experimental data. The LECs are, therefore, dependent on the chosen cutoff (and cutoff sharpness), *i.e.*

$$V_{\rm NN}(\boldsymbol{p}',\boldsymbol{p})=V_{\rm NN}^{\rm LO}(\boldsymbol{p}',\boldsymbol{p};\Lambda)f_\Lambda(\boldsymbol{p}',\boldsymbol{p}), \tag{2.58}$$

Table 2.3: The diagrams that contribute to the on-shell 1PE potential, $V_{1\pi}$, the irreducible 2PE potential, $V_{2\pi}$, the irreducible two-nucleon contact potential, V_{ct}, up to N^{2}LO. The black dots, blue rhombi, and red square denote vertices of interaction index $\Delta = 0$, 1, and 2, respectively. The large grey blob indicate that only the irreducible part of the diagram contributes *i.e.* $\mathcal{G} - G$. Note that diagrams that only renormalise or shift diagrams of lower orders are not included in this table [20].

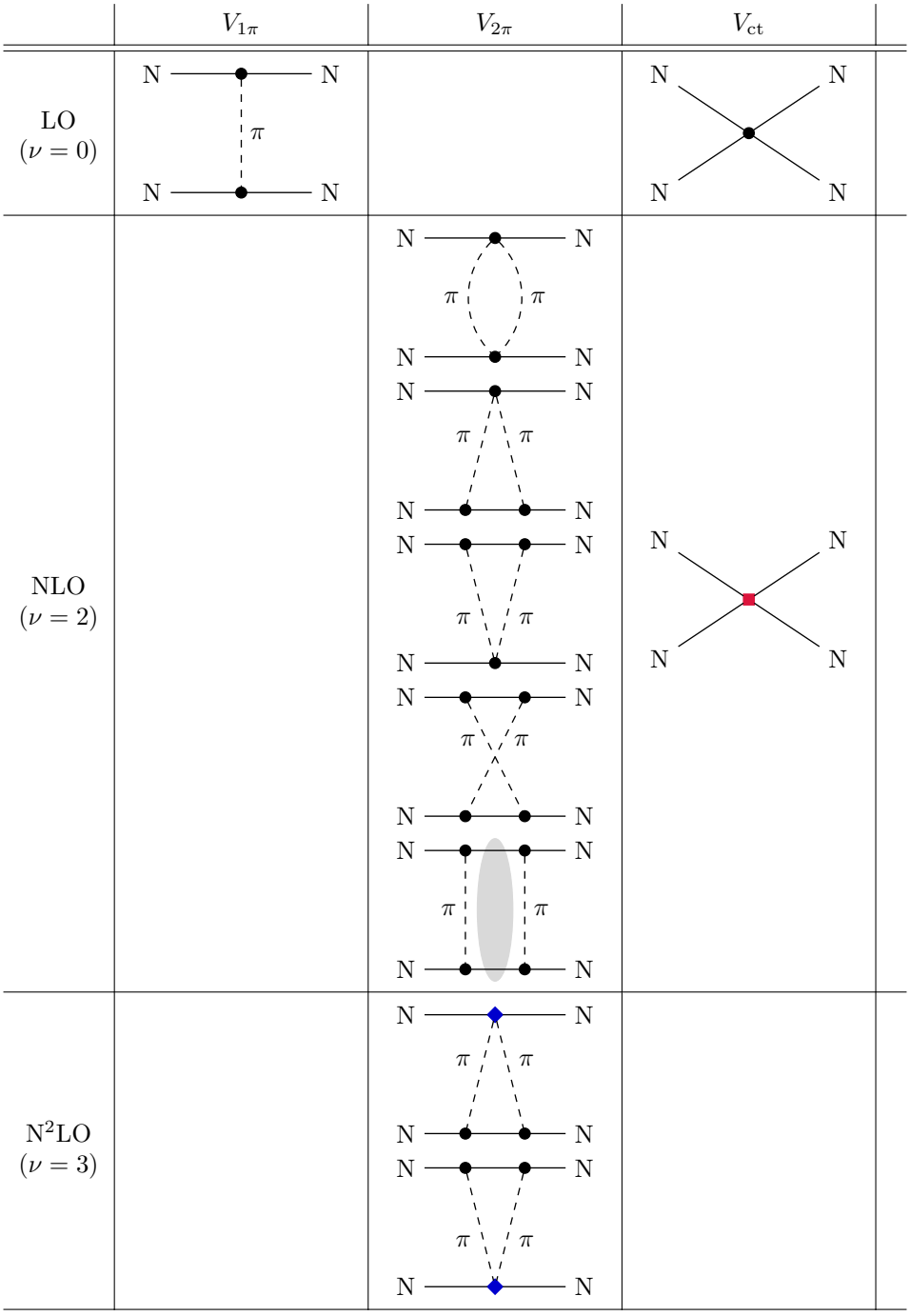

where

$$V_{\mathrm{NN}}^{\mathrm{LO}}(\boldsymbol{p}', \boldsymbol{p}; \Lambda) = -\frac{g_A^2}{4f_\pi^2}[\boldsymbol{\tau}^{(1)} \cdot \boldsymbol{\tau}^{(2)}]\frac{[\boldsymbol{\sigma}^{(1)} \cdot \boldsymbol{K}][\boldsymbol{\sigma}^{(2)} \cdot \boldsymbol{K}]}{|\boldsymbol{K}|^2 + m_\pi^2} + C_{\mathrm{S}}(\Lambda) + C_{\mathrm{T}}(\Lambda)[\boldsymbol{\sigma}^{(1)} \cdot \boldsymbol{\sigma}^{(2)}]. \tag{2.59}$$

The resulting potential, $V_{\mathrm{NN}}, (\boldsymbol{p}', \boldsymbol{p})$ and the quantities predicted with the potential should, however, be independent of the choice of Λ (and n) given that the fitting of the LECs resolves the low-momentum details of the potential.

3

Scattering Theory

The first sections (section 3.1) in this chapter cover the general basics of quantum mechanical scattering theory and introduce the relevant concepts and operators. The second section (section 3.2) introduces the problem of scattering of two particles with spin and isospin. The third section (section 3.3) is the main body of the chapter and concerns the more specific problem of NN scattering. Subsection 3.3.1 takes a detailed look at the relevant states both in the relative momentum state basis and the *Partial-Wave States* (PWS) basis. Subsection 3.3.2 investigates the symmetries of the NN states and LO χEFT potential (see chapter 2). These symmetries are of high interest for the project as they constrain the scattering matrix (discussed in subsection 3.3.4) and allow us, in chapter 4, to distil the NN scattering quantities down to five complex *scattering amplitudes*. Subsection 3.3.3 presents the *Lippmann-Schwinger equation* in the relevant basis for the numerical treatment of the NN scattering problem in part II of this thesis. The closing subsection (subsection 3.4) introduces the concept of minimal relativity, which scales the LO χEFT potential of chapter 2 such that it is consistent with our non-relativistic treatment of the scattering problem as presented in this chapter.

3.1 Scattering Theory in Operators

The dynamics of a closed and isolated quantum mechanical system[1] is governed by the *time-dependent Schrödinger equation*

$$i\frac{d}{dt}\left|\psi(t)\right\rangle = H\left|\psi(t)\right\rangle, \tag{3.1}$$

[1] A quantum mechanical system is closed when the dynamics of the system can be represented with a unitary time-evolution operator, *i.e.* the Hamiltonian is Hermitian. An isolated system additionally requires that the energy of the system is conserved in time, *i.e.* there are no energy or matter exchanges between the system and some outside environment. Note that all isolated systems are closed, but not all closed systems are isolated [22].

where H is the *Hamiltonian* of the system and the time-dependent solution states (vectors) $|\psi(t)\rangle$ are elements of an *Hilbert space*[2] $\mathscr{H}$. The Hamiltonian is *Hermitian*[3], *i.e.* $H^\dagger = H$, and can generally be expressed as

$$H = H_0 + V, \tag{3.2}$$

where H_0 is the free Hamiltonian that determines the kinetic energy of the system, and V is the potential that determines the potential energy of the system. The Hilbert space $\mathscr{H}$ is spanned by the eigenstates of the Hamiltonian, *i.e.* the solutions $|\psi\rangle \equiv |\psi(t_0)\rangle$ to the *time-independend Schrödinger equation*

$$H\,|\psi\rangle = E\,|\psi\rangle\,, \tag{3.3}$$

where the eigenvalues E are interpreted as the total eigenenergies (kinetic plus potential energy) of the states $|\psi\rangle \in \mathscr{H}$. The time-dependent states $|\psi(t)\rangle \in \mathscr{H}$ are related to the time-independent states $|\psi\rangle \equiv |\psi(t_0)\rangle \in \mathscr{H}$ as

$$|\psi(t)\rangle = U(t,t_0)\,|\psi(t_0)\rangle\,, \quad U(t,t_0) = e^{-iH(t-t_0)}, \tag{3.4}$$

where $U(t,t_0)$ is the so-called *time-evolution operator*. This relation is realised by noting that the states $|\psi(t)\rangle = U(t,t_0)\,|\psi(t_0)\rangle$ are general solutions to the time-dependent Schrödinger equation. Note also that the time-evolution operator, as given in (3.4), is unitary, *i.e.*

$$U^\dagger(t,t_0)U(t,t_0) = 1, \tag{3.5}$$

given that the Hamiltonian is Hermitian (and trivially that $[H,H] = 0$).

When investigating the dynamics of a scattering system, it is necessary to assume that the potential in the Hamiltonian is an interaction potential that is local in position-space, *i.e.*

$$V(\boldsymbol{x}',\boldsymbol{x}) \equiv \langle \boldsymbol{x}'|\,V\,|\boldsymbol{x}\rangle = V(\boldsymbol{x})\delta^{(3)}(\boldsymbol{x}'-\boldsymbol{x}), \tag{3.6}$$

where $|\boldsymbol{x}\rangle$ (and $|\boldsymbol{x}'\rangle$) are position eigenstates. The definition of the space coordinate depends on the scattering system in question; for a specific system, see section 3.2. It is also assumed[4] that the potential obeys [25]:

1. The potential has finite range and approaches zero sufficiently fast for large $r \equiv |\boldsymbol{x}|$, more precisely $|V(\boldsymbol{x})| < cr^{-3}$ as $r \to \infty$ for some constant $c \in \mathbb{R}$.

2. The potential is less singular than $r^{-3/2}$, *i.e.* $|V(\boldsymbol{x})| < cr^{-3/2}$ for some constant $c \in \mathbb{R}$, in the $r \to 0$ limit.

[2] A Hilbert space is a real or complex vector space $\mathscr{H}$ with an inner product $\langle x,y\rangle$, that is conjugate symmetric, linear in its first argument, and positive definite when $x = y$, for all $x,y \in \mathscr{H}$ [23].

[3] The Hermitian property of the Hamiltonian (of a closed system) is fundamental as it ensures that the eigenenergies are real, that the eigenstates are orthogonal, and that the time-evolution operator is unitary [24].

[4] Note that these assumptions are not strictly necessary to treat the interaction as a scattering problem, but lenient enough for the regularised potential presented in chapter 2.

3. The potential is continuous for $0 < r < \infty$, except perhaps at a finite number of finite discontinuities.

The time parameter t_0 is then chosen to be $t_0 = 0$ and defined to be a time $t = 0$ close to the time of the scattering event, *i.e.* that the system state is in the vicinity of the non-zero potential region in the Hilbert space around $t = 0$. It is then given that the state of the scattering system at time t, $|\psi(t)\rangle \in \mathscr{H}$, is given by

$$|\psi(t)\rangle = U(t)\,|\psi\rangle\,, \quad U(t) = U(t,0) = e^{-iHt}, \tag{3.7}$$

where $|\psi\rangle \equiv |\psi(0)\rangle \in \mathscr{H}$ is the scattering state of the system at time $t = 0$.

If the potential obeys the above conditions, then for every scattering state[5] $|\psi\rangle \in \mathscr{H}$ there exists an in-asymptote state $|\psi_{\text{in}}\rangle \in \mathscr{H}$ and an out-asymptote state $|\psi_{\text{out}}\rangle \in \mathscr{H}$ such that

$$\lim_{t\to-\infty}\left[U(t)\,|\psi\rangle - U_0(t)\,|\psi_{\text{in}}\rangle\right] = 0, \quad \lim_{t\to\infty}\left[U(t)\,|\psi\rangle - U_0(t)\,|\psi_{\text{out}}\rangle\right] = 0, \tag{3.8}$$

where $U_0(t) \equiv e^{-iH_0t}$ is the free time-evolution operator. The scattering state can, therefore, be expressed as

$$|\psi\rangle = \Omega_+\,|\psi_{\text{in}}\rangle\,, \quad |\psi\rangle = \Omega_-\,|\psi_{\text{out}}\rangle\,, \quad \Omega_\pm \equiv \lim_{t\to\mp\infty} U^\dagger(t)U_0(t), \tag{3.9}$$

where $\Omega_\pm$ are the so-called *Møller operators* [25]. It is also true that every state $|\psi_{\text{in}}\rangle$ ($|\psi_{\text{out}}\rangle$) in $\mathscr{H}$ can be considered to be the in (out) asymptote for some scattering state with a unique out (in) asymptote $|\psi_{\text{out}}\rangle$ ($|\psi_{\text{in}}\rangle$) in $\mathscr{H}$. The Møller operators can therefore be thought of as isometric operators that map states as

$$\Omega_+ : \mathscr{H} \to \mathscr{R}, \quad \Omega_+^\dagger : \mathscr{R} \to \mathscr{H}, \tag{3.10}$$

$$\Omega_- : \mathscr{H} \to \mathscr{R}, \quad \Omega_- : \mathscr{R} \to \mathscr{H}, \tag{3.11}$$

where $\mathscr{R}$ is the subspace of $\mathscr{H} = \mathscr{B} \oplus \mathscr{R}$ containing all scattered states, and $\mathscr{B}$ is the subspace of all bound states. The isometric nature of the Møller operators implies that $\Omega_\pm^\dagger\Omega_\pm = 1$ and that the relations (3.9) can be inverted. It is thus given that the out-asymptote can be determined from the in-asymptote as

$$|\psi_{\text{out}}\rangle = S\,|\psi_{\text{in}}\rangle\,, \quad S \equiv \Omega_-^\dagger\Omega_+, \tag{3.12}$$

where S is the *scattering operator*, which is a unique map from $\mathscr{H}$ to $\mathscr{H}$, *i.e.* the S operator is unitary $S^\dagger S = 1$.

3.1.1 The Lippmann-Schwinger Operator Equation

This subsection considers the *free states* $|\phi_{\boldsymbol{k}}\rangle \in \mathscr{H}$ to be defined as solutions to the free Schrödinger equation

$$H_0\,|\phi_{\boldsymbol{k}}\rangle = E\,|\phi_{\boldsymbol{k}}\rangle\,, \quad E = \frac{|\boldsymbol{k}|^2}{2\mu}, \tag{3.13}$$

[5] A scattering state is a state with both an in- and an out-asymptote, unlike a bound state, which has neither an in- nor out-asymptote.

where H_0 is the free Hamiltonian and E is the eigenenergy (on-shell energy). The *scattered states* $|\psi_{\boldsymbol{k}}^{\pm}\rangle \in \mathscr{H}$ are then defined to be the solutions to the full Schrödinger equation with the eigenenergy given by the on-shell energy E, *i.e.*

$$H\,|\psi_{\boldsymbol{k}}^{\pm}\rangle = E\,|\psi_{\boldsymbol{k}}^{\pm}\rangle\,, \tag{3.14}$$

where $H = H_0 + V$ is the full Hamiltonain and V is the potential operator. For (3.13) and (3.14) to be true simultaneously, the scattering and free states must satisfy

$$|\psi_{\boldsymbol{k}}^{\pm}\rangle = |\phi_{\boldsymbol{k}}\rangle + G_0^{\pm}(E)V\,|\psi_{\boldsymbol{k}}^{\pm}\rangle\,, \quad G_0^{\pm}(E) = \frac{1}{E - H_0 \pm i\epsilon}, \tag{3.15}$$

where $G_0^{+}(E)$ and $G_0^{-}(E)$ are the free *retarded* and *advanced Green's operator*, respectively, for the on-shell energy [25, 26], and $i\epsilon$ is a small complex ($\epsilon \to 0^{+}$, $\epsilon \in \mathbb{R}$) shift of the Green's operator's singularites[6]. This equation is called the LS *equation* for the scattering state $|\psi_{\boldsymbol{k}}^{\pm}\rangle$. The $|\psi_{\boldsymbol{k}}^{-}\rangle$ results in a unphysical collapsing scattering wave making $|\psi_{\boldsymbol{k}}^{+}\rangle$, resulting in a outwards radiating spherically scattering wave, the only physical solution to the scattering problem [27].

The $T^{\pm}$ operator is introduced and defined to satisfy

$$T^{\pm}(E)\,|\phi_{\boldsymbol{k}}\rangle = V\,|\psi_{\boldsymbol{k}}^{\pm}\rangle\,, \quad E = \frac{|\boldsymbol{k}|^2}{2\mu}, \tag{3.16}$$

where E is the on-shell energy. Equation (3.15) can then be rewritten as

$$|\psi_{\boldsymbol{k}}^{\pm}\rangle = |\phi_{\boldsymbol{k}}\rangle + G_0^{\pm}(E)T^{\pm}(E)\,|\phi_{\boldsymbol{k}}\rangle\,. \tag{3.17}$$

By multiplying both sides of this equation from the left with V and implementing the definition of $T^{\pm}$, one discovers the *LS operator equation*

$$T^{\pm}(E) = V + VG_0^{\pm}(E)T^{\pm}(E). \tag{3.18}$$

An alternative, but equivalent, expression for the T operator can, by manipulating (3.18), be found as

$$T^{\pm}(E) = V + VG^{\pm}(E)V, \quad G^{\pm}(E) = \frac{1}{E - H \pm i\epsilon}, \tag{3.19}$$

where $G^{\pm}(E)$ is the full Greens operator and H is the full Hamiltonian. It is from this equation apparent that $[T^{\pm}(E)]^{\dagger} = T^{\mp}(E)$, given that the potential is Hermitian.

At last, the definition of the S operator implies that

$$\langle\phi_{\boldsymbol{k}'}|\,S\,|\phi_{\boldsymbol{k}}\rangle = \langle\psi_{\boldsymbol{k}'}^{\mp}|\psi_{\boldsymbol{k}}^{\pm}\rangle\,. \tag{3.20}$$

It can then, with the use of (3.17), be shown that

$$S(E) = \mathbb{1} - 2i\pi\delta(E - H_0)T^{+}(E), \tag{3.21}$$

where $S(E)$ is the S operator for on-shell energy E [27].

[6]The purpose of the $i\epsilon$ term is to move the singularities of the momentum space free Green's function $G_0^{\pm}(\boldsymbol{p}', \boldsymbol{p}; E) \equiv \langle\boldsymbol{p}'|\,G_0^{\pm}(E)\,|\boldsymbol{p}\rangle$ from the real axis such that it is *well defined* for all $E \in \mathbb{R}^{+}$, *i.e.* making $(E - H_0 \pm i\epsilon)$ invertible, which it is not for $\epsilon = 0$ [26]. Physically, the inclusion of $+i\epsilon$ ($\epsilon > 0$) is equivalent to the boundary condition that the scattering wave radiates outwards, in contrast to $-i\epsilon$ that results in a collapsing scattering wave [27].

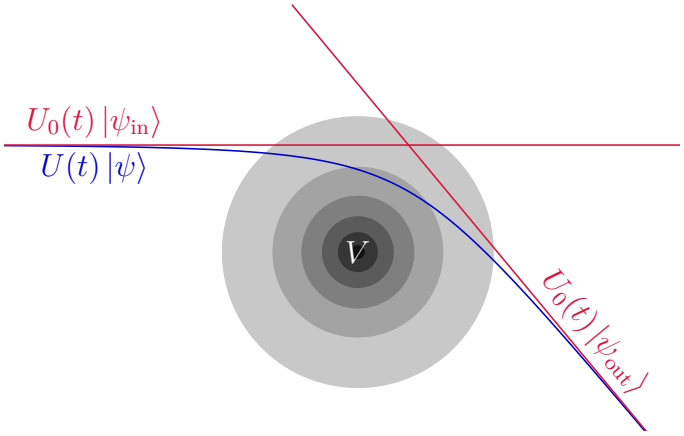

Figure 3.1: The time-dependent trajectory of the scattering state $|\psi(t)\rangle = U(t)\,|\psi\rangle$ (blue) under the effect of a potential (V) in the Hilbert space. The trajectories of the freely evolving states (red) $|\psi_{\text{in}}(t)\rangle = U_0(t)\,|\psi_{\text{in}}\rangle$ and $|\psi_{\text{out}}(t)\rangle = U_0(t)\,|\psi_{\text{out}}\rangle$ are asymptotes of the scattering state at $t \to -\infty$ and $t \to +\infty$, respectively.

3.2 Two-Particle Scattering

This section considers a system of two massive particles with masses and canonical coordinates[7] given by $\{m_i, (\boldsymbol{x}_i, \boldsymbol{p}_i)\}_{i=1,2}$, where the particles are scattered of each other through a mutual interaction potential. The fact that the single-particle coordinates $(\boldsymbol{x}_i, \boldsymbol{p}_i)$ are canonical is realised by evaluating the commutation relation of the quantum mechanical position-space operators $\boldsymbol{x}_i$ and $\boldsymbol{p}_i = -i\boldsymbol{\nabla}_{\boldsymbol{x}_i}$ as it acts on a wave function $\psi(\boldsymbol{x}_i) \equiv \langle \boldsymbol{x}_i | \psi \rangle$, which gives

$$[\boldsymbol{x}_i, \boldsymbol{p}_i]\psi(\boldsymbol{x}_i) = -i\boldsymbol{x}_i \cdot \boldsymbol{\nabla}_{\boldsymbol{x}_i}\psi(\boldsymbol{x}_i) + i\boldsymbol{\nabla}_{\boldsymbol{x}_i} \cdot [\boldsymbol{x}_i\psi(\boldsymbol{x}_i)] = i\psi(\boldsymbol{x}_i). \tag{3.22}$$

It is thus given that the single-particle coordinates $(\boldsymbol{x}_i, \boldsymbol{p}_i)$, for particle $i = 1, 2$, satisfy the canonical computation relations

$$[\boldsymbol{x}_i, \boldsymbol{x}_i] = [\boldsymbol{p}_i, \boldsymbol{p}_i] = 0, \quad [\boldsymbol{x}_i, \boldsymbol{p}_i] = i, \tag{3.23}$$

and is thus canonical coordinates [24]. Note also that

$$[\boldsymbol{x}_1, \boldsymbol{x}_2] = [\boldsymbol{p}_1, \boldsymbol{p}_2] = 0, \quad [\boldsymbol{x}_1, \boldsymbol{p}_2] = [\boldsymbol{x}_2, \boldsymbol{p}_1] = 0. \tag{3.24}$$

The dynamics of the two-particle system is governed by the (full) Hamiltonian

$$H = \frac{|\boldsymbol{p}_1|^2}{2m_1} + \frac{|\boldsymbol{p}_2|^2}{2m_1} + V_{12}(\boldsymbol{x}_1 - \boldsymbol{x}_2) = H_0 + V_{12}(\boldsymbol{x}_1 - \boldsymbol{x}_2) \tag{3.25}$$

where H_0 is the free Hamiltonian of the two-particle system and $V_{12}(\boldsymbol{x}_1 - \boldsymbol{x}_2)$ is the interaction potential [27]. The potential is assumed to be local and transitional invariant, *i.e.* only depending on the relative position of the particles, $\boldsymbol{x} \equiv \boldsymbol{x}_1 - \boldsymbol{x}_2$. The Hilbert space of the two-particle system is given by

$$\mathscr{H}^{12} = \mathscr{H}^1 \otimes \mathscr{H}^2, \tag{3.26}$$

[7] A set of coordinates $(\boldsymbol{x}, \boldsymbol{p})$ are canonical in quantum mechanics if they satisfy the canonical commutation relation $[\boldsymbol{x}, \boldsymbol{p}] = i$ [27].

where $\mathscr{H}^i$ is the individual Hilbert space of particle $i = 1, 2$.

The canonical coordinates of the two-particle system $\{(\boldsymbol{x}_i, \boldsymbol{p}_i)\}_{i=1,2}$ can be used to define *center-of-mass* (c.m.) coordinates $(\bar{\boldsymbol{x}}, \bar{\boldsymbol{p}})$ and relative coordinates $(\boldsymbol{x}, \boldsymbol{p})$ as

$$\bar{\boldsymbol{x}} \equiv \frac{m_1\boldsymbol{x}_1 + m_2\boldsymbol{x}_2}{m_1 + m_2}, \qquad \bar{\boldsymbol{p}} \equiv \boldsymbol{p}_1 + \boldsymbol{p}_2 \tag{3.27a}$$

$$\boldsymbol{x} \equiv \boldsymbol{x}_1 - \boldsymbol{x}_2, \qquad \boldsymbol{p} \equiv \frac{m_2\boldsymbol{p}_1 - m_1\boldsymbol{p}_2}{m_1 + m_2} \tag{3.27b}$$

By then defining the total mass M and reduced mass μ of the two-particle system as

$$M \equiv m_1 + m_2, \quad \mu \equiv \frac{m_1 m_2}{m_1 + m_2}, \tag{3.28}$$

the Hamiltonian, in (3.25), can be written as

$$H = \frac{|\bar{\boldsymbol{p}}|^2}{2M} + \left[\frac{|\boldsymbol{p}|^2}{2\mu} + V_{12}(\boldsymbol{x})\right] \equiv H_{\text{c.m.}} + H_{\text{rel.}}, \tag{3.29}$$

where $H_{\text{c.m.}} = H_{0,\text{c.m.}}$ is the full c.m. Hamiltonian and $H_{\text{rel.}} = H_{0,\text{rel.}} + V_{12}(\boldsymbol{x})$ is the full relative Hamiltonian, and $H_{0,\text{c.m.}} = |\bar{\boldsymbol{p}}|^2/(2M)$ and $H_{0,\text{rel.}} = |\boldsymbol{p}|^2/(2\mu)$ are the corresponding free Hamiltonians. The commutation relations (3.23) and (3.24) implies that the c.m. and relative coordinates satisfy the canonical commutation relations

$$\begin{aligned} [\bar{\boldsymbol{x}}, \bar{\boldsymbol{x}}] = [\bar{\boldsymbol{p}}, \bar{\boldsymbol{p}}] = 0, \quad [\bar{\boldsymbol{x}}, \bar{\boldsymbol{p}}] = i, \\ [\boldsymbol{x}, \boldsymbol{x}] = [\boldsymbol{p}, \boldsymbol{p}] = 0, \quad [\boldsymbol{x}, \boldsymbol{p}] = i, \end{aligned} \tag{3.30}$$

and are thus canonical coordinates. It is thus given that the two-particle Hilbert space can be expressed as

$$\mathscr{H}^{12} = \mathscr{H}^{\text{c.m.}} \otimes \mathscr{H}^{\text{rel.}}, \tag{3.31}$$

where $\mathscr{H}^{\text{c.m.}}$ describes the motion of the c.m. position only and $\mathscr{H}^{\text{rel.}}$ describes the relative motion.

3.2.1 States for Two Particles with Spin and Isospin

For a system of two particles with spin and isospin, the two-particle states can be expressed as

$$|\bar{\boldsymbol{p}}\rangle \otimes |\boldsymbol{p}\rangle \otimes |s_1, s_2; m_{s_1}, m_{s_2}\rangle \otimes |t_1, t_2; m_{t_1}, m_{t_2}\rangle\,, \tag{3.32}$$

where $|\bar{\boldsymbol{p}}\rangle \in \mathscr{H}^{\text{c.m.}}$ are the two-particle c.m. momentum eigenstates and $|\boldsymbol{p}\rangle \otimes |s_1, s_2; m_{s_1}, m_{s_2}\rangle \otimes |t_1, t_2; m_{t_1}, m_{t_2}\rangle \in \mathscr{H}^{\text{rel.}}$ are the two-particle relative states composed of the relative momentum, spin, and isospin states. The two-particle uncoupled spin states are given by

$$|s_1, s_2; m_{s,1}, m_{s,2}\rangle = |s_1, m_{s,1}\rangle \otimes |s_2, m_{s,2}\rangle\,, \tag{3.33}$$

where s_n is the single-particle spin quantum number and $m_{s,n} \in \{-s_n, -s_n + 1, \ldots, s_n\}$ is the single-particle spin projection of particle $n = 1, 2$. The two-particle uncoupled isospin states are, similarly, given by

$$|t_1, t_2; m_{t,1}, m_{t,2}\rangle = |t_1, m_{t,1}\rangle \otimes |t_2, m_{t,2}\rangle \,, \tag{3.34}$$

where t_n is the single-particle isospin quantum number and $m_{t,n} \in \{-t_n, -t_n + 1, \ldots, t_n\}$ is the single-particle isospin projection of particle $n = 1, 2$. The uncoupled spin and isospin states are defined such that

$$[\boldsymbol{S}^{(n)}]^2 \, |s_n, m_{s,n}\rangle = s_n(s_n+1) \, |s_n, m_{s,n}\rangle \,, \quad S_z^{(n)} \, |s_n, m_{t,n}\rangle = m_{s,n} \, |s_n, m_{t,n}\rangle \,, \tag{3.35}$$

$$[\boldsymbol{T}^{(n)}]^2 \, |t_n, m_{t,n}\rangle = t_n(t_n+1) \, |t_n, m_{t,n}\rangle \,, \quad T_z^{(n)} \, |t_n, m_{t,n}\rangle = m_{t,n} \, |t_n, m_{t,n}\rangle \,, \tag{3.36}$$

where $\boldsymbol{S}^{(n)} = (S_x^{(n)}, S_y^{(n)}, S_z^{(n)})^T$ and $\boldsymbol{T}^{(n)} = (T_x^{(n)}, T_y^{(n)}, T_z^{(n)})^T$ are the spin and isospin operators[8], respectively, of particle $n = 1, 2$. The two-particle uncoupled states can be expressed in terms of coupled states as

$$|s_1, s_2; m_{s,1}, m_{s,2}\rangle = \sum_s \sum_{m_s=-s}^{s} C^{s,m_s}_{s_1,s_2;m_{s,1},m_{t,2}} \, |s_1, s_2; s, m_s\rangle \,, \tag{3.37}$$

$$|t_1, t_2; m_{t,1}, m_{t,2}\rangle = \sum_t \sum_{m_t=-t}^{t} C^{t,m_t}_{t_1,t_2;m_{t,1},m_{t,2}} \, |t_1, t_2; t, m_t\rangle \,, \tag{3.38}$$

where $C^{j,m_j}_{j_1,j_2;m_{j,1},m_{j,2}} \equiv \langle j_1, j_2; m_{j,1}, m_{j,2} | j_1, j_2; j, m_j\rangle$ are the *Clebsch-Gordan coefficients*. In accordance with the vector addition rules $\boldsymbol{J} = \boldsymbol{J}^{(1)} \otimes \mathbb{1}^{(2)} + \mathbb{1}^{(1)} \otimes \boldsymbol{J}^{(2)}$, the Clebsch-Gordan coefficients $C^{j,m_j}_{j_1,j_2;m_{j,1},m_{j,2}}$ vanishes unless the quantum numbers $\{j, j_1, j_2\}$ fulfils the triangle conditions[9] (triangle inequalities)

$$|j_1 - j_2| \leq j \leq j_1 + j_2, \quad |j_2 - j| \leq j_1 \leq j_2 + j, \quad |j - j_1| \leq j_2 \leq j + j_1, \tag{3.39}$$

and the corresponding projections $\{m_j, m_{j,1}, m_{j,2}\}$ satisfy[10]

$$m = m_{j,1} + m_{j,2}. \tag{3.40}$$

It is thus given that the Clebsch-Gordan coefficients satisfy

$$C^{j,m_j}_{j_1,j_2;m_{j,1},m_{j,2}} = \delta^{m_j - m_{j,2}}_{m_{j,1}} C^{j,m_j}_{j_1,j_2;m_j - m_{j,2},m_{j,2}}, \tag{3.41}$$

and the unitarity relations[11]

$$\sum_{m_{j,1}=-j_1}^{j_1} \sum_{m_{j,2}=-j_2}^{j_2} C^{j',m'_j}_{j_1,j_2;m_{j,1},m_{j,2}} C^{j,m_j}_{j_1,j_2;m_{j,1},m_{j,2}} = \delta_{j'j} \delta_{m'_j m_j} \tag{3.42}$$

$$\sum_j \sum_{m_j=-j}^{j} C^{j,m_j}_{j_1,j_2;m'_{j,1},m'_{j,2}} C^{j,m_j}_{j_1,j_2;m_{j,1},m_{j,2}} = \delta_{m'_{j,1} m_{j,1}} \delta_{m'_{j,2} m_{j,1}}, \tag{3.43}$$

[8]Note that the single-particle spin and isospin operators in this chapter are related to those in chapter 2 as $\boldsymbol{S}^{(n)} \equiv \frac{1}{2}\boldsymbol{\sigma}^{(n)}$ and $\boldsymbol{T}^{(n)} \equiv \frac{1}{2}\boldsymbol{\tau}^{(n)}$, respectively.

[9]Note that the triangle inequalities are cyclical and all are true if one is true.

[10]Note that this equality is the direct consequence of $J_z = J_z^{(1)} \otimes \mathbb{1}^{(2)} + \mathbb{1}^{(1)} \otimes J_z^{(2)}$.

[11]These relations are easily derived from the completeness identities of the orthonormal $|j_1, j_2; m_{j,1}, m_{j,2}\rangle$ and $|j_1, j_2; j, m_j\rangle$ states.

where $\delta_m^{m'} = \delta_{m'm}$ is the Kronecker delta [28]. An alternative to the Clebsch-Gordan coefficients are the so-called *Wigner 3j-symbols*, which are related to the Clebsch-Gordan coefficients as [24]

$$C^{j,m}_{j_1,j_2;m_1,m_2} \equiv \langle j_1, j_2; m_1, m_2 | j_1, j_2; j, m \rangle = \\ = (-1)^{j_1 - j_2 + m} \sqrt{2j+1} \begin{pmatrix} j_1 & j_2 & j \\ m_1 & m_2 & -m \end{pmatrix}. \quad (3.44)$$

The Wigner 3j-symbols will be used in the numerical implementation of the project.

The coupled spin operator $\boldsymbol{S} = (S_x, S_y, S_z)^2$ and the coupled isospin operators $\boldsymbol{T} = (T_x, T_y, T_z)^2$ are defined, in relation to the corresponding single-particle operators, as[12]

$$\boldsymbol{S} \equiv \boldsymbol{S}^{(1)} \otimes \mathbb{1}^{(2)} + \mathbb{1}^{(1)} \otimes \boldsymbol{S}^{(2)}, \quad (3.45)$$

$$\boldsymbol{T} \equiv \boldsymbol{T}^{(1)} \otimes \mathbb{1}^{(2)} + \mathbb{1}^{(1)} \otimes \boldsymbol{T}^{(2)}, \quad (3.46)$$

and the coupled spin and isospin states are defined such that

$$\begin{aligned} \boldsymbol{S}^2 \left| s_1, s_2; s, m_s \right\rangle &= s(s+1) \left| s_1, s_2; s, m_s \right\rangle, \\ S_z \left| s_1, s_2; s, m_s \right\rangle &= m_s \left| s_1, s_2; s, m_s \right\rangle, \end{aligned} \quad (3.47)$$

and

$$\begin{aligned} \boldsymbol{T}^2 \left| t_1, t_2; t, m_t \right\rangle &= t(t+1) \left| t_1, t_2; t, m_t \right\rangle, \\ T_z \left| t_1, t_2; t, m_t \right\rangle &= m_t \left| t_1, t_2; t, m_t \right\rangle, \end{aligned} \quad (3.48)$$

where $s \in \{|s_1 - s_2|, |s_1 - s_2| + 1, \ldots, s_1 + s_2\}$ and $m_s = m_{s,1} + m_{s,1} \in \{-s, -s+1, \ldots, s\}$ are the (total) spin quantum number and spin projection, respectively, and $t \in \{|t_1 - t_2|, |t_1 - t_2| + 1, \ldots, t_1 + t_2\}$ and $m_t = m_{t,1} + m_{t,1} \in \{-t, -t+1, \ldots, t\}$ are the (total) isospin quantum number and isospin projection, respectively[13]. The expressions (3.37) and (3.38) can be inverted as

$$\left| s_1, s_2; s, m_s \right\rangle = \sum_{m_{s,1}} \sum_{m_{s,2}} C^{s,m_s}_{s_1,s_2;m_{s,1},m_{s,2}} \left| s_1, s_2; m_{s,1}, m_{s,2} \right\rangle, \quad (3.49)$$

$$\left| t_1, t_2; t, m_t \right\rangle = \sum_{m_{t,1}} \sum_{m_{t,2}} C^{t,m_t}_{t_1,t_2;m_{t,1},m_{t,2}} \left| t_1, t_2; m_{t,1}, m_{t,2} \right\rangle, \quad (3.50)$$

where the sums are taken over all $m_{s,n} \in \{-s_n, -s_n + 1, \ldots, s_n\}$ and $m_{t,n} \in \{-t_n, -t_n + 1, \ldots, t_n\}$ for both $n = 1, 2$. It is apparent from this relation that

$$\begin{aligned} [\boldsymbol{S}^{(1)} \otimes \mathbb{1}^{(2)}]^2 \left| s_1, s_2; s, m_s \right\rangle &= s_1(s_1+1) \left| s_1, s_2; s, m_s \right\rangle, \\ [\mathbb{1}^{(1)} \otimes \boldsymbol{S}^{(2)}]^2 \left| s_1, s_2; s, m_t \right\rangle &= s_2(s_2+1) \left| s_1, s_2; s, m_s \right\rangle, \end{aligned} \quad (3.51)$$

and

$$\begin{aligned} [\boldsymbol{T}^{(1)} \otimes \mathbb{1}^{(2)}]^2 \left| t_1, t_2; t, m_t \right\rangle &= t_1(t_1+1) \left| t_1, t_2; t, m_t \right\rangle, \\ [\mathbb{1}^{(1)} \otimes \boldsymbol{T}^{(2)}]^2 \left| t_1, t_2; t, m_t \right\rangle &= t_2(t_2+1) \left| t_1, t_2; t, m_t \right\rangle. \end{aligned} \quad (3.52)$$

[12] Note that $\boldsymbol{J} \otimes \mathbb{1} \equiv (J_x \otimes \mathbb{1}, J_y \otimes \mathbb{1}, J_z \otimes \mathbb{1})^T$ and $\mathbb{1} \otimes \boldsymbol{J} \equiv (\mathbb{1} \otimes J_x, \mathbb{1} \otimes J_y, \mathbb{1} \otimes J_z)^T$, given that $\boldsymbol{J} = (J_x, J_y, J_z)^T$.

[13] The thesis will from now on refer to the total spin and total isospin as spin and isospin.

3.3 Nucleon-Nucleon Scattering

The NN system contains two nucleons $n = 1, 2$, each defined to have single-particle spin $s_n = 1/2$ and single-particle isospin $t_n = 1/2$. The Hilbert space of two-nucleon states is given by

$$\mathscr{H}^{12} = \mathscr{H}^1 \otimes \mathscr{H}^2, \quad \mathscr{H}^n \equiv \mathscr{H}^n_{\text{spatial}} \otimes \mathscr{H}^n_{\text{spin}} \otimes \mathscr{H}^n_{\text{isospin}}, \tag{3.53}$$

where $\mathscr{H}^n$ is the Hilbert space of the single-particle states of nucleon $n = 1, 2$. As shown in section 3.2, the tensor product of the spatial Hilbert spaces for the two particles can, by defining c.m. and relative canonical coordinates as in (3.27), be redefined as

$$\mathscr{H}^1_{\text{spatial}} \otimes \mathscr{H}^2_{\text{spatial}} = \mathscr{H}^{\text{c.m.}}_{\text{spatial}} \otimes \mathscr{H}^{\text{rel.}}_{\text{spatial}}. \tag{3.54}$$

The tensor product of the two spin Hilbert spaces and the tensor product of the two isospin Hilbert spaces is then defined to be the NN spin and isospin Hilbert spaces as

$$\mathscr{H}^{\text{NN}}_{\text{spin}} \equiv \mathscr{H}^1_{\text{spin}} \otimes \mathscr{H}^2_{\text{spin}}, \quad \mathscr{H}^{\text{NN}}_{\text{isospin}} \equiv \mathscr{H}^1_{\text{isospin}} \otimes \mathscr{H}^2_{\text{isospin}}. \tag{3.55}$$

The Hilbert space of the two-nucleon states can then be expressed as

$$\mathscr{H}^{12} = \mathscr{H}^{\text{c.m.}}_{\text{spatial}} \otimes \mathscr{H}^{\text{NN}}, \quad \mathscr{H}^{\text{NN}} \equiv \mathscr{H}^{\text{rel.}}_{\text{spatial}} \otimes \mathscr{H}^{\text{NN}}_{\text{spin}} \otimes \mathscr{H}^{\text{NN}}_{\text{isospin}}, \tag{3.56}$$

where $\mathscr{H}^{\text{NN}}$ is the Hilbert space of the relative two-nucleon states $|\Phi_{\text{NN}}\rangle$, which are the states of interest when investigating NN scattering. The relative two-nucleon states $|\Phi_{\text{NN}}\rangle \in \mathscr{H}^{\text{NN}}$ are decomposed, in analogy with the tensor product decomposition of $\mathscr{H}^{\text{NN}}$ in (3.56), as

$$|\Phi_{\text{NN}}\rangle \equiv |\boldsymbol{p}\rangle \otimes |\phi_{\text{spin}}\rangle \otimes |\phi_{\text{isospin}}\rangle\,, \tag{3.57}$$

where $|\boldsymbol{p}\rangle \in \mathscr{H}^{\text{rel.}}_{\text{spatial}}$ are the relative momentum eigenstates, $|\phi_{\text{spin}}\rangle \in \mathscr{H}^{\text{NN}}_{\text{spin}}$ are the spin eigenstates, and $|\phi_{\text{isospin}}\rangle \in \mathscr{H}^{\text{NN}}_{\text{isospin}}$ are the isospin eignestates.

3.3.1 Nucleon-Nucleon States

Nucleons have single-particle isospin $t_1 = 1/2$ and the possible single-particle isospin projections $m_{t,1} = \pm 1/2$, where the proton (p) is defined as the $m_{t,1} = 1/2$ state and the neutron (n) is defined as the $m_{t,1} = -1/2$, *i.e.* $|p_1\rangle \equiv |t_1 = \frac{1}{2}, m_{t,1} = \frac{1}{2}\rangle$ and $|n_1\rangle \equiv |t_1 = \frac{1}{2}, m_{t,1} = -\frac{1}{2}\rangle$. The coupled isospin states for a two-nucleon system is, trivially from (3.50), given by[14]

$$|\phi_{\text{isospin}}\rangle \equiv |t, m_t\rangle = \sum_{m_{t,1}} \sum_{m_{t,2}} C^{t,m_t}_{\frac{1}{2},\frac{1}{2};m_{t,1},m_{t,2}} |m_{t,1}, m_{t,2}\rangle\,, \tag{3.58}$$

where the sums are taken over $m_{t,1}, m_{t,2} \in \{-\frac{1}{2}, \frac{1}{2}\}$. The coupled NN isospin basis contains four states, which can be expressed in terms of uncoupled NN isospin states

[14]Note that t_1 and t_2 were dropped from the state notaion since they are redundant for the NN isospin states $|t, m_t\rangle \equiv |t_1 = \frac{1}{2}, t_2 = \frac{1}{2}; t, m_t\rangle$ and $|m_{t,1}, m_{t,2}\rangle \equiv |t_1 = \frac{1}{2}, t_2 = \frac{1}{2}; m_{t,1}, m_{t,2}\rangle$.

as

$$\begin{cases} |t=1, m_t=1\rangle = |p_1\rangle \otimes |p_2\rangle \,, \\ |t=1, m_t=0\rangle = \dfrac{|p_1\rangle \otimes |n_2\rangle + |n_1\rangle \otimes |p_2\rangle}{\sqrt{2}}, \\ |t=1, m_t=-1\rangle = |n_1\rangle \otimes |n_2\rangle \,, \\ |t=0, m_t=0\rangle = \dfrac{|p_1\rangle \otimes |n_2\rangle - |n_1\rangle \otimes |p_2\rangle}{\sqrt{2}}, \end{cases} \tag{3.59}$$

where $|p_i\rangle \equiv |t_i = \frac{1}{2}, m_{t,i} = \frac{1}{2}\rangle$ and $|n_i\rangle \equiv |t_i = \frac{1}{2}, m_{t,i} = -\frac{1}{2}\rangle$ is the proton and neutron single-particle isospin eigenstates, respectively, of nucleon $i = 1, 2$. The triplet isospin ($t = 1$) states are symmetric under the exchange of the two nucleons, where $m_t = 1$, $m_t = 0$, and $m_t = -1$ are the symmetric *proton-proton* (*pp*), *np*, and *neutron-neutron* (*nn*) coupled isospin states, respectively. The singlet ($t = 0$) state is antisymmetric under the exchange of the two nucleons, where the only possible isospin projection $m_t = 0$ is the antisymmetric *np* coupled isospin state.

Nucleons also have single-particle spin $s_1 = 1/2$ and can thus have the possible single-particle spin projections $m_{s,1} = \pm 1/2$. Unlike the single-particle isospin projection, both the neutron and proton can have $m_{s,1} = \pm 1/2$. The coupled spin states for a two-nucleon system is, trivially from (3.49), given by[15]

$$|\phi_{\text{spin}}\rangle \equiv |s, m_s\rangle = \sum_{m_{s,1}} \sum_{m_{s,2}} C^{s,m_s}_{\frac{1}{2},\frac{1}{2};m_{s,1},m_{s,2}} |m_{s,1}, m_{s,2}\rangle \,, \tag{3.60}$$

where the sums are taken over $m_{s,1}, m_{s,2} \in \{-\frac{1}{2}, \frac{1}{2}\}$. The coupled NN spin basis contains four states, which can be expressed in terms of uncoupled NN spin states as

$$\begin{cases} |s=1, m_s=1\rangle = |\lambda_1^+\rangle \otimes |\lambda_2^+\rangle \,, \\ |s=1, m_s=0\rangle = \dfrac{|\lambda_1^+\rangle \otimes |\lambda_2^-\rangle + |\lambda_1^-\rangle \otimes |\lambda_2^+\rangle}{\sqrt{2}}, \\ |s=1, m_s=-1\rangle = |\lambda_1^-\rangle \otimes |\lambda_2^-\rangle \,, \\ |s=0, m_s=0\rangle = \dfrac{|\lambda_1^+\rangle \otimes |\lambda_2^-\rangle - |\lambda_1^-\rangle \otimes |\lambda_2^+\rangle}{\sqrt{2}}, \end{cases} \tag{3.61}$$

where $|\lambda_n^\pm\rangle \equiv |s_n = \frac{1}{2}, m_{s,n} = \pm\frac{1}{2}\rangle$ are the $m_{s,n} = \pm 1/2$ nucleon spin eigenstates for nucleon $n = 1, 2$. As for the coupled NN isospin states, the triplet spin ($s = 1$) and singlet spin ($s = 0$) states are symmetric and antisymmetric, respectively, under the exchange of the two particles.

[15]Note that s_1 and s_2 were dropped from the state notation since they are redundant for the NN spin states $|s, m_s\rangle \equiv |s_1 = \frac{1}{2}, s_2 = \frac{1}{2}; s, m_s\rangle$ and $|m_{s,1}, m_{s,2}\rangle \equiv |s_1 = \frac{1}{2}, s_2 = \frac{1}{2}; m_{s,1}, m_{s,2}\rangle$.

The relative NN states $|\Phi_{\mathrm{NN}}\rangle \in \mathscr{H}^{\mathrm{NN}}$ in the coupled spin and isospin basis is, by inserting (3.58) and (3.60) into (3.57), given as

$$|\Phi_{\mathrm{NN}}\rangle = |\boldsymbol{p}, s, m_s, t, m_t\rangle \,. \tag{3.62}$$

In this thesis, the relativistic normalisation of the relative momentum eigenstates is employed, meaning that

$$\langle \boldsymbol{p}'|\boldsymbol{p}\rangle = (2\pi)^3 \delta^{(3)}(\boldsymbol{p}' - \boldsymbol{p}) \tag{3.63}$$

and thus that the relative NN states (3.62) are normalised as

$$\langle \boldsymbol{p}', s', m_s', t', m_t'|\boldsymbol{p}, s, m_s, t, m_t\rangle = (2\pi)^3 \delta^{(3)}(\boldsymbol{p}' - \boldsymbol{p}) \delta_{s's} \delta_{m_s' m_s} \delta_{t't} \delta_{m_t' m_t}. \tag{3.64}$$

The completeness identity of the relative momentum states, $|\boldsymbol{p}\rangle \in \mathscr{H}^{\mathrm{rel.}}_{\mathrm{spatial}}$, and the relative NN states, $|\boldsymbol{q}, s, m_s, t, m_t\rangle \in \mathscr{H}^{\mathrm{NN}}$, are thus given by

$$\mathbb{1}^{(\mathrm{spatial})} = \int_{\mathbb{R}^3} \frac{d\boldsymbol{p}}{(2\pi)^3} \, |\boldsymbol{p}\rangle \, \langle \boldsymbol{p}| \tag{3.65}$$

and

$$\mathbb{1} = \sum_{s=0}^{1} \sum_{m_s=-s}^{s} \sum_{t=0}^{1} \sum_{m_t=-t}^{t} \int_{\mathbb{R}^3} \frac{d\boldsymbol{p}}{(2\pi)^3} \, |\boldsymbol{q}, s, m_s, t, m_t\rangle \, \langle \boldsymbol{p}, s, m_s, t, m_t| \,, \tag{3.66}$$

respectively, where formally $\mathbb{1} = \mathbb{1}^{(\mathrm{spatial})} \otimes \mathbb{1}^{(\mathrm{spin})} \otimes \mathbb{1}^{(\mathrm{isospin})}$.

3.3.1.1 Nucleon-Nucleon Partial Wave States

A three-dimensional vector, like the momentum vector, can be uniquely identified by its magnitude $p \equiv |\boldsymbol{p}|$ and its direction in space $\hat{\boldsymbol{p}} \equiv \boldsymbol{p}/|\boldsymbol{p}|$. The relative momentum eigenstates $|\boldsymbol{p}\rangle \in \mathscr{H}^{\mathrm{rel.}}_{\mathrm{spatial}}$ can thus be decomposed as[16]

$$|\boldsymbol{p}\rangle = (2\pi)^{3/2} \sum_{\ell=0}^{\infty} \sum_{m_\ell=\ell}^{\ell} Y^{*\ell}_{m_\ell}(\hat{\boldsymbol{p}}) \, |p, \ell, m_\ell\rangle \,, \tag{3.67}$$

where $Y^{\ell}_{m_\ell}(\hat{\boldsymbol{p}}) \equiv \langle \hat{\boldsymbol{p}}|\ell, m_\ell\rangle$ are the *spherical harmonics* and $|p, \ell, m_\ell\rangle = |p\rangle \otimes |\ell, m_\ell\rangle$ are the so-called PWS, composed of the momentum magnitude and orbital angular momentum states [27]. The relative momentum direction $\hat{\boldsymbol{p}}$ has two degrees of freedom, which in spherical coordinates are given by the polar angle $\vartheta_{\boldsymbol{p}} \in [0, \pi]$ and the azimuthal angle $\varphi_{\boldsymbol{p}} \in [0, 2\pi)$, which means that the spherical harmonics can be parameterised as $Y^{\ell}_{m_\ell}(\hat{\boldsymbol{p}}) \equiv Y^{\ell}_{m_\ell}(\vartheta_{\boldsymbol{p}}, \varphi_{\boldsymbol{p}})$. The spherical harmonics satisfy the completeness relation

$$\sum_{\ell=0}^{\infty} \sum_{m_\ell=-\ell}^{\ell} Y^{\ell}_{m_\ell}(\hat{\boldsymbol{p}}') Y^{*\ell}_{m_\ell}(\hat{\boldsymbol{p}}) = \delta^{(2)}(\hat{\boldsymbol{p}}' - \hat{\boldsymbol{p}}), \tag{3.68}$$

and orthogonality and normalisation relation

$$\int_{\Omega} d\hat{\boldsymbol{p}} \, Y^{\ell'}_{m'_\ell}(\hat{\boldsymbol{p}}) Y^{*\ell}_{m_\ell}(\hat{\boldsymbol{p}}) = \delta_{\ell'\ell} \delta_{m'_\ell m_\ell}, \tag{3.69}$$

[16] Some sources, like [29], uses a different phase convention for the spherical harmonics, which implies sign differences in phase shifts but does not effect observables.

given that $\langle \ell', m'_\ell | \ell, m_\ell \rangle = \delta_{\ell'\ell}\delta_{m'_\ell m_\ell}$ and $\langle \hat{\boldsymbol{p}}' | \hat{\boldsymbol{p}} \rangle = \delta^{(2)}(\hat{\boldsymbol{p}}' - \hat{\boldsymbol{p}})$ [28]. The partial wave decomposition of the relative momentum states implies that the relative spatial Hilbert space decomposes as

$$\mathscr{H}^{\text{rel.}}_{\text{spatial}} = \mathscr{H}^{\text{rel.}}_{\text{mag.}} \otimes \mathscr{H}^{\text{rel.}}_{\text{dir.}} \equiv \mathscr{H}^{\text{rel.}}_{\text{mag.}} \otimes \mathscr{H}^{\text{NN}}_{\text{orbital}}, \tag{3.70}$$

where $\mathscr{H}^{\text{rel.}}_{\text{mag.}}$ is the Hilbert space of the relative momentum magnitude states $|p\rangle$ and $\mathscr{H}^{\text{NN}}_{\text{orbital}}$ is the Hilbert space of the orbital angular momentum states $|\ell, m_\ell\rangle$. The states $|\ell, m_\ell\rangle$ are defined such that

$$\boldsymbol{L}^2 |\ell, m_\ell\rangle = \ell(\ell+1) |\ell, m_\ell\rangle , \quad L_z |\ell, m_\ell\rangle = m_\ell |\ell, m_\ell\rangle , \tag{3.71}$$

where $\boldsymbol{L} = (L_x, L_y, L_z)^T$, $\ell \in \{0, 1, 2, \dots\}$, and $m_\ell \in \{-\ell, -\ell+1, \dots, \ell\}$ are the orbital angular momentum operators, quantum number, and projection, respectively.

The total angular momentum states $|\ell, s; j, m_j\rangle \in \mathscr{H}^{\text{NN}}_{\text{tot. ang.}} \equiv \mathscr{H}^{\text{NN}}_{\text{orbital}} \otimes \mathscr{H}^{\text{NN}}_{\text{spin}}$ are then introduced to satisfy

$$\boldsymbol{J}^2 |\ell, s; j, m_j\rangle = j(j+1) |\ell, s; j, m_j\rangle , \quad J_z |\ell, s; j, m_j\rangle = m_j |\ell, s; j, m_j\rangle , \tag{3.72}$$

where $\boldsymbol{J} \equiv \boldsymbol{L}^{(\text{orbital})} \otimes \mathbb{1}^{(\text{spin})} + \mathbb{1}^{(\text{orbital})} \otimes \boldsymbol{S}^{(\text{spin})}$, $j \in \{|\ell - s|, |\ell - s| + 1, \dots, \ell + s\}$, and $m_j = m_\ell + m_s \in \{-j, -j+1, \dots, j\}$ are the total angular momentum operators, quantum number, and projection. These total angular momentum states are related to the states $|\ell, s; m_\ell, m_s\rangle \equiv |\ell, m_\ell\rangle \otimes |s, m_s\rangle \in \mathscr{H}^{\text{NN}}_{\text{orbital}} \otimes \mathscr{H}^{\text{NN}}_{\text{spin}}$ as

$$\begin{aligned} |\ell, s; m_\ell, m_s\rangle &= \sum_{j=|\ell-s|}^{\ell+s} \sum_{m_j=-j}^{j} C^{j,m_j}_{\ell,s;m_\ell,m_s} |\ell, s; j, m_j\rangle , \\ |\ell, s; j, m_j\rangle &= \sum_{m_\ell=-\ell}^{\ell} \sum_{m_s=-s}^{s} C^{j,m_j}_{\ell,s;m_\ell,m_s} |\ell, s; m_\ell, m_s\rangle . \end{aligned} \tag{3.73}$$

The partial wave expansion of the relative NN states $|\Phi_{\text{NN}}\rangle = |\boldsymbol{p}, s, m_s, t, m_t\rangle \in \mathscr{H}^{\text{NN}}$ is, by first inserting (3.67) and then (3.73) into (3.62), given as

$$\begin{aligned} &|\boldsymbol{p}, s, m_s, t, m_t\rangle = \\ &\quad = (2\pi)^{3/2} \sum_{\ell=0}^{\infty} \sum_{m_\ell=\ell}^{\ell} \sum_{j=|\ell-s|}^{\ell+s} \sum_{m_j=-j}^{j} C^{j,m_j}_{\ell,s;m_\ell,m_s} Y^{*\ell}_{m_\ell}(\hat{\boldsymbol{p}}) |\ell, s; p, j, m_j, t, m_t\rangle = \\ &\quad = (2\pi)^{3/2} \sum_{j=0}^{\infty} \sum_{m_j=-j}^{j} \sum_{\ell=|j-s|}^{j+s} C^{j,m_j}_{\ell,s;m_j-m_s,m_s} Y^{*\ell}_{m_j-m_s}(\hat{\boldsymbol{p}}) |\ell, s; p, j, m_j, t, m_t\rangle , \end{aligned} \tag{3.74}$$

where $|\ell, s; p, j, m_j, t, m_t\rangle \equiv |p\rangle \otimes |\ell, s; j, m_j\rangle \otimes |t, m_t\rangle \in \mathscr{H}^{\text{rel.}}_{\text{mag.}} \otimes \mathscr{H}^{\text{NN}}_{\text{tot. ang.}} \otimes \mathscr{H}^{\text{NN}}_{\text{isopsin}}$ are the *total angular momentum Partial-Wave States* (jPWS). The normalisation of the jPWS is

$$\langle \ell', s'; p', j', m'_j, t', m'_t | \ell, s; p, j, m_j, t, m_t\rangle = \frac{\delta(p'-p)}{p^2} \delta_{\ell'\ell}\delta_{s's}\delta_{j'j}\delta_{m'_j m_j}\delta_{t't}\delta_{m'_t m_t}, \tag{3.75}$$

which is implicit from (3.64) and (3.67). The completeness identity of the jPWS is then given as

$$\mathbb{1} = \sum_{t,m_t} \sum_{j,m_j} \sum_{s,\ell} \int_{\mathbb{R}^+} dp\, p^2 \, |\ell, s; p, j, m_j, t, m_t\rangle \, \langle \ell, s; p, j, m_j, t, m_t| \,, \tag{3.76}$$

where the sums are taken over $t \in \{0, 1\}$, $m_t \in \{-t, -t+1, \ldots, t\}$, $j \in \mathbb{N}$, $m_j \in \{-j, -j+1, \ldots, j\}$, $s \in \{0, 1\}$, and $\ell \in \{|j-s|, |j-s|+1, \ldots, j+s\}$. The relation between the relative NN states $|\boldsymbol{p}, s, m_s, t, m_t\rangle$ and the jPWS can also be expressed as

$$\begin{aligned} &\langle \boldsymbol{p}', s', m_s', t', m_t' | \ell, s; p, j, m_j, t, m_t\rangle = \\ &\qquad = (2\pi)^{3/2} \frac{\delta(p'-p)}{p^2} \delta_{s's} \delta_{t't} \delta_{m_t' m_t} C^{j,m_j}_{\ell,s;m_j-m_s',m_s'} Y^{\ell}_{m_j-m_s'}(\hat{\boldsymbol{p}}'). \end{aligned} \tag{3.77}$$

3.3.2 Symmetries

The nucleons can be treated as identical particles since the isospin quantum number and projection are included in the NN state notation. Nucleons are fermions and will thus obey fermionic statistics, which implies that the two-nucleon states must be totally antisymmetric under the exchange of the two nucleons. The antisymmetric relative NN states can be expressed as

$$|\boldsymbol{p}, s, m_s, t, m_t\rangle_a \equiv (1 - \hat{\Pi}) \, |\boldsymbol{p}, s, m_s, t, m_t\rangle \,, \tag{3.78}$$

where $\hat{\Pi}$ is the permutation operator that permutes the particles in the three spaces $\mathscr{H}^{\text{rel.}}_{\text{spatial}}$, $\mathscr{H}^{\text{NN}}_{\text{spin}}$, and $\mathscr{H}^{\text{NN}}_{\text{isospin}}$. As discussed earlier in this section, the (singlet) triplet spin and isospin states are (antisymmetric) symmetric under the exchange of the two nucleons. The permutation of the coupled spin and isospin states can thus be expressed as

$$\hat{\Pi} \, |s, m_s\rangle = (-1)^{s+1} \, |s, m_s\rangle \,, \quad \hat{\Pi} \, |t, m_t\rangle = (-1)^{t+1} \, |t, m_t\rangle \,. \tag{3.79}$$

It is from the definitions of the relative canonical coordinates (3.27b) given that the permutation operator acts on the relative momentum states as

$$\hat{\Pi} \, |\boldsymbol{p}\rangle = |-\boldsymbol{p}\rangle \,. \tag{3.80}$$

By expanding the relative momentum states into PWS, the effect of the permutation operator becomes

$$\begin{aligned} \hat{\Pi} \, |\boldsymbol{p}\rangle = |-\boldsymbol{p}\rangle &= (2\pi)^{3/2} \sum_{\ell=0}^{\infty} \sum_{m_\ell=-\ell}^{\ell} Y^{*\ell}_{m_\ell}(-\hat{\boldsymbol{p}}) \, |p, \ell, m_\ell\rangle = \\ &= (2\pi)^{3/2} \sum_{\ell=0}^{\infty} \sum_{m_\ell=-\ell}^{\ell} (-1)^{\ell} Y^{*\ell}_{m_\ell}(\hat{\boldsymbol{p}}) \, |p, \ell, m_\ell\rangle \,, \end{aligned} \tag{3.81}$$

where the last equality utilises the periodicity property $Y^{\ell}_{m_\ell}(-\hat{\boldsymbol{p}}) = (-1)^{\ell} Y^{\ell}_{m_\ell}(\hat{\boldsymbol{p}})$ of the spherical harmonics [28]. The antisymmetric relative NN states can thus be expressed in terms of the jPWS as

$$\begin{aligned} &|\boldsymbol{p}, s, m_s, t, m_t\rangle_a = \\ &= (2\pi)^{3/2} \sum_{\ell,j,m_j} [1-(-1)^{\ell+s+t}] C^{j,m_j}_{\ell,s;m_j-m_s,m_s} Y^{*\ell}_{m_j-m_s}(\hat{\boldsymbol{p}}) \, |\ell, s; p, j, m_j, t, m_t\rangle \,, \end{aligned} \tag{3.82}$$

where the sums are taken over all $\ell, j \in \{0, 1, 2, \dots\}$ and $m_j \in \{-j, -j+1, \dots, j\}$ such that $|j-s| \leq \ell \leq j+s$. The result is that only partial waves for which $\ell+s+t$ is an odd number contribute to the two-nucleon states (direct result of the Pauli principle), *i.e.*

$$(-1)^{\ell+s+t} = -1. \tag{3.83}$$

Consequently, the isospin quantum number $t \in \{0, 1\}$ is directly implicit from the orbital angular momentum and spin quantum numbers.

3.3.2.1 Invariance Principles and Conserved Quantum Numbers

The symmetries of the NN scattering problem are determined by the full (relative) Hamiltonian of the system $H = H_0 + V_{\mathrm{NN}}$, consisting of a free Hamiltonian and an NN interaction potential. The free Hamiltonian consists of a relative kinetic term

$$\frac{|\boldsymbol{p}|^2}{2\mu}, \tag{3.84}$$

where $\boldsymbol{p}$ is the relative canonical momentum operator as defined in (3.27b) and μ is the reduced mass. The interaction potential of interest in this project, presented in equation (2.58), carries the operator dependence

$$\boldsymbol{\tau}^{(1)} \cdot \boldsymbol{\tau}^{(2)}, \quad [\boldsymbol{\sigma}^{(1)} \cdot \boldsymbol{K}][\boldsymbol{\sigma}^{(2)} \cdot \boldsymbol{K}], \quad \boldsymbol{\sigma}^{(1)} \cdot \boldsymbol{\sigma}^{(2)}, \quad |\boldsymbol{K}|^2, \quad |\boldsymbol{p}|^2, \tag{3.85}$$

where $\boldsymbol{K} \equiv \boldsymbol{p}' - \boldsymbol{p}$ is the momentum transfer, $\boldsymbol{\sigma}^{(n)}$ and $\boldsymbol{\tau}^{(n)}$ are the Pauli spin operator and isospin operator[17], respectively, of nucleon $n = 1, 2$.

Total angular momentum conservation and Rotational invariance
The conservation of the total angular momentum quantum number and projection is identified as (spatial) rotational invariance (spherical symmetry) of the Hamiltonian, *i.e.*

$$[\boldsymbol{J}, H] = 0 \iff H \longrightarrow \hat{\mathscr{R}} H \hat{\mathscr{R}}^{\dagger} = H, \quad \hat{\mathscr{R}} = e^{-i\boldsymbol{\omega}\cdot\boldsymbol{J}} \approx \mathbb{1} - i \sum_i \omega_i J_i, \tag{3.86}$$

where $\hat{\mathscr{R}}$ is a unitary rotation operator, $\boldsymbol{\omega}$ determines the rotation axis and angle, and $\boldsymbol{J} = (J_x, J_y, J_z)^T$ are the total angular momentum operators. The transformation properties of $\hat{\mathscr{R}}$ are determined by the commutation relations between the

[17] The vector components are identified with the three Pauli matrices and are related to the single-particle spin and isospin operators used in this chaptor as $\boldsymbol{S}^{(n)} = \frac{1}{2}\boldsymbol{\sigma}^{(n)}$ and $\boldsymbol{T}^{(n)} = \frac{1}{2}\boldsymbol{\tau}^{(n)}$.

transformed operator and the total angular momentum operators. The only operators that can have a non-zero commutation relation with $\boldsymbol{J}$, and are relevant for the Hamiltonian in question, are the single-particle spin operators $\boldsymbol{S}^{(n)} = \frac{1}{2}\boldsymbol{\sigma}^{(n)}$, and the relative canonical momentum vector $\boldsymbol{p}$, which satisfy[18]

$$[J_i, S_j^{(n)}] = i\sum_k \varepsilon_{ijk} S_k^{(n)}, \quad [J_i, p_j] = i\sum_k \varepsilon_{ijk} p_k, \tag{3.87}$$

where the summation over repeated indices is understood. The fact that they have the same commutation relation implies that they also transform in the same way under the rotation

$$\begin{aligned} p_i &\longrightarrow \hat{\mathscr{R}} p_i \hat{\mathscr{R}}^\dagger = R_{ij} p_j, \\ S_i^{(n)} &\longrightarrow \hat{\mathscr{R}} S_i^{(n)} \hat{\mathscr{R}}^\dagger = R_{ij} S_j^{(n)}, \end{aligned} \tag{3.88}$$

where $R_{ij} \in SO(3)$ is a real orthogonal rotation matrix, *i.e.* $R_{ij}R_{ik} = \delta_{jk}$ [30], and the summation over repeated indices is understood. It is then trivial to show that

$$K_i = p_i' - p_i \longrightarrow \hat{\mathscr{R}} K_i \hat{\mathscr{R}}^\dagger = R_{ij} K_j, \tag{3.89}$$

$$\sigma_i^{(n)} = 2S_i^{(n)} \longrightarrow \hat{\mathscr{R}} \sigma_i^{(n)} \hat{\mathscr{R}}^\dagger = R_{ij} \sigma_j^{(n)}. \tag{3.90}$$

The orthogonality of the matrix $R_{ij} \in SO(3)$ implies that the scalar product of any two vectors $\boldsymbol{A}$ and $\boldsymbol{B}$ that transform like (3.88) under rotation is invariant under rotation, *i.e.*

$$\boldsymbol{A}\cdot\boldsymbol{B} \longrightarrow \hat{\mathscr{R}}[\boldsymbol{A}\cdot\boldsymbol{B}]\hat{\mathscr{R}}^\dagger = \hat{\mathscr{R}} A_i \hat{\mathscr{R}}^\dagger \hat{\mathscr{R}} B_i \hat{\mathscr{R}}^\dagger = R_{ij}R_{ik}A_jB_k = \boldsymbol{A}\cdot\boldsymbol{B}, \tag{3.91}$$

All terms in (3.84) and (3.85) are consequently rotationally invariant, and

$$[\boldsymbol{J}, H] = 0, \tag{3.92}$$

which implies that the total angular momentum quantum number and projection are conserved in the scattering process.

Isospin conservation

The only isospin operator dependence of the Hamiltonian is contained in

$$\boldsymbol{\tau}^{(1)}\cdot\boldsymbol{\tau}^{(2)} = 4\sum_i T_i^{(1)} \otimes T_i^{(2)}, \tag{3.93}$$

where $\boldsymbol{T}^{(n)} = (T_x^{(n)}, T_y^{(n)}, T_z^{(n)})^T$ are the single-particle isospin operators acting on nucleon $n = 1, 2$. The only non-trivial part of the commutator between the isospin operators $\boldsymbol{T} = (T_x, T_y, T_z)^T$ and the Hamiltonian is thus

$$[T_i, H] = 4\sum_j \Big([T_i^{(1)}, T_j^{(1)}] \otimes T_j^{(2)} + T_j^{(1)} \otimes [T_i^{(2)}, T_j^{(2)}] \Big), \tag{3.94}$$

[18] Note that the first commutation relation is trivial from $[J_i, J_j] = i\sum_k \varepsilon_{ijk} J_k$ and $\boldsymbol{J} = \boldsymbol{L} + \boldsymbol{S}$. The second can be derived from $\boldsymbol{L} = \boldsymbol{x} \times \boldsymbol{p}$ and the canonical commutation relation [24]. Note also that the only other non-commuting operators are $\boldsymbol{L}$ and $\boldsymbol{x}$, which have the same relation.

given that $T_i = T_i^{(1)} \otimes \mathbb{1}^{(2)} + \mathbb{1}^{(1)} \otimes T_i^{(2)}$. The matrix representation of the Pauli isospin operators $\boldsymbol{\tau}^{(n)}$ are the three Pauli matrices, which imply that the single-particle isospin operators $\boldsymbol{T}^{(n)} = \frac{1}{2}\boldsymbol{\tau}^{(n)}$ commute with each other as

$$[T_i^{(n)}, T_j^{(n)}] = i \sum_k \varepsilon_{ijk} T_k^{(n)}, \tag{3.95}$$

where ε_{ijk} is the totally antisymmetric *Levi-Civita tensor* [30]. It is then given that

$$\begin{aligned}[T_i, H] = 4i \sum_{j,k} \varepsilon_{ijk} \Big[T_k^{(1)} \otimes T_j^{(2)} + T_j^{(1)} \otimes T_k^{(2)} \Big] = \\ = 4i \sum_{j,k} \varepsilon_{ijk} \Big[T_k^{(1)} \otimes T_j^{(2)} - T_k^{(1)} \otimes T_j^{(2)} \Big],\end{aligned} \tag{3.96}$$

which is zero for all $i = x, y, z$. It has thus been shown that

$$[\boldsymbol{T}, H] = 0, \tag{3.97}$$

which implies that the Hamiltonian conserves the isospin quantum number and projection.

Isospin conservation can be identified as the Hamiltonian being invariant under isospin rotations

$$H \longrightarrow \hat{\mathscr{Q}} H \hat{\mathscr{Q}}^\dagger = H, \quad \hat{\mathscr{Q}} = e^{-i\boldsymbol{\omega}\cdot\boldsymbol{T}} \approx \mathbb{1} - i \sum_i \omega_i T_i, \tag{3.98}$$

where $\hat{\mathscr{Q}}$ is a unitary isospin-rotation operator, $\boldsymbol{\omega}$ determines the rotation axis and angle, and $\boldsymbol{T} = (T_x, T_y, T_z)^T$ are the isospin operators. Similar to the (spatial) rotations, the isospin rotations transform the single-particle isospin operators as

$$T_i^{(n)} \longrightarrow \hat{\mathscr{Q}} T_i^{(n)} \hat{\mathscr{Q}}^\dagger = R_{ij} T_j^{(n)}, \tag{3.99}$$

where $R_{ij} \in SO(3)$ is a real orthogonal rotation matrix and the summation over repeated indices is understood. The fact that the Hamiltonian is invariant under this transformation can easily be realised.

Parity invariance and Spin conservation
Parity (or space inversion) is a discrete transformation which is applied to the coordinate system, changing a right-handed system to a left-handed system. It can be understood from the relative canonical coordinates (3.27b) that they transform under parity as

$$\begin{aligned}\boldsymbol{x} &\longrightarrow \hat{\mathscr{P}} \boldsymbol{x} \hat{\mathscr{P}} = -\boldsymbol{x}, \\ \boldsymbol{p} &\longrightarrow \hat{\mathscr{P}} \boldsymbol{p} \hat{\mathscr{P}} = -\boldsymbol{p}.\end{aligned} \tag{3.100}$$

Given that all terms (3.84) and (3.85) contain an even number of momenta, it can be concluded that the Hamiltonian is parity invariant, *i.e.*

$$[\hat{\mathscr{P}}, H] = 0. \tag{3.101}$$

Note that the parity operators' action on the relative momentum states is equivalent to that of the permutation operator (3.81). The parity invariance can, therefore, be identified with the conservation of $(-1)^\ell$.

Combining the conservation of parity and the isospin quantum number with the Pauli principle (3.83) implies that $s' - s$ must be even. Since the spin quantum number can only take the values $s', s \in \{0, 1\}$, the spin quantum number has to be conserved. The conservation of the spin quantum number can be associated with the Hamiltonian being invariant under permutation in spin space, which can be realised as a unitary and Hermitian operator $\hat{\mathscr{S}}$ acting on the single-particle spin operators $\boldsymbol{S}^{(n)} = \frac{1}{2}\boldsymbol{\sigma}^{(n)}$ as [29]

$$\begin{aligned} \boldsymbol{S}^{(1)} &\longrightarrow \hat{\mathscr{S}}\boldsymbol{S}^{(1)}\hat{\mathscr{S}} = \boldsymbol{S}^{(2)}, \\ \boldsymbol{S}^{(2)} &\longrightarrow \hat{\mathscr{S}}\boldsymbol{S}^{(2)}\hat{\mathscr{S}} = \boldsymbol{S}^{(1)}. \end{aligned} \tag{3.102}$$

Time-reversal invariance

Time reversal is a discrete transformation that acts on a space-time as

$$(t, \boldsymbol{x}) \longrightarrow \hat{\mathscr{T}}(t, \boldsymbol{x})\hat{\mathscr{T}}^\dagger = (-t, \boldsymbol{x}), \tag{3.103}$$

where $\hat{\mathscr{T}}$ is the antiunitary time-rotation operator. Note that the antiunitarity implies that [14]

$$\langle\psi_{\text{in}}| S |\psi_{\text{out}}\rangle = \langle\psi_{\text{out}}| \hat{\mathscr{T}}^\dagger\hat{\mathscr{T}}S^\dagger |\psi_{\text{in}}\rangle . \tag{3.104}$$

The ingoing relative momentum, outgoing relative momentum, and the single-particle spin operators $\boldsymbol{S}^{(n)} = \frac{1}{2}\boldsymbol{\sigma}^{(n)}$ transform under time reversal as

$$\begin{aligned} \boldsymbol{p} &\longrightarrow \hat{\mathscr{T}}\boldsymbol{p}\hat{\mathscr{T}}^\dagger = -\boldsymbol{p}', \\ \boldsymbol{p}' &\longrightarrow \hat{\mathscr{T}}\boldsymbol{p}'\hat{\mathscr{T}}^\dagger = -\boldsymbol{p}, \\ \boldsymbol{S}^{(n)} &\longrightarrow \hat{\mathscr{T}}\boldsymbol{S}^{(n)}\hat{\mathscr{T}}^\dagger = -\boldsymbol{S}^{(n)}. \end{aligned} \tag{3.105}$$

It is thus given that the momentum transfer and Pauli spin operators transform as

$$\boldsymbol{K} = \boldsymbol{p}' - \boldsymbol{p} \longrightarrow \hat{\mathscr{T}}\boldsymbol{K}\hat{\mathscr{T}}^\dagger = \boldsymbol{K}, \tag{3.106}$$

$$\boldsymbol{\sigma}^{(n)} = 2\boldsymbol{S}^{(n)} \longrightarrow \hat{\mathscr{T}}\boldsymbol{\sigma}^{(n)}\hat{\mathscr{T}}^\dagger = -\boldsymbol{\sigma}^{(n)}. \tag{3.107}$$

All terms (3.84) and (3.85) contain an even number of $\boldsymbol{\sigma}^{(n)}$ and are thus invariant under time reversal, which implies that

$$[\hat{\mathscr{T}}, H] = 0. \tag{3.108}$$

Note also that the time-reversal operator acts on the relative momentum states as

$$\hat{\mathscr{T}} |\boldsymbol{p}\rangle = |-\boldsymbol{p}\rangle , \tag{3.109}$$

and on the coupled spin states[19] as [29, 31]

$$\hat{\mathscr{T}} |s, m_s\rangle = (-1)^{s-m_s} |s, m_s\rangle . \tag{3.110}$$

[19]Note that the time-reversal operator acts in the same way on single-particle spin, total angular momentum, and orbital angular momentum states.

3.3.2.2 The S, T, and V Matrix

The conserved quantum numbers of the scattering problem in question, discussed in subsubsection (3.3.2.1), result in the potential in the jPWS basis being constrained as

$$\langle \ell', s'; p', j', m_j', t', m_t' | \, V \, | \ell, s; p, j, m_j, t, m_t \rangle \equiv \\ \equiv \delta_{s's} \delta_{j'j} \delta_{m_j' m_j} \delta_{t't} \delta_{m_t' m_t} V^{jst}_{\ell'\ell}(p', p), \quad (3.111)$$

which, due to (3.19), is directly reflected in the T-matrix elements

$$\langle \ell', s'; p', j', m_j', t', m_t' | \, T \, | \ell, s; p, j, m_j, t, m_t \rangle \equiv \\ \equiv \delta_{s's} \delta_{j'j} \delta_{m_j' m_j} \delta_{t't} \delta_{m_t' m_t} T^{jst}_{\ell'\ell}(p', p). \quad (3.112)$$

As presented in section 3.1, the on-shell T operator is related to the on-shell S operator as

$$S(E) = \mathbb{1} - 2i\pi\delta(E - H_0) T^+(E), \quad (3.113)$$

where H_0 is the free Hamiltonian and $E = k^2/(2\mu)$ is the on-shell energy. It is thus convenient to define the on-shell S-matrix elements as

$$\langle \ell', s'; p', j', m_j', t', m_t' | \, S \, | \ell, s; p, j, m_j, t, m_t \rangle \equiv \\ \equiv \delta_{s's} \delta_{j'j} \delta_{m_j' m_j} \delta_{t't} \delta_{m_t' m_t} \frac{\delta(p' - p)}{p^2} S^{jst}_{\ell'\ell}(p', p), \quad (3.114)$$

such that

$$S^{jst}_{\ell'\ell}(k, k) = \delta_{\ell'\ell} - 2i\pi\mu k T^{jst}_{\ell'\ell}(k, k; k). \quad (3.115)$$

The antiunitarity of the time-reversal operator (3.104), in combination with rotational, parity, and time-reversal invariance, implies that the S matrix is symmetric

$$S^{jst}_{\ell'\ell} = S^{jst}_{\ell\ell'}. \quad (3.116)$$

In the relativistic NN basis, the S-matrix elements are given by

$$\langle \boldsymbol{p}', s', m_s', t', m_t' | \, S \, | \boldsymbol{p}, s, m_s, t, m_t \rangle \equiv \delta_{s's} \delta_{m_s' m_s} \delta_{t't} \delta_{m_t' m_t} \frac{(2\pi)^3 \delta(p' - p)}{p^2} S^{st}_{m_s' m_s}(\boldsymbol{p}', \boldsymbol{p}), \quad (3.117)$$

such that

$$S^{st}_{m_s' m_s}(\boldsymbol{p}', \boldsymbol{p}) = \delta^{(2)}(\hat{\boldsymbol{p}}' - \hat{\boldsymbol{p}}) - \frac{i\mu k}{(2\pi)^2} T^{st}_{m_s' m_s}(\boldsymbol{p}', \boldsymbol{p}; k), \quad (3.118)$$

where $k = |\boldsymbol{p}| = |\boldsymbol{p}'|$ is the on shell momentum, see appendix A. The antiunitarity of the time-reversal operator (3.104), in combination with the time-reversal invariance of the Hamiltonian, implies that

$$S^{st}_{m_s' m_s}(\boldsymbol{p}', \boldsymbol{p}) = (-1)^{-m_s' - m_s} S^{st}_{-m_s - m_s'}(-\boldsymbol{p}, -\boldsymbol{p}') = \\ = (-1)^{-m_s' - m_s} S^{st}_{-m_s - m_s'}(\boldsymbol{p}, \boldsymbol{p}'), \quad (3.119)$$

where the last equality is true due to parity invariance.

The unitarity of the S operator, $S^\dagger S = \mathbb{1}$, can in the jPWS basis be relised as

$$\sum_{\ell''=|j-s|}^{j+s} S^{*jst}_{\ell''\ell'}(p,p) S^{jst}_{\ell''\ell}(p,p) = \delta_{\ell'\ell}. \tag{3.120}$$

In the relative NN basis the unitarity implies that

$$\sum_{m_s''=-s}^{s} \int_\Omega d\hat{\boldsymbol{q}}\, S^{*st}_{m_s''m_s'}(\boldsymbol{q},\boldsymbol{p}') S^{st}_{m_s''m_s'}(\boldsymbol{q},\boldsymbol{p}) = \delta_{m_s'm_s}\delta^{(2)}(\hat{\boldsymbol{p}}' - \hat{\boldsymbol{p}}), \tag{3.121}$$

qiven that $|\boldsymbol{p}| = |\boldsymbol{p}'| = |\boldsymbol{q}|$ is the on-shell momentum. The momentum $\boldsymbol{q}$, which in a given expression is integrated over, will from now on be referred to as an *intermediate momentum*.

3.3.3 The Lippmann-Schwinger Equation for NN Scattering

Recaling the operator LS equation from subsection 3.1.1 and the completeness identity of the relative momentum states (3.65), the LS equation in the relative momentum basis reads

$$T(\boldsymbol{p}',\boldsymbol{p};k) = V(\boldsymbol{p}',\boldsymbol{p}) + \int_{\mathbb{R}^3} \frac{d\boldsymbol{q}}{(2\pi)^3} V(\boldsymbol{p}',\boldsymbol{q}) \frac{2\mu}{k^2 - q^2 + i\epsilon} T(\boldsymbol{q},\boldsymbol{p};k), \tag{3.122}$$

where $q \equiv |\boldsymbol{q}|$ is the magnitude of the intermediate momentum, μ is the reduced mass, and $V(\boldsymbol{p}',\boldsymbol{p}) = \langle \boldsymbol{p}'| V |\boldsymbol{p}\rangle$ and $T(\boldsymbol{p}',\boldsymbol{p};k) = \langle \boldsymbol{p}'| T^+(E) |\boldsymbol{p}\rangle$ are the potential matrix and T matrix at on-shell momentum $k = \sqrt{2\mu E}$, respectively. Similarly, the LS equation in the relative NN state basis is

$$\begin{aligned} T^{st}_{m_s'm_s}(\boldsymbol{p}',\boldsymbol{p};k) &= V^{st}_{m_s'm_s}(\boldsymbol{p}',\boldsymbol{p}) \\ &\quad + \sum_{m_s''=-s}^{s} \int_{\mathbb{R}^3} \frac{d\boldsymbol{q}}{(2\pi)^3} V^{st}_{m_s'm_s''}(\boldsymbol{p}',\boldsymbol{q}) \frac{2\mu}{k^2 - q^2 + i\epsilon} T^{st}_{m_s''m_s}(\boldsymbol{q},\boldsymbol{p};k), \end{aligned} \tag{3.123}$$

where $V^{st}_{m_s'm_s}(\boldsymbol{p}',\boldsymbol{p})$ and $T^{st}_{m_s'm_s}(\boldsymbol{p}',\boldsymbol{p};k)$ are the V-matrix and T-matrix elements in relative NN state basis, respectively, defined as

$$V^{st}_{m_s'm_s}(\boldsymbol{p}',\boldsymbol{p}) \equiv \langle s, m_s', t, m_t| V(\boldsymbol{p}',\boldsymbol{p}) |s, m_s, t, m_t\rangle\,, \tag{3.124}$$

$$T^{st}_{m_s'm_s}(\boldsymbol{p}',\boldsymbol{p};k) \equiv \langle s, m_s', t, m_t| T(\boldsymbol{p}',\boldsymbol{p};k) |s, m_s, t, m_t\rangle\,. \tag{3.125}$$

In similar fashion can the LS equation in the jPWS basis be derived, with the completeness identity (3.76), to be

$$\begin{aligned} T^{jst}_{\ell'\ell}(p',p;k) &= V^{jst}_{\ell'\ell}(p',p) \\ &\quad + \sum_{\ell''=|s-j|}^{|s+j|} \int_0^\infty dq\, q^2 V^{jst}_{\ell'\ell''}(p',q) \frac{2\mu}{k^2 - q^2 + i\epsilon} T^{jst}_{\ell''\ell}(q,p;k), \end{aligned} \tag{3.126}$$

where $V^{jst}_{\ell'\ell}(p',p)$ and $T^{jst}_{\ell'\ell}(p',p;k)$ are the V-matrix and T-matrix elements in the jPWS basis as given in (3.112) and (3.111), respectively. The S-matrix elements can then be determined from the on-shell solutions $T^{jst}_{\ell'\ell}(k,k;k)$ according to (3.115).

The jPWS basis S matrix for uncoupled channels, where $\ell' = \ell$, is a unitary 1×1 matrix that can be parameterised by a real phase shift[20] $\delta^{js}_\ell(k)$ as

$$\mathbf{S}^{jst} = \left(S^{jst}_{\ell\ell}\right), \quad S^{jst}_{\ell\ell} = e^{2i\delta^{js}_\ell}. \tag{3.127}$$

This phase shift can, with the use of (3.115), be expressed in terms of the on-shell T-matrix element as

$$\delta^{js}_\ell(k) = \frac{1}{2i}\ln\left[1 - 2i\pi\mu k T^{jst}_{\ell\ell}(k,k;k)\right]. \tag{3.128}$$

For coupled channels, where the orbital angular momentum quantum numbers take the possible values $\ell', \ell = j \pm 1$, the PWS basis S matrix is a unitary 2×2 matrix

$$\mathbf{S}^{jst} = \begin{pmatrix} S^{jst}_{\ell'=j-1,\ell=j-1} & S^{jst}_{\ell'=j-1,\ell=j+1} \\ S^{jst}_{\ell'=j+1,\ell=j-1} & S^{jst}_{\ell'=j+1,\ell=j+1} \end{pmatrix}. \tag{3.129}$$

This S matrix can be parameterised by three real phase shifts[21], which in the Stapp convention are δ^j_-, δ^j_+, and ϵ^j (bar phase shifts[22]) such that [32]

$$\mathbf{S}^{jst} = \begin{pmatrix} \cos(2\epsilon^j)e^{2i\delta^j_-} & i\sin(2\epsilon^j)e^{i(\delta^j_- + \delta^j_+)} \\ i\sin(2\epsilon^j)e^{i(\delta^j_- + \delta^j_+)} & \cos(2\epsilon^j)e^{2i\delta^j_+} \end{pmatrix}. \tag{3.130}$$

Note that the symmetry of the jPWS S matrix, as seen in (3.116), is clearly established in this expression.

3.3.4 The Scattering Matrix

The scattering matrix, M, in the relative momentum basis is defined as (see appendix A)

$$M(\boldsymbol{p}',\boldsymbol{p}) \equiv -\frac{\mu}{2\pi}T(\boldsymbol{p}',\boldsymbol{p};k), \quad k = |\boldsymbol{p}| = |\boldsymbol{p}'|, \tag{3.131}$$

where $T(\boldsymbol{p}',\boldsymbol{p};k) \equiv \langle \boldsymbol{p}'|\, T^+(E)\, |\boldsymbol{p}\rangle$ is the on-shell T matrix at on-shell energy $E = k^2/(2\mu)$ and μ is the reduced mass [29], such that

$$S(\boldsymbol{p}',\boldsymbol{p}) = \delta^{(2)}(\hat{\boldsymbol{p}}' - \hat{\boldsymbol{p}}) + \frac{ik}{2\pi}M(\boldsymbol{p}',\boldsymbol{p}). \tag{3.132}$$

[20] Note that the phase shifts do not carry an isospin superscript as the isospin is implicit from s and ℓ due to the Pauli principle (3.83).

[21] Note that the phase shifts of coupled channels do not need to specify the spin quantum number as coupled channels always have $s = 1$.

[22] They are called bar phase shifts since there usually denoted as $\{\bar{\delta}^j_-, \bar{\delta}^j_+, \bar{\epsilon}^j\}$. The bar has been dropped in this thesis, as no other convention for the phase shifts of coupled channels will be used.

In the case of two-nucleon scattering, where the two nucleons are treated as identical particles, the M-matrix elements are given by

$$M^{st}_{m'_s m_s}(\boldsymbol{p}', \boldsymbol{p}) = -\frac{\mu}{2\pi} \langle \boldsymbol{p}', s, m'_s, t, m_t | \, T^+(E) \, | \boldsymbol{p}, s, m_s, t, m_t \rangle_a = \\ = -\frac{\mu}{2\pi} \langle \boldsymbol{p}', s, m'_s, t, m_t | \, T^+(E)[1 - \hat{\Pi}] \, | \boldsymbol{p}, s, m_s, t, m_t \rangle \,, \quad (3.133)$$

where $|\boldsymbol{p}| = |\boldsymbol{p}'| = k = \sqrt{2\mu E}$ is the on-shell momentum, $\hat{\Pi}$ is the permutation operator that exchanges the two-nucleons in all Hilbert spaces, and $|\boldsymbol{p}, s, m_s, t, m_t\rangle$ are the relative NN states. By inserting (3.74) and (3.82), the M-matrix elements can be expressed as

$$M^{st}_{m'_s m_s}(\boldsymbol{p}', \boldsymbol{p}) = -\mu(2\pi)^2 \sum_{j, m_j} \sum_{\ell', \ell} C^{j, m_j}_{\ell', s; m_j - m'_s, m'_s} C^{j, m_j}_{\ell, s; m_j - m_s, m_s} \\ \cdot Y^{\ell'}_{m_j - m'_s}(\hat{\boldsymbol{p}}') Y^{*\ell}_{m_j - m_s}(\hat{\boldsymbol{p}}) [1 - (-1)^{\ell + s + t}] T^{jst}_{\ell' \ell}(k, k; k), \quad (3.134)$$

where $T^{jst}_{\ell' \ell}(k, k; k)$ is the on-shell jPWS T-matrix elements as defined in (3.112). By defining the c.m. system such that the direction of the ingoing relative momentum defines the z-axis, the second spherical harmonics becomes [28]

$$Y^{*\ell}_{m_j - m_s}(\hat{\boldsymbol{p}}) = \delta_{m_j m_s} \sqrt{\frac{2\ell + 1}{4\pi}}. \quad (3.135)$$

The direction of the outgoing relative momentum can then be characterised by a c.m. polar angle (scattering angle) $\vartheta \in [0, \pi]$ and azimuthal angle $\varphi \in [0, 2\pi)$, and (3.134) becomes

$$M^{st}_{m'_s m_s}(\vartheta, \varphi; k) = -\frac{\mu(2\pi)^2}{2\sqrt{\pi}} \sum_{j, \ell', \ell} \sqrt{2\ell + 1} C^{j, m_s}_{\ell', s; m_s - m'_s, m'_s} C^{j, m_s}_{\ell, s; 0, m_s} Y^{\ell'}_{m_s - m'_s}(\vartheta, \varphi) \\ \cdot [1 - (-1)^{\ell + s + t}] T^{jst}_{\ell' \ell}(k, k; k). \quad (3.136)$$

The M-matrix elements can alternatively be expressed in terms of the jPWS S-matrix elements, by inserting (3.115), as

$$M^{st}_{m'_s m_s}(\vartheta, \varphi; k) = \frac{\sqrt{\pi}}{ik} \sum_{j, \ell', \ell} \sqrt{2\ell + 1} C^{j, m_s}_{\ell', s; m_s - m'_s, m'_s} C^{j, m_s}_{\ell, s; 0, m_s} Y^{\ell'}_{m_s - m'_s}(\vartheta, \varphi) \\ \cdot [1 - (-1)^{\ell + s + t}] [S^{jst}_{\ell' \ell}(k, k) - \delta_{\ell' \ell}]. \quad (3.137)$$

Note that the M-matrix elements still carry a coupled isospin superscript.

Due to the isospin conservation, M can be thought of as an operator in the coupled isospin space as

$$M(\boldsymbol{p}', \boldsymbol{p}) = \left(\frac{1}{4} \mathbb{1} - [\boldsymbol{T}^{(1)} \otimes \mathbb{1}^{(2)}] \cdot [\mathbb{1}^{(2)} \otimes \boldsymbol{T}^{(2)}] \right) M^{t=0}(\boldsymbol{p}', \boldsymbol{p}) \\ + \left(\frac{3}{4} \mathbb{1} + [\boldsymbol{T}^{(1)} \otimes \mathbb{1}^{(2)}] \cdot [\mathbb{1}^{(2)} \otimes \boldsymbol{T}^{(2)}] \right) M^{t=1}(\boldsymbol{p}', \boldsymbol{p}). \quad (3.138)$$

As can be understood from the possible two-nucleon coupled isospin states shown in (3.59), the M-matrix elements for nn and pp scattering are

$$M^{s}_{m'_s m_s}(\boldsymbol{p}', \boldsymbol{p}) = M^{s,t=1}_{m'_s m_s}(\boldsymbol{p}', \boldsymbol{p}), \tag{3.139}$$

and for np scattering M-matrix elements become

$$M^{s}_{m'_s m_s}(\boldsymbol{p}', \boldsymbol{p}) = \frac{1}{2}\Big[M^{s,t=0}_{m'_s m_s}(\boldsymbol{p}', \boldsymbol{p}) + M^{s,t=1}_{m'_s m_s}(\boldsymbol{p}', \boldsymbol{p})\Big]. \tag{3.140}$$

Note also that M-matrix elements for $np \to pn$ scattering are

$$M^{s}_{m'_s m_s}(\boldsymbol{p}', \boldsymbol{p}) = \frac{1}{2}\Big[M^{s,t=1}_{m'_s m_s}(\boldsymbol{p}', \boldsymbol{p}) - M^{s,t=0}_{m'_s m_s}(\boldsymbol{p}', \boldsymbol{p})\Big]. \tag{3.141}$$

In the uncoupled spin basis, see (3.60), the two-nucleon spin states are determined by single-particle spin projections of the two nucleons. In accordance with (3.60), the M-matrix elements in the uncoupled spin basis are

$$M_{m'_{s,1},m'_{s,2};m_{s,1},m_{s,2}}(\boldsymbol{p}', \boldsymbol{p}) = \sum_{s} \sum_{m'_s, m_s} C^{s,m'_s}_{\frac{1}{2},\frac{1}{2};m'_{s,1},m'_{s,2}} C^{s,m_s}_{\frac{1}{2},\frac{1}{2};m_{s,1},m_{s,2}} M^{s}_{m'_s,m_s}(\boldsymbol{p}', \boldsymbol{p}). \tag{3.142}$$

The M matrix in this basis can thus be expressed as a 4×4 matrix

$$\mathbf{M} = \begin{pmatrix} M^1_{11} & \frac{1}{\sqrt{2}}M^1_{10} & \frac{1}{\sqrt{2}}M^1_{10} & M^1_{1-1} \\ \frac{1}{\sqrt{2}}M^1_{01} & \frac{1}{2}(M^1_{00} + M^0_{00}) & \frac{1}{2}(M^1_{00} - M^0_{00}) & \frac{1}{\sqrt{2}}M^1_{0-1} \\ \frac{1}{\sqrt{2}}M^1_{01} & \frac{1}{2}(M^1_{00} - M^0_{00}) & \frac{1}{2}(M^1_{00} + M^0_{00}) & \frac{1}{\sqrt{2}}M^1_{0-1} \\ M^1_{-11} & \frac{1}{\sqrt{2}}M^1_{-10} & \frac{1}{\sqrt{2}}M^1_{-10} & M^1_{-1-1} \end{pmatrix}, \tag{3.143}$$

where the M elements in the matrix are the coupled spin M-matrix elements $M^{s}_{m'_s m_s}(\boldsymbol{p}', \boldsymbol{p})$ [29] for the specific type of NN scattering.

3.4 Relativistic Nucleon-Nucleon Scattering

The treatment of the scattering problem in this chapter has until now been completely non-relativistic. When building the two-nucleon potential as done in chapter 2, the underlying theory is a quantum field theory and thus relativistic. As can be understood from the derivation of the χEFT Lagrangian terms, the heavy baryon formalism takes the theory to the non-relativistic limit. There are, however, still some "minimal relativity" that has to be accounted for.

Recall the operator Bethe-Salpeter equation used in deriving the NN potential in section 2.3

$$\bar{T} = \mathcal{V}\mathcal{G}\bar{T}, \tag{3.144}$$

where $\mathcal{G}$ is the relativistic two-nucleon propagator, $\bar{T}$ is the relativistic T operator, and $\mathcal{V}$ is the sum of all irreducible diagrams describing the two-nucleon interaction. This equation can equivalently be expressed in terms of two coupled equations

$$\bar{T} = \bar{V}G\bar{T}, \quad \bar{V} = \mathcal{V} + \mathcal{V}(\mathcal{G} - G)V, \tag{3.145}$$

where V is the relativistic NN potential and G is a covariant three-dimensional propagator. Using the propagator G proposed by R. Blankenbecler and R. Sugar [33], (3.145) results in the so-called Blankenbecler-Sugar equation in the relative momentum basis

$$\bar{T}(\boldsymbol{p}', \boldsymbol{p}; k) = \bar{V}(\boldsymbol{p}', \boldsymbol{p}) + \int_{\mathbb{R}^3} \frac{d\boldsymbol{q}}{(2\pi)^3 2E_q} \bar{V}(\boldsymbol{p}', \boldsymbol{q}) \frac{8\mu^2}{k^2 - q^2 + i\epsilon} \bar{T}(\boldsymbol{q}, \boldsymbol{p}; k), \tag{3.146}$$

where $E_q = \sqrt{|\boldsymbol{q}|^2 + 4\mu^2}$ and $q \equiv |\boldsymbol{q}|$. By scaling the relativistic V and T matrices as

$$\bar{V}(\boldsymbol{p}', \boldsymbol{p}) \longrightarrow V(\boldsymbol{p}', \boldsymbol{p}) = \sqrt{\frac{2\mu}{E_{p'}}} \bar{V}(\boldsymbol{p}', \boldsymbol{p}) \sqrt{\frac{2\mu}{E_p}}, \tag{3.147}$$

$$\bar{T}(\boldsymbol{p}', \boldsymbol{p}; k) \longrightarrow T(\boldsymbol{p}', \boldsymbol{p}; k) = \sqrt{\frac{2\mu}{E_{p'}}} \bar{T}(\boldsymbol{p}', \boldsymbol{p}; k) \sqrt{\frac{2\mu}{E_p}}, \tag{3.148}$$

the Blankenbecler-Sugar equation takes the form

$$T(\boldsymbol{p}', \boldsymbol{p}; k) = V(\boldsymbol{p}', \boldsymbol{p}) + \int_{\mathbb{R}^3} \frac{d\boldsymbol{q}}{(2\pi)^3} V(\boldsymbol{p}', \boldsymbol{q}) \frac{2\mu}{k^2 - q^2 + i\epsilon} T(\boldsymbol{q}, \boldsymbol{p}; k). \tag{3.149}$$

This equation can be recognised as the non-relativistic LS given in (3.122). The so-called "minimal relativistic" potential $V(\boldsymbol{p}', \boldsymbol{p})$ can thus be treated as a non-relativistic potential in the non-relativistic LS equation.

In the laboratory frame the two-nucleon scattering problem considers an incoming nucleon projectile with mass m_{P} and laboratory kinetic energy T_{lab} and a nucleon target of mass m_{T} at rest. The relative on-shell momentum can then be expressed as [34]

$$k = \sqrt{\frac{m_{\mathrm{T}}^2 T_{\mathrm{lab}}(2m_{\mathrm{P}} + T_{\mathrm{lab}})}{(m_{\mathrm{P}} + m_{\mathrm{T}})^2 + 2m_{\mathrm{T}} T_{\mathrm{lab}}}}. \tag{3.150}$$

4

Nucleon-Nucleon Scattering Amplitudes and Observables

This chapter builds upon the scattering theory presented in chapter 3 to derive the NN scattering quantities. Section 4.1 applies the symmetries of the NN system in subsection 3.3.2 to constrain the M matrix, resulting in the five complex NN scattering amplitudes. The M matrix is then used to define various NN scattering observables.

4.1 NN Scattering Amplitudes

In subsection 3.3.4, the scattering matrix M was derived from the T matrix, which allows it to be determined from an interaction potential through the LS equation. At a naive first glance of the uncoupled M-matrix (3.143), it appears to carry ten independent complex degrees of freedom. However, the symmetries of the system, all presented in subsection 3.3.2, decrease these complex degrees of freedom by half.

The spherical symmetry of the potential is carried directly to the T matrix, as can be trivially understood from (3.19). The relevant rotation transformations are given in (3.88) and imply that the NN M matrix only can depend on the trivial constant ($\propto \mathbb{1}_{4\times4}$) and scalars ($4\times4$ matrices) built of the $\boldsymbol{\sigma}^{(n)}$, the vector of the three Pauli spin matrices acting on the states of nucleon $n = 1, 2$, and the ingoing and outgoing relative momentum three-vectors. The M matrix can thus only be built of terms proportional to

$$\begin{cases} \mathbb{1}^{(1)}_{2\times2} \otimes \mathbb{1}^{(2)}_{2\times2}, \\ [\boldsymbol{\sigma}^{(1)} \otimes \mathbb{1}^{(2)}_{2\times2}] \cdot \hat{\boldsymbol{m}}, \\ [\mathbb{1}^{(1)}_{2\times2} \otimes \boldsymbol{\sigma}^{(2)}] \cdot \hat{\boldsymbol{m}}, \\ ([\boldsymbol{\sigma}^{(1)} \otimes \mathbb{1}^{(2)}_{2\times2}] \times [\mathbb{1}^{(1)}_{2\times2} \otimes \boldsymbol{\sigma}^{(2)}]) \cdot \hat{\boldsymbol{m}}, \\ [\boldsymbol{\sigma}^{(1)} \cdot \hat{\boldsymbol{m}}] \otimes [\boldsymbol{\sigma}^{(2)} \cdot \hat{\boldsymbol{m}}'], \end{cases} \tag{4.1}$$

where $\hat{\boldsymbol{m}}, \hat{\boldsymbol{m}}' \in \{\hat{\boldsymbol{K}}, \hat{\boldsymbol{P}}, \hat{\boldsymbol{N}}\}$ can be ether the momentum transfer unitvector $\hat{\boldsymbol{K}}$, the

momentum average unitvector $\hat{\boldsymbol{P}}$, or the normal vector to the c.m. scattering plane, $\hat{\boldsymbol{N}}$, (see figure 4.1b), defined as

$$\hat{\boldsymbol{K}} \equiv \frac{\boldsymbol{p}' - \boldsymbol{p}}{|\boldsymbol{p}' - \boldsymbol{p}|}, \quad \hat{\boldsymbol{P}} \equiv \frac{\boldsymbol{p}' + \boldsymbol{p}}{|\boldsymbol{p}' + \boldsymbol{p}|}, \quad \hat{\boldsymbol{N}} = \frac{\boldsymbol{p} \times \boldsymbol{p}'}{|\boldsymbol{p} \times \boldsymbol{p}'|}, \tag{4.2}$$

where $\boldsymbol{p}$ and $\boldsymbol{p}'$ are the ingoing and outgoing relative momentum, respectively.

The parity (3.100), time-reversal (3.105), and spin-space permutation (3.102) invariance of the Hamiltonian imply that the M matrix must be invariant under the three sets of transformations

$$\begin{aligned}
&\text{Parity:} && \hat{\boldsymbol{K}} \to -\hat{\boldsymbol{K}}, && \hat{\boldsymbol{P}} \to -\hat{\boldsymbol{P}} \\
&\text{Time reversal:} && \hat{\boldsymbol{P}} \to -\hat{\boldsymbol{P}}, && \hat{\boldsymbol{N}} \to -\hat{\boldsymbol{N}}, \quad \boldsymbol{\sigma}^{(n)} \to -\boldsymbol{\sigma}^{(n)} \\
&\text{spin-space permutation:} && \boldsymbol{\sigma}^{(1)} \to \boldsymbol{\sigma}^{(2)}, && \boldsymbol{\sigma}^{(2)} \to \boldsymbol{\sigma}^{(1)}
\end{aligned} \tag{4.3}$$

The only terms (4.1) that are invariant under these transformations are

$$\begin{cases}
\mathbb{1}^{(1)}_{2\times2} \otimes \mathbb{1}^{(2)}_{2\times2}, \\
[\boldsymbol{\sigma}^{(1)} \otimes \mathbb{1}^{(2)}_{2\times2} + \mathbb{1}^{(1)}_{2\times2} \otimes \boldsymbol{\sigma}^{(2)}] \cdot \hat{\boldsymbol{N}}, \\
[\boldsymbol{\sigma}^{(1)} \cdot \hat{\boldsymbol{N}}] \otimes [\boldsymbol{\sigma}^{(2)} \cdot \hat{\boldsymbol{N}}], \\
[\boldsymbol{\sigma}^{(1)} \cdot \hat{\boldsymbol{P}}] \otimes [\boldsymbol{\sigma}^{(2)} \cdot \hat{\boldsymbol{P}}], \\
[\boldsymbol{\sigma}^{(1)} \cdot \hat{\boldsymbol{K}}] \otimes [\boldsymbol{\sigma}^{(2)} \cdot \hat{\boldsymbol{K}}],
\end{cases} \tag{4.4}$$

and the most general M matrix, obeying all relevant symmetries as discussed in subsubsection 3.3.2.1, can thus be expressed as

$$\begin{aligned}
\mathbf{M}(\vartheta, \varphi; k) = {} & A_1(\vartheta, \varphi; k)[\mathbb{1}^{(1)}_{2\times2} \otimes \mathbb{1}^{(2)}_{2\times2}] \\
& + A_2(\vartheta, \varphi; k)([\boldsymbol{\sigma}^{(1)} \otimes \mathbb{1}^{(2)}_{2\times2} + \mathbb{1}^{(1)}_{2\times2} \otimes \boldsymbol{\sigma}^{(2)}] \cdot \hat{\boldsymbol{N}}) \\
& + A_3(\vartheta, \varphi; k)([\boldsymbol{\sigma}^{(1)} \cdot \hat{\boldsymbol{N}}] \otimes [\boldsymbol{\sigma}^{(2)} \cdot \hat{\boldsymbol{N}}]) \\
& + A_4(\vartheta, \varphi; k)([\boldsymbol{\sigma}^{(1)} \cdot \hat{\boldsymbol{P}}] \otimes [\boldsymbol{\sigma}^{(2)} \cdot \hat{\boldsymbol{P}}]) \\
& + A_5(\vartheta, \varphi; k)([\boldsymbol{\sigma}^{(1)} \cdot \hat{\boldsymbol{K}}] \otimes [\boldsymbol{\sigma}^{(2)} \cdot \hat{\boldsymbol{K}}]),
\end{aligned} \tag{4.5}$$

where the five complex functions $\{A_i\}_{i=1}^5$ are the so-called *NN scattering amplitudes* [12] in the I-call Lucas convention. For additional simplification of the problem, the c.m. system can be defined such that the outgoing relative momentum lies in the xz-plane, *i.e.* $\varphi = 0$ and

$$\boldsymbol{p} = k \begin{pmatrix} 0 \\ 0 \\ 1 \end{pmatrix}, \quad \boldsymbol{p}' = k \begin{pmatrix} \sin(\vartheta) \\ 0 \\ \cos(\vartheta) \end{pmatrix}, \tag{4.6}$$

where $\boldsymbol{p}$ is the ingoing relative mometum, $\boldsymbol{p}'$ is the outgoing relative mometum, and k is the on-shell momentum. In that case the M matrix and the five ($i = 1, 2, 3, 4, 5$) scattering amplitudes becomes

$$\mathbf{M}(k, \vartheta) \equiv \mathbf{M}(\vartheta, \varphi = 0; k), \quad A_i(k, \vartheta) \equiv A_i(\vartheta, \varphi = 0; k), \tag{4.7}$$

and the momentum transfer, momentum average, and normal unitvector are given by [29]

$$\hat{\boldsymbol{K}} = \begin{pmatrix} \cos(\vartheta/2) \\ 0 \\ -\sin(\vartheta/2) \end{pmatrix}, \quad \hat{\boldsymbol{P}} = \begin{pmatrix} \sin(\vartheta/2) \\ 0 \\ \cos(\vartheta/2) \end{pmatrix}, \quad \hat{\boldsymbol{N}} = \begin{pmatrix} 0 \\ 1 \\ 0 \end{pmatrix}. \tag{4.8}$$

By defining five matrices $\{\mathbf{M}_i(k,\vartheta)\}_{i=1}^5$ given by the terms (4.4), such that the M matrix is

$$\mathbf{M}(k,\vartheta) = \sum_{i=1}^{5} A_i(k,\vartheta)\mathbf{M}_i(k,\vartheta), \tag{4.9}$$

the scattering amplitudes can be identified as

$$A_i(k,\vartheta) = \begin{cases} \dfrac{1}{4}\mathrm{Tr}\{\mathbf{M}(k,\vartheta)\mathbf{M}_i(k,\vartheta)\} & \text{for } i = 1,3,4,5, \\ \dfrac{1}{8}\mathrm{Tr}\{\mathbf{M}(k,\vartheta)\mathbf{M}_i(k,\vartheta)\} & \text{for } i = 2, \end{cases} \tag{4.10}$$

due to the traclesness and multiplication relation of the Pauli matrices. The NN Lucas scattering amplitudes can thus be expressed in terms of the M-matrix elements for the specific type of NN scattering (see subsection 3.3.4), $M^s_{m'_s m_s}(k,\vartheta) \equiv M^s_{m'_s m_s}(\vartheta, \varphi = 0; k)$, as

$$\begin{cases} A_1 = \dfrac{1}{4}\Big[M^0_{00} + M^1_{00} + 2M^1_{11}\Big], \\ A_2 = \dfrac{i}{2\sqrt{2}}\Big[M^1_{10} - M^1_{01}\Big], \\ A_3 = \dfrac{1}{4}\Big[-M^0_{00} + M^1_{00} - 2M^1_{1-1}\Big], \\ A_4 = \dfrac{1}{2}[c - d], \\ A_5 = \dfrac{1}{2}[c + d], \end{cases} \tag{4.11}$$

where

$$\begin{aligned} c &= \frac{1}{2}\Big[-M^0_{00} + M^1_{11} + M^1_{1-1}\Big], \\ d &= \frac{\cos(\vartheta)}{2}\Big[M^1_{00} - M^1_{11} + M^1_{1-1}\Big] - \frac{\sin(\vartheta)}{\sqrt{2}}\Big[M^1_{10} + M^1_{01}\Big]. \end{aligned} \tag{4.12}$$

Note that the above expression utilised that [29]

$$\begin{aligned} M^1_{11}(k,\vartheta) &= M^1_{-1-1}(k,\vartheta), \quad M^1_{1-1}(k,\vartheta) = M^1_{-11}(k,\vartheta), \\ M^1_{01}(k,\vartheta) &= -M^1_{0-1}(k,\vartheta), \quad M^1_{10}(k,\vartheta) = -M^1_{-10}(k,\vartheta), \end{aligned} \tag{4.13}$$

which is a consequence of the time-reversal invariance constraint (3.119) at $\varphi = 0$.

The convention used in (4.5) and (4.10) is just one of many[1]. The two conventions that will be considered in this project are the *Saclay amplitudes*

$$\begin{cases} a = A_1 + A_3, \\ b = A_1 - A_3, \\ c = A_5 + A_4, \\ d = A_5 - A_4, \\ e = 2A_2, \end{cases} \tag{4.14}$$

and the *helicity amplitudes* [12]

$$\begin{cases} M_1 = A_1 \dfrac{\cos(\vartheta)+1}{2} + iA_2 \sin(\vartheta) + A_3 \dfrac{\cos(\vartheta)-1}{2} - A_4, \\ M_2 = A_1 \dfrac{\cos(\vartheta)-1}{2} + iA_2 \sin(\vartheta) + A_3 \dfrac{\cos(\vartheta)+1}{2} + A_5, \\ M_3 = A_1 \dfrac{\cos(\vartheta)+1}{2} + iA_2 \sin(\vartheta) + A_3 \dfrac{\cos(\vartheta)-1}{2} + A_4, \\ M_4 = -A_1 \dfrac{\cos(\vartheta)-1}{2} - iA_2 \sin(\vartheta) - A_3 \dfrac{\cos(\vartheta)+1}{2} + A_5, \\ M_5 = -A_1 \dfrac{\sin(\vartheta)}{2} + iA_2 \cos(\vartheta) - A_3 \dfrac{\sin(\vartheta)}{2}. \end{cases} \tag{4.15}$$

Note that the Saclay and helicity amplitudes, like the Lucas amplitudes, are functions of the on-shell momentum k and the polar scattering angle $\vartheta \in [0, \pi]$.

At the $\vartheta \in \{0, \pi\}$ boundaries, the M-matrix elements $M^s_{m'_s m_s}(k, \vartheta)$ are zero for $m'_s \neq m_s$, as can be understood from (3.137). It is then given from (4.11) that the Lucas Amplitudes are constrained as [12]

$$A_2(k, 0) = A_2(k, \pi) = 0, \quad A_3(k, 0) = A_5(k, 0), \quad A_3(k, 0) = A_4(k, 0). \tag{4.16}$$

The $\vartheta \in \{0, \pi\}$ boundary constraints for the Saclay and helicity amplitudes are shown in table 4.1.

Table 4.1: The $\vartheta \in \{0, \pi\}$ boundary constraints, due to rotational invariance, of the scattering amplitudes in the Lucas, Saclay, and helicity convention [12].

	Lucas Amplitudes	Saclay Amplitudes	Helicity Amplitudes
$\vartheta = 0$	$A_2 = 0$ $A_3 = A_5$	$e = 0$ $a - b = c + d$	$M_5 = 0$ $M_4 = 0$
$\vartheta = \pi$	$A_2 = 0$ $A_3 = A_4$	$e = 0$ $a - b = c - d$	$M_5 = 0$ $M_3 = 0$

[1]For a comprehensive compilation of different NN scattering amplitude conventions see [12].

4.1.1 Constraint from Unitarity of S Operator

The unitarity of the S operator, $S^\dagger S = \mathbb{1}$, implies that the S-matrix elements in the relative NN state basis are constrained as (see subsubsection 3.3.2.2)

$$\sum_{m_s''=-s}^{s} \int_\Omega d\hat{\boldsymbol{q}}\, S^{*st}_{m_s'' m_s'}(\boldsymbol{q},\boldsymbol{p}') S^{st}_{m_s'' m_s'}(\boldsymbol{q},\boldsymbol{p}) = \delta_{m_s' m_s}\delta^{(2)}(\hat{\boldsymbol{p}}' - \hat{\boldsymbol{p}}). \tag{4.17}$$

The M-matrix elements, as defined in subsection 3.3.4, are related to the S-matrix elements as

$$S^{st}_{m_s' m_s}(\boldsymbol{p}',\boldsymbol{p}) = \delta^{(2)}(\hat{\boldsymbol{p}}' - \hat{\boldsymbol{p}})\delta_{m_s' m_s} + \frac{ik}{2\pi} M^{st}_{m_s' m_s}(\boldsymbol{p}',\boldsymbol{p}). \tag{4.18}$$

It is then trivial that the unitarity of the S operator constrains the M-matrix elements. This constraint can be realised, by inserting (4.18) into (4.17), as

$$\frac{2\pi}{ik}\Big[M^{st}_{m_s' m_s}(\boldsymbol{p}',\boldsymbol{p}) - M^{*st}_{m_s m_s'}(\boldsymbol{p},\boldsymbol{p}')\Big] = \sum_{m_s''=-s}^{s} \int_\Omega d\hat{\boldsymbol{q}}\, M^{*st}_{m_s'' m_s'}(\boldsymbol{q},\boldsymbol{p}') M^{st}_{m_s'' m_s}(\boldsymbol{q},\boldsymbol{p}), \tag{4.19}$$

where $k = |\boldsymbol{p}| = |\boldsymbol{p}'| = |\boldsymbol{q}|$ is the on-shell momentum. Equation (4.19) can equivalently be expressed in terms of the M matrix in the uncoupled spin basis (3.143) as

$$\frac{2\pi}{ik}\Big[\mathbf{M}(\boldsymbol{p}',\boldsymbol{p}) - \mathbf{M}^\dagger(\boldsymbol{p},\boldsymbol{p}')\Big] = \int_\Omega d\hat{\boldsymbol{q}}\, \mathbf{M}^\dagger(\boldsymbol{q},\boldsymbol{p}')\mathbf{M}(\boldsymbol{q},\boldsymbol{p}). \tag{4.20}$$

4.2 Nucleon-Nucleon Scattering Observables

There are $4^4 = 256$ differential NN scattering observable types (see subsection 4.2.1) and 3 total cross section types (see subsection 4.2.2).

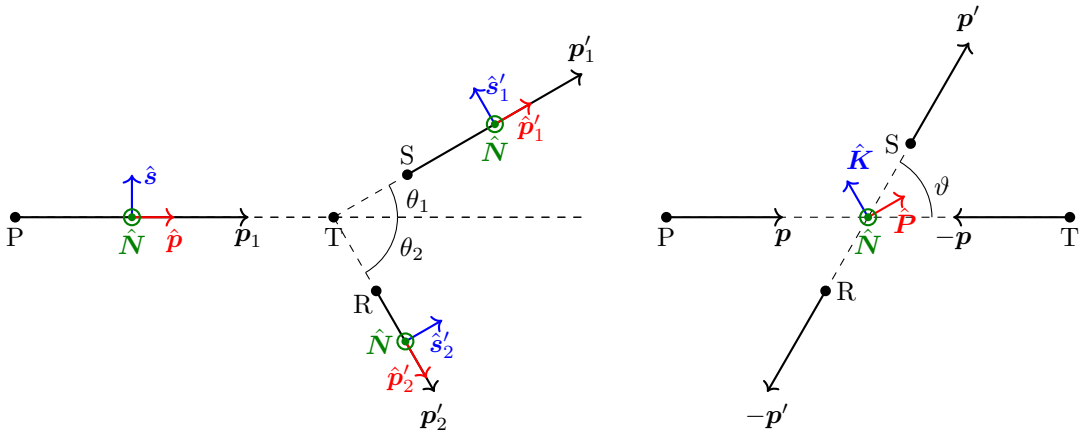

(a) Laboratory frame **(b)** Center-of-mass frame

Figure 4.1: The two-nucleon scattering event in the (a) laboratory frame and (b) the c.m. frame. The polarisation unit vectors in each frame are shown as the blue, red, and green vectors.

4.2.1 Differential scattering observables

The differential observables can be identified using a tensor notation as

$$\sigma O_{P_\mathrm{S}P_\mathrm{R}P_\mathrm{P}P_\mathrm{T}}(k,\vartheta) = \frac{1}{4}\mathrm{Tr}\Big\{\big[\sigma^{(1)}_{P_\mathrm{S}} \otimes \sigma^{(2)}_{P_\mathrm{R}}\big]\mathbf{M}(k,\vartheta)\big[\sigma^{(1)}_{P_\mathrm{P}} \otimes \sigma^{(2)}_{P_\mathrm{T}}\big]\mathbf{M}^\dagger(k,\vartheta)\Big\}, \tag{4.21}$$

where $\mathbf{M}$ is the uncoupled M matrix as given in (3.143) as a function of the on-shell momentum and the c.m. polar scattering angle, and the four indices P_S, P_R, P_P, and P_T represent the polarisation vectors of the scattered, recoil, projectile, and target particle, respectively. The 2×2 matrices $\sigma^{(n)}_{P_i}$ are given by

$$\sigma^{(n)}_{P_i} = \begin{cases} \mathbb{1}^{(n)}_{2\times 2} & \text{if } P_i = 0, \\ \boldsymbol{\sigma}^{(n)} \cdot \hat{\boldsymbol{P}}_i & \text{if } P_i \neq 0, \end{cases} \tag{4.22}$$

where $\boldsymbol{\sigma}^{(n)} = (\sigma^{(n)}_x, \sigma^{(n)}_y, \sigma^{(n)}_z)^T$ and $\mathbb{1}^{(n)}_{2\times 2}$ are the vector of the three 2×2 Pauli matrices and the 2×2 identity matrix, respecively, action on the single-particle spin state of nucleon $n = 1, 2$. The unit vectors $\hat{\boldsymbol{P}}_i$ are the direction of the polarisation vector of the scattered ($i = \mathrm{S}$), recoil ($i = \mathrm{R}$), projectile ($i = \mathrm{P}$), and target ($i = \mathrm{T}$) particles. The polarisation directions can be seen in figure 4.1. The unitful factor σ in (4.21) is the unpolarised differential cross section defined as

$$\sigma(k,\vartheta) \equiv \sigma O_{0000}(k,\vartheta) = \frac{1}{4}\mathrm{Tr}\Big\{\mathbf{M}(k,\vartheta)\mathbf{M}^\dagger(k,\vartheta)\Big\}. \tag{4.23}$$

The polarisation vector has three dimensions, and its direction will thus be considered to be given by one of three linearly independent unit vectors (or unpolarised) defined in relation to the momenta of the projectile, scattered, and recoil particles. In the laboratory frame, the polarisation direction is considered to be longitudinal, transverse, or given by the normal vector of the scattering plane. The longitudinal polarisation directions are given by $\hat{\boldsymbol{p}}$ (for the projectile and target particle), $\hat{\boldsymbol{p}}'_1$ (for the scattered particle), and $\hat{\boldsymbol{p}}'_2$ (for the recoil particle), which are the directions of the projectile (same as the direction of the relative momentum in the c.m. frame), scattered, and recoil particles momentum, respectively. The transverse polarisation directions are given by

$$\hat{\boldsymbol{s}} \equiv \frac{\hat{\boldsymbol{N}} \times \hat{\boldsymbol{p}}}{|\hat{\boldsymbol{N}} \times \hat{\boldsymbol{p}}|}, \quad \hat{\boldsymbol{s}}'_1 \equiv \frac{\hat{\boldsymbol{N}} \times \hat{\boldsymbol{p}}'_1}{|\hat{\boldsymbol{N}} \times \hat{\boldsymbol{p}}'_1|}, \quad \hat{\boldsymbol{s}}'_2 \equiv \frac{\hat{\boldsymbol{N}} \times \hat{\boldsymbol{p}}'_2}{|\hat{\boldsymbol{N}} \times \hat{\boldsymbol{p}}'_2|} \tag{4.24}$$

for the projectile and target, scattered, and recoil particles, respectively. The polarisation direction normal to the scattering plane is given by

$$\hat{\boldsymbol{N}} = \frac{\hat{\boldsymbol{p}} \times \hat{\boldsymbol{p}}'_1}{|\hat{\boldsymbol{p}} \times \hat{\boldsymbol{p}}'_1|} = \frac{\hat{\boldsymbol{p}}'_2 \times \hat{\boldsymbol{p}}}{|\hat{\boldsymbol{p}}'_2 \times \hat{\boldsymbol{p}}|} = \frac{\hat{\boldsymbol{p}}'_2 \times \hat{\boldsymbol{p}}'_1}{|\hat{\boldsymbol{p}}'_2 \times \hat{\boldsymbol{p}}'_1|}, \tag{4.25}$$

for all particles. An observable in the laboratory frame can thus be identified as

$$\sigma O_{P_\mathrm{S}P_\mathrm{R}P_\mathrm{P}P_\mathrm{T}}(k,\vartheta), \quad \begin{cases} P_\mathrm{P}, P_\mathrm{T} \in \{0, N, s, p\}, \\ P_\mathrm{S} \in \{0, N, s'_1, p'_1\}, \\ P_\mathrm{R} \in \{0, N, s'_2, p'_2\}. \end{cases} \tag{4.26}$$

In the c.m. frame, the polarisation direction is considered to be given by the normal vector to the scattering plane, the momentum transfer $\boldsymbol{K}$, or the momentum average $\boldsymbol{P}$, as seen in figure 4.1b. The direction of the normal vector of the scattering plane is the same as for the laboratory system and can, in the c.m. frame, be identified as

$$\hat{\boldsymbol{N}} = \frac{\boldsymbol{p} \times \boldsymbol{p}'}{|\boldsymbol{p} \times \boldsymbol{p}'|}, \tag{4.27}$$

where $\boldsymbol{p}$ is the ingoing relative momentum and $\boldsymbol{p}'$ is the ingoing relative momentum. The direction of the momentum transfer and the momentum average are defined as

$$\hat{\boldsymbol{K}} \equiv \frac{\boldsymbol{p}' - \boldsymbol{p}}{|\boldsymbol{p}' - \boldsymbol{p}|}, \quad \hat{\boldsymbol{P}} \equiv \frac{\boldsymbol{p}' + \boldsymbol{p}}{|\boldsymbol{p}' + \boldsymbol{p}|}. \tag{4.28}$$

An observable, in the c.m. frame, can thus be identified as

$$\sigma O_{P_\mathrm{S} P_\mathrm{R} P_\mathrm{P} P_\mathrm{T}}(k, \vartheta), \quad P_\mathrm{P}, P_\mathrm{T}, P_\mathrm{S}, P_\mathrm{R} \in \{0, N, K, P\}, \tag{4.29}$$

where the possible indices $\{0, N, K, P\}$ refer to no polarisation and the unit vectors shown in figure 4.1b.

The $4^4 = 256$ differential observables can be divided into categories as seen in table 4.2. All of these observables are, however, not independent quantities if one assumes parity conservation, the generalised Pauli principle, and time-reversal invariance. The implications of these symmetries will here be considered with the polarisation directions of the c.m. frame, see equation (4.29). Parity conservation implies that only observable types with an even number of K and P are non-zero, given that $\hat{\boldsymbol{K}}$ and $\hat{\boldsymbol{P}}$, as defined in (4.28), change sign under space inversion ($\hat{\boldsymbol{N}}$ is unchanged). The generalised Pauli principle (including isospin invariance) requires an equality between two observable types related by interchanging the projectile with the target and the scattered with the recoil particle state and momenta. For a general observable type, this implies that

$$O_{P_\mathrm{S} P_\mathrm{R} P_\mathrm{P} P_\mathrm{T}} = (-1)^{[K]+[P]} O_{P_\mathrm{R} P_\mathrm{S} P_\mathrm{T} P_\mathrm{P}}, \tag{4.30}$$

where $[K]$ and $[P]$ is the number of the indices $\{P_\mathrm{S}, P_\mathrm{R}, P_\mathrm{P}, P_\mathrm{T}\}$ that is K and P, respectively. Combining this with the parity conservation implies that

$$O_{P_\mathrm{S} P_\mathrm{R} P_\mathrm{P} P_\mathrm{T}} = O_{P_\mathrm{R} P_\mathrm{S} P_\mathrm{T} P_\mathrm{P}}. \tag{4.31}$$

Time-reversal invariance implies that

$$O_{P_\mathrm{S} P_\mathrm{R} P_\mathrm{P} P_\mathrm{T}} = (-1)^{[K]} O_{P_\mathrm{P} P_\mathrm{T} P_\mathrm{S} P_\mathrm{R}}. \tag{4.32}$$

This can be realised by noting that the effect of time-reversal may be expressed by changing the sign of the ingoing relative momentum $\boldsymbol{p}$, the outgoing relative momentum $\boldsymbol{p}'$, and the vector of Pauli matrices acting on nucleon $n = 1, 2$, $\boldsymbol{\sigma}^{(n)}$, and interchanging the initial and final states and momenta. The transformation of the c.m. polarisation directions, resulting from time-reversal, is then [12]

$$\hat{\boldsymbol{K}} \longrightarrow \hat{\boldsymbol{K}}, \quad \hat{\boldsymbol{P}} \longrightarrow -\hat{\boldsymbol{P}}, \quad \hat{\boldsymbol{N}} \longrightarrow -\hat{\boldsymbol{N}}. \tag{4.33}$$

At last, the NN scattering matrix satisfies the identity

$$\left[\sigma_N^{(1)} \otimes \sigma_N^{(2)}\right]\mathbf{M}\left[\sigma_N^{(1)} \otimes \sigma_N^{(2)}\right] = \mathbf{M}, \tag{4.34}$$

which is the invariance of reflection in the scattering plane (the so-called Bohr's rule) [12], and can be verified with (4.5). In conclusion, only 25 of the 4^4 differetnial NN scattering observables are non-zero and linearly independent[2] [12]: 1 scalar (the unpolarised differential cross section), 1 one-component tesor (P_{N000}), 12 two-component tensors, 9 three-component tensors, and 2 four-component tensors.

Table 4.2: The categorisation of the tensor factors of the differential observable types.

Measured quantity	Unpolarised projectile Unpolarised target	Polarised projectile Unpolarised target	Unpolarised projectile Polarised target	Polarised projectile Polarised target
Differential cross section	O_{0000} $(\equiv I_{0000})$	$O_{00P_\mathrm{P}0}$ $(\equiv A_{00P_\mathrm{P}0})$	O_{000P_T} $(\equiv A_{000P_\mathrm{T}})$	$O_{00P_\mathrm{P}P_\mathrm{T}}$ $(\equiv A_{00P_\mathrm{P}P_\mathrm{T}})$
Polarisation of scattered particle	$O_{P_\mathrm{S}000}$ $(\equiv P_{P_\mathrm{S}000})$	$O_{P_\mathrm{S}0P_\mathrm{P}0}$ $(\equiv D_{P_\mathrm{S}0P_\mathrm{P}0})$	$O_{P_\mathrm{S}00P_\mathrm{T}}$ $(\equiv K_{P_\mathrm{S}00P_\mathrm{T}})$	$O_{P_\mathrm{S}0P_\mathrm{P}P_\mathrm{T}}$ $(\equiv M_{P_\mathrm{S}0P_\mathrm{P}P_\mathrm{T}})$
Polarisation of recoil particle	$O_{0P_\mathrm{R}00}$ $(\equiv P_{0P_\mathrm{R}00})$	$O_{0P_\mathrm{R}P_\mathrm{P}0}$ $(\equiv K_{0P_\mathrm{R}P_\mathrm{P}0})$	$O_{0P_\mathrm{R}0P_\mathrm{T}}$ $(\equiv D_{0P_\mathrm{R}0P_\mathrm{T}})$	$O_{0P_\mathrm{R}P_\mathrm{P}P_\mathrm{T}}$ $(\equiv N_{0P_\mathrm{R}P_\mathrm{P}P_\mathrm{T}})$
Correlation of polarisations	$O_{P_\mathrm{S}P_\mathrm{R}00}$ $(\equiv C_{P_\mathrm{S}P_\mathrm{R}00})$	$O_{P_\mathrm{S}P_\mathrm{R}P_\mathrm{P}0}$ $(\equiv C_{P_\mathrm{S}P_\mathrm{R}P_\mathrm{P}0})$	$O_{P_\mathrm{S}P_\mathrm{R}0P_\mathrm{T}}$ $(\equiv C_{P_\mathrm{S}P_\mathrm{R}0P_\mathrm{T}})$	$O_{P_\mathrm{S}P_\mathrm{R}P_\mathrm{P}P_\mathrm{T}}$ $(\equiv C_{P_\mathrm{S}P_\mathrm{R}P_\mathrm{P}P_\mathrm{T}})$

4.2.2 Total cross sections

The total cross section is the only observable type that cannot be identified using the tensor notation (4.21). The total cross section σ_{tot} can generally be expressed as

$$\sigma_{\mathrm{tot}}(k; \boldsymbol{P}_\mathrm{P}, \boldsymbol{P}_\mathrm{T}) = \sigma_{0,\mathrm{tot}}(k) + \sigma_{1,\mathrm{tot}}(k)[\boldsymbol{P}_\mathrm{P} \cdot \boldsymbol{P}_\mathrm{T}] + \sigma_{2,\mathrm{tot}}(k)[\boldsymbol{P}_\mathrm{P} \cdot \hat{\boldsymbol{p}}][\boldsymbol{P}_\mathrm{T} \cdot \hat{\boldsymbol{p}}], \tag{4.35}$$

where k is the on-shell momentum, $\boldsymbol{P}_\mathrm{P}$ is the polarisation vector of the projectile particle, $\boldsymbol{P}_\mathrm{T}$ is the polarisation vector of the target particle, and $\hat{\boldsymbol{p}}$ is the direction of the relative momenta (same as the direction of the projectile particle momentum) [12]. The first term, $\sigma_{0,\mathrm{tot}}$, is the unpolarised total cross section, and can be determined as

$$\sigma_{0,\mathrm{tot}}(k) = 2\pi \int_0^\pi d\vartheta \, \sin(\vartheta) \sigma O_{0000}(k, \vartheta) \tag{4.36}$$

where $\sigma O_{0000}(k, \vartheta) \equiv \sigma(k, \vartheta)$ is the unpolarised differential cross section as defined in figure 4.1b. The factor $\sigma_{1,\mathrm{tot}}$, in the second term of (4.35), is given by

$$\sigma_{1,\mathrm{tot}}(k) = \pi \int_0^\pi d\vartheta \, \sin(\vartheta)[\sigma O_{00ss}(k, \vartheta) + \sigma O_{00NN}(k, \vartheta)], \tag{4.37}$$

[2]For detailed derivation and listing of the non-zero and linearly independent differential observable types see [12].

and can be interpreted as the contribution to the total cross section from transverse projectile and target polarisation, *i.e.* orthogonal to the projectile momentum. The factor $\sigma_{2,\mathrm{tot}}$ in the last term in (4.35) can be expressed as

$$\sigma_{2,\mathrm{tot}}(k) = 2\pi \int_0^\pi d\vartheta \, \sin(\vartheta) \sigma O_{00pp}(k,\vartheta) - \sigma_{1,\mathrm{tot}}(k). \tag{4.38}$$

The integral term can be interpreted as the contribution to the total cross section from longitudinal projectile and target polarisation, *i.e.* parallel to the projectile momentum [35, 36]. Note that the $\sigma_{1,\mathrm{tot}}$ and $\sigma_{2,\mathrm{tot}}$ should not be taken as literal total cross sections, as they can take negative values. The only "real" total cross sections are σ_{tot} and $\sigma_{0,\mathrm{tot}}$, which are positive definite [12].

The three total cross section related observable types can thus be quantified as the total cross section $\sigma_{\mathrm{tot}}(k)$, the transverse total cross section

$$\sigma_T(k) \equiv \sigma_{\mathrm{tot}}(k;\uparrow\downarrow) - \sigma_{\mathrm{tot}}(k;\uparrow\uparrow) = -2\sigma_{1,\mathrm{tot}}(k), \tag{4.39}$$

and the longitudinal total cross section

$$\sigma_L(k) \equiv \sigma_{\mathrm{tot}}(k;\leftrightarrows) - \sigma_{\mathrm{tot}}(k;\rightrightarrows) = -2[\sigma_{1,\mathrm{tot}}(k) + \sigma_{2,\mathrm{tot}}(k)]. \tag{4.40}$$

The vertical and horizontal arrows indicate that the polarisation direction of the particles is transverse and longitudinal to the projectile momentum, respectively. The two arrows pointing in the same direction, *i.e.* ($\uparrow\uparrow$) and ($\rightrightarrows$), implies that $\hat{\boldsymbol{P}}_{\mathrm{P}} = \hat{\boldsymbol{P}}_{\mathrm{T}}$, and the two arrows pointing in the opposite direction, *e.i.* ($\uparrow\downarrow$) and ($\leftrightarrows$), implies that $\hat{\boldsymbol{P}}_{\mathrm{P}} = -\hat{\boldsymbol{P}}_{\mathrm{T}}$.

4.2.2.1 Optical Theorem for NN Scattering

In the case of forward scattering ($\vartheta = 0$), where $\boldsymbol{p}' = \boldsymbol{p} \equiv \boldsymbol{k}$, the constraint from the unitarity of the S operator (4.19) becomes

$$\frac{2\pi}{ik}\Big[\mathbf{M}(0,0;k) - \mathbf{M}^\dagger(0,0;k)\Big] = \\ = \int_0^\pi d\vartheta_{\boldsymbol{q}} \, \sin(\vartheta_{\boldsymbol{q}}) \int_0^{2\pi} d\varphi_{\boldsymbol{q}} \, \mathbf{M}^\dagger(\vartheta_{\boldsymbol{q}},\varphi_{\boldsymbol{q}};k)\mathbf{M}(\vartheta_{\boldsymbol{q}},\varphi_{\boldsymbol{q}};k). \tag{4.41}$$

The right side of this equation contains an integral over the azimuthal angle of $\boldsymbol{q}$, which has to be handled with care since certain elements of the M matrix are not constant for all $\varphi_{\boldsymbol{q}}$. This φ dependence of the M-matrix elements can, however, be factored out as

$$M^s_{m'_s m_s}(\vartheta,\varphi;k) = e^{-i(m'_s - m_s)\varphi} M^s_{m'_s m_s}(k,\vartheta), \tag{4.42}$$

which can be realised from (3.137) and $Y^\ell_{m_\ell}(\vartheta,\varphi) = e^{im_\ell\varphi} Y^\ell_{m_\ell}(\vartheta,0)$ [28].

Looking at the definition of the matrix $\boldsymbol{M}$ (3.143), it is given that

$$\frac{1}{4}\mathrm{Tr}\Big\{\mathbf{M}^\dagger(\vartheta_{\boldsymbol{q}},\varphi_{\boldsymbol{q}};k)\mathbf{M}(\vartheta_{\boldsymbol{q}},\varphi_{\boldsymbol{q}};k)\Big\} = \\ = \frac{1}{4}\mathrm{Tr}\Big\{\mathbf{M}^\dagger(k,\vartheta_{\boldsymbol{q}})\mathbf{M}(k,\vartheta_{\boldsymbol{q}})\Big\} = \sigma O_{0000}(k,\vartheta_{\boldsymbol{q}}), \tag{4.43}$$

i.e. the unpolarised differential cross section is independent of the azimuthal scattering angle. Note that this finding is not unique and applies to all differential scattering observables. It is thus given that, by taking the trace on both sides of the unitarity constraint (4.41), the unpolarised total cross section can be related to the scattering amplitudes as

$$\frac{4\pi}{k}\mathrm{Im}[A_1(k,0)] = 2\pi\int_0^\pi d\vartheta_{\boldsymbol{q}}\,\sin(\vartheta_{\boldsymbol{q}})\sigma O_{0000}(k,\vartheta_{\boldsymbol{q}}) = \sigma_{0,\mathrm{tot}}(k). \tag{4.44}$$

The direction of the ingoing momentum is defined to be parallel to the z-axis and independent of the scattering angles. The differential observable σO_{00pp}, appearing in the longitudinal total cross section, can thus be expressed in terms of the φ dependent M matrix as

$$\begin{aligned}\sigma O_{00pp}(k,\vartheta) &= \frac{1}{4}\mathrm{Tr}\Big\{\mathbf{M}^\dagger(k,\vartheta)\mathbf{M}(k,\vartheta)[\sigma_z^{(1)}\otimes\sigma_z^{(2)}]\Big\} = \\ &= \frac{1}{4}\mathrm{Tr}\Big\{\mathbf{M}^\dagger(\vartheta,\varphi;k)\mathbf{M}(\vartheta,\varphi;k)[\sigma_z^{(1)}\otimes\sigma_z^{(2)}]\Big\}.\end{aligned} \tag{4.45}$$

The unitarity constraint (4.41) can thus provide an expression for $\sigma_{1,\mathrm{tot}}+\sigma_{2,\mathrm{tot}}$ as

$$\frac{4\pi}{k}\mathrm{Im}[A_4(k,0)] = 2\pi\int_0^\pi d\vartheta_{\boldsymbol{q}}\,\sin(\vartheta_{\boldsymbol{q}})\sigma O_{00pp}(k,\vartheta_{\boldsymbol{q}}) = \sigma_{1,\mathrm{tot}}+\sigma_{2,\mathrm{tot}}, \tag{4.46}$$

given that the momentum average unitvector is $\hat{\boldsymbol{P}} = \hat{\boldsymbol{p}}$ for $\boldsymbol{p} = \boldsymbol{p'}$.

The differential observables σO_{00ss} and σO_{00NN}, appearing in $\sigma_{1,\mathrm{tot}}$, are as independent of the azimuthal scattering angle. The integral over each of them separately can, however, not be related to the scattering amplitudes at $\vartheta = 0$ since the unitvectors $\hat{\boldsymbol{N}}$ and $\hat{\boldsymbol{s}}$ depend on φ. It can, however, be shown that

$$\begin{aligned}&\frac{1}{4}\mathrm{Tr}\Big\{\mathbf{M}^\dagger(\vartheta,\varphi;k)\mathbf{M}(\vartheta,\varphi;k)[\sigma_x^{(1)}\otimes\sigma_x^{(2)}+\sigma_y^{(1)}\otimes\sigma_y^{(2)}]\Big\} = \\ &\qquad= \frac{1}{4}\mathrm{Tr}\Big\{\mathbf{M}^\dagger(k,\vartheta)\mathbf{M}(k,\vartheta)[\sigma_x^{(1)}\otimes\sigma_x^{(2)}+\sigma_y^{(1)}\otimes\sigma_y^{(2)}]\Big\} = \\ &\qquad\qquad= \sigma O_{00ss}(k,\vartheta)+\sigma O_{00NN}(k,\vartheta).\end{aligned} \tag{4.47}$$

The unitarity constraint (4.41) can then, by multiplying both sides with $\sigma_x^{(1)}\otimes\sigma_x^{(2)}+\sigma_y^{(1)}\otimes\sigma_y^{(2)}$ and taking the trace, provide the relation

$$\frac{4\pi}{k}\mathrm{Im}[A_5(k,0)] = \pi\int_0^\pi d\vartheta_{\boldsymbol{q}}\,\sin(\vartheta_{\boldsymbol{q}})[\sigma O_{00ss}(k,\vartheta)+\sigma O_{00NN}(k,\vartheta)] = \sigma_{1,\mathrm{tot}}. \tag{4.48}$$

Note that this equation utilises the fact that $A_3(k,0) = A_5(k,0)$ as was discovered in section 4.1.

The three expressions found above give the total cross sections as the imaginary parts of the non-zero NN scattering amplitudes in the forward direction as

$$\sigma_{0,\text{tot}} = \frac{4\pi}{k}\text{Im}[A_1(k,0)], \tag{4.49}$$

$$\sigma_{1,\text{tot}} = \frac{4\pi}{k}\text{Im}[A_5(k,0)] = \frac{4\pi}{k}\text{Im}[A_3(k,0)], \tag{4.50}$$

$$\sigma_{2,\text{tot}} = \frac{4\pi}{k}\text{Im}[A_4(k,0) - A_5(k,0)] = \frac{4\pi}{k}\text{Im}[A_4(k,0) - A_3(k,0)], \tag{4.51}$$

and are collectively known as the *optical theorem* for NN scattering [12].

Part II

Methods and Implementation

5

Bayesian Effective Field Theory Truncation Errors

The aim of this project is to investigate the errors of NN scattering observables due to the truncation of the χEFT potential, as discussed in chapter 2. The systematic scheme in which the contributions to the NN interaction potential are considered order-by-order is utilised to consider the NN scattering quantities in a similar expansion. The systematic convergence of a well-constructed EFT allows the truncation errors (defined in section 5.1) to be estimated from the determined predictions BUQ. The BUQ model that was used in this study was implemented with a Gaussian-process (*Gaussian Process* (GP)) model and described in section 5.2.

5.1 EFT Truncation Errors

In chapter 2 the χEFT potential is considered as an expansion

$$V(\vec{\alpha}) = \sum_{\nu=0}^{\infty} V^{(\nu)}(\vec{\alpha}), \tag{5.1}$$

where $V^{(\nu)}(\vec{\alpha})$ is the contribution from the Feynman diagrams of chiral order ν, dependent on the LECs $\vec{\alpha}$. The chiral order of a Feynman diagram is determined with some power counting scheme, in this thesis Weinberg power counting, such that the importance of each term in the expansion can be considered to be given by the corresponding power of an expansion parameter

$$Q = \frac{\Lambda_\pi}{\Lambda_\chi}, \tag{5.2}$$

where Λ_π and Λ_χ are the soft and hard scales of the theory, respectively. For χEFT, the soft scale is given by the scale of the average pion mass $m_\pi \approx 138.039\,\text{MeV}$ [16] or the relative momentum of two nucleons. The hard scale (also known as the chiral-symmetry breaking scale) is of the scale of the $\rho(770)$ mass $m_\rho \approx 775.26\,\text{MeV} \sim 1\,\text{GeV}$ [16].

A NN scattering quantity[1] $y(\vec{x};\vec{\alpha})$, dependent on d independent variables[2] $\vec{x} \in \mathbb{R}^d$, determined with the EFT potential with the LECs $\vec{\alpha}$ can in a similar fashion be considered as an expansion

$$y(\vec{x};\vec{\alpha}) = \sum_{\nu=0}^{\infty} y^{(\nu)}(\vec{x};\vec{\alpha}), \tag{5.3}$$

where $y^{(\nu)}(\vec{x};\vec{\alpha})$ is the contribution to the quantity corresponding to the potential contribution $V^{(\nu)}(\vec{\alpha})$. The dependence of the LECs will from now on be suppressed from the notation, *i.e.* $y^{(\nu)}(\vec{x}) \equiv y^{(\nu)}(\vec{x};\vec{\alpha})$. When the potential is truncated at an order κ, by only considering the contributions up to a chiral order κ, the predicted quantity becomes

$$y_\kappa(\vec{x}) = \sum_{\nu=0}^{\kappa} y^{(\nu)}(\vec{x}). \tag{5.4}$$

The error of such a truncation can then be identified as the contributions of the remaining terms in the expansion (5.3) [8], *i.e.*

$$\delta y_\kappa(\vec{x}) = \sum_{\nu=\kappa+1}^{\infty} y^{(\nu)}(\vec{x}), \tag{5.5}$$

such that

$$y(\vec{x}) = y_\kappa(\vec{x}) + \delta y_\kappa(\vec{x}). \tag{5.6}$$

By introducing a dimensionful reference function of the quantity $y_{\text{ref}}(\vec{x}) \sim y(\vec{x})$, which sets the scale of the quantity, and the dimensionless expansion factor $Q^\nu(\vec{x})$ of the χEFT, each term in the expansion (5.3) can be written as

$$y^{(\nu)}(\vec{x}) = y_{\text{ref}}(\vec{x}) c^{(\nu)}(\vec{x}) Q^\nu(\vec{x}). \tag{5.7}$$

For appropriately chosen reference function and expansion parameter[3], it is assumed that all expansion coefficients $c^{(\nu)}$ are of natural scale, *i.e.* $c^{(\nu)} \sim \mathcal{O}(1)$ [7]. The truncated quantity and truncation error can then be expressed as [8]

$$\begin{cases} y_\kappa(\vec{x}) = y_{\text{ref}}(\vec{x}) \sum_{\nu=0}^{\kappa} c^{(\nu)}(\vec{x}) Q^\nu(\vec{x}), \\ \delta y_\kappa(\vec{x}) = y_{\text{ref}}(\vec{x}) \sum_{\nu=\kappa+1}^{\infty} c^{(\nu)}(\vec{x}) Q^\nu(\vec{x}), \end{cases} \tag{5.8}$$

and the expansion coefficients can be identified as

$$c^{(\nu)}(\vec{x}) = \frac{y^{(\nu)}(\vec{x})}{y_{\text{ref}}(\vec{x}) Q^\nu(\vec{x})} = \frac{y_\nu(\vec{x}) - y_{\nu-1}(\vec{x})}{y_{\text{ref}}(\vec{x}) Q^\nu(\vec{x})}. \tag{5.9}$$

[1] The scattering quantity could be, for example, a scattering amplitude or observable.

[2] *E.g.* $\vec{x} = (T_{\text{lab}}, \vartheta)$ for NN scattering amplitudes, where T_{lab} is a laboratory kinetic energy and ϑ is a c.m. polar scattering angle.

[3] Note that the expansion parameter is given by $Q(\vec{x}) = \Lambda_\pi(\vec{x})/\Lambda_\chi$ and what is "choosen" is the value of Λ_χ and the function $\Lambda_\pi(\vec{x})$, which *e.g.* in the context of two-nucleon scattering could be $\Lambda_\chi = 775\,\text{MeV}$ and $\Lambda_\pi(p) = \max(p, m_\pi)$, where k is the relative on-shell momentum of the two nucleons.

Note that for χEFT the potential of chiral order $\nu = 1$ is zero due to various symmetries (see chapter 2), resulting in $y^{(1)}(\vec{x}) = 0$ and thus $c^{(1)}(\vec{x}) = 0$ of all quantities.

5.2 Bayesian Uncertainty Quantification

For a reference function $y_{\text{ref}}(x)$ that captures the scale of the quantity and an expansion parameter that reflects the ChPT expansion, the expansion coefficient $c^{(\nu)}$ is expected to be of natural scale. In Bayesian terms, one imposes a naturalness *prior* for the expansion coefficients. The naturalness *prior* implies that the coefficients have distributions of a characteristic size and are thus assumed to share one distribution, which reflects the systematic convergence of a well-constructed EFT [8, 10]. Under this assumption, the unknown coefficients $c^{(\nu>\kappa)}$ can be inferred from the known coefficients $c^{(\nu\leq\kappa)}$ by using them to identify the hyperparameters of the coefficients distribution, this procedure is refered to the BUQ model for a EFT. It is also important not to ignore the prior knowledge that a physical quantity is not pointwise independent, but correlated to its value at nearby points, *i.e.* they have a non-zero correlation length across its independent variables [8]. This prior is implemented by considering the expansion coefficient curves $c^{(\nu)}(\vec{x})$ as draws from a GP with a covariance function.

5.2.1 Gaussian Process Error Model

The expansion coefficients $c^{(\nu)}(\vec{x})$ in (5.8) are assumed to be *independent and identically distributed* (i.i.d.) draws from a GP as

$$c^{(\nu)}(\boldsymbol{x})|\boldsymbol{\Theta} \overset{\text{i.i.d.}}{\sim} \mathcal{GP}[m(\boldsymbol{x}), \bar{c}^2 r(\boldsymbol{x}, \boldsymbol{x}'; \ell)], \tag{5.10}$$

where $\boldsymbol{x} = \{\vec{x}_i\}_i$ is a set of input points[4], $\boldsymbol{\Theta} = \{m, \bar{c}^2, \ell\}$ is the set of GP hyperparameters, and $r(\vec{x}, \vec{x}'; \ell)$ is the covariance function [37]. The hyperparameters are the diagonal $d \times d$ covariance length matrix ℓ, the marginal varaince $\bar{c}^2$, and the mean function $m(\vec{x}) \equiv \langle c^{(\nu)}(\vec{x})\rangle$. The covariance length matrix is defined as

$$\ell = \bigoplus_{i=1}^{d} \ell_{x_i}^2 = \begin{pmatrix} \ell_{x_1}^2 & 0 & \cdots & 0 \\ 0 & \ell_{x_2}^2 & \cdots & 0 \\ \vdots & \vdots & \ddots & \vdots \\ 0 & 0 & \cdots & \ell_{x_d}^2 \end{pmatrix}, \tag{5.11}$$

where $\{\ell_{x_i}\}_{i=2}^{d}$ are the correlation length across the independent variabels $\vec{x} = (x_1, x_2, \ldots, x_d)^T$. The covariance function is chosen to reflect the correlation structure of the *Gauss-Legendre* (GL) kernel[5].

[4]Note that a function $f(\boldsymbol{x})$ of the set $\boldsymbol{x} = \{\vec{x}_i\}_i$ is interpreted as $f(\boldsymbol{x}) = \{f(\vec{x}_i)\}_i$. The covariance function are considered similarly as $r(\boldsymbol{x}, \boldsymbol{x}'; \ell) = \{r(\vec{x}_i, \vec{x}_j; \ell)\}_{i,j}$. This notation is necessary since the draws from a GP are for the set $\boldsymbol{x} = \{\vec{x}_i\}_i$, which can not be done individually due to the correlations over the input parameters.

[5]In the implementation of this project, we used a radial basis function kernel, *i.e.* a squared-exponential covariance function, see section 7.3.

Given that the truncation error, in equation (5.8), is a sum of i.i.d. draws from a GP, the truncation error itself can be considered as draws from a GP

$$\delta y_\kappa(\boldsymbol{x})|\boldsymbol{\Theta}, y_{\text{ref}}, Q \sim \mathcal{GP}[M_\kappa(\boldsymbol{x}), \bar{c}^2 R_\kappa(\boldsymbol{x}, \boldsymbol{x}'; \ell)], \tag{5.12}$$

where the mean function is given by

$$M_\kappa(\vec{x}) = y_{\text{ref}}(\vec{x}) \frac{Q^{\kappa+1}(\vec{x})}{1 - Q(\vec{x})} m(\vec{x}), \tag{5.13}$$

and the covariance function is given by

$$R_\kappa(\vec{x}, \vec{x}'; \ell) = y_{\text{ref}}(\vec{x}) y_{\text{ref}}(\vec{x}') \frac{[Q(\vec{x})Q(\vec{x}')]^{\kappa+1}}{1 - Q(\vec{x})Q(\vec{x}')} r(\vec{x}, \vec{x}'; \ell). \tag{5.14}$$

These expressions can be realised by considering a set of Gaussian distributed variables $X_i(\vec{x}) \sim \mathcal{N}[\mu_i(\vec{x}), \sigma_i^2(\vec{x}, \vec{x}')]$, and noting that the mean and variance of $Y(\vec{x}) = \sum_i A_1(\vec{x}) X_i(\vec{x})$ can be described with a Gaussian distribution with mean and variance

$$\begin{cases} \langle Y(\vec{x}) \rangle = \sum_i A_i(\vec{x}) \mu_i(\vec{x}), \\ \\ \text{Var}[Y(\vec{x})] = \sum_i A_i(\vec{x}) A_i(\vec{x}') \sigma_i^2(\vec{x}, \vec{x}'). \end{cases} \tag{5.15}$$

The mean function and covariance function of the truncation error will thus be given by geometric sums of $Q(\vec{x})$ and $Q(\vec{x})Q(\vec{x}')$, respectively, resulting in the expressions in equations (5.13) and (5.14) [8].

The BUQ of a EFT truncation error can thus generally be considered to consist of three steps. First, choosing priors for the GP hyperparameters and constructing the kernel. Second, predict the quantity at different orders and determine the corresponding expansion coefficients, which are used to train the GP kernel. Third, extract the mean, marginal variance, and correlation lengths maximum *a posteriori* values from the expansion coefficient GP to determine the corresponding function for the truncation error as seen in equations (5.13) and (5.14). The resulting distribution will then give the truncation error distribution of the truncated quantity y_κ. For an example of such a procedure see [9].

6

Numerical Solution of the Nucleon-Nucleon Scattering Problem

The Numerical solution to the LS equation, presented in sebsection 3.3.3, is enabled by approximating the LS integral with a sum over GL quadrature points. The GL points $\{x_i\}_i^N$ and corresponding weights $\{\tilde{w}_i\}_i^N$ are defined such that

$$\int_{-1}^{1} dx\, f(x) \approx \sum_{i=1}^{N} \tilde{w}_i f(x_i). \tag{6.1}$$

With these points any integral over $p \in [A, B]$ can be approximated as

$$\int_A^B dp\, f(p) \approx \sum_{i=1}^{N} w_i f(p_i), \quad \begin{cases} p_i = \dfrac{B+A}{2} + \dfrac{B-A}{2} x_i, \\ w_i = \dfrac{B-A}{2} \tilde{w}_i. \end{cases} \tag{6.2}$$

In the case of the integral in the LS equation, $A = 0$ and $B = \infty$, and the appropriate scaling is

$$\begin{cases} p_i = \dfrac{1+x_i}{1-x_i} C, \\ w_i = \dfrac{2\tilde{w}_i}{(1-x_i)^2} C, \end{cases} \tag{6.3}$$

where C determines the median value of the points $\{p_i\}_i^N$ [27].

6.1 Solver for the Lippmann-Schwinger Equation

The LS equation in the jPWS basis is known from (3.126) to be

$$T^{jst}_{\ell'\ell}(p', p; k) = V^{jst}_{\ell'\ell}(p', p) + \sum_{\ell''=|s-j|}^{|s+j|} \int_{\mathbb{R}^+} dq\, q^2 V^{jst}_{\ell'\ell''}(p', q) \frac{2\mu}{k^2 - q^2 + i\epsilon} T^{jst}_{\ell''\ell}(q, p; k). \tag{6.4}$$

The identities

$$\frac{1}{k^2-q^2+i\epsilon} = \mathcal{P}\frac{1}{k^2-q^2} - i\frac{\pi}{2k}\delta(k-q), \tag{6.5}$$

and

$$\mathcal{P}\int_{\mathbb{R}^+} dq\, \frac{f(q)}{k^2-q^2} = \int_{\mathbb{R}^+} dq\, \frac{f(q)-f(k)}{k^2-q^2}, \tag{6.6}$$

where $\mathcal{P}$ denoted the *Cauchy principal value* [27], implies that the integral in (6.4) can be rewritten as

$$I_{\mathbb{R}^+} = 2\mu\int_{\mathbb{R}^+} dq\, \frac{q^2 V^{jst}_{\ell'\ell''}(p',q)T^{jst}_{\ell''\ell}(q,p;k) - k^2 V^{jst}_{\ell'\ell''}(p',k)T^{jst}_{\ell''\ell}(k,p;k)}{k^2-q^2} - i\pi\mu k V^{jst}_{\ell'\ell''}(p',k)T^{jst}_{\ell''\ell}(k,p;k). \tag{6.7}$$

The numerical solution is then enabled by approximating the integral with a sum over the GL quadrature points (6.3) as

$$I_{\mathbb{R}^+} = 2\mu\sum_{l=1}^{N}\omega_i \frac{p_i^2 V^{jst}_{\ell'\ell''}(p',p_i)T^{jst}_{\ell''\ell}(q,p_i;k) - k^2 V^{jst}_{\ell'\ell''}(p',k)T^{jst}_{\ell''\ell}(k,p;k)}{k^2-p_i^2} - i\pi\mu k V^{jst}_{\ell'\ell''}(p',k)T^{jst}_{\ell''\ell}(k,p;k). \tag{6.8}$$

The LS equation can then be evaluated on the GL momentum grid as

$$T^{jst}_{\ell'\ell}(p_i,p_j;p_0) = V^{jst}_{\ell'\ell}(p_i,p_j) + \sum_{\ell''}\sum_{k=0}^{N} D_k V^{jst}_{\ell'\ell''}(p_i,p_k)T^{jst}_{\ell''\ell}(p_k,p_j;p_0), \tag{6.9}$$

where $p_0 = k$ is the on-shell relative momentum and

$$D_i = \begin{cases} -2\mu p_0\left[\sum_{j=1}^{N}\frac{w_j}{p_0^2-p_j^2} + i\frac{\pi}{2}\right] & \text{for } i=0, \\ 2\mu\frac{w_i p_i^2}{p_0^2-p_i^2} & \text{for } i=1,2,\ldots,N. \end{cases} \tag{6.10}$$

In the case where $V_{\ell'\ell}(p',p) = 0$ for $p', p > B > k$, the integral $I_{\mathbb{R}^+}$ can be expressed as

$$I_{\mathbb{R}^+} = I_{[0,B]} - k^2 V^{jst}_{\ell'\ell''}(p',k)T^{jst}_{\ell''\ell}(k,p;k)\int_B^\infty dq\, \frac{1}{k^2-q^2}, \tag{6.11}$$

where $I_{[0,B]}$ is given by (6.7) but with the integral going over $q \in [0,B]$. The integral over $q \in [B,\infty)$ in (6.11) can analytically be solved as [23]

$$\int_{B>k}^{\infty} dq\, \frac{1}{k^2-q^2} = -\frac{1}{k}\tanh^{-1}\left(\frac{k}{B}\right). \tag{6.12}$$

The D_i elements are then modified as

$$D_i = \begin{cases} -2\mu p_0\left[\sum_{j=1}^{N}\frac{w_j}{p_0^2-p_j^2} + i\frac{\pi}{2} - \tanh^{-1}\left(\frac{k}{B}\right)\right] & \text{for } i=0, \\ 2\mu\frac{w_i p_i^2}{p_0^2-p_i^2} & \text{for } i=1,2,\ldots,N, \end{cases} \tag{6.13}$$

where the GL points are scaled to approximate a integral from $A = 0$ to B, as in (6.2).

Equation (6.9) can be expressed as a matrix equation by defining a $N + 1$ column vector $\mathbf{D}$ through the elements $[\mathbf{D}]_i \equiv D_i$ and two $(N + 1) \times (N + 1)$ matrices $\mathbf{T}_{\ell'\ell}$ and $\mathbf{V}_{\ell'\ell}$ such that

$$[\mathbf{T}_{\ell'\ell}]_{ij} \equiv T^{jst}_{\ell'\ell}(p_i, p_j; p_0), \quad [\mathbf{V}_{\ell'\ell}]_{ij} \equiv V^{jst}_{\ell'\ell}(p_i, p_j). \tag{6.14}$$

For uncouples channels, $\ell' = \ell$, must $\ell'' = \ell$ and (6.9) can be solved, with matrix inversion, as

$$\mathbf{T} = \mathbf{F}^{-1}\mathbf{V}, \quad [\mathbf{F}]_{ij} = \delta_{ij} - [\mathbf{D}]_j[\mathbf{V}]_{ij}, \tag{6.15}$$

where $\mathbf{T} \equiv \mathbf{T}_{\ell\ell}$ and $\mathbf{V} \equiv \mathbf{V}_{\ell\ell}$. The on-shell T-matrix element is then identified as

$$T^{jst}_{\ell\ell}(p_0, p_0; p_0) = [\mathbf{T}]_{00}. \tag{6.16}$$

For couled channes, where $\ell' = j \pm 1$ and $\ell = j \pm 1$, must $\ell'' = j \pm 1$ and (6.9) can be solved as

$$\widetilde{\mathbf{T}} = \widetilde{\mathbf{F}}^{-1}\widetilde{\mathbf{V}}, \quad [\widetilde{\mathbf{F}}]_{ij} = \delta_{ij} - [\widetilde{\mathbf{D}}]_j[\widetilde{\mathbf{V}}]_{ij}, \tag{6.17}$$

where

$$\widetilde{\mathbf{D}} \equiv \begin{pmatrix} \mathbf{D} \\ \mathbf{D} \end{pmatrix}, \quad \widetilde{\mathbf{T}} \equiv \begin{pmatrix} \mathbf{T}_{j-1,j-1} & \mathbf{T}_{j-1,j+1} \\ \mathbf{T}_{j+1,j-1} & \mathbf{T}_{j+1,j+1} \end{pmatrix}, \quad \widetilde{\mathbf{V}} \equiv \begin{pmatrix} \mathbf{V}_{j-1,j-1} & \mathbf{V}_{j-1,j+1} \\ \mathbf{V}_{j+1,j-1} & \mathbf{V}_{j+1,j+1} \end{pmatrix}. \tag{6.18}$$

The on-shell T-matrix elements for the coupled channels are identified as

$$\begin{aligned} T^{jst}_{j-1,j-1}(p_0, p_0; p_0) &= [\widetilde{\mathbf{T}}]_{0,0}, \quad T^{jst}_{j-1,j+1}(p_0, p_0; p_0) = [\widetilde{\mathbf{T}}]_{0,N+1}, \\ T^{jst}_{j+1,j-1}(p_0, p_0; p_0) &= [\widetilde{\mathbf{T}}]_{N+1,0}, \quad T^{jst}_{j+1,j+1}(p_0, p_0; p_0) = [\widetilde{\mathbf{T}}]_{N+1,N+1}. \end{aligned} \tag{6.19}$$

7

Project-Specific Implementation

The implementation of this project is comprised of three parts. The first part involves predicting the five complex scattering amplitudes for the case of *np* scattering[1] by numerically solving the LS equation, utilising the method presented in chapter 6 with the numerical parameters specified in section 7.2. The potential used for these predictions was the LO WPC χEFT potential, which was theoretically presented in 2 and will be specified in section 7.1. A Bayesian uncertainty model was then built for the truncation errors of these predicted values of the scattering amplitudes. The Bayesian uncertainty model is more generally presented in chapter 5, and the project-specific implementation of this model on the NN scattering amplitudes and the choices of variables are presented in section 7.3. The last part consists of propagating the resulting uncertainty distributions of the five amplitudes to various scattering observables, which is briefly discussed in the last paragraph of section 7.3.

This procedure was implemented for two different NN scattering amplitude conventions, namely the Saclay and helicity conventions defined in section 4.1. As seen in chapter 4, these conventions have constraints for forward and backward scattering. These constraints are then implemented into the error model as briefly discussed in the last paragraph of section 7.3.

This project was implemented in Python, and the code is provided as open source in [38].

7.1 Leading Order Interaction Potential

The potential used in this project is the LO WPC χEFT potential presented in chapter 2, with LECs [39]

$$\tilde{C}_{^1S_0} = -0.0010768\,\text{MeV}^{-2}, \quad \tilde{C}_{^3S_1} = -0.0007172\,\text{MeV}^{-2}, \tag{7.1}$$

[1]Note that the framework constructed in this project is far from specific to *np* scattering and could equally well be applied to any NN scattering.

where $\tilde{C}_{^1S_0} = 4\pi(C_\mathrm{S} - 3C_\mathrm{T})$ and $\tilde{C}_{^3S_1} = 4\pi(C_\mathrm{S} + C_\mathrm{T})$ correspond to the partial waves[2] $^1S_0$ and $^3S_1$, respectively [2]. These values were determined by B. D. Carlsson *et al.* [39] for a potential with a regulator

$$f_\Lambda(\boldsymbol{p}', \boldsymbol{p}) = e^{-\left[\frac{|\boldsymbol{p}'|}{\Lambda}\right]^{2n}} e^{-\left[\frac{|\boldsymbol{p}|}{\Lambda}\right]^{2n}}, \tag{7.2}$$

with a cutoff $\Lambda = 500\,\mathrm{MeV}$ and cutoff sharpness $n = 3$ [39], which is thus the regulator that was used in this project. The values used for the axial-vector coupling constant, the pion decay constant, and the average pion mass were $g_\mathrm{A} = 1.276$, $f_\pi = 92.4\,\mathrm{MeV}$ [39], and $m_\pi = 138.039\,\mathrm{MeV}$ [40]. Note that these values are consistent with those used in the determination of the LECs [39].

7.2 Numerical Predictions of Scattering Amplitudes and Observables

For the potential (section 7.1) to be used in the jPWS LS equation, the potential had to be transformed into the jPWS basis, which was done in accordance with [41]. These expressions contain integrals over $\cos(\vartheta) \in [-1, 1]$, which were approximated with GL points as introduced in the leading paragraph in chapter 6. In this implementation, $N_\mathrm{pot} = 50$ GL points were used to approximate the potential integrals. Similarly, $N_\mathrm{LS} = 50$ GL points were used to approximate the LS integral. Note that the regularised potential can be considered to be zero for in- and out-going relative momenta $p, p' > B = 2000\,\mathrm{MeV} \gg \Lambda = 500\,\mathrm{MeV}$. As discussed in chapter 6, this implies that GL points that approximate an integral over relative momenta $q \in [0, B]$ can be used in the numerical solution of the LS equation.

As seen in chapter 3 (specifically subsection 3.3.4), the M-matrix elements are given as a sum over the jPWS basis S-matrix elements. Of particular interest is the sum over the total angular momentum quantum numbers as it goes from zero to infinity. This is obviously numerically problematic and requires the sum to be truncated at some max value j_max. In this implementation, $j_\mathrm{max} = 25$ was used for all calculations, which was determined to be appropriate for the energies considered, *i.e.* $T_\mathrm{lab} < 200\,\mathrm{MeV}$.

The choices of $N_\mathrm{LS} = 50$, $N_\mathrm{pot} = 50$, and $j_\mathrm{max} = 25$ were motivated by investigating the *Relative Root Mean Squared Error* (RRMSE)[3] for the LO *np* amplitudes in the Lucas convention (defined in chapter 4). The convergence plots are shown in figure 7.1, where the fully converged values of the amplitudes were determined with

[2]The partial waves are here given in the spectroscopic notation $^{(2s+1)}L(\ell)_j$, where s, ℓ, and j are the total spin, orbital angular momentum, and total angular momentum quantum numbers, respectively, and $L(\ell) : \{0, 1, 2 \dots\} \to \{S, P, D, \dots\}$ [24]. The S in these expressions must not be confused with the scattering operator or S-matrix elements.

[3]The considered expression of the RRMSE of amplitudes was $\mathrm{RRMSE}(\boldsymbol{\Omega}; \vec{x}) \equiv \sqrt{\sum_i |y_i(\vec{x}; \boldsymbol{\Omega}) - \hat{y}_i(\vec{x})|^2 / \sum_i |\hat{y}_i(\vec{x})|^2}$, where $\{y_i(\vec{x}; \boldsymbol{\Omega})\}_{i=1}^5$ are the scattering amplitudes for $\vec{x} = (T_\mathrm{lab}, \vartheta)$ detemined with the numerical parameters $\boldsymbol{\Omega} = \{N_\mathrm{LS}, N_\mathrm{pot}, j_\mathrm{max}\}$. The amplitudes $\{\hat{y}_i(\vec{x})\}_{i=1}^5$ are considered the true values for $\vec{x} = (T_\mathrm{lab}, \vartheta)$.

$N_{\mathrm{LS}} = 100$, $N_{\mathrm{pot}} = 100$, and $j_{\max} = 50$. The maximum values of the amplitude RRMSE for the implemented choices of numerical parameters, for laboratory kinetic energies $T_{\mathrm{lab}} \in [20, 200]\,\mathrm{MeV}$, can be seen in table 7.1.

Table 7.1: The maximum value (over angles) of the RRMSE for the LO *np* Lucas scattering amplitudes predictions with the numerical parameters $\mathbf{\Omega} = \{N_{\mathrm{LS}} = 50, N_{\mathrm{pot}} = 50, j_{\max} = 25\}$, for laboratory kinetic energies $T_{\mathrm{lab}} \in [20, 200]\,\mathrm{MeV}$. The c.m. polar scattering angles associated with the maximum value are indicated in the second column. The fully converged values of the amplitudes, used in the RRMSEs, were determined with $N_{\mathrm{LS}} = 100$, $N_{\mathrm{pot}} = 100$, and $j_{\max} = 50$.

T_{lab} [MeV]	ϑ [deg]	RRMSE$(\mathbf{\Omega}; T_{\mathrm{lab}}, \vartheta)$
20	≈ 78.637	$\approx 6.645 \cdot 10^{-9}$
100	180	$\approx 3.097 \cdot 10^{-7}$
150	180	$\approx 5.686 \cdot 10^{-7}$
200	180	$\approx 3.264 \cdot 10^{-5}$

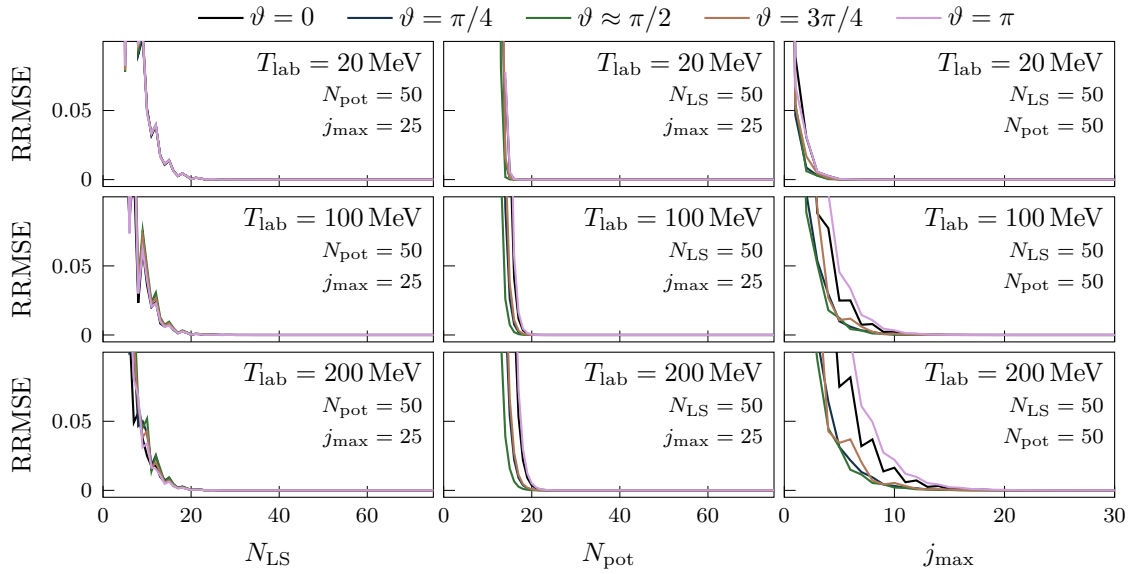

Figure 7.1: The convergence of the RRMSE for the LO *np* Lucas scattering amplitudes predictions as a functions of the number of GL points used for the approximation of the LS integral (N_{LS}) and the potential integrals (N_{pot}), and the maximum number of the total angular momentum quantum number considerd for the M-matrix elements ($j_{\max}$). The fully converged values of the scattering amplitudes, used in all RRMSEs, were determined with $N_{\mathrm{LS}} = 100$, $N_{\mathrm{pot}} = 100$, and $j_{\max} = 50$.

The numerical solution of the LS equation was implemented in Python. The package `scipy.special` [42] was used for special functions like the spherical harmonics and Legendre polynomials. The package `wigxjpf` [43] was used for the $3j$-symbol (equivalent to the Clebsch-Gordan coefficients).

7.3 Bayesian Uncertainty Quantification Model

When building the uncertainty model for NN scattering amplitudes[4] $\{y_i(T_{\text{lab}}, \vartheta)\}_{i=1}^{5}$, the real and imaginary parts of each amplitude are considered as independent expansions in the χEFT expansion parameter Q (see chapter 5) as

$$\text{Re}[y_i(T_{\text{lab}}, \vartheta)] = y_{\text{ref}}(T_{\text{lab}}, \vartheta) \sum_{n=0}^{\infty} c_{i,\Re}^{(n)}(T_{\text{lab}}, \vartheta) Q^n(T_{\text{lab}}, \vartheta), \tag{7.3}$$

$$\text{Im}[y_i(T_{\text{lab}}, \vartheta)] = y_{\text{ref}}(T_{\text{lab}}, \vartheta) \sum_{n=0}^{\infty} c_{i,\Im}^{(n)}(T_{\text{lab}}, \vartheta) Q^n(T_{\text{lab}}, \vartheta). \tag{7.4}$$

As can be read from the above equations, the same dimensionfull ($[y_{\text{ref}}] = [y_i] = \text{fm}$) reference function $y_{\text{ref}} : \mathbb{R}^2 \to \mathbb{R}$ was used for all amplitudes. The reference function should thus be chosen such that it captures the general scale of all five amplitudes in a given convention and the expansion coefficients $\{c_{i,\Re}^{(n)}, c_{i,\Im}^{(n)}\}_{i=1}^{5}$ can be considered to be of natural scale. In the implementation of this project, a constant reference value $y_{\text{ref}} \equiv y_{\text{ref}}(T_{\text{lab}}, \vartheta) = 0.5\,\text{fm}$ was used for all np Saclay and helicity amplitudes. This choice is motivated by noting (see figure C.1 in appendix C) that the it keeps an general naturalness of the LO expansion coefficients across the five amplitudes, for laboratory kinetic energies $T_{\text{lab}} \in [20, 250]\,\text{MeV}$ and c.m. polar scattering angles $\vartheta \in [0, \pi]$. For the expansion parameter, this project used a soft scale given by the largest value between the pion mass and the relative momentum of the np system [34], with the intent to capture the essence of the χEFT expansion[5]. The expansion parameter considered for the expansions was thus given by

$$Q(T_{\text{lab}}) = \frac{\max[k, m_\pi]}{\Lambda_\chi}, \quad k = \sqrt{\frac{m_p^2 T_{\text{lab}}(2m_n + T_{\text{lab}})}{(m_n + m_p)^2 + 2m_p T_{\text{lab}}}}, \tag{7.5}$$

where $m_\pi \approx 138.039\,\text{MeV}$, $m_p \approx 938.2721\,\text{MeV}$, and $m_n \approx 939.5654\,\text{MeV}$ are the pion, proton (target) and nucleon (projectile) masses [16], and Λ_χ is the hard scale. The hard scale used was $\Lambda_\chi = 600\,\text{MeV}$ [7, 9, 34].

Given that the expansion coefficients $\{c_{i,\Re}^{(n)}, c_{i,\Im}^{(n)}\}_{i=1}^{5}$ are assumed to be of natural scale, the expansion coefficients of different orders are assumed to be i.i.d. draws from a GP. The coefficients in (7.3) and (7.4) can thus be considered to be distributed as

$$c_{i,\Re}^{(n)}(\boldsymbol{x})|\boldsymbol{\Theta}_{i,\Re} \overset{\text{i.i.d.}}{\sim} \mathcal{GP}[m_{i,\Re}(\boldsymbol{x}), \bar{c}_{i,\Re}^2 r(\boldsymbol{x}, \boldsymbol{x}'; \ell_{i,\Re})], \tag{7.6}$$

$$c_{i,\Im}^{(n)}(\boldsymbol{x})|\boldsymbol{\Theta}_{i,\Re} \overset{\text{i.i.d.}}{\sim} \mathcal{GP}[m_{i,\Re}(\boldsymbol{x}), \bar{c}_{i,\Im}^2 r(\boldsymbol{x}, \boldsymbol{x}'; \ell_{i,\Im})], \tag{7.7}$$

where $\boldsymbol{x} = \{(T_{\text{lab}}, \vartheta)_i\}_{i=1}$ is a set of $(T_{\text{lab}}, \vartheta)$ points and $\boldsymbol{\Theta}_{i,\Re/\Im} = \{m, \bar{c}^2, \ell\}_{i,\Re/\Im}$ are the hyperparameters of the GPs. The correlation length matrix ℓ, for each GP is

[4] Note that the amplitudes $\{y_i\}_{i=1}^{5}$ in this section can represent the amplitudes in any convention, *e.g.* Saclay or helicity.

[5] Note that this is a choice that has been implemented in numerous previous studies of χEFT truncation errors, *e.g.* [6, 9]. There are other alternatives to the harsh maximum function aiming to smoothen the transition around $k = m_\pi$ [7, 13].

now given by

$$\ell = \begin{pmatrix} \ell_{T_{\text{lab}}}^2 & 0 \\ 0 & \ell_\vartheta^2 \end{pmatrix}, \tag{7.8}$$

where $\ell_{T_{\text{lab}}}$ and ℓ_ϑ are the correlation lengths across laboratory kinetic energies and c.m. polar scattering angles, respectively. The hyperparameters would then, ideally, be determined by training the GPs with the corresponding expansion coefficients up to some order κ, which were determined by predicting the NN scattering amplitudes with the χEFT potential truncated at chiral orders $\nu = 1, 2, \ldots, \kappa$. This project only considers the WPC LO χEFT potential (presented at the end of chapter 2), which only gives the LO expansion coefficients and is not enough to train the GPs.

In the implementation of this project, one fixed zero-mean[6] GP was used for the expansion parameters of all amplitudes, *i.e.*

$$c_{i,\Re/\Im}^{(n)}(\boldsymbol{x})|\boldsymbol{\Theta} \overset{\text{i.i.d.}}{\sim} \mathcal{GP}[0, \bar{c}^2 r(\boldsymbol{x}, \boldsymbol{x}'; \ell)], \tag{7.9}$$

where the hyperparameters $\boldsymbol{\Theta} = \{0, \bar{c}^2, \ell\}$ was chosen as $\bar{c}^2 = 1^2$, $\ell_{T_{\text{lab}}} = 60\,\text{MeV}$ and $\ell_\vartheta = 30\,\text{deg}$. These values were motivated by comparing previous EFT truncation error studies of *np* observables, by I. Svensson[7] *et al.* [9]. They trained GPs for 15 different differential observable types as functions of T_{lab} and ϑ and found that the correlation lengths $\ell_{T_{\text{lab}}} \in [45, 83]\,\text{MeV}$ and $\ell_\vartheta \in [24, 39]\,\text{deg}$, and marginal variances $\bar{c}^2 \in [0.22^2, 1.27^2]$, with mean values of $\ell_{T_{\text{lab}}} \approx 68\,\text{MeV}$, $\ell_\vartheta \approx 31\,\text{deg}$, and $\bar{c}^2 \approx 0.69^2$. The implemented hyperparameters are thus conservative choices consistent with the general scale of their findings[8]. Note also (from figure C.2 in appendix C) that the the LO expansion coefficients $\{c_{i,\Re}^{(0)}, c_{i,\Im}^{(0)}\}_{i=1}^5$ (given $y_{\text{ref}} = 0.5\,\text{fm}$) are generally between $\pm 2\bar{c} = \pm 2$ for laboratory kinetic energies $T_{\text{lab}} \in [20, 250]\,\text{MeV}$ and c.m. polar scattering angles $\vartheta \in [0, \pi]$, sugesting that $\bar{c}^2 = 1^2$ was appropriate as a conservative choise.

A squared-exponential kernel to parameterise the correlation structure was implemented in this project[9], *i.e.* a covariance function given by

$$r(\vec{x}, \vec{x}'; \ell) = \exp\left\{-\frac{(\vec{x} - \vec{x}')^T \ell^{-1} (\vec{x} - \vec{x}')}{2}\right\}. \tag{7.10}$$

This choice is equivalent to assuming stationarity, meaning that the covariance between two points only depends on the difference between the points and not their

[6] The choice of a zero mean reflects the expectation that the predictions made are the best *a priori* knowledge about the *np* scattering amplitude values, and that the truncation error distributions are expected to be centred around zero.

[7] It is important to note that I. Svensson *et al.* used a WPC χEFT potential with a non-local regulator, similar to the potential considered in this project. This similarity makes their results particularly applicable to this study.

[8] Note also that an article by B. McClung *et al.* [13] recently conducted a study on truncation errors of *np* scattering amplitudes (in the Wolfenstein convention). Their study only considered correlations across momentum transfers and could thus not be used to infer the correlation lengths in this project. They did, however, find marginal variances between $\bar{c}^2 \approx 0.38^2$ and $\bar{c}^2 \approx 1^2$, which is consistent with our conservative choice of $\bar{c}^2 = 1^2$.

[9] We used a `RBF` kernel from the `GPy` Python package [44].

absolute locations. This choice is motivated by the fact that it is the kernel used by I. Svensson *et al.* [9], and is thus required when using correlation lengths and a marginal variance based on their results.

The truncation errors of the real and imaginary parts of each *np* scattering amplitude predicted with the LO χEFT potential were, as understood from chapter 5, given as draws from a GP

$$\mathrm{Re}[\delta y_{i,0}(\boldsymbol{x})], \mathrm{Im}[\delta y_{i,0}(\boldsymbol{x})] | \boldsymbol{\Theta}, y_{\mathrm{ref}}, Q \sim \mathcal{GP}[0, \bar{c}^2 R_0(\boldsymbol{x}, \boldsymbol{x}'; \ell)], \tag{7.11}$$

where the covariance function $R_0(\boldsymbol{x}, \boldsymbol{x}'; \ell)$ is defined as in (5.14). Boundary constraints, which constrain certain amplitudes to be zero at $\vartheta = 0$ and/or $\vartheta = \pi$, were then implemented by requiring the truncation error to be zero at $\vartheta = 0$ and/or $\vartheta = \pi$ for the constrained amplitudes. By adding these errors to the predicted values of the amplitudes, the amplitudes with uncertainties from the truncation error became

$$y_i(T_{\mathrm{lab}}, \vartheta) = y_{i,0}(T_{\mathrm{lab}}, \vartheta) + \delta y_{i,0}(T_{\mathrm{lab}}, \vartheta). \tag{7.12}$$

These uncertainties could then be propagated to various *np* observables by sampling the uncertainty distributions of the amplitudes and using them to reconstruct the M matrix as given in section 4.1, and then use the formulas in section 4.2 to get the corresponding samples of various scattering observables.

The angular boundary constraints for the helicity amplitudes

$$\begin{cases} M_5(T_{\mathrm{lab}}, \vartheta = 0) = M_5(T_{\mathrm{lab}}, \vartheta = \pi) = 0, \\ M_4(T_{\mathrm{lab}}, \vartheta = 0) = M_3(T_{\mathrm{lab}}, \vartheta = \pi) = 0, \end{cases} \tag{7.13}$$

and for the Saclay amplitudes[10]

$$e(T_{\mathrm{lab}}, \vartheta = 0) = e(T_{\mathrm{lab}}, \vartheta = \pi) = 0, \tag{7.14}$$

where implemented into the error model by training the corresponding GPs such that the uncertainties are zero for the constrained points. This method works well for the purposes of this project. Still, more rigorous methods exist to incorporate continuous boundary constraints into GPs [45], which might become relevant in further studies into the error model for correlated truncation errors between different observable types. The GPs were constructed using the Python package `GPy` [44].

7.3.1 Propagation of Uncertenties

In the context of the uncertainty propagation, the truncation errors can be considered as samples distributed as in (7.11), *i.e.* with mean and variance [46]

$$\langle \delta y_{i,0}(\vec{x}) \rangle = 0, \quad \mathrm{Var}[\delta y_{i,0}(\vec{x})] = 2\bar{c}^2 R_{i,0}(\vec{x}, \vec{x}; \ell), \tag{7.15}$$

[10]Note that the interamplitudinal constraints of the Saclay amplitudes (see chapter 4) were not considered in this implementation. These constraints are equivalent to the constraints of the third and fourth helicity amplitudes and contribute to angle-dependent correlations between different observable types. The simplicity with which these constraints are implemented is the reason for considering the helicity convention.

where $\vec{x} = (T_{\text{lab}}, \vartheta)$ and the covariance function $R_{i,0}$ carries an amplitude index since they are considered to contain the amplitude-specific boundary constraints. Note that the factor of two in the variance stems from the equal contributions from the real and imaginary parts of $\delta y_{i,0}(T_{\text{lab}}, \vartheta)$.

For the propagation of the amplitude uncertainties to observables to be consistent with the *prior* that the LO prediction is the best knowlage of the observable, the mean of the resulting distribution of a differential observable $\sigma O_{P_{\text{S}}P_{\text{R}}P_{\text{P}}P_{\text{T}}}(T_{\text{lab}}, \vartheta)$ should be given by the LO prediction $\sigma O^{(0)}_{P_{\text{S}}P_{\text{R}}P_{\text{P}}P_{\text{T}}}(T_{\text{lab}}, \vartheta)$. All differential observables can in general be expressed in terms of the amplitudes $\{y_i(T_{\text{lab}}, \vartheta) = y_{i,0}(T_{\text{lab}}, \vartheta) + \delta y_{i,0}(T_{\text{lab}}, \vartheta)\}_{i=1}^{5}$ as [12]

$$\sigma O_{P_{\text{S}}P_{\text{R}}P_{\text{P}}P_{\text{T}}}(\vec{x}) = \sum_{i,j=1}^{5} \Big(B_{ij,\Re}(\vec{x}) \text{Re}[y_i^*(\vec{x}) y_j(\vec{x})] + B_{ij,\Im}(\vec{x}) \text{Im}[y_i^*(\vec{x}) y_j(\vec{x})] \Big), \quad (7.16)$$

where the values of the non-probabilistic functions $B_{ij,\Re}(\vec{x}) = B_{ji,\Re}(\vec{x}) \in \mathbb{R}$ and $B_{ij,\Im}(\vec{x}) = -B_{ji,\Im}(\vec{x}) \in \mathbb{R}$ are convention dependent but not of particular interest in this section[11]. The mean of the product $y_i^*(\vec{x}) y_j(\vec{x})$ is given by

$$\langle y_i^*(\vec{x}) y_j(\vec{x}) \rangle = \begin{cases} |y_{i,0}(\vec{x})|^2 + 2\bar{c}^2 R_{i,0}(\vec{x}, \vec{x}; \ell) & \text{for } i = j, \\ y_{i,0}^*(\vec{x}) y_{j,0}(\vec{x}) & \text{for } i \neq j, \end{cases} \quad (7.17)$$

given that the truncation errors of amplitudes are independent zero-mean distributed samples. The mean of a general differential observable is thus

$$\langle \sigma O_{P_{\text{S}}P_{\text{R}}P_{\text{P}}P_{\text{T}}}(\vec{x}) \rangle = \sigma O^{(0)}_{P_{\text{S}}P_{\text{R}}P_{\text{P}}P_{\text{T}}}(\vec{x}) + 2 \sum_{i=1}^{5} B_{ii,\Re}(\vec{x}) \bar{c}^2 R_{i,0}(\vec{x}, \vec{x}; \ell). \quad (7.18)$$

It is apparent that the variance of the amplitudes shifts the mean of the observables, in this thesis dubbed *the foldback effect*, and is consistent with the square of a Gaussian distribution. This shift is, however, not consistent with the *a priori* expectation that the mean of the observables should be given by the LO predictions. One simple fix to the foldback effect, which was implemented in this project, is to correct the observable distributions by applying an equivalent shift in the opposite direction, *i.e.*

$$\sigma O_{P_{\text{S}}P_{\text{R}}P_{\text{P}}P_{\text{T}}}(\vec{x}) \longrightarrow \sigma \tilde{O}_{P_{\text{S}}P_{\text{R}}P_{\text{P}}P_{\text{T}}}(\vec{x}) = \\ = \sigma O_{P_{\text{S}}P_{\text{R}}P_{\text{P}}P_{\text{T}}}(\vec{x}) - 2 \sum_{i=1}^{5} B_{ii,\Re}(\vec{x}) \bar{c}^2 R_{i,0}(\vec{x}, \vec{x}; \ell), \quad (7.19)$$

such that the mean of the mean-corrected distribution $\tilde{O}_{P_{\text{S}}P_{\text{R}}P_{\text{P}}P_{\text{T}}}(\vec{x})$ is given by the LO prediction or the obserable. For future purposes, the mean correction of a general observable will be defined as

$$\langle \sigma O_{P_{\text{S}}P_{\text{R}}P_{\text{P}}P_{\text{T}}}(\vec{x}) \rangle_{\text{corr}} \equiv 2 \sum_{i=1}^{5} B_{ii,\Re}(\vec{x}) \bar{c}^2 R_{i,0}(\vec{x}, \vec{x}; \ell). \quad (7.20)$$

[11],They can be identified for a specific convention in [12].

The foldback effect is, however, not limited to shifting the mean but is actually a more fundamental phenomenon resulting in the observables being given by non-Gaussian distributions [47]. Additional consequences of the effect are that different observables acquire different distributions depending on their amplitude dependence and LO predictions for different laboratory kinetic energies and c.m. polar scattering angles. This will be discussed more in the results part of this thesis.

Part III

Results and Discussion

8

Results

The results presented in this chapter can be grouped into three major categories, each assigned one section. Section 8.1 presents the distributions of the *np* scattering amplitudes resulting from the BUQ model specified in section 7.3. Both the helicity and Saclay conventions were considered. These distributions were then propagated to various differential observables. The resulting distributions for certain chosen observable types are presented in section 8.2. This section contains the quintessential results of this study. Firstly, the angle and energy dependence of the resulting observable distributions are analysed and how they are shaped by their relation to the amplitudes and the correction to the foldback effect. Secondly, the correlations between the observable types are investigated. Finally, section 8.3 examines the constraint imposed by the unitarity of the scattering operator. This analysis was conducted by comparing the resulting distributions of the total cross sections as determined by the optical theorem and by integrating differential observables, as theoretically outlined in subsection 4.2.2.

8.1 Neutron-Proton Scattering Amplitudes

The BUQ model discussed in chapter 7 was applied to the LO *np* scattering amplitudes in the helicity and Saclay conventions for $T_{\text{lab}} = 100\,\text{MeV}$ and $\vartheta \in [0, \pi]$. The 68.2 % and 95.4 % *Equal-Tailed Interval*s (ETIs) and median of the resulting distributions for the different conventions can be seen in figure 8.1. These distributions are also compared to the LO predictions (equal to the mean of the distributions) and the corresponding empirical *Partial-Wave Analysis* (PWA) values [48] retrieved from NN-online [49]. Other energies were also investigated, but did not provide any additional insights, and can be seen in appendix C.

The distributions of the real and imaginary parts of each amplitude are Gaussian for all laboratory kinetic energies and c.m. polar scattering angles, with means equal to the LO predictions and *Standard Deviation*s (StDs) given by $\sqrt{\bar{c}^2 R_{i,0}(\vec{x}, \vec{x}; \ell)}$, $\vec{x} = (T_{\text{lab}}, \vartheta)$. The covariance functions $R_{i,0}(\vec{x}, \vec{x}'; \ell)$ contain the *a priori* assigned correlation lengths across T_{lab} and ϑ, which results in the smoothness of the sampled

curves. The covariance function also contains the angular boundary constraints

$$\begin{Bmatrix} M_5(T_{\text{lab}}, 0) = M_5(T_{\text{lab}}, \pi) = 0 \\ M_4(T_{\text{lab}}, 0) = M_3(T_{\text{lab}}, \pi) = 0 \end{Bmatrix}, \quad \Big\{ e(T_{\text{lab}}, 0) = e(T_{\text{lab}}, \pi) = 0 \Big\}, \tag{8.1}$$

for the helicity amplitudes $\{M_i(T_{\text{lab}}, \vartheta)\}_{i=3}^{5}$ and the last Saclay amplitude $\{e(T_{\text{lab}}, \vartheta)\}$, respectively. The success of the implementation can be identified in figure 8.1, where the uncertainties of the constrained amplitudes are zero at the specified boundaries. The interamplitudinal constraint of the Saclay amplitudes, corresponding to the constraints of the third and fourth helicity amplitudes (see section 4.1), was not considered. This is because we wished to keep the amplitude distributions independent of each other, promoting the helicity amplitudes to an ideal choice in this context. Both conventions are, however, considered in the analysis since they provide insights into how the convention on which the error model is applied affects the propagation of the truncation errors to observables.

The distributions of the amplitudes are in figure 8.1 compared with empirical values from PWA [49]. It is important to note that the amplitudes investigated in this project are only LO predictions, and are therefore not expected to be in strong agreement with the empirical values. What we are interested in is how the truncation error uncertainties relate to the empirical values. Even this comparison is rather arbitrary, given that the distributions themselves are conservatively chosen. Nonetheless, the conservative nature of the hyperparameter choices is clearly reflected for most of the amplitudes as the empirical values reside primarily within the one StD band for the helicity amplitudes and the two StD band for the Saclay amplitudes. In actuality, we only expect approximately 68 % (95 %) of the empirical values to lie within the one (two) StD band [23]. A clear outlier in this respect is the imaginary part of the first helicity amplitude, for which the empirical values lie over two StDs from the predictions, indicating that the chosen marginal variance was not large enough for this amplitude. Such discrepancies might be solved by independently determining the hyperparameters for the real and imaginary parts of each amplitude, by training the GPs with order-by-order expansion coefficients.

These amplitude distributions constitute an intermediate step allowing us to propagate the truncation errors to observables.

8.2 Error Propagation: Differential Observables

The distributions of the *np* helicity and Saclay amplitudes, shown in figure 8.1, were sampled and propagated to the differential observables specified in table 8.1. $2 \cdot 10^4$ samples were drawn for each amplitude, and the resulting distributions of the observables were mean-corrected as described in subsection 7.3.1. We denote the uncorrected observables, the mean-corrected observable, and the mean correction as $Z(T_{\text{lab}}, \vartheta)$, $\tilde{Z}(T_{\text{lab}}, \vartheta)$, and $\langle Z(T_{\text{lab}}, \vartheta) \rangle_{\text{corr}}$, respectively, such that

$$\tilde{Z}(T_{\text{lab}}, \vartheta) = Z(T_{\text{lab}}, \vartheta) - \langle Z(T_{\text{lab}}, \vartheta) \rangle_{\text{corr}} . \tag{8.2}$$

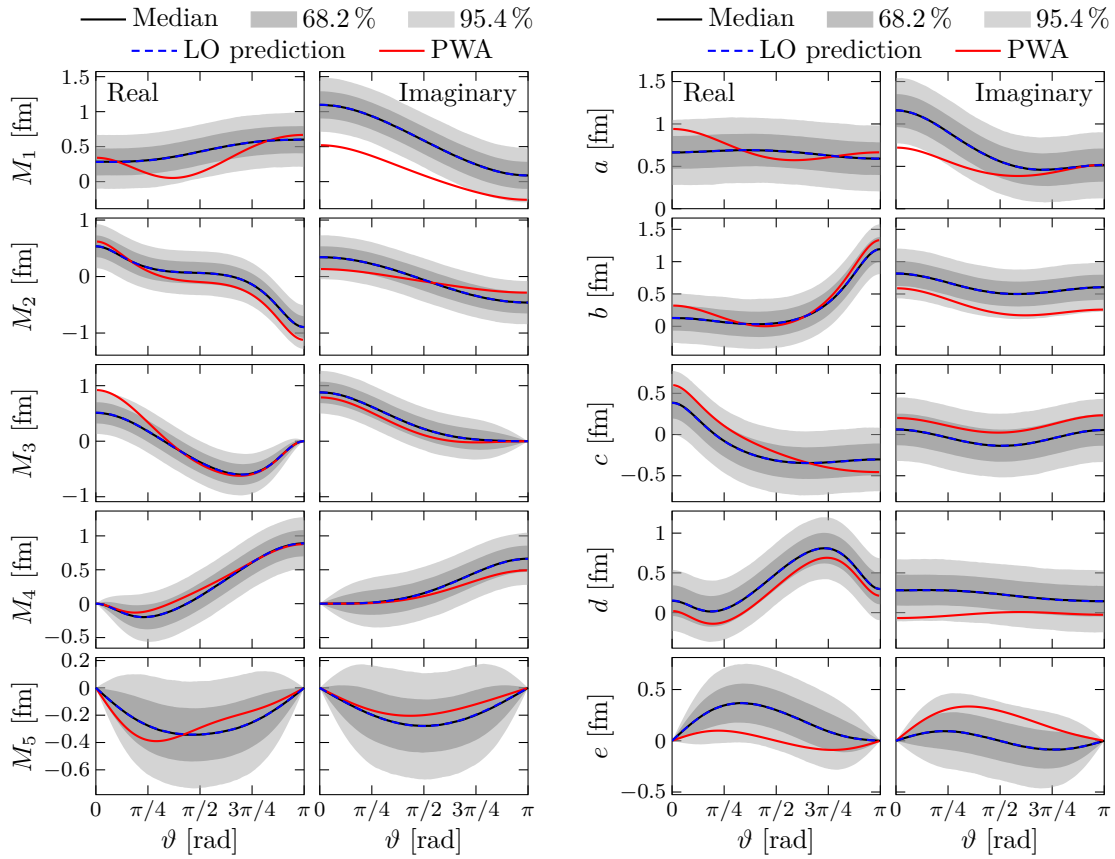

(a) Helicity convention **(b)** Saclay convention

Figure 8.1: The LO χEFT truncation error distribution of the np scattering amplitudes applied to the LO predictions of the amplitudes in the helicity (a) and Saclay (b) convention for laboratory kinetic energy $T_{\text{lab}} = 100\,\text{MeV}$ and c.m. polar scattering angles $\vartheta \in [0, \pi]$. The medians of the distributions are indicated with solid black lines, and the first and second StD bands are indicated by the filled dark and light grey areas, respectively. The LO predictions are shown as dashed blue lines. These curves are compared to the empirical PWA values [48] retrieved from NN-online [49], shown as solid red curves.

Note that the mean corrections only affect the mean of the distributions and not the shape or correlations between observables.

The observables in table 8.1 were chosen because they gave the most representative results, but are not outliers, and another set would have shown similar results to those presented in this section. However, the unpolarised differential cross section $\sigma(T_{\text{lab}}, \vartheta)$ exhibits unique characteristics regarding interobservabial correlated truncation errors. As presented in subsection 8.2.1, our results revealed that the truncation errors of various differential observables were related to those of $\sigma(T_{\text{lab}}, \vartheta)$ through hard inequalities.

The model predictions for the differential np scattering observables defined in table

Table 8.1: The notation and definitions of the considered np scattering observables [9]. The unpolarised, transverse, and longitudinal total cross sections are defined in subsection 4.2.2. The tensor notation for the differential observables is defined in subsection 4.2.1. The polarisation directions illustrated for the differential observables are defined as in figure 4.1a, where the angle indicated with the curved arrow is the laboratory frame scattering angle $\theta_1 = \vartheta/2$. The c.m. polar scattering angle ϑ is defined as in figure 4.1b. The laboratory kinetic energy T_{lab} is related to the relative on-shell momentum as in equation (3.150).

Notation	Definition	Acronym
$\sigma_{0,\text{tot}}(T_{\text{lab}})$	unpolarised total cross section	SGT
$\sigma_{\text{T}}(T_{\text{lab}})$	$\sigma_{\text{tot}}(T_{\text{lab}};\uparrow\downarrow) - \sigma_{\text{tot}}(T_{\text{lab}};\uparrow\uparrow)$	SGTT
$\sigma_{\text{L}}(T_{\text{lab}})$	$\sigma_{\text{tot}}(T_{\text{lab}};\leftrightarrows) - \sigma_{\text{tot}}(T_{\text{lab}};\rightrightarrows)$	SGTL

Notation	Tensor	Illustration	Acronym
$\sigma(T_{\text{lab}},\vartheta)$	$\sigma O_{0000}(T_{\text{lab}},\vartheta)$	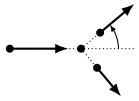	DSG
$A_{xx}(T_{\text{lab}},\vartheta)$	$\sigma O_{00ss}(T_{\text{lab}},\vartheta)$	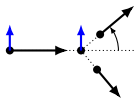	AXX
$A_{yy}(T_{\text{lab}},\vartheta)$	$\sigma O_{00NN}(T_{\text{lab}},\vartheta)$	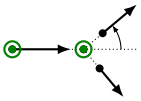	AYY
$A_{zz}(T_{\text{lab}},\vartheta)$	$\sigma O_{00pp}(T_{\text{lab}},\vartheta)$	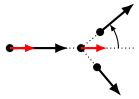	AZZ
$A_{y}(T_{\text{lab}},\vartheta)$	$\sigma O_{N000}(T_{\text{lab}},\vartheta)$	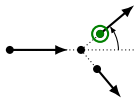	P
$D(T_{\text{lab}},\vartheta)$	$\sigma O_{N0N0}(T_{\text{lab}},\vartheta)$	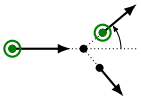	D
$D_t(T_{\text{lab}},\vartheta)$	$\sigma O_{0NN0}(T_{\text{lab}},\vartheta)$	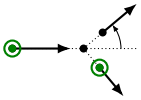	DT
$N^y_{zz}(T_{\text{lab}},\vartheta)$	$\sigma O_{0Npp}(T_{\text{lab}},\vartheta)$	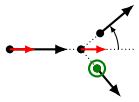	NNKK

8.1 are shown in figure 8.2, with uncertainties propagated from both the LO helicity and Saclay amplitude distributions seen in figure 8.1. The boundary constraints

$$M_5(T_{\text{lab}},0) = M_5(T_{\text{lab}},\pi) = 0, \quad e(T_{\text{lab}},0) = e(T_{\text{lab}},\pi) = 0, \tag{8.3}$$

resulted in similar constraints for observables. Examples of this are the uncertainties of $A_y(T_{\text{lab}},\vartheta)$ and $N^y_{zz}(T_{\text{lab}},\vartheta)$, which are zero for forward and backward scattering.

The second constraint of the helicity amplitudes

$$M_4(T_{\text{lab}}, 0) = M_3(T_{\text{lab}}, \pi) = 0, \tag{8.4}$$

which counterpart for the Saclay amplitudes was not considered, result in the smaller uncertainties at $\vartheta \in \{0, \pi\}$ for certain observables, *e.g.* $A_{yy}(T_{\text{lab}}, \vartheta)$ and $D_t(T_{\text{lab}}, \vartheta)$. This can be understood from their explicit expressions in terms of the helicity amplitudes $\{M_i(T_{\text{lab}}, \vartheta)\}_{i=1}^{5}$ [12]

$$A_{yy}(\vec{x}) = \text{Re}[M_1^*(\vec{x})M_2(\vec{x}) - M_3^*(\vec{x})M_4(\vec{x})] + 2|M_5(\vec{x})|^2 \tag{8.5}$$

$$D_t(\vec{x}) = -\text{Re}[M_1^*(\vec{x})M_4(\vec{x}) - M_2^*(\vec{x})M_3(\vec{x})] + 2|M_5(\vec{x})|^2, \tag{8.6}$$

which at $\vartheta \in \{0, \pi\}$ becomes

$$\begin{cases} A_{yy}(T_{\text{lab}}, 0) = \text{Re}[M_1^*(T_{\text{lab}}, 0)M_2(T_{\text{lab}}, 0)] = A_{xx}(T_{\text{lab}}, 0), \\ A_{yy}(T_{\text{lab}}, \pi) = \text{Re}[M_1^*(T_{\text{lab}}, \pi)M_2(T_{\text{lab}}, \pi)] = A_{xx}(T_{\text{lab}}, \pi), \end{cases} \tag{8.7}$$

and

$$\begin{cases} D_t(T_{\text{lab}}, 0) = \text{Re}[M_2^*(T_{\text{lab}}, 0)M_3(T_{\text{lab}}, 0)], \\ D_t(T_{\text{lab}}, \pi) = -\text{Re}[M_1^*(T_{\text{lab}}, \pi)M_4(T_{\text{lab}}, \pi)]. \end{cases} \tag{8.8}$$

Note that equation (8.7) states that $A_{yy} = A_{xx}$ for $\vartheta \in \{0, \pi\}$, the implications of this will be seen clearly in subsection 8.2.1. The effects of the constraints of these helicity amplitudes are not unique to these observable types but constrain the uncertainties of most observables. The reason these effects do not show up as clearly for many observable types in figure 8.2a comes from competing effects. One such effect can be seen for $A_{xx}(T_{\text{lab}}, \vartheta)$, $A_{zz}(T_{\text{lab}}, \vartheta)$, and $A_y(T_{\text{lab}}, \vartheta)$ around $\vartheta = \pi/2$ in figure 8.2a, where their distributions become narrower. This can be understood by noting that the variance of the observables not only depends on the variances of the amplitudes but also on the mean (LO predictions) of the amplitudes, which is shown in appendix B. The narrowing effects around $\vartheta = \pi/2$ can thus be understood by, from figure 8.1a, noting that the amplitudes M_2, M_3, and M_4 are relatively close to zero at $\vartheta = \pi/2$ compared to their maximum and/or minimum values. The foldback effect, discussed in chapter 7, was the last identified effect that shapes the distributions. As discussed in chapter 7, the mean shifting part of this effect has been corrected with success[1]. This is, however, only a part of the grand foldback effect, which can be described by noting that the differential observables are given by non-Gaussian distributions. These effects predominantly affect observables dependent on a large addition order[2] of absolute squares of amplitudes, for which distributions becomes non-symmetric and acquires elongated tails. This can most clearly be seen for the unpolarised differential cross section distribution propagated from the helicity distributions as

$$\sigma(\vec{x}) = \frac{1}{2}\Big[|M_1(\vec{x})|^2 + |M_2(\vec{x})|^2 + |M_3(\vec{x})|^2 + |M_4(\vec{x})|^2 + 4|M_5(\vec{x})|^2\Big], \tag{8.9}$$

[1]The mean of the distributions are not shown in figure 8.2 but lands on the LO prediction of the observabels, as it was designed to do

[2]Addition order means the number of additions minus the number of subtractions, *e.g.* $(|y_1| + |y_2| + |y_1|)/2$ has addition order 3/2 and $(|y_1| + |y_2| - |y_1|)/2$ has addition order 1/2

where the foldback effect results in a large bump in the uncertainty for $\vartheta \in [\pi/4, 3\pi/4]$. On the contrary, the unpolarised differential cross section distribution propagated from the Saclay amplitudes (see figure 8.2b) does not exhibit the same level of tail elongation. This is understood from the expression

$$\sigma(\vec{x}) = \frac{1}{2}\Big[|a(\vec{x})|^2 + |b(\vec{x})|^2 + |c(\vec{x})|^2 + |d(\vec{x})|^2 + |e(\vec{x})|^2\Big], \tag{8.10}$$

which has a lower additionorder than (8.9).

The convention to which the error model was applied changed the results when considering a fixed kernel distribution constant for all amplitudes (except for boundary constraints). It is, however, expected that the hyperparameter would be different for different conventions and the amplitudes within one convention. This can be seen from the distributions of the real and imaginary parts of the helicity amplitudes in figure 8.1a, where the fifth helicity amplitude is significantly smaller than the other ones, suggesting that the marginal variance is much too large for this amplitude. This is also what we see in the truncation error distributions of the observables in figure 8.2a, where the foldback effect effectively hijacks the shape of the distributions of certain observables at intermediate angles. The Saclay amplitudes in figure 8.1b, on the other hand, are much more consistent in their scales and actually seem to be described very well by our chosen hyperparameters, when comparing their distributions to empirical values. This is reflected by the observable distributions propagated from the Saclay truncation errors (figure 8.2b), which, compared to the helicity amplitudes, are less disturbed by the foldback effect. The benefit of the helicity convention is that it easily allows us to implement all constraints (except for the explicit unitarity constraint). The choice of convention is, thus, not as arbitrary in the context of truncation error quantifications. These ambiguities may, however, be resolved by training the hyperparameters independently for a specific amplitude convention.

Throughout the implementation chapter and the above results, the resulting distributions of the differential observables as propagated from Gaussian distributed scattering amplitudes have been mentioned. Since the real and imaginary parts of the amplitudes $\{y_i\}_{i=1}^5$ are independent variables, terms like $\mathrm{Re}[y_i^* y_j]$ and $\mathrm{Im}[y_i^* y_j]$, $i \neq j$ give symmetric (but non-Gaussian) distributions. The terms $|y_i|^2$, however, result in scaled non-central χ^2-distributions of order 2 [47], and are the leading cause of the foldback effect, see subsection 7.3.1. In more specific terms[3]

$$|y_i|^2 \sim \sigma_i^2 \chi_2^2(\lambda_i), \quad \lambda_i = \frac{|y_{i,0}|^2}{\sigma_i^2}, \tag{8.11}$$

where λ_i is the non-central parameter, $y_{i,0} \in \mathbb{C}$ is the mean of y_i, and σ_i^2 is the variance of the real and imaginary parts of y_i. The moment ratios $\alpha_{i,3}$ and $\alpha_{i,4}$ of

[3]Note also that in the case where the real and imaginary parts of the amplitudes do not have the same variance, one will instead find that $|\mathrm{Re}[y_i]|^2 \sim \sigma_{i,\Re}^2 \chi_1^2(\lambda_{i,\Re})$ and $|\mathrm{Im}[y_i]|^2 \sim \sigma_{i,\Im}^2 \chi_1^2(\lambda_{i,\Im})$.

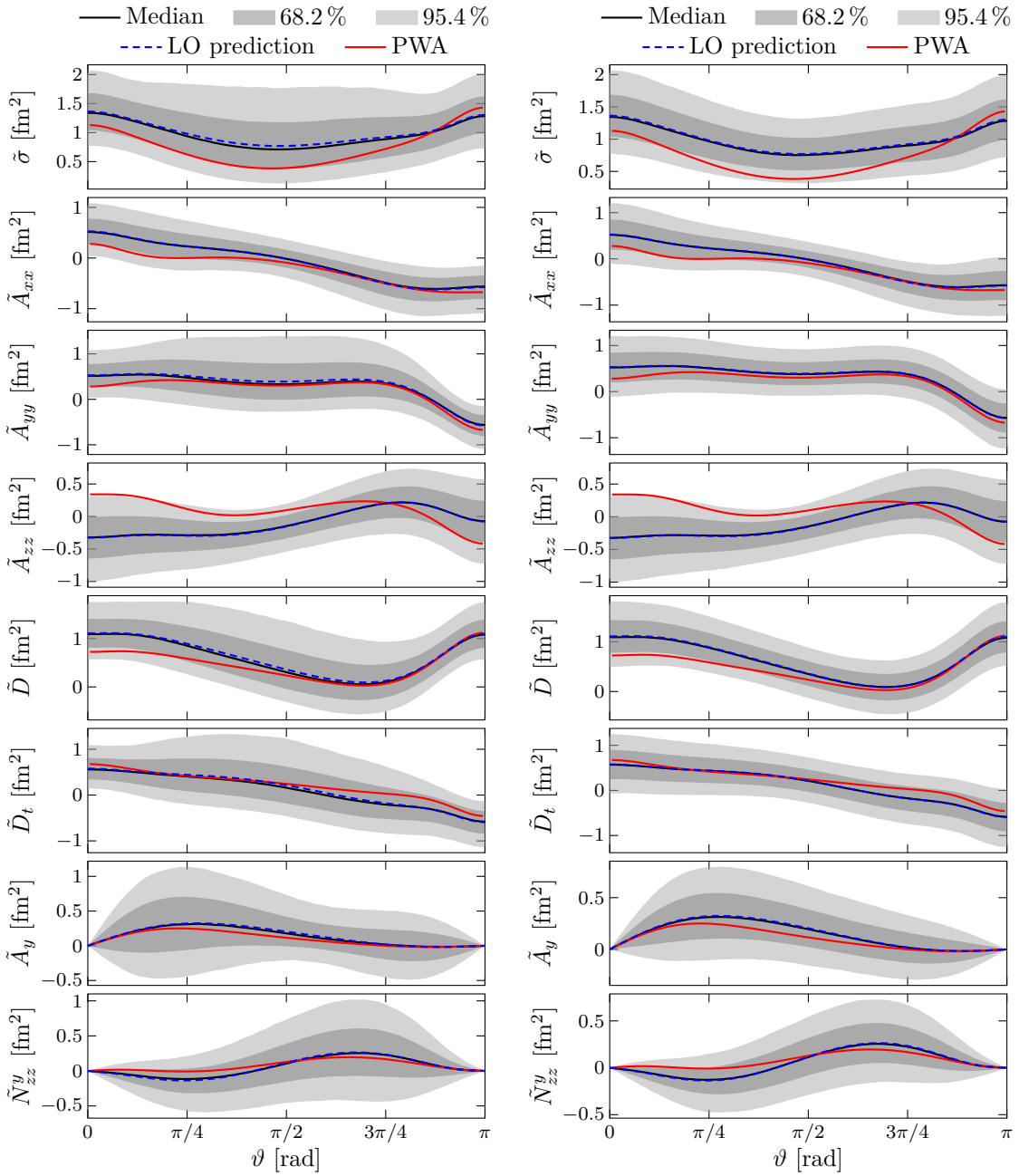

(a) From helicity amplitudes **(b)** From Saclay amplitudes

Figure 8.2: The mean-corrected truncation error distributions of the differential np scattering observables defined in table 8.1, for laboratory kinetic energy $T_{\text{lab}} = 100\,\text{MeV}$ and c.m. polar scattering angles $\vartheta \in [0, \pi]$. The distributions are constructed from $2 \cdot 10^4$ samples (for each of 150 evenly distributed ϑ points) of the distributions of the helicity (a) and Saclay (b) amplitudes shown in figure 8.1. The medians of the distributions are indicated with solid black lines, and the 68.2 % and 95.4 % ETIs are indicated by the filled dark and light grey areas, respectively. The LO predictions are shown as dashed blue lines. The red curves are the observables determined with the scattering amplitudes from PWA, see figure 8.1.

the $\chi^2_2(\lambda_i)$ distributions are given by

$$\alpha_{i,3} = \frac{\sqrt{8}(2+3\lambda_i)}{(2+2\lambda_i)^{3/2}}, \quad \alpha_{i,4} - 3 = \frac{12(2+4\lambda_i)}{(2+2\lambda_i)^2}, \tag{8.12}$$

and scales as $\lambda_i^{-1/2}$ and λ_i^{-1} [47]. The moment ratio $\alpha_{i,3}$ describes the *skewness* (tail enlargement and symmetry, zero for Gaussian) of the distribution, and $\alpha_{i,4}$ describes the *kurtosis* (combined tail weight and peak sharpness compared with the normal law, 3 for Gaussian) [47, 50]. The differences between the observable distributions propagated from the helicity and Saclay amplitudes can thus clearly be recognised in that the non-central parameters of the Saclay amplitudes are larger compared to the helicity amplitudes (specifically the M_5 amplitude). As discussed in the previous paragraph, the excessive foldback effects of the helicity amplitudes should thus be mitigated when independently training the GP hyperparameters for the amplitudes.

8.2.1 Correlated Errors: Differential Observables

The correlations between the mean-corrected differential *np* scattering observables in figure 8.2 were investigated for laboratory kinetic energy $T_{\text{lab}} = 100\,\text{MeV}$ and c.m. polar scattering angle $\vartheta = \pi/4$. The joint posteriors resulting from 10^5 samples of the helicity and Saclay amplitudes are shown in figures 8.3 and 8.4, respectively. These figures provide interesting results and insights, such as the hard inequalities between the unpolarised differential cross section and various observables in both conventions. These figures only show the covariances for one $(T_{\text{lab}}, \vartheta)$ point, which does not provide the full picture of the correlations. Similar figures for other energies and angles can be seen in appendix C. The results are, however, completed with figure 8.5, which plots the Pearson correlation coefficients of the correlation between the differential observables defined in table 8.1, determined using $2 \cdot 10^3$ samples for each point on a grid of 131×100 evenly distributed $(T_{\text{lab}}, \vartheta)$ points in $T_{\text{lab}} \in [20, 150]\,\text{MeV}$ and $\vartheta \in [0, \pi]$. This figure shows the angle and energy dependence of the interobservabial correlations. The Pearson correlation coefficient of two variables Z_1 and Z_2 is defined as [51]

$$\rho \equiv \frac{\text{Cov}(Z_1, Z_2)}{\sqrt{\sigma^2_{Z_1}\sigma^2_{Z_2}}}, \tag{8.13}$$

where $\text{Cov}(Z_1, Z_2)$ is the covariance of Z_1 and Z_2, and $\sigma^2_{Z_i}$ is the variance of Z_i, $i = 1, 2$.

The first observations made from figures 8.3 and 8.4 are the hard bounds between the unpolarised differential cross section, $\sigma(T_{\text{lab}}, \theta)$, and various observables, shown with red lines in the figures. These constraints are independent of the energy and angle and result from the amplitude expressions. For the uncorrected observables, these inequalities are given by $|Z(\vec{x})| \leq \sigma(\vec{x})$ where $Z(\vec{x})$ is any differential observable. This is consistent with how the differential observables are defined, *i.e.* as different spin projections of the projectile, target, scattered, and recoil particle states onto the respective basis vectors [12] and the unpolarised differential cross section is the sum over all outgoing states and average over ingoing states [29]. As expected, these

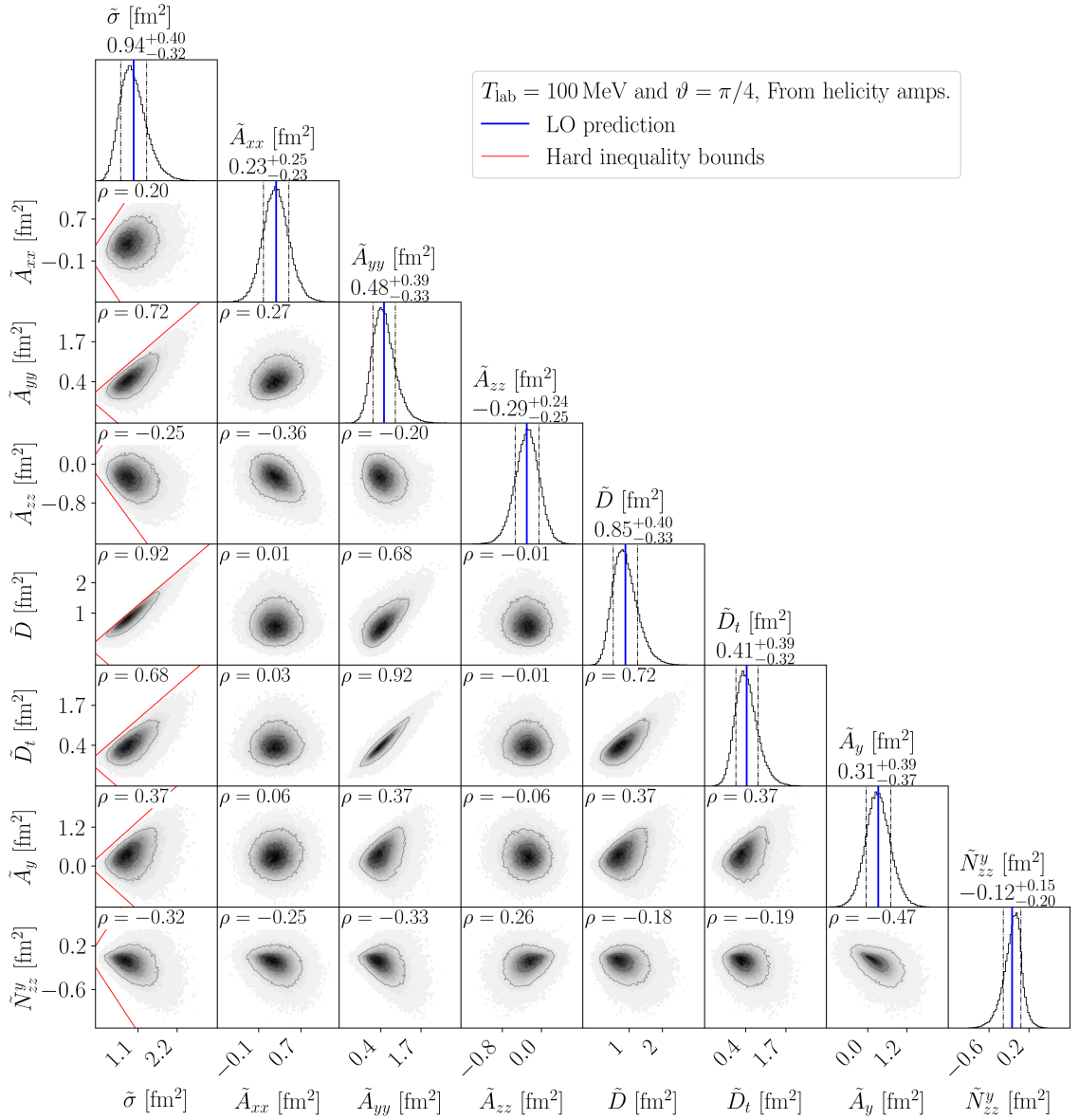

Figure 8.3: The mean-corrected joint distributions of the differential observable types in table 8.1, for laboratory kinetic energy $T_{\text{lab}} = 100\,\text{MeV}$ and c.m. polar scattering angle $\vartheta = \pi/4$. The distributions were constructed from 10^5 samples of the helicity amplitude distributions shown in figure 8.1a. The dot-dashed lines indicate the 68.2 % ETI with values indicated by the numbers above each column. The blue lines in the diagonal plots are the LO prediction, and the red lines indicate the bounds from hard inequalities between observable types. ρ is the Pearson correlation coefficient, representing the level of correlation between the observable types.

inequalities can be shown for all observables, from their expressions in terms of the scattering amplitudes as given in [12]. For the corrected observable distributions, the inequalities can be derived by inserting (8.2) and getting

$$|\tilde{Z}(\vec{x}) + \langle Z(\vec{x})\rangle_{\text{corr}}| \leq \sigma + \langle \sigma(\vec{x})\rangle_{\text{corr}}\,, \tag{8.14}$$

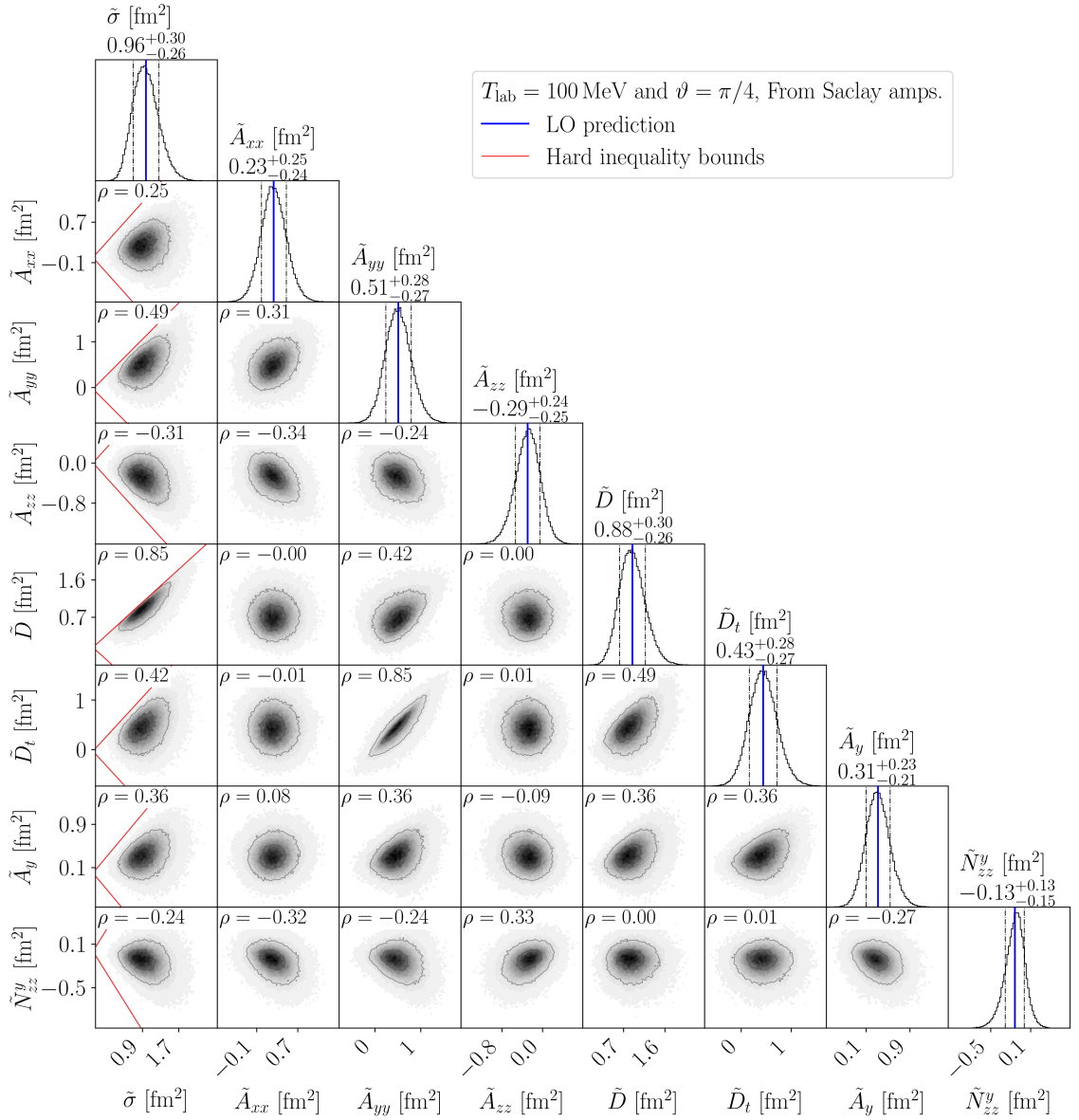

Figure 8.4: Same as figure 8.3, except that the differential observable distributions were constructed from samples of the Saclay amplitude distributions shown in figure 8.1b.

or equivalently

$$-\tilde{\sigma}(\vec{x}) - \langle\sigma(\vec{x})\rangle_{\text{corr}} - \langle Z(\vec{x})\rangle_{\text{corr}} \leq \tilde{Z}(\vec{x}) \leq \tilde{\sigma}(\vec{x}) + \langle\sigma(\vec{x})\rangle_{\text{corr}} - \langle Z(\vec{x})\rangle_{\text{corr}}\,, \tag{8.15}$$

which are the red lines plotted in figures 8.3 and 8.4, with the mean corrections for the respective convention.

The results from the propagation of the helicity (figure 8.3) and Saclay (figure 8.4) amplitude distributions show similar results. The general shapes of the joint distributions are the same, but the level of correlation (characterised by the Pearson correlation coefficients) differs. This is a combination of the fact that the helicity

amplitudes are more constrained from the start, and that the implemented error model is (except for constraints) independent of the convention, but the propagation is not. A clear example of this is the unpolarised differential cross section, which in the Saclay convention depends equally on all amplitudes, but in the helicity convention the fifth amplitude has a coefficient four times larger than the others.

Figure 8.5 shows the correlation (characterised by the Pearson correlation coefficient) between different observable types (propagated from helicity amplitudes) for laboratory energies $T_{\text{lab}} \in [20, 150]$ and c.m. polar scattering angles $\vartheta \in [0, \pi]$. Note first that there is a lot of energy dependence around $T_{\text{lab}} \approx 40\,\text{MeV}$. This is close to where the on-shell relative momentum passes the pion mass. There is also a distinct dependence on the scattering angle. A clear example of such dependence is the correlation between A_{xx} and A_{yy}, which is total for $\vartheta = 0, \pi$ but not for intermediate angles. This is a direct consequence of the boundary constraints of the helicity amplitudes, as hinted at in equation 8.7.

8.3 Unitarity and Total Cross Section

The uncertainties of the scattering amplitudes for $T_{\text{lab}} = 100\,\text{MeV}$ were propagated to the unpolarised total cross section, $\sigma_{0,\text{tot}}(T_{\text{lab}})$, the transverse total cross section, $\sigma_{\text{T}}(T_{\text{lab}})$, and the longitudinal total cross section, $\sigma_{\text{L}}(T_{\text{lab}})$, with $7.5 \cdot 10^4$ amplitude samples. The resulting distributions are shown in figures 8.6, 8.7, and 8.8, respectively, as propagated from the helicity and Saclay amplitude truncation errors (figure 8.1). Two methods were used and compared in these figures: the optical theorem and integration of mean-corrected differential observables as presented in subsection 4.2.2. The integrals were approximated with $N = 100$ GL quadrature points between $A = 0$ and $B = \pi$, see equation (6.2).

The averages from the two methods and conventions agree well with each other for all total cross sections, and are equal to the LO predictions, due to the mean correction. However, the widths and shapes of the distributions differ, which is a clear sign that the amplitude samples violate the unitarity constraints presented in chapter 4. The foldback effects that resulted from the propagation to the differential observables, discussed in section 8.2, clearly propagate to the total cross sections through the integral expressions. These effects are, however, not present in the distributions propagated through the optical theorem expressions, as they do not depend on any squares of amplitudes.

The comparison between the total cross sections determined with the integral expressions and the optical theorem directly reflects how well the samples obey the unitarity constraint. This is because the optical theorem is a direct application of the unitarity constraint onto the integral expression. The fact that unitarity was not broken on average can be concluded from the results in figures 8.9, 8.10, and 8.11,

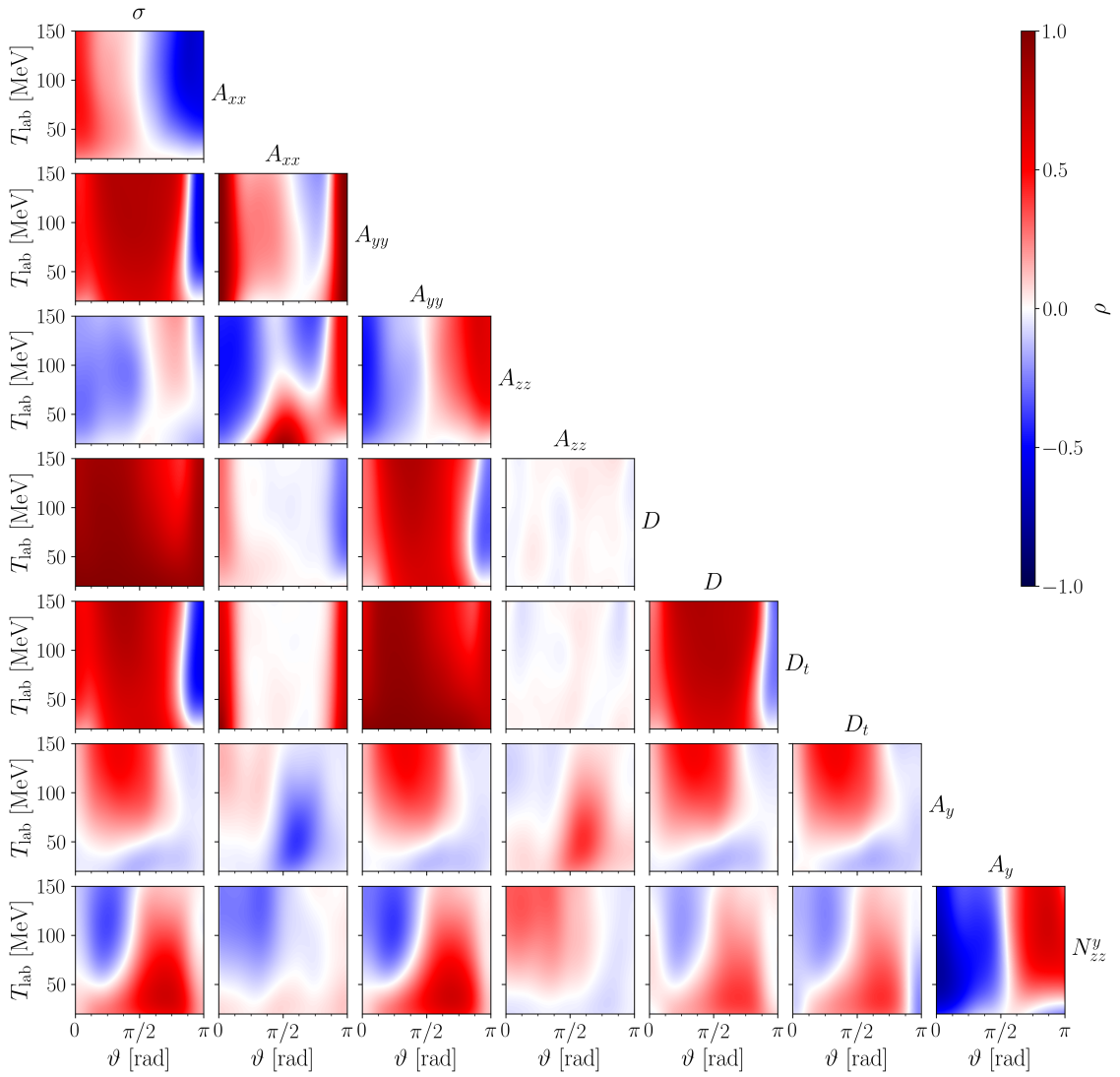

Figure 8.5: The Pearson correlation coefficients $\rho(T_{\mathrm{lab}}, \vartheta)$, representing the correlation level, between the differential observables in table 8.1, for laboratory kinetic energy $T_{\mathrm{lab}} \in [20, 150]\,\mathrm{MeV}$ and c.m. polar scattering angle $\vartheta = [0, \pi]$. The coefficients were determined with $2 \cdot 10^3$ samples of the LO helicity amplitudes with truncation error distributions for each of the 131×100 evenly distributed $(T_{\mathrm{lab}}, \vartheta)$ points.

showing the distributions of

$$\Delta\sigma_{0,\mathrm{tot}}(T_{\mathrm{lab}}) \equiv \tilde{\sigma}_{0,\mathrm{tot}}(T_{\mathrm{lab}}) - \sigma_{0,\mathrm{tot}}(T_{\mathrm{lab}}), \tag{8.16}$$

$$\Delta\sigma_{\mathrm{T}}(T_{\mathrm{lab}}) \equiv \tilde{\sigma}_{\mathrm{T}}(T_{\mathrm{lab}}) - \sigma_{\mathrm{T}}(T_{\mathrm{lab}}), \tag{8.17}$$

$$\Delta\sigma_{\mathrm{L}}(T_{\mathrm{lab}}) \equiv \tilde{\sigma}_{\mathrm{L}}(T_{\mathrm{lab}}) - \sigma_{\mathrm{L}}(T_{\mathrm{lab}}), \tag{8.18}$$

where $\{\tilde{\sigma}_{0,\mathrm{tot}}, \tilde{\sigma}_{\mathrm{T}}, \tilde{\sigma}_{\mathrm{L}}\}$ and $\{\sigma_{0,\mathrm{tot}}, \sigma_{\mathrm{T}}, \sigma_{\mathrm{L}}\}$ are the total cross sections determined by integrating mean-corrected differeintial observables and the optical theorem, respectively. The figures also show that the individual samples did not respect the unitarity constraint. The level of unitarity breaking of a signal sample could be seen as equiv-

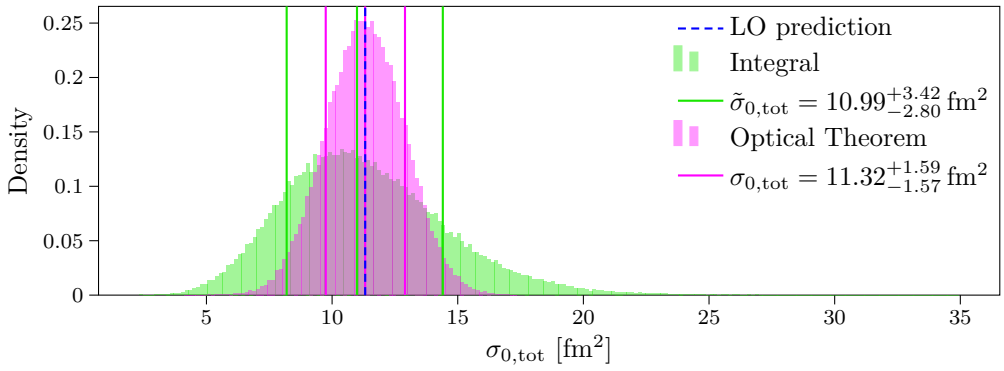

(a) From helicity amplitudes

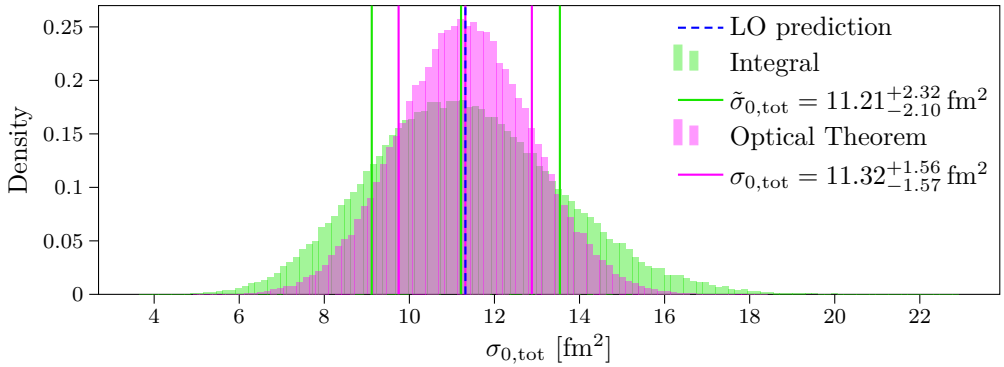

(b) From Saclay amplitudes

Figure 8.6: The LO χEFT truncation errors of the unpolarised total cross section for $T_{\mathrm{lab}} = 100\,\mathrm{MeV}$, propagated from the corresponding distributions of the helicity (a) and Saclay (b) amplitudes shown in figure 8.1. The green and magenta histograms indicate the distributions resulting from the integral over mean-corrected differential cross sections and the optical theorem, respectively. The solid green and magenta lines indicated the 68.2 % ETI and the median of the two distributions. The dashed blue line is the LO prediction (integration and optical theorem equivalent).

alently random as the samples themselves, but due to the mean correction, centred around zero. This was, however, to be expected with the error model that was used. The model considers a correlation length, a marginal variance, and a mean. Every sample of amplitudes is a smooth curve over $\vartheta \in [0, \pi]$, and the boundary conditions require these curves to start and/or end at zero for specific amplitudes. The shape of the curves is, however, constrained by the unitarity constraint, but is not implemented into the model, meaning that they are essentially random. The investigation into the explicit implementation of the unitarity constraint into the error model will be considered as future work.

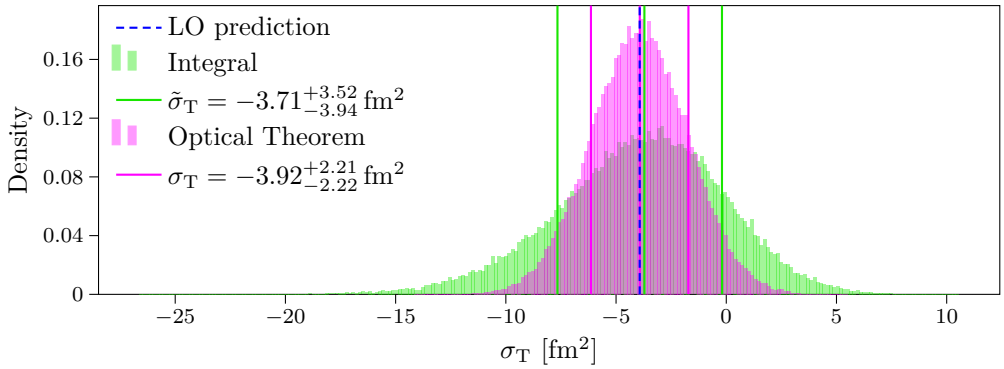

(a) From helicity amplitudes

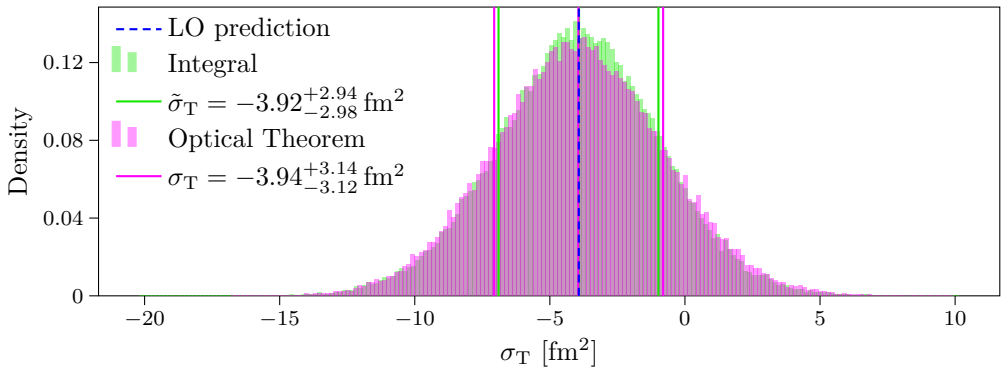

(b) From Saclay amplitudes

Figure 8.7: The LO χEFT truncation errors of the transverse total cross section for $T_{\mathrm{lab}} = 100\,\mathrm{MeV}$, propagated from the corresponding distributions of the helicity (a) and Saclay (b) amplitudes shown in figure 8.1. The histograms and lines descriptions are the same as in figure 8.6.

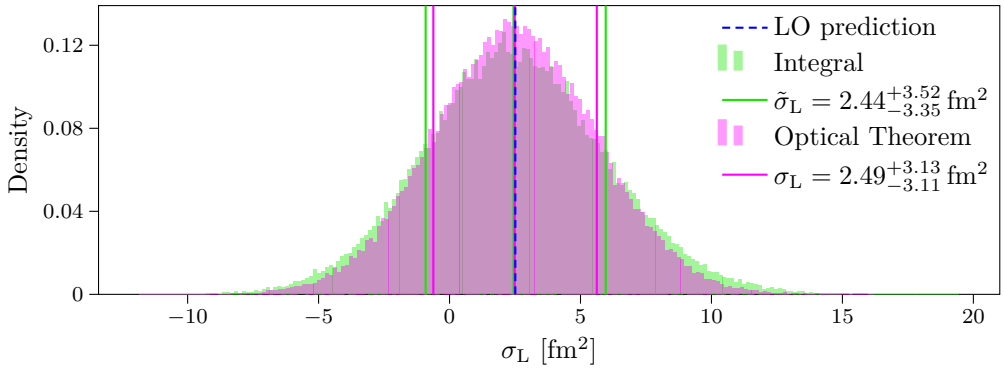

(a) From helicity amplitudes

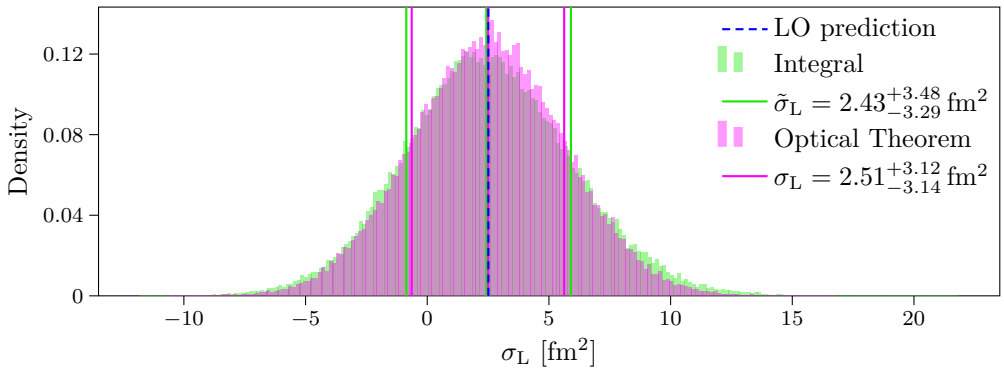

(b) From Saclay amplitudes

Figure 8.8: The LO χEFT truncation errors of the longitudinal total cross section for $T_{\mathrm{lab}} = 100\,\mathrm{MeV}$, propagated from the corresponding distributions of the helicity (a) and Saclay (b) amplitudes shown in figure 8.1. The histograms and lines descriptions are the same as in figure 8.6.

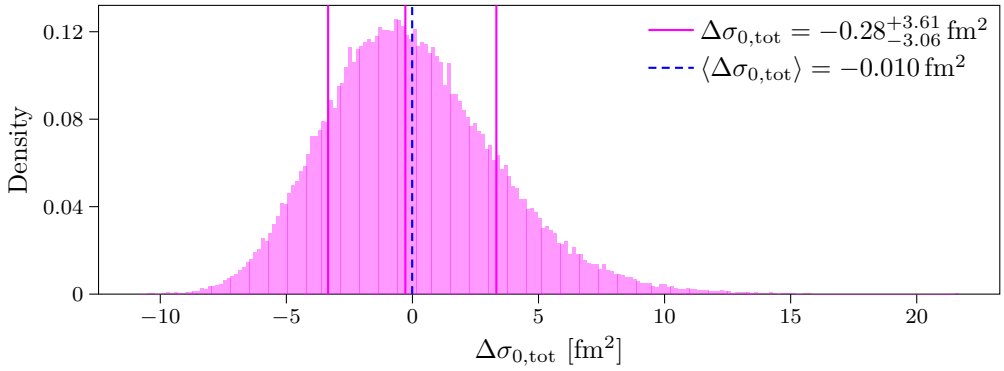

(a) From helicity amplitudes

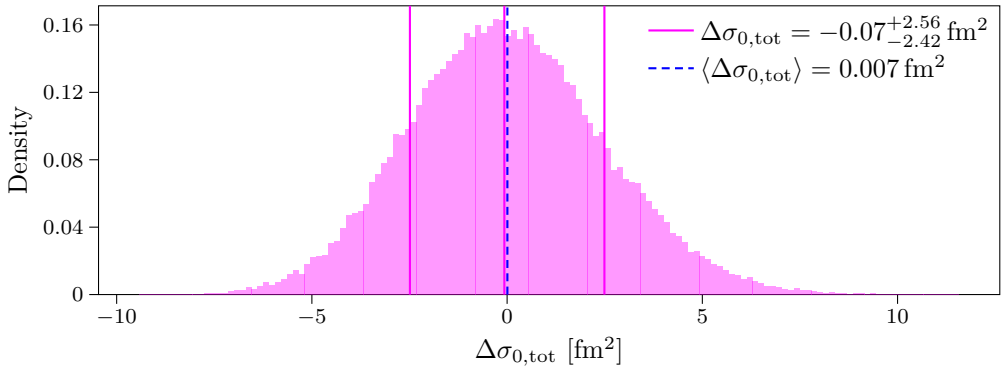

(b) From Saclay amplitudes

Figure 8.9: The distribution of $\Delta\sigma_{0,\mathrm{tot}}$ (magenta histogram), defined in equation (8.16), for $T_{\mathrm{lab}} = 100\,\mathrm{MeV}$, propagated from the corresponding distributions of the helicity (a) and Saclay (b) amplitudes shown in figure 8.1. The solid magenta lines indicated the 68.2 % ETI and the median of the $\Delta\sigma_{0,\mathrm{tot}}$ distributions. The dashed blue line is the mean of the $\Delta\sigma_{0,\mathrm{tot}}$ distribution.

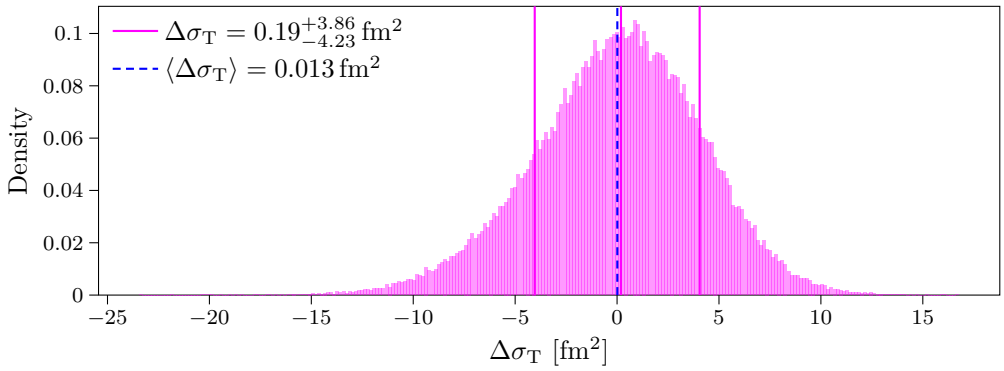

(a) From helicity amplitudes

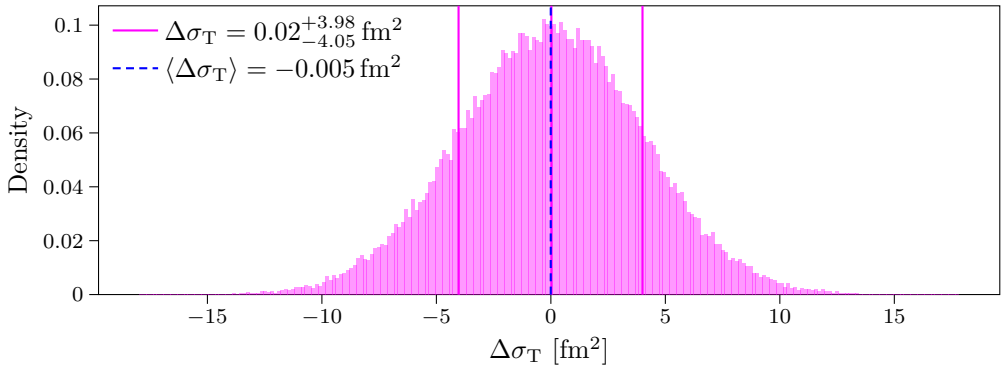

(b) From Saclay amplitudes

Figure 8.10: The distribution $\Delta\sigma_T$ (magenta histogram), defined in equation (8.17), for $T_{lab} = 100\,\mathrm{MeV}$, propagated from the corresponding distributions of the helicity (a) and Saclay (b) amplitudes shown in figure 8.1. The solid magenta lines indicated the 68.2 % ETI and the median of the $\Delta\sigma_T$ distributions. The dashed blue line is the mean of the $\Delta\sigma_T$ distribution.

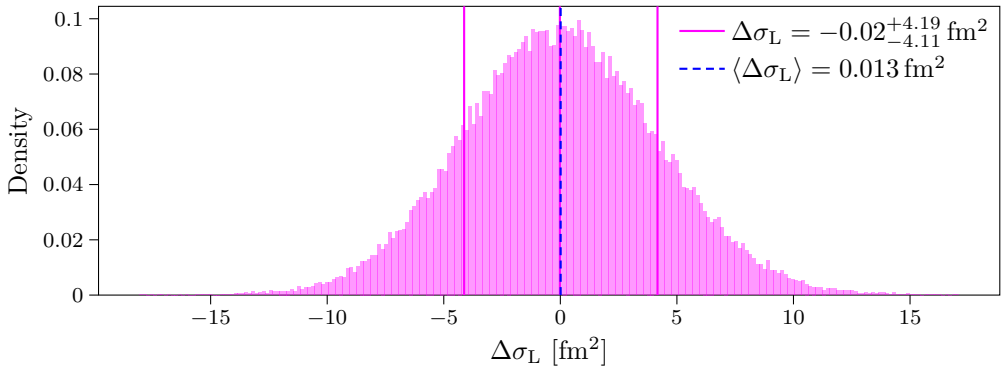

(a) From helicity amplitudes

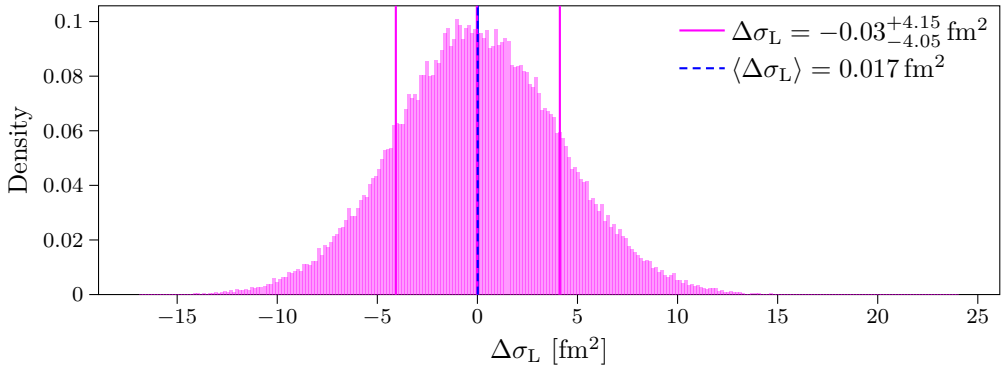

(b) From Saclay amplitudes

Figure 8.11: The distribution $\Delta\sigma_L$ (magenta histogram), defined in equation (8.18), for $T_{lab} = 100$ MeV, propagated from the corresponding distributions of the helicity (a) and Saclay (b) amplitudes shown in figure 8.1. The solid magenta lines indicated the 68.2 % ETI and the median of the $\Delta\sigma_L$ distributions. The dashed blue line is the mean of the $\Delta\sigma_L$ distribution.

9

Conclusion and Outlook

This thesis describes a study that aimed to implement a BUQ model for χEFT truncation errors at the level of NN scattering amplitudes and propagate the errors to NN scattering observables. The correlations between the resulting distributions were then investigated. In addition, the thesis set out to examine the implications of the unitarity of the scattering operator and to what extent the constructed error model violates this implicit constraint.

The BUQ model for χEFT truncation errors of the LO *np* scattering amplitudes, implemented with a fixed kernel GP correlated over laboratory kinetic energies and c.m. polar scattering angles, gave as expected angle-independent variances for the unconstrained *np* scattering amplitudes. The constrained amplitudes had zero variance at the constrained bounds and increased smoothly for intermediate angles. The median (and mean consistent with a Gaussian distribution) of the amplitude distributions lies on the LO prediction, reflecting the *a priori* assumption that the predicted value is the best knowledge at hand for the amplitude values. These observations are all signs that the implementation of the error model on the scattering amplitudes was successful.

The propagation of the χEFT truncation errors of the *np* scattering amplitudes to *np* scattering observables successfully resulted in correlations between the different observable types. This is a significant step in understanding the EFT truncation errors, as it gives rise to joint distributions by letting the known physics of the scattering process constrain the truncation errors. The propagation of the relatively simple truncation error distributions of the amplitudes managed to instil rather complex relations between the corresponding truncation error distributions of the observables. The boundary constraints propagate directly to both angle-dependent observable truncation errors and interobservabial correlations. The relations between the amplitudes and observables additionally result in hard inequalities between the unpolarised differential cross section and various differential observable types. In other words, the error model presented in this thesis incorporates a high level of physics knowledge about the underlying symmetries and invariance principles of NN interactions.

The mean correction scheme, motivated by the *a priori* expectation that the mean should be given by the LO prediction, gave the desired result. The truncation error distributions of observables significantly impacted by the foldback effect[1] have a median shifted from the mean and an elongated tail, which are clear signs of the resulting non-Gaussian distributions of the observables. However, this is not considered to be particularly problematic, given that it most likely stems from the distribution-defining hyperparameters being out of balance for certain amplitudes. This is not terribly surprising as the project implemented a fixed kernel GP, and the problem may resolve itself when the hyperparameters of the error model of the scattering amplitudes are actually determined independently. The importance of the mean-correcting scheme should not be underestimated, as it is the driving force behind the error model respecting the unitarity constraint on average.

Outlook

This project advances the state of the art by moving beyond the independent treatment of observables to a framework that incorporates (almost) all known constraints on NN scattering quantities. As such, the work brings us to the very doorstep of one of the most fundamental principles in quantum scattering theory: the unitarity of the scattering operator. While the error model presented in this thesis manages to enforce an average compliance with this constraint, it was also observed that individual samples within the model fail to respect unitarity. Fortunately, this thesis dedicates several pages to exploring the unitarity constraint in detail, particularly through its implications for the NN scattering amplitudes via the M-matrix. Surprisingly, explicit formulations of these relations are scarce in the literature[2]. This work, therefore, serves as both a foundation and an invitation for further developments, most notably, the explicit implementation of unitarity into an improved error model.

A more straightforward extension of this project would be to consider higher chiral effective field theory (χEFT) truncation orders. This would allow for independent training of the GP modelling truncation errors in the scattering amplitudes within the adopted formalism.

On a more general note, the framework presented in this thesis allows further studies to increase the physical rigour of the correlated EFT truncation errors considered. It can be incorporated into various inference procedures relating to EFTs and observables. Such procedures, where this framework can contribute, are the inference of EFT LECs and predictions of observables, where the physical agreement is not just paramount but basically the point.

[1] The effects resulting from squaring a Gaussian distribution, *i.e.* a mean shifted with the variance of the Gaussian from the squared mean of the Gaussian and an elongated tail; consistent with a non-central χ^2 distribution.

[2] We only found a few sources stating similar expressions, *e.g.* [52], none of which got it right (I reserve the right to be the one who is wrong). Note, however, that the optical theorem is a specific case of this constraint, which is not so rare.

References

[1] H. Yukawa, "On the interaction of elementary particles. I," *Proceedings of the Physico-Mathematical Society of Japan. 3rd Series*, vol. 17, pp. 48–57, 1935. DOI: 10.11429/ppmsj1919.17.0_48.

[2] R. Machleidt and D. R. Entem, "Chiral effective field theory and nuclear forces," *Physics Reports*, vol. 503, no. 1, pp. 1–75, Jun. 2011. DOI: 10.1016/j.physrep.2011.02.001.

[3] S. Weinberg, "Phenomenological lagrangians," *Physica A*, vol. 96, no. 1, pp. 327–340, 1979. DOI: 10.1016/0378-4371(79)90223-1.

[4] S. Weinberg, "Nuclear forces from chiral lagrangians," *Physics Letters B*, vol. 251, no. 2, pp. 288–292, 1990. DOI: 10.1016/0370-2693(90)90938-3.

[5] S. Weinberg, "Effective chiral lagrangians for nucleon-pion interactions and nuclear forces," *Nuclear Physics B*, vol. 363, no. 1, pp. 3–18, 1991. DOI: 10.1016/0550-3213(91)90231-L.

[6] R. J. Furnstahl, N. Klco, D. R. Phillips, and S. Wesolowski, "Quantifying truncation errors in effective field theory," *Physical Review C*, vol. 92, no. 2, p. 024 005, Aug. 2015. DOI: 10.1103/PhysRevC.92.024005.

[7] J. A. Melendez, S. Wesolowski, and R. J. Furnstahl, "Bayesian truncation errors in chiral effective field theory: Nucleon-nucleon observables," *Physical Review C*, vol. 96, no. 2, p. 024 003, Aug. 2017. DOI: 10.1103/PhysRevC.96.024003.

[8] J. A. Melendez, R. J. Furnstahl, D. R. Phillips, M. T. Pratola, and S. Wesolowski, "Quantifying correlated truncation errors in effective field theory," *Physical Review C*, vol. 100, no. 4, p. 044 001, Oct. 2019. DOI: 10.1103/PhysRevC.100.044001.

[9] I. Svensson, A. Ekström, and C. Forssén, "Inference of the low-energy constants in Δ-full chiral effective field theory including a correlated truncation error," *Physical Review C*, vol. 109, no. 6, p. 064 003, Jun. 2024. DOI: 10.1103/PhysRevC.109.064003.

[10] P. J. Millican, R. J. Furnstahl, J. A. Melendez, D. R. Phillips, and M. T. Pratola, "Assessing correlated truncation errors in modern nucleon-nucleon potentials," *Physical Review C*, vol. 110, no. 4, p. 044 002, Oct. 2024. DOI: 10.1103/PhysRevC.110.044002.

[11] B. Hu et al., "Ab initio predictions link the neutron skin ^{208}Pb to nuclear forces," *Nature Physics*, vol. 18, no. 10, pp. 1196–1200, 2022. DOI: 10.1038/s41567-022-01715-8.

[12] J. Bystricky, F. Lehar, and P. Winternitz, "Formalism of nucleon-nucleon elastic scattering experiments," *Le Journal De Physique*, vol. 39, no. 1, 1978. DOI: 10.1051/jphys:019780039010100.

[13] B. McClung, Ch. Elster, and D. R. Phillips, *Order-by-order uncertainties of nucleon-nucleon wolfenstein amplitudes in chiral effective field theory*, 2025. arXiv: 2501.09231 [nucl-th].

[14] S. Weinberg, *The Quantum Theory of Fields: Volume I Foundations*. Cambridge, United Kingdom: Cambridge University Prss, 2005, ISBN: 9780521670531.

[15] S. Weinberg, *The Quantum Theory of Fields: Volume II Modern Applications*. Cambridge, United Kingdom: Cambridge University Prss, 2005, ISBN: 9780521670548.

[16] S. Navas et al. (Particle Data Group), "Review of particle physics," *Physical Review D*, vol. 110, no. 3, p. 030 001, Aug. 2024. DOI: 10.1103/PhysRevD.110.030001.

[17] S. Scherer, *Introduction to chiral perturbation theory*, 2002. arXiv: hep-ph/0210398 [hep-ph].

[18] M. E. Peskin and D. V. Schroeder, *An Introduction to Quantum Field Theory*. Boca Raton, Florida, USA: CRC Press, 2019, ISBN: 9780367320560.

[19] J. Gasser, M. E. Sainio, and A. Švarc, "Nucleons with chiral loops," *Nuclear Physics B*, vol. 307, no. 4, pp. 779–853, 1988. DOI: 10.1016/0550-3213(88)90108-3.

[20] E. Epelbaum, H.-W. Hammer, and U.-G. Meißner, "Modern theory of nuclear forces," *Reviews of Modern Physics*, vol. 81, no. 4, pp. 1773–1825, Dec. 2009. DOI: 10.1103/RevModPhys.81.1773.

[21] E. Epelbaum, U.-G. Meißner, and W. Glöckle, "Nuclear forces in the chiral limit," *Nuclear Physics A*, vol. 714, no. 3, pp. 535–574, 2003. DOI: 10.1016/S0375-9474(02)01393-3.

[22] H.-P. Breuer and F. Petruccione, *The Theory of Open Quantum Systems*. Oxford, Great Britain: Oxford University Press, 2002, ISBN: 9780198520634.

[23] L. Råde, B. Westergren, and F. Wikström, *Mathematics Handbook: for Science and Engineering*, 6th ed. Lund, Sweden: Studentlitteratur, 2019, ISBN: 9789144128436.

[24] J. J. Sakurai and J. Napolitano, *Modern Quantum Mechanics*, 3rd ed. Cambridge, United Kingdom: Cambridge University Press, 2021, ISBN: 9781108473224.

[25] J. R. Taylor, *Scattering Theory: The Quantum Theory of Nonrelativistic Collisions*, Dover ed. Mineola, New York, USA: Dover Publications Inc., 2006, ISBN: 9780486450131.

[26] E. N. Economou, *Green's Functions in Quantum Physics* (Springer Series in Solid-State Sciences). Berlin, Germany: Springer-Verlag, 1979, ISBN: 9780387091549.

[27] R. H. Landau, *Quantum Mechanics II: A Second Course in Quantum Theory*, 2nd ed. Hoboken, New Jersey, USA: John Wiley & Sons, 1996, ISBN: 9780471116080.

[28] D. A. Varshalovich, A. N. Moskalev, and V. K. Khersonskii, *Quantum Theory of Angular Momentum*. Singapore: World Scientific Publishing, 1988, ISBN: 9789971509965.

[29] W. Glöckle, *The Quantum Mechanical Few-Body Problem*. Berlin, Germany: Springer-Verlag, 1983, ISBN: 9783642820830.

[30] A. Zee, *Group Theory in a Nutshell for Physicists* (In a Nutshell). Princeton, New Jersey, USA: Princeton University Press, 2016, ISBN: 9780691162690.

[31] P. E. Wormer and J. Paldus, "Angular momentum diagrams," in ser. Advances in Quantum Chemistry, J. Sabin and E. Brändas, Eds., vol. 51, Academic Press, 2006, pp. 59–123. DOI: 10.1016/S0065-3276(06)51002-0.

[32] H. P. Stapp, T. J. Ypsilantis, and N. Metropolis, "Phase-shifts analysis of 310-MeV proton-proton scattering experiments," *Physical Review*, no. 1, 1957.

[33] R. Blankenbecler and R. Sugar, "Linear integral equations for relativistic multichannel scattering," *Physical Review*, vol. 142, no. 4, pp. 1051–1059, 1966. DOI: 10.1103/PhysRev.142.1051.

[34] E. Epelbaum, H. Krebs, and U.-G. Meißner, "Improved chiral nucleon-nucleon potential up to next-to-next-to-next-to-leading order," *The European Physical Journal A*, vol. 51, no. 53, 2015. DOI: 10.1140/epja/i2015-15053-8.

[35] F. Perrot et al., "Measurement of the total cross section difference $\Delta\sigma_T(pp)$ in the energy range from 0.43 to 2.4 gev," *Nuclear Physics B*, vol. 278, no. 4, pp. 881–904, 1986. DOI: 10.1016/0550-3213(86)90423-2.

[36] J. Bystricky et al., "Measurement of the spin correlation parameter A_{00kk} for pp elastic scattering in the energy range 0.72–1.1 GeV," *Nuclear Physics B*, vol. 258, pp. 483–504, 1985. DOI: https://doi.org/10.1016/0550-3213(85)90623-6.

[37] C. E. Rasmussen and C. K. I. Williams, *Gaussian Processes for Machine Learning*. Cambridge, Massachusetts, USA: The MIT Press, 2006, ISBN: 9780262182539.

[38] L. I. G. B. Abrahamsson, *MSc-EFTtrer-NNscatt*, Public GitHub repository. [Online]. Available: https://github.com/Lucas010723/MSc-EFTtrer-NNscatt.

[39] B. D. Carlsson et al., "Uncertainty analysis and order-by-order optimization of chiral nuclear interactions," *Phys. Rev. X*, vol. 6, no. 1, p. 011 019, Feb. 2016. DOI: 10.1103/PhysRevX.6.011019.

[40] J. Beringer et al. (Particle Data Group), "Review of particle physics," *Physical Review D*, vol. 86, no. 1, p. 010 001, Jul. 2012. DOI: 10.1103/PhysRevD.86.010001.

[41] K. Erkelenz, R. Alzetta, and K. Holinde, "Momentum space calculations and helicity formalism in nuclear physics," *Nuclear Physics A*, vol. 176, no. 2, pp. 413–432, 1971. DOI: 10.1016/0375-9474(71)90279-X.

[42] P. Virtanen et al., "SciPy 1.0: Fundamental algorithms for scientific computing in python," *Nature Methods*, vol. 17, no. 3, pp. 261–272, 2020. DOI: 10.1038/s41592-019-0686-2.

[43] H. T. Johansson and C. Forssén, "Fast and accurate evaluation of wigner 3j, 6j, and 9j symbols using prime factorization and multiword integer arithmetic," *SIAM Journal on Scientific Computing*, vol. 38, no. 1, A376–A384, 2016. DOI: 10.1137/15M1021908.

[44] GPy developers, *GPy: A gaussian process framework in python*, Public GitHub repository, Jul. 23, 2024. Accessed: May 30, 2025. [Online]. Available: http://github.com/SheffieldML/GPy.

[45] I. Vernon, S. E. Jackson, and J. A. Cumming, "Known boundary emulation of complex computer models," *SIAM/ASA Journal on Uncertainty Quantification*, vol. 7, no. 3, pp. 838–876, 2019. DOI: 10.1137/18M1164457.

[46] K. I. Park, *Fundamentals of Probability and Stochastic Processes with Applications to Communications*. Holmdel, New Jersey, USA: Springer, 2017, ISBN: 9783319680750.

[47] N. L. Johnson, S. Kotz, and N. Balakrishnan, *Continuous Univariate Distributions, Volume 2* (Wiley Series in Probability and Statistics), 2nd ed. New York City, New York, USA: John Wiley & Sons Inc, 1995, ISBN: 9780471584940.

[48] V. G. J. Stoks, R. A. M. Klomp, M. C. M. Rentmeester, and J. J. de Swart, "Partial-wave analysis of all nucleon-nucleon scattering data below 350 mev," *Physical Review C*, vol. 48, no. 2, pp. 792–815, Sep. 1993. DOI: 10.1103/PhysRevC.48.792.

[49] "NN-OnLine," Theoretical High-Energy Physics Group, Radboud University Nijmegen, Accessed: May 31, 2025. [Online]. Available: https://nn-online.org.

[50] N. L. Johnson, S. Kotz, and N. Balakrishnan, *Continuous Univariate Distributions, Volume 1* (Wiley Series in Probability and Statistics), 2nd ed. New York City, New York, USA: John Wiley & Sons Inc, 1994, ISBN: 9780471584957.

[51] J. L. Rodgers and W. A. Nicewander, "Thirteen ways to look at the correlation coefficient," *The American Statistician*, vol. 42, no. 1, pp. 59–66, 1988. DOI: 10.1080/00031305.1988.10475524.

[52] N. Hoshizaki, "Appendix. formalism of nucleon-nucleon scattering," *Progress of Theoretical Physics Supplement*, vol. 42, pp. 107–159, Jun. 1968. DOI: 10.1143/PTPS.42.107.

[53] J. V. Michalowicz, J. M. Nichols, F. Bucholtz, and C. C. Olson, "An isserlis' theorem for mixed gaussian variables: Application to the auto-bispectral density," *Journal of Statistical Physics*, vol. 136, no. 1, pp. 89–102, 2009. DOI: 10.1007/s10955-009-9768-3.

A

Scattering with Generally Normalised States

In this appendix, the momentum eigenstates $|\boldsymbol{p}\rangle$ and position eigenstates $|\boldsymbol{x}\rangle$ have a general normalisation

$$\langle \boldsymbol{p}'|\boldsymbol{p}\rangle = C_{\text{mom.}}^2 \delta^{(3)}(\boldsymbol{p}'-\boldsymbol{p}), \quad \langle \boldsymbol{x}'|\boldsymbol{x}\rangle = C_{\text{pos.}}^2 \delta^{(3)}(\boldsymbol{x}'-\boldsymbol{x}), \quad C_{\text{mom.}}, C_{\text{pos.}} \in \mathbb{R}, \tag{A.1}$$

and will thus have the completeness identities

$$\mathbb{1} = \frac{1}{C_{\text{mom.}}^2} \int_{\mathbb{R}^3} d\boldsymbol{p}\ |\boldsymbol{p}\rangle \langle \boldsymbol{p}|\,, \quad \mathbb{1} = \frac{1}{C_{\text{pos.}}^2} \int_{\mathbb{R}^3} d\boldsymbol{x}\ |\boldsymbol{x}\rangle \langle \boldsymbol{x}|\,. \tag{A.2}$$

The free wave function is, therefore, given by

$$\phi_{\boldsymbol{p}}(\boldsymbol{x}) \equiv \langle \boldsymbol{x}|\boldsymbol{p}\rangle = \frac{C_{\text{pos.}} C_{\text{mom.}}}{(2\pi)^{3/2}} e^{i\boldsymbol{x}\cdot\boldsymbol{p}}, \tag{A.3}$$

which is a constant times a plane wave, and can be realised by comparing the definition of the three-dimensional Dirac delta function

$$\delta^{(3)}(\boldsymbol{p}'-\boldsymbol{p}) = \int_{\mathbb{R}^3} d\boldsymbol{x}\, \frac{e^{i\boldsymbol{x}\cdot(\boldsymbol{p}-\boldsymbol{p}')}}{(2\pi)^3}, \tag{A.4}$$

with

$$\delta^{(3)}(\boldsymbol{p}'-\boldsymbol{p}) = \frac{1}{C_{\text{mom.}}^2} \langle \boldsymbol{p}'|\boldsymbol{p}\rangle = \frac{1}{C_{\text{pos.}}^2 C_{\text{mom.}}^2} \int_{\mathbb{R}^3} d\boldsymbol{x}\ \langle \boldsymbol{p}'|\boldsymbol{x}\rangle \langle \boldsymbol{x}|\boldsymbol{p}\rangle\,. \tag{A.5}$$

The PWS $|p,\ell,m\rangle$ are defined in relation to the momentum eigenstates as

$$|\boldsymbol{p}\rangle = \sum_{\ell=0}^{\infty} \sum_{m=-\ell}^{\ell} \frac{C_{\text{mom.}}}{C_{\text{PW}}} e^{-i\omega\ell} Y_m^{*\ell}(\hat{\boldsymbol{p}})\, |p,\ell,m\rangle\,, \tag{A.6}$$

where $C_{\text{PW}} \in \mathbb{R}$ is a real normalisation constants, $\omega \in [0, 2\pi]$ is a constant phase, and $Y_m^{\ell}(\hat{\boldsymbol{p}}) \equiv \langle \hat{\boldsymbol{p}}|\ell, m\rangle$ are the spherical harmonics. The normalisation and completeness identity of the PWS are thus

$$\langle p',\ell',m'|p,\ell,m\rangle = C_{\text{PW}}^2 \delta_{\ell'\ell} \delta_{m'm} \frac{\delta(p'-p)}{p^2}, \tag{A.7}$$

and

$$\mathbb{1} = \frac{1}{C_{\text{PW}}^2} \sum_{\ell,m} \int_{\mathbb{R}^+} dp\, p^2 \left|p, \ell, m\right\rangle \left\langle p, \ell, m\right| . \tag{A.8}$$

A.1 The Scattering Amplitude Matrix

In accordance with (3.15), the scattered state $|\psi_{\boldsymbol{k}}^{\pm}\rangle$ can be expressed as

$$|\psi_{\boldsymbol{k}}^{\pm}\rangle = |\boldsymbol{k}\rangle + G_0^{\pm}(E_k) V |\psi_{\boldsymbol{k}}^{\pm}\rangle , \quad G_0^{\pm}(E_k) = \frac{1}{E_k - H_0 \pm i\epsilon}, \tag{A.9}$$

where $E_k = |\boldsymbol{k}|^2/(2\mu)$ is the on-shell energy, with the on-shell momentum $k = |\boldsymbol{k}|$ and reduced mass μ. The scattered wave function $\psi_{\boldsymbol{k}}^{\pm}(\boldsymbol{x}) \equiv \langle \boldsymbol{x}|\psi_{\boldsymbol{k}}^{\pm}\rangle$ is then given by

$$\begin{aligned} \psi_{\boldsymbol{k}}^{\pm}(\boldsymbol{x}) &= \phi_{\boldsymbol{k}}(\boldsymbol{x}) + \langle \boldsymbol{x}| G_0^{\pm}(E_k) V |\psi_{\boldsymbol{k}}^{\pm}\rangle = \\ &= \phi_{\boldsymbol{k}}(\boldsymbol{x}) + \frac{1}{C_{\text{pos.}}^2} \int_{\boldsymbol{R}^3} d\boldsymbol{x}'\, G_0^{\pm}(\boldsymbol{x}, \boldsymbol{x}'; E_k) \langle \boldsymbol{x}'| V |\psi_{\boldsymbol{k}}^{\pm}\rangle , \end{aligned} \tag{A.10}$$

where the Greens function in the position basis can be expressed as

$$\begin{aligned} G_0^{\pm}(\boldsymbol{x}, \boldsymbol{x}'; E_k) \equiv \langle \boldsymbol{x}| G_0^{\pm}(E_k) |\boldsymbol{x}'\rangle &= \frac{1}{C_{\text{mom.}}^2} \int_{\mathbb{R}^3} d\boldsymbol{p}\, \frac{\langle \boldsymbol{x}|\boldsymbol{p}\rangle \langle \boldsymbol{p}|\boldsymbol{x}'\rangle}{E_k - E_{\boldsymbol{p}} \pm i\epsilon} = \\ &= \frac{2C_{\text{pos.}}^2 \mu}{(2\pi)^3} \int_{\mathbb{R}^3} d\boldsymbol{p}\, \frac{e^{i\boldsymbol{p}\cdot(\boldsymbol{x}-\boldsymbol{x}')}}{|\boldsymbol{k}|^2 - |\boldsymbol{p}|^2 \pm i\epsilon}. \end{aligned} \tag{A.11}$$

This integral can be solved in the $\epsilon \to 0^+$ limit as (see *e.g.* [25, 27])

$$G_0^{\pm}(\boldsymbol{x}, \boldsymbol{x}'; E_k) = -\frac{C_{\text{pos.}}^2 \mu}{2\pi|\boldsymbol{x} - \boldsymbol{x}'|} e^{\pm ik|\boldsymbol{x}-\boldsymbol{x}'|}. \tag{A.12}$$

Inserting this into (A.10) gives

$$\psi_{\boldsymbol{k}}^{\pm}(\boldsymbol{x}) = \phi_{\boldsymbol{k}}(\boldsymbol{x}) - \frac{(2\pi)^2 \mu}{C_{\text{pos.}}^2 C_{\text{mom.}}^2} \int_{\boldsymbol{R}^3} d\boldsymbol{x}'\, \frac{e^{\pm ik|\boldsymbol{x}-\boldsymbol{x}'|}}{|\boldsymbol{x} - \boldsymbol{x}'|} \langle \boldsymbol{x}'| V |\psi_{\boldsymbol{k}}^{\pm}\rangle . \tag{A.13}$$

Given that the potential satisfy the properties[1] discussed in section 3.1, the $|\boldsymbol{x}| \to \infty$ asymptote to the scattered wave function can be expressed as [25]

$$\psi_{\boldsymbol{k}}^{\pm}(\boldsymbol{x}) \sim \phi_{\boldsymbol{k}}(\boldsymbol{x}) - \frac{\mu}{2\pi} \int_{\boldsymbol{R}^3} d\boldsymbol{x}'\, e^{\mp ik\hat{\boldsymbol{x}}\cdot\boldsymbol{x}'} \langle \boldsymbol{x}'| V |\psi_{\boldsymbol{k}}^{\pm}\rangle \frac{e^{\pm ik|\boldsymbol{x}|}}{|\boldsymbol{x}|}. \tag{A.14}$$

The integral in the second term can be rewritten as

$$\begin{aligned} \int_{\boldsymbol{R}^3} d\boldsymbol{x}'\, e^{\mp ik\hat{\boldsymbol{x}}\cdot\boldsymbol{x}'} \langle \boldsymbol{x}'| V |\psi_{\boldsymbol{k}}^{\pm}\rangle &= \frac{(2\pi)^{3/2}}{C_{\text{pos.}} C_{\text{mom.}}} \int_{\boldsymbol{R}^3} d\boldsymbol{x}'\, \langle \pm k\hat{\boldsymbol{x}}|\boldsymbol{x}'\rangle \langle \boldsymbol{x}'| V |\psi_{\boldsymbol{k}}^{\pm}\rangle = \\ &= \frac{(2\pi)^{3/2} C_{\text{pos.}}}{C_{\text{mom.}}} \langle \pm k\hat{\boldsymbol{x}}| V |\psi_{\boldsymbol{k}}^{\pm}\rangle = \frac{(2\pi)^{3/2} C_{\text{pos.}}}{C_{\text{mom.}}} \langle \pm k\hat{\boldsymbol{x}}| T^{\pm}(E_k) |\boldsymbol{k}\rangle , \end{aligned} \tag{A.15}$$

[1] Particularly that $|V(\boldsymbol{x})| < c|\boldsymbol{x}|^{-3}$ as $|\boldsymbol{x}| \to \infty$ for some constant $c \in \mathbb{R}$.

where $T^{\pm}(E_k)$ is the T operator for on-shell energy $E_k = |\boldsymbol{k}|^2/(2\mu)$. Equation (A.14) can thus equivalent to

$$\psi^{\pm}_{\boldsymbol{k}}(\boldsymbol{x}) \sim \phi_{\boldsymbol{k}}(\boldsymbol{x}) - \frac{\sqrt{2\pi}C_{\text{pos.}}\mu}{C_{\text{mom.}}} \langle \pm k\hat{\boldsymbol{x}}| \, T^{\pm}(E_k) \, |\boldsymbol{k}\rangle \, \frac{e^{\pm ik|\boldsymbol{x}|}}{|\boldsymbol{x}|}. \tag{A.16}$$

The wave function $\psi^{-}_{\boldsymbol{k}}(\boldsymbol{x})$ corresponds to a plane wave plus a spherically collapsing wave, which is not physical. The wave function $\psi^{+}_{\boldsymbol{k}}(\boldsymbol{x})$ is thus the only physical solution, and has per (A.16) the asymptotic form

$$\psi^{+}_{\boldsymbol{k}}(\boldsymbol{x}) \sim \frac{C_{\text{pos.}}C_{\text{mom.}}}{(2\pi)^{3/2}} \left[e^{i\boldsymbol{x}\cdot\boldsymbol{k}} + M(k\hat{\boldsymbol{x}}, \boldsymbol{k}) \frac{e^{ik|\boldsymbol{x}|}}{|\boldsymbol{x}|} \right], \tag{A.17}$$

where $M(\boldsymbol{k}', \boldsymbol{k})$ is the scattering amplitude given by

$$M(\boldsymbol{k}', \boldsymbol{k}) = -\frac{(2\pi)^2\mu}{C^2_{\text{mom.}}} \langle \boldsymbol{k}'| \, T^{+}(E_k) \, |\boldsymbol{k}\rangle \, . \tag{A.18}$$

By inserting (A.6), the scattering amplitude can be expanded in terms of the PWS as

$$\begin{aligned} &M(\boldsymbol{k}', \boldsymbol{k}) = \\ &\quad = -\frac{(2\pi)^2\mu}{C^2_{\text{PW}}} \sum_{\ell',m'} \sum_{\ell,m} e^{i\omega(\ell'-\ell)} Y^{\ell'}_{m'}(\hat{\boldsymbol{k}}') Y^{*\ell}_{m}(\hat{\boldsymbol{k}}) \, \langle k', \ell', m'| \, T^{+}(E_k) \, |k, \ell, m\rangle \, . \end{aligned} \tag{A.19}$$

Note that the scattering amplitude is independent of the basis normalisation, which is the result of defining it as the asymptotic distortion to the plane wave as in (A.17).

A.2 The S Matrix

Form equation (3.15), it is given that the S operator is related to the on-shell T operator as

$$S(E) = \mathbb{1} - 2i\pi\delta(E - H_0)T^{+}(E). \tag{A.20}$$

The expectation value of S, in the momentum basis, is thus

$$\langle \boldsymbol{k}'| \, S \, |\boldsymbol{k}\rangle = \langle \boldsymbol{k}'|\boldsymbol{k}\rangle - 2i\pi\delta(E_k - E_{k'})T(\boldsymbol{k}', \boldsymbol{k}; k), \tag{A.21}$$

where $k = |\boldsymbol{k}| = \sqrt{2\mu E_k}$ is the on-shell momentum and $T(\boldsymbol{k}', \boldsymbol{k}; k) \equiv \langle \boldsymbol{k}'| \, T^{+}(E_k) \, |\boldsymbol{k}\rangle$ is the momentum basis T matrix. By inserting the momentum eigenstate normalisation and rewriting the Dirac delta functions, this equation becomes

$$\langle \boldsymbol{k}'| \, S \, |\boldsymbol{k}\rangle = C^2_{\text{mom.}} \frac{\delta(k - k')}{k^2} \left[\delta^{(2)}(\hat{\boldsymbol{k}}' - \hat{\boldsymbol{k}}) - \frac{2i\pi\mu k}{C^2_{\text{mom.}}} T(\boldsymbol{k}', \boldsymbol{k}; k) \right]. \tag{A.22}$$

The S matrix is then defined as

$$S(\boldsymbol{k}', \boldsymbol{k}) = \delta^{(2)}(\hat{\boldsymbol{k}}' - \hat{\boldsymbol{k}}) - \frac{2i\pi\mu k}{C^2_{\text{mom.}}} T(\boldsymbol{k}', \boldsymbol{k}; k), \tag{A.23}$$

such that it is independent of the normalisation of the momentum states and

$$\langle \boldsymbol{k}' | \, S \, | \boldsymbol{k} \rangle = C^2_{\text{mom.}} \frac{\delta(k - k')}{k^2} S(\boldsymbol{k}', \boldsymbol{k}). \tag{A.24}$$

The S matrix can then be expressed in terms of the scattering amplitudes, by inserting (A.18), as

$$S(\boldsymbol{k}', \boldsymbol{k}) = \delta^{(2)}(\hat{\boldsymbol{k}}' - \hat{\boldsymbol{k}}) + \frac{ik}{2\pi} M(\boldsymbol{k}', \boldsymbol{k}). \tag{A.25}$$

It is then apparent that the S matrix, like the M matrix, is independent of the normalisation of the momentum states.

The expectation value of the S operator, in the PWS basis, is

$$\langle k', \ell', m' | \, S \, | k, \ell, m \rangle = \langle k', \ell', m' | k, \ell, m \rangle - 2i\pi\delta(E_k - E_{k'}) \, \langle k', \ell', m' | \, T^+(E_k) \, | k, \ell, m \rangle \, , \tag{A.26}$$

where $k = \sqrt{2\mu E_k}$ ia the on-shell momentum. By inserting the PWS normalisation (A.7) and rewriting the Dirac delta function, this equation becomes

$$\langle k', \ell', m' | \, S \, | k, \ell, m \rangle = C^2_{\text{PW}} \frac{\delta(k' - k)}{k^2} \left[\delta_{\ell'\ell} \delta_{m'm} - \frac{2i\pi\mu k}{C^2_{\text{PW}}} \, \langle k', \ell', m' | \, T^+(E_k) \, | k, \ell, m \rangle \right]. \tag{A.27}$$

The PWS basis S matrix is thus defined as

$$S^{\ell'\ell}_{m'm}(k, k) = \delta_{\ell'\ell} \delta_{m'm} - \frac{2i\pi\mu k}{C^2_{\text{PW}}} \, \langle k, \ell', m' | \, T^+(E_k) \, | k, \ell, m \rangle \, , \tag{A.28}$$

such that $S^{\ell'\ell}_{m'm}(k, k)$ is independent of the PWS normalisation and

$$\langle k', \ell', m' | \, S \, | k, \ell, m \rangle = C^2_{\text{PW}} \frac{\delta(k' - k)}{k^2} S^{\ell'\ell}_{m'm}(k, k). \tag{A.29}$$

A.3 Application for Particles with Spin and Isospin

Note that the content in the above sections is quite general. For particles with spin and isospin, like those handled in this thesis, the momentum states will instead be given by

$$|\boldsymbol{p}\rangle \longrightarrow |\boldsymbol{p}, s, m_s, t, m_t\rangle \equiv |\boldsymbol{p}\rangle \otimes |s, m_s\rangle \otimes |t, m_t\rangle \, , \tag{A.30}$$

where $|s, m_s\rangle$ are coupled spin states and $|t, m_t\rangle$ are coupled isospin states. The normalisation of these states can be handled similarly to what has been done previously in this appendix, *i.e.*

$$\langle \boldsymbol{p}', s', m'_s, t', m'_t | \boldsymbol{p}, s, m_s, t, m_t \rangle = C^2_{\text{mom.}} \delta^{(3)}(\boldsymbol{p}' - \boldsymbol{p}) \delta_{s's} \delta_{t't} \delta_{m'_s m_s} \delta_{m'_t m_t}. \tag{A.31}$$

The PWS of interest are the jPWS, which couple the orbital angular momentum PWS with the coupled spin states such that

$$|\boldsymbol{p}, s, m_s, t, m_t\rangle = \\ = \sum_{j=0}^{\infty} \sum_{m_j=-j}^{j} \sum_{\ell=|j-s|}^{j+s} \frac{C_{\text{mom.}}}{C_{\text{PW}}} e^{-i\omega\ell} C^{j,m_j}_{\ell,s;m_j-m_s,m_s} Y^{*\ell}_{m_j-m_s}(\hat{\boldsymbol{p}}) \, |\ell, s; p, j, m_j, t, m_t\rangle \,, \quad \text{(A.32)}$$

where $C^{j,m_j}_{\ell,s;m_j-m_s,m_s}$ are the Clebsch-Gordan coefficients from the spin-orbital angular momentum coupling. The jPWS are then normalised as

$$\langle \ell', s'; p', j', m'_j, t', m'_t | \ell, s; p, j, m_j, t, m_t\rangle = C^2_{\text{PW}} \frac{\delta(p'-p)}{p^2} \delta_{j'j} \delta_{\ell'\ell} \delta_{s's} \delta_{t't} \delta_{m'_j m_j} \delta_{m'_t m_t}. \quad \text{(A.33)}$$

The basis independent scattering amplitude is then given by

$$M^{s't';st}_{m'_s m'_t; m_s m_t}(\boldsymbol{k}', \boldsymbol{k}) = -\frac{(2\pi)^2 \mu}{C^2_{\text{mom.}}} \langle \boldsymbol{k}', s', m'_s, t', m'_t | \, T^+(E_k) \, |\boldsymbol{k}, s, m_s, t, m_t\rangle \,, \quad \text{(A.34)}$$

or equivalently by

$$M^{s't';st}_{m'_s m'_t; m_s m_t}(\boldsymbol{k}', \boldsymbol{k}) = -\frac{(2\pi)^2 \mu}{C^2_{\text{PW}}} \sum_{j',\ell',m'_j} \sum_{j,\ell,m_j} e^{i\omega(\ell'-\ell)} C^{j',m'_j}_{\ell',s';m'_j-m'_s,m'_s} C^{j,m_j}_{\ell,s;m_j-m_s,m_s} \cdot \\ \cdot Y^{\ell'}_{m'_j-m'_s}(\hat{\boldsymbol{k}}') Y^{*\ell}_{m_j-m_s}(\hat{\boldsymbol{k}}) \, \langle \ell', s'; k', j', m'_j, t', m'_t | \, T^+(E_k) \, |\ell, s; k, j, m_j, t, m_t\rangle \,. \quad \text{(A.35)}$$

The S matrix is in the momentum basis given by

$$S^{s't';st}_{m'_s m'_t; m_s m_t}(\boldsymbol{k}', \boldsymbol{k}) = \delta^{(2)}(\hat{\boldsymbol{k}}' - \hat{\boldsymbol{k}}) \delta_{s's} \delta_{m'_s m_s} \delta_{t't} \delta_{m'_t m_t} + \frac{ik}{2\pi} M^{s't';st}_{m'_s m'_t; m_s m_t}(\boldsymbol{k}', \boldsymbol{k}), \quad \text{(A.36)}$$

and in the jPWS basis given by

$$S^{j'\ell's't';j\ell st}_{m'_j m'_t; m_j m_t}(\boldsymbol{k}', \boldsymbol{k}) = \delta_{j'j} \delta_{\ell'\ell} \delta_{s's} \delta_{t't} \delta_{m'_j m_j} \delta_{m'_t m_t} + \\ - \frac{2i\pi\mu k}{C^2_{\text{PW}}} \langle \ell', s'; k, j', m'_j, t', m'_t | \, T^+(E_k) \, |\ell, s; k, j, m_j, t, m_t\rangle \,. \quad \text{(A.37)}$$

Note that these expressions can be drastically simplified when considering the symmetries of the system in question, but they will keep their general form.

B

Variances of Differential Observables

In subsection 7.3.1, it was stated that a general differential observable $\sigma O_{P_\mathrm{S}P_\mathrm{R}P_\mathrm{P}P_\mathrm{T}}(T_\mathrm{lab},\vartheta)$ can be expressed as

$$\sigma O_{P_\mathrm{S}P_\mathrm{R}P_\mathrm{P}P_\mathrm{T}}(\vec{x}) = \sum_{i,j=1}^{5}\Big(B_{ij,\Re}(\vec{x})\mathrm{Re}[y_i^*(\vec{x})y_j(\vec{x})] + B_{ij,\Im}(\vec{x})\mathrm{Im}[y_i^*(\vec{x})y_j(\vec{x})]\Big), \quad \text{(B.1)}$$

where $B_{ij,\Re}(\vec{x}) = B_{ji,\Re}(\vec{x}) \in \mathbb{R}$ and $B_{ij,\Im}(\vec{x}) = -B_{ji,\Im}(\vec{x}) \in \mathbb{R}$ are deterministic functions that depend on the convention of the scattering amplitudes $\{y_i(\vec{x}\}_{i=1}^5$. The scattering amplitudes are separated into two parts $y_i(\vec{x}) = y_{i,0}(\vec{x}) + \delta y_{i,0}(\vec{x})$, where $y_{i,0}(\vec{x})$ is the mean of the amplitude distribution (the LO prediction) and $\delta y_{i,0}(\vec{x})$ is the independent complex zero-mean Gaussian-distributed truncation errors. Note that symmetry and antisymmetry of $B_{ij,\Re}(\vec{x})$ and $B_{ij,\Im}(\vec{x})$ stems from

$$\mathrm{Re}[y_i^*(\vec{x})y_j(\vec{x})] = \mathrm{Re}[y_j^*(\vec{x})y_i(\vec{x})], \quad \mathrm{Im}[y_i^*(\vec{x})y_j(\vec{x})] = -\mathrm{Im}[y_j^*(\vec{x})y_i(\vec{x})], \quad \text{(B.2)}$$

and implies that $B_{ii,\Im}(\vec{x}) = 0$. By defining the Hermitean matrix $\mathbf{B} \in \mathbb{C}^{5\times5}$ and vector $\boldsymbol{y} = \boldsymbol{y}_0 + \delta\boldsymbol{y}_0 \in \mathbb{C}^5$ as

$$[\mathbf{B}]_{ij} \equiv B_{ji,\Re}(\vec{x}) - iB_{ji,\Im}(\vec{x}), \quad [\boldsymbol{y}_0]_i \equiv y_{i,0}(\vec{x}), \quad [\delta\boldsymbol{y}_0]_i \equiv \delta y_{i,0}(\vec{x}), \quad \text{(B.3)}$$

a observable $Z = \sigma O_{P_\mathrm{S}P_\mathrm{R}P_\mathrm{P}P_\mathrm{T}}(\vec{x})$ can be expressed as

$$Z = \boldsymbol{y}^\dagger\mathbf{B}\boldsymbol{y} = \underbrace{\boldsymbol{y}_0^\dagger\mathbf{B}\boldsymbol{y}_0}_{\equiv Z_0} + \underbrace{2\mathrm{Re}[\boldsymbol{y}_0^\dagger\mathbf{B}\delta\boldsymbol{y}_0]}_{\equiv Z_1} + \underbrace{\delta\boldsymbol{y}_0^\dagger\mathbf{B}\delta\boldsymbol{y}_0}_{\equiv Z_2}. \quad \text{(B.4)}$$

Note that $Z_0 \equiv \boldsymbol{y}_0^\dagger\mathbf{B}\boldsymbol{y}_0$ is the LO prediction of the observable. The mean of Z is thus

$$\langle Z\rangle = Z_0 + 2\mathrm{Tr}\{\mathbf{B}\boldsymbol{\Sigma}\}, \quad \boldsymbol{\Sigma} \equiv \mathrm{diag}\{\sigma_1^2(\vec{x}),\sigma_2^2(\vec{x}),\ldots,\sigma_5^2(\vec{x})\}, \quad \text{(B.5)}$$

where $\sigma_i^2(\vec{x}) \equiv \bar{c}^2R_{i,0}(\vec{x},\vec{x};\ell)$ are the variance of amplitude $y_i(\vec{x})$. The trace term comes from the mean of Z_2 as

$$\langle Z_2\rangle = \langle\delta\boldsymbol{y}_0^\dagger\mathbf{B}\delta\boldsymbol{y}_0\rangle = \sum_{a,b=1}^{5}B_{ab}\langle\delta y_{a,0}^*\delta y_{b,0}\rangle = 2\sum_{a,b=1}^{5}B_{ab}\Sigma_{ba} = 2\mathrm{Tr}\{\mathbf{B}\boldsymbol{\Sigma}\}, \quad \text{(B.6)}$$

where $\langle \delta y^*_{a,0} \delta y_{b,0} \rangle = 2\Sigma_{ab} = 2[\mathbf{\Sigma}]_{ab}$ (the factor comes from the equal contibutions from the real and imaginary parts of $\delta y_{a,0}$) and $B_{ab} = [\mathbf{B}]_{ab}$. Note that equation (B.5) is an equivalent expression to that found in subsection 7.3.1.

The variance of Z is given by [46]

$$\mathrm{Var}[Z] = \langle Z^2 \rangle - \langle Z \rangle^2 . \tag{B.7}$$

The mean of Z^2 (second moment $\langle Z^2 \rangle$) is

$$\langle Z^2 \rangle = Z_0^2 + 4Z_0 \mathrm{Tr}\{\mathbf{B\Sigma}\} + \langle Z_1^2 \rangle + \langle Z_2^2 \rangle , \tag{B.8}$$

which can be understood from the fact that the mean of an odd multiple of zero-mean distributed variables is zero and (B.6). To determine $\langle Z_1^2 \rangle$, the complex scalar $w_1 \equiv \boldsymbol{y}_0^\dagger \mathbf{B} \delta \boldsymbol{y}_0$ such that

$$Z_1 = 2\mathrm{Re}[w_1] = w_1 + w_1^* . \tag{B.9}$$

It is then given that

$$\langle Z_1^2 \rangle = \langle w_1^2 \rangle + \langle (w_1^*)^2 \rangle + 2 \langle |w_1|^2 \rangle . \tag{B.10}$$

The first two terms are zero since

$$\langle (w_1^*)^2 \rangle^* = \langle w_1^2 \rangle = \boldsymbol{y}_0^\dagger \mathbf{B} \langle \delta \boldsymbol{y}_0 \delta \boldsymbol{y}_0^T \rangle \mathbf{B}^T \boldsymbol{y}_0^* = \boldsymbol{y}_0^\dagger \mathbf{B} [\mathbf{\Sigma} - \mathbf{\Sigma}] \mathbf{B}^T \boldsymbol{y}_0^* = 0, \tag{B.11}$$

where the third equality uses that

$$\begin{cases} \langle \mathrm{Re}[\delta \boldsymbol{y}_0] \mathrm{Re}[\delta \boldsymbol{y}_0]^T \rangle = \langle \mathrm{Im}[\delta \boldsymbol{y}_0] \mathrm{Im}[\delta \boldsymbol{y}_0]^T \rangle = \mathbf{\Sigma}, \\ \langle \mathrm{Re}[\delta \boldsymbol{y}_0] \mathrm{Im}[\delta \boldsymbol{y}_0]^T \rangle = \langle \mathrm{Im}[\delta \boldsymbol{y}_0] \mathrm{Re}[\delta \boldsymbol{y}_0]^T \rangle = 0. \end{cases} \tag{B.12}$$

Equation (B.10) will thus become

$$\langle Z_1^2 \rangle = 2 \langle |w_1|^2 \rangle = 2 \boldsymbol{y}_0^\dagger \mathbf{B} \langle \delta \boldsymbol{y}_0 \delta \boldsymbol{y}_0^\dagger \rangle \mathbf{B} \boldsymbol{y}_0 = 4 \boldsymbol{y}_0^\dagger \mathbf{B\Sigma B} \boldsymbol{y}_0 . \tag{B.13}$$

The last term in (B.8) can be determined as

$$\langle Z_2^2 \rangle = \langle \delta \boldsymbol{y}_0^\dagger \mathbf{B} \delta \boldsymbol{y}_0 \delta \boldsymbol{y}_0^\dagger \mathbf{B} \delta \boldsymbol{y}_0 \rangle = \sum_{a,b,c,d=1}^{5} B_{ab} B_{cd} \langle \delta y^*_{a,0} \delta y_{b,0} \delta y^*_{c,0} \delta y_{d,0} \rangle =$$

$$= 4 \sum_{a,b,c,d=1}^{5} B_{ab} B_{cd} [\Sigma_{ba} \Sigma_{cd} + \Sigma_{ad} \Sigma_{bc}], \tag{B.14}$$

where a combination of Isserlis's theorem [53] and (B.12) was utilised in the last equality. The final expression of $\langle Z_2^2 \rangle$ is provided by recognising that both terms can be expressed as traces as

$$\langle Z_2^2 \rangle = 4(\mathrm{Tr}\{\mathbf{B\Sigma}\})^2 + 4\mathrm{Tr}\{\mathbf{B\Sigma B\Sigma}\}. \tag{B.15}$$

Equation (B.8) can thus be expressed as

$$\langle Z^2 \rangle = (Z_0 + 2\mathrm{Tr}\{\mathbf{B\Sigma}\})^2 + 4 \boldsymbol{y}_0^\dagger \mathbf{B\Sigma B} \boldsymbol{y}_0 + 4\mathrm{Tr}\{\mathbf{B\Sigma B\Sigma}\}. \tag{B.16}$$

The variance of Z is the given by noting that the first term of (B.16) is $\langle Z \rangle^2$, and can thus be expressed as

$$\mathrm{Var}[Z] = 4\boldsymbol{y}_0^\dagger \mathbf{B}\boldsymbol{\Sigma}\mathbf{B}\boldsymbol{y}_0 + 4\mathrm{Tr}\{\mathbf{B}\boldsymbol{\Sigma}\mathbf{B}\boldsymbol{\Sigma}\}. \tag{B.17}$$

In conclusion, the variance of a general differential observable $\sigma O_{P_\mathrm{S} P_\mathrm{R} P_\mathrm{P} P_\mathrm{T}}(T_\mathrm{lab}, \vartheta)$, as given in (B.1), is given by

$$\begin{aligned}\mathrm{Var}[\sigma O_{P_\mathrm{S} P_\mathrm{R} P_\mathrm{P} P_\mathrm{T}}(\vec{x})] = 4\sum_{i=1}^{5}\left|\sum_{j=1}^{5}[B_{ij,\Re}(\vec{x}) - iB_{ij,\Im}(\vec{x})]y_{j,0}(\vec{x})\right|^2 \bar{c}^2 R_{i,0}(\vec{x},\vec{x};\ell) \\ + \sum_{i,j=1}^{5}[B_{ij,\Re}^2(\vec{x}) + B_{ij,\Im}^2(\vec{x})]\bar{c}^4 R_{i,0}(\vec{x},\vec{x};\ell)R_{j,0}(\vec{x},\vec{x};\ell).\end{aligned} \tag{B.18}$$

C

Additional Results

This appendix contains supplementary results that do not provide any particular new insights. They do, however, ensure some completeness of the analysis. The figures in this appendix will be equivalent to those presented in the main results, but for different laboratory kinetic energies and/or c.m. polar scattering angles. The exceptions to this rule are figures C.1 and C.2, which show the LO predictions of the np scattering amplitudes and expansion coefficients ($y_{\text{ref}} = 0.5\,\text{fm}$), respectively, in the helicity and Saclay conventions. The purpose of these figures is to supplement (and validate) the motivation for the chosen hyperparameters of the implemented error model presented in section 7.3.

C.1 Energy and Angle Dependence of LO Predictions of Scattering amplitudes

The LO WPC χEFT predictions of the five complex np scattering amplitudes for laboratory kinetic energies $T_{\text{lab}} \in [20, 150]\,\text{MeV}$ and c.m. polar scattering angles $\vartheta \in [0\pi]$ were determined with the potential specified in section 7.1. They are presented in the helicity and Saclay convention in figure C.1. The corresponding LO expansion coefficients were then determined with a constant reference function $y_{\text{ref}} = 0.5\,\text{fm}$ and are shown in figure C.2. The colour scales of these heatmaps are given in terms of the marginal variance of the implemented error model, $\bar{c}^2 = 1^2$. Figure C.2 shows that the LO expansion coefficients are generally of natural scale, indicating that the reference function is appropriate. It can also be seen that the coefficients generally (with some exceptions) remain within $\pm 2\bar{c} = \pm 2$, indicating that the marginal variance was not too optimistic.

C.2 Differential Observable

This section presents additional results concerning the propagation of truncation errors from np scattering amplitudes to differential observables. The figures below resemble those in section 8.2, but pertain to a different laboratory kinetic energy or c.m. polar scattering angle. This section also includes a figure illustrating the

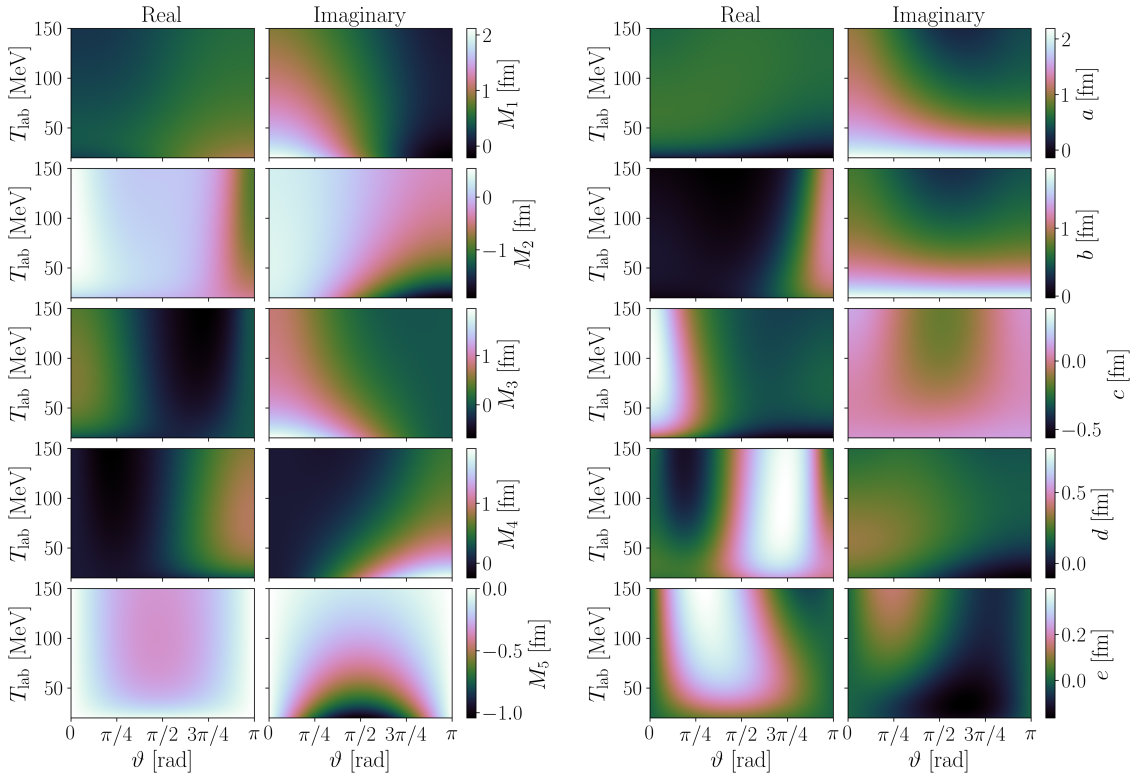

(a) Helicity amplitudes **(b)** Saclay amplitudes

Figure C.1: The WPC LO prediction of the np scattering amplitudes in the helicity (a) and Saclay (b) convention, for laboratory kinetic energies $T_{\mathrm{lab}} \in [20, 250]\,\mathrm{MeV}$ and c.m. polar scattering angles $\vartheta \in [0, \pi]$.

interobservabial Pearson correlation coefficient (similar to figure 8.5), resulting from propagating the Saclay amplitudes to various differential observables.

C.3 Total cross sections

This section presents additional results concerning the propagation of truncation errors from np scattering amplitudes to total cross sections. The figures below resemble those in section 8.3, but pertain to a different laboratory kinetic energy.

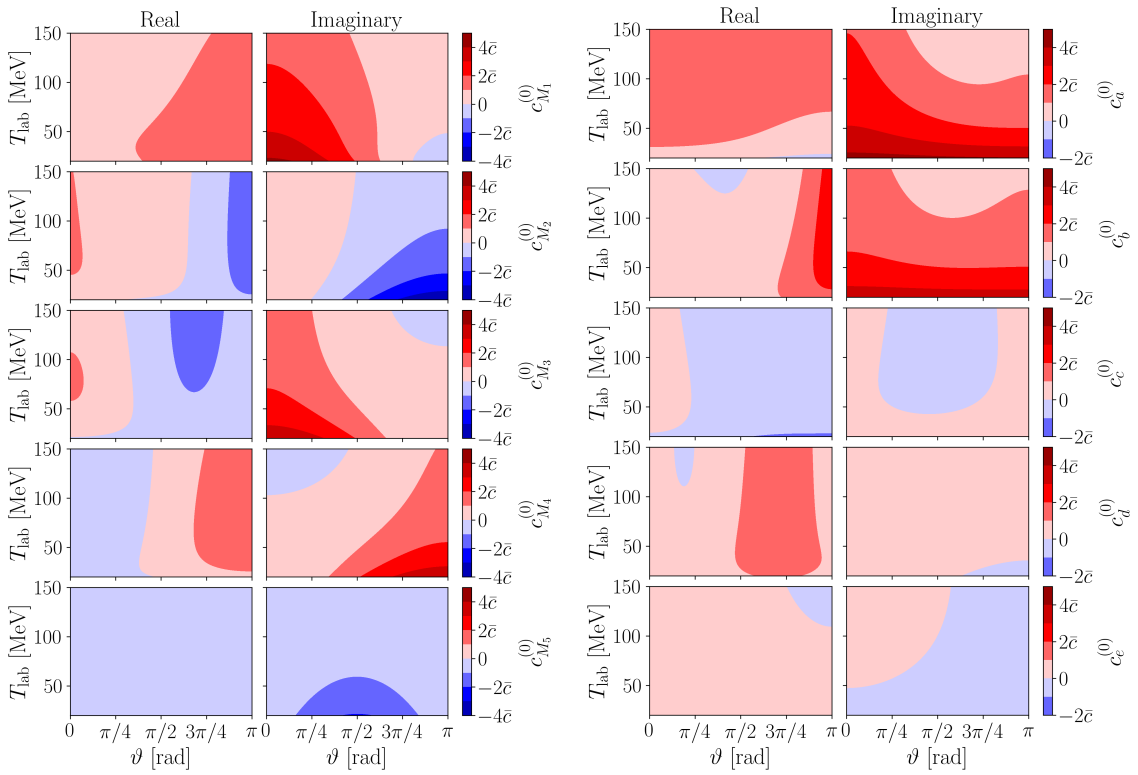

(a) Helicity amplitudes **(b)** Saclay amplitudes

Figure C.2: The LO expansion coefficients determined from the *np* scattering amplitudes in figure C.1 with $y_{\mathrm{ref}} = 0.5\,\mathrm{fm}$ indicated in relation to the marginal StD $\bar{c} = 1$.

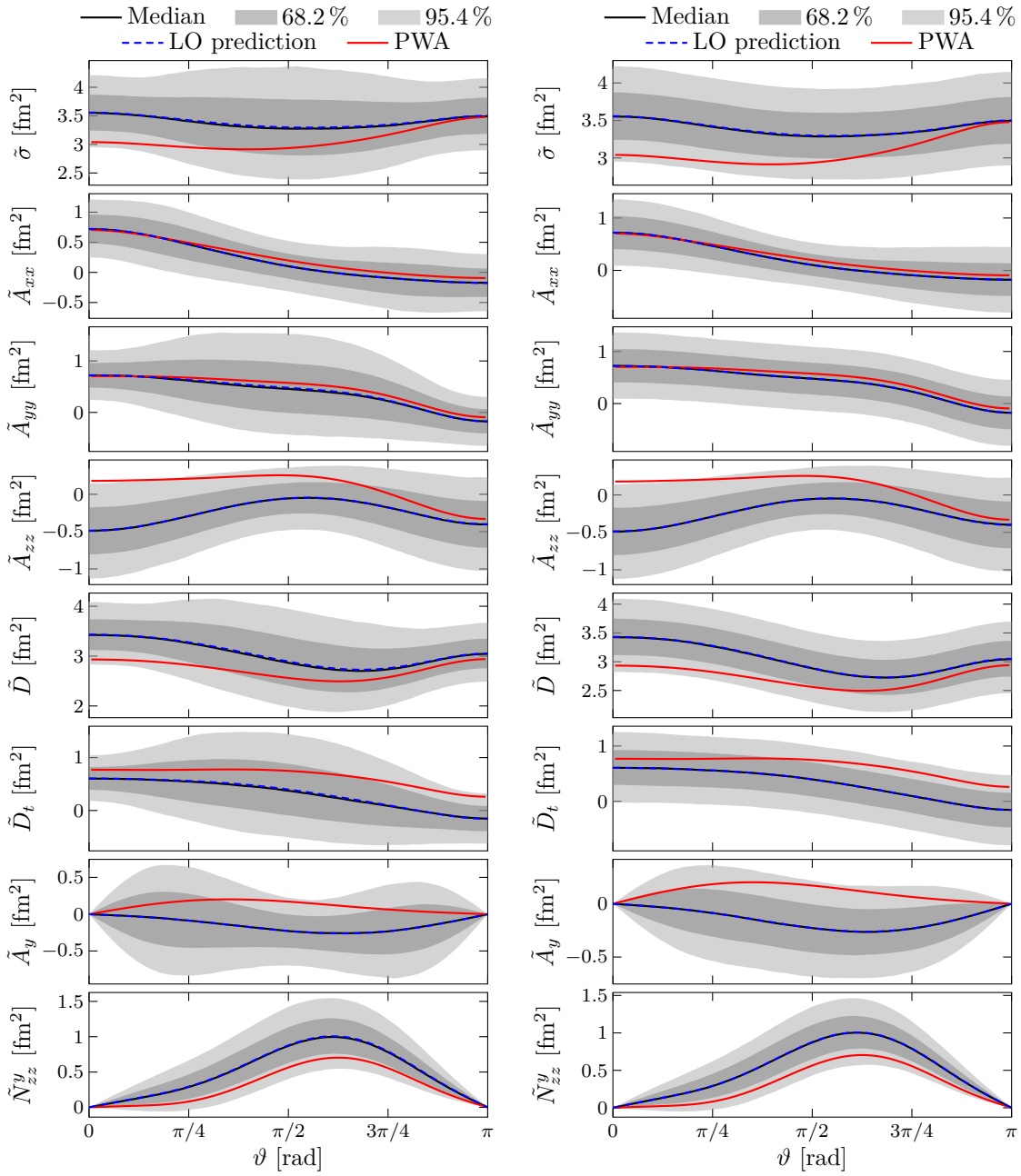

(a) From helicity amplitudes **(b)** From Saclay amplitudes

Figure C.3: Same as figure 8.2 but for laboratory kinetic energy $T_{\text{lab}} = 25\,\text{MeV}$.

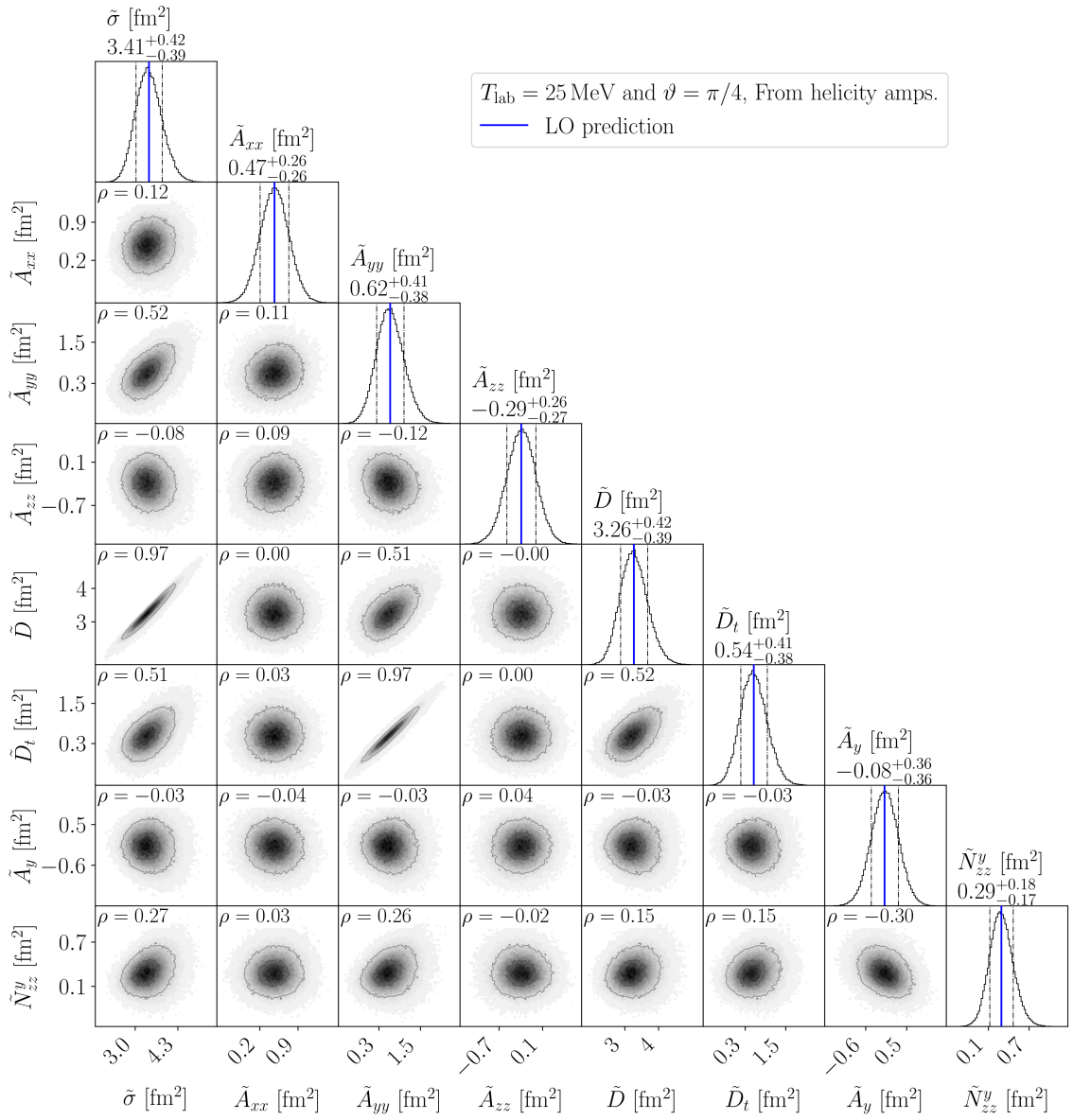

Figure C.4: Same as figure 8.3 but for laboratory kinetic energy $T_{\mathrm{lab}} = 25\,\mathrm{MeV}$ and without lines indicating the hard inequalities.

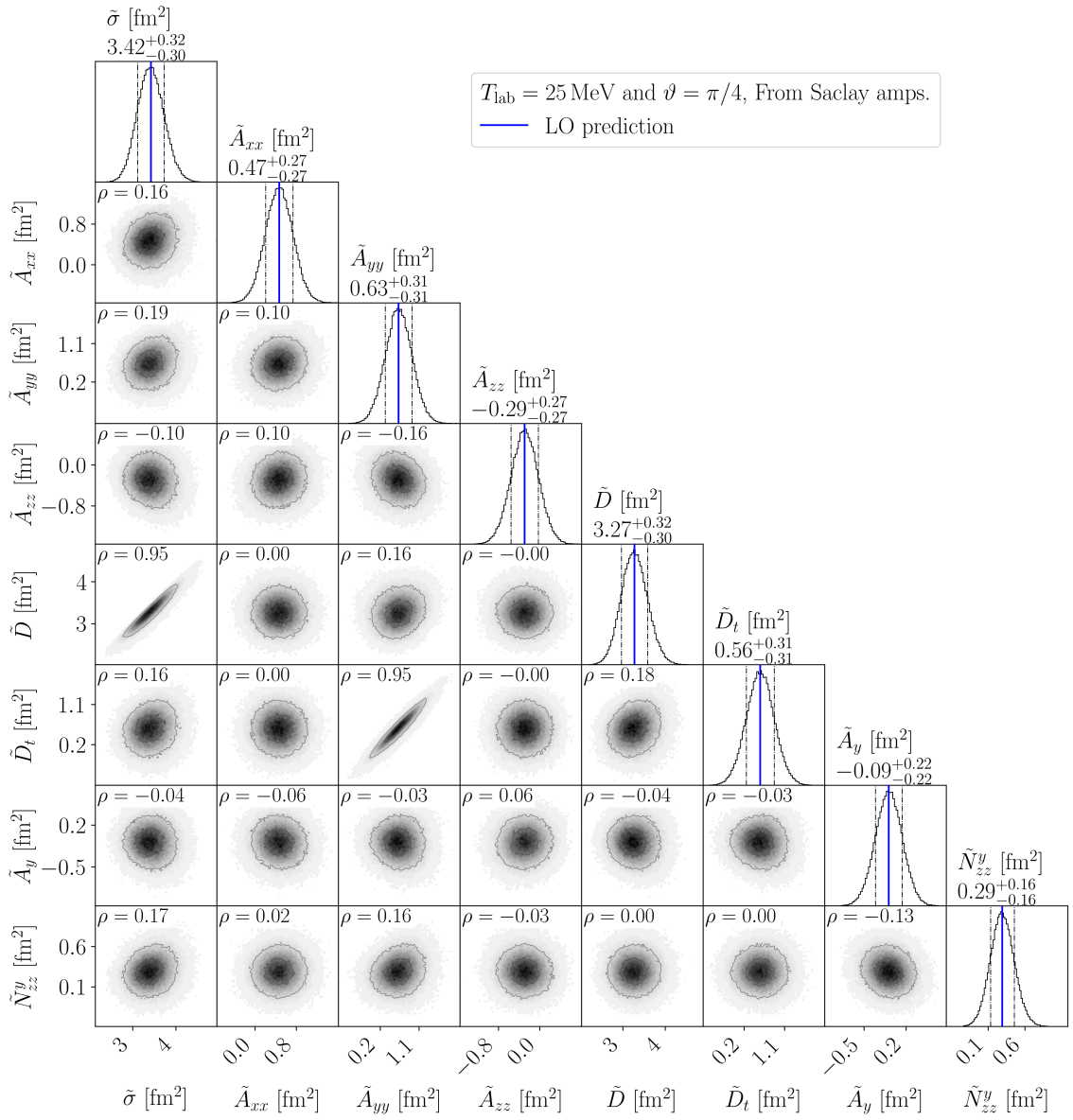

Figure C.5: Same as figure 8.4 but for laboratory kinetic energy $T_{\mathrm{lab}} = 25\,\mathrm{MeV}$ and without lines indicating the hard inequalities.

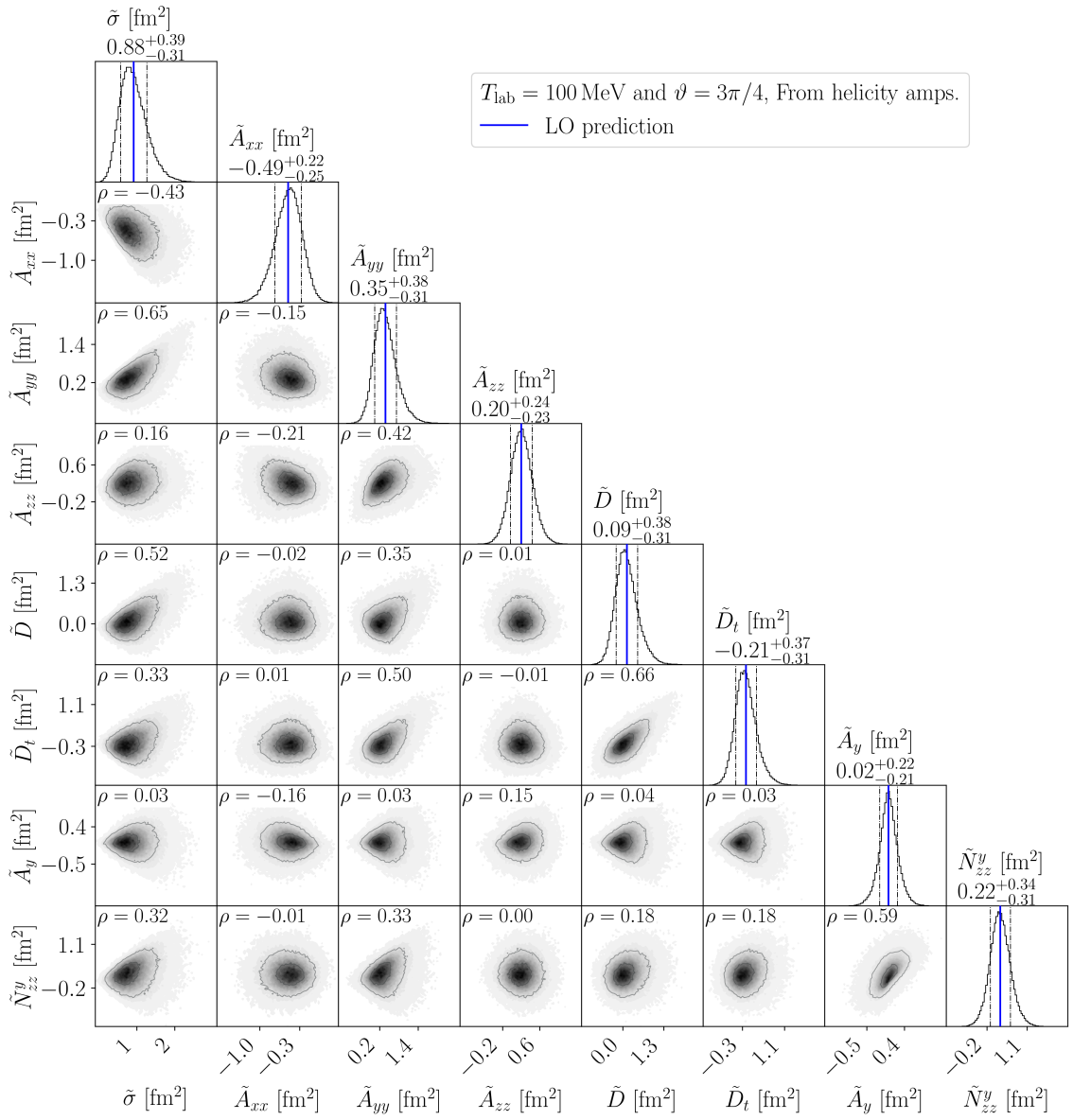

Figure C.6: Same as figure 8.3 but for c.m. polar scattering angle $\vartheta = 3\pi/4$ and without lines indicating the hard inequalities.

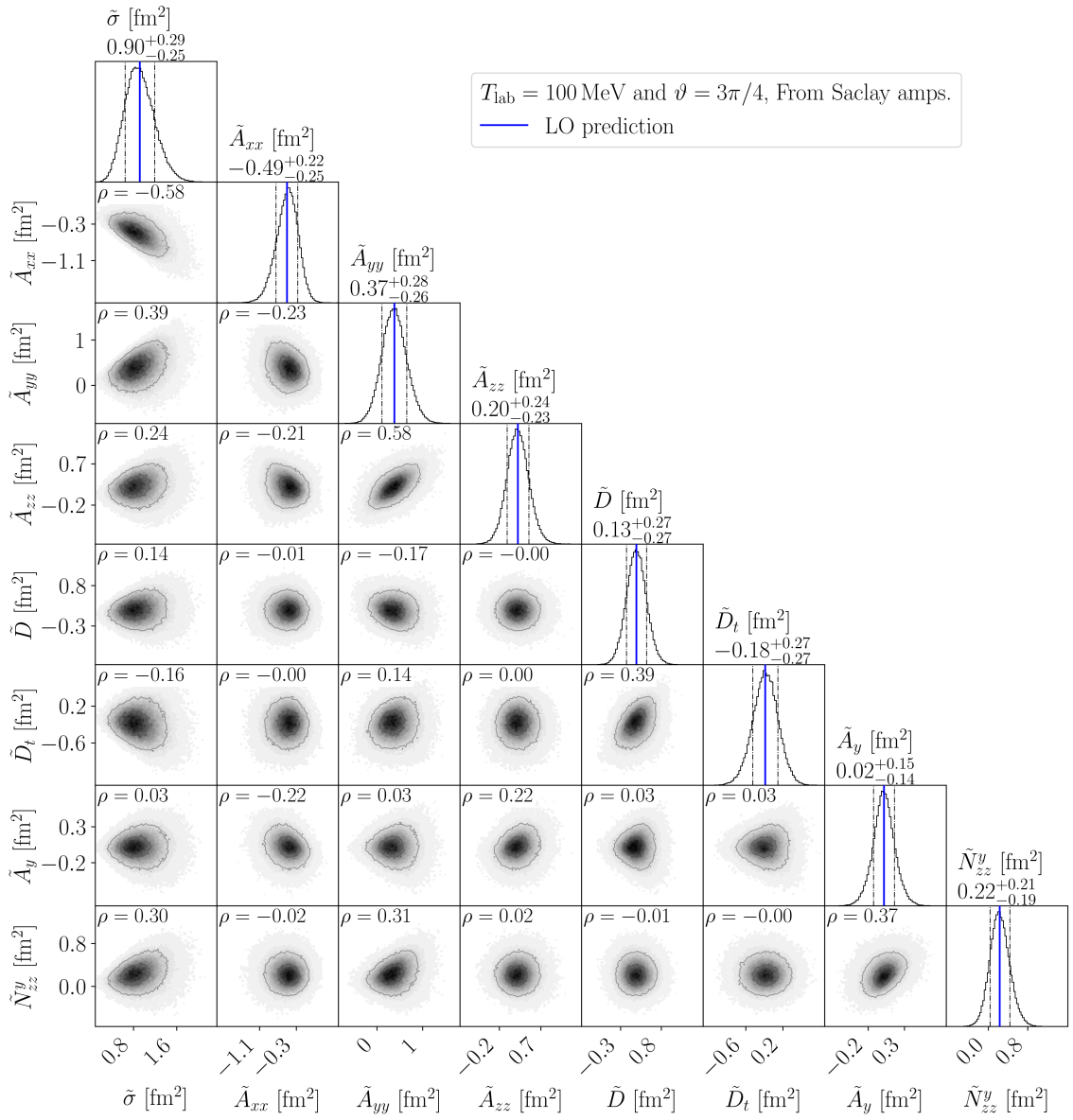

Figure C.7: Same as figure 8.4 but for c.m. polar scattering angle $\vartheta = 3\pi/4$ and without lines indicating the hard inequalities.

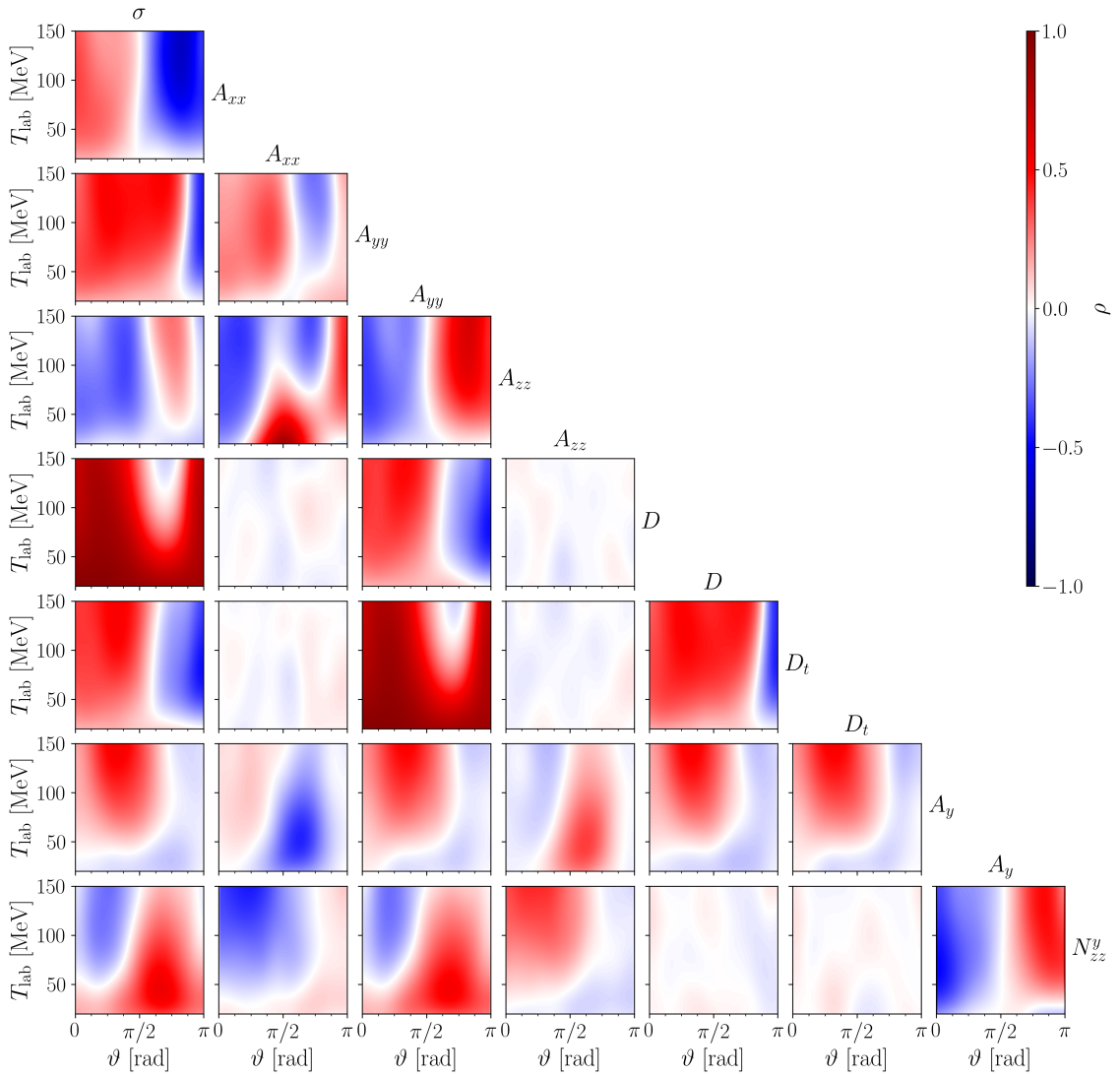

Figure C.8: Same as figure 8.5, except that the interobservabial Pearson correlation coefficients were determined with samples of the Saclay amplitude distributions.

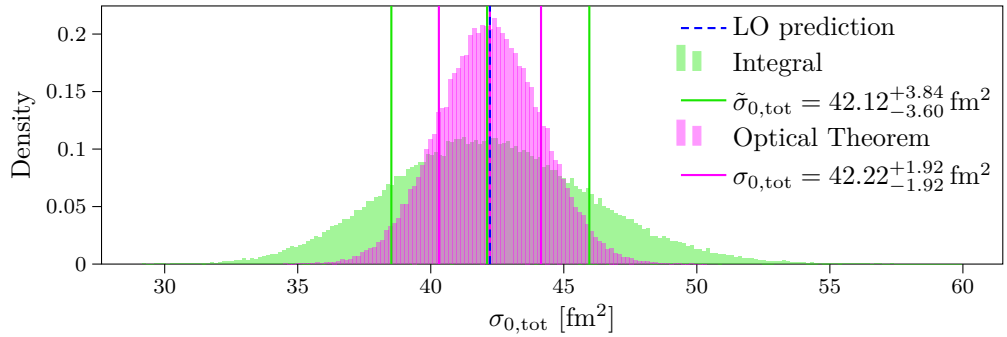

(a) From helicity amplitudes

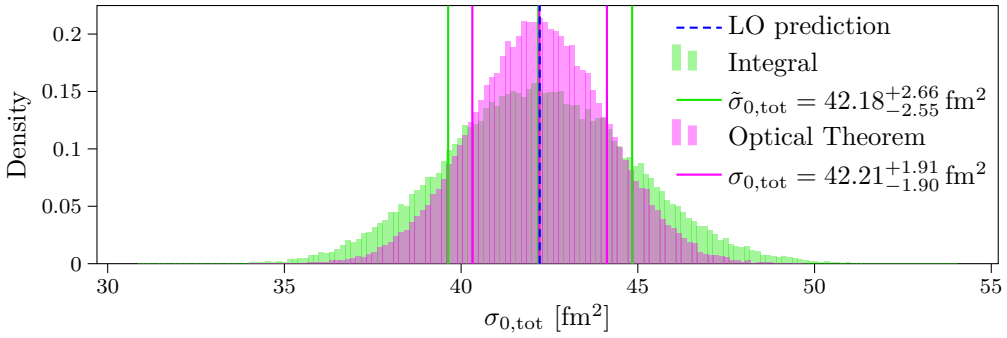

(b) From Saclay amplitudes

Figure C.9: Same as figure 8.6 but for laboratory kinetic energy $T_{\mathrm{lab}} = 25\,\mathrm{MeV}$.

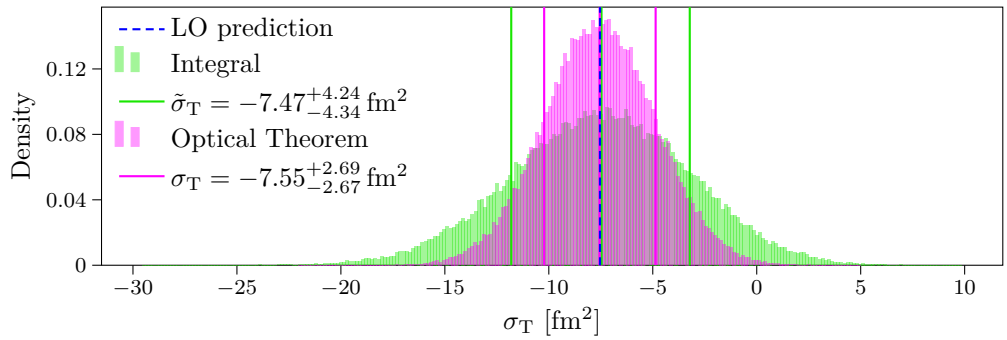

(a) From helicity amplitudes

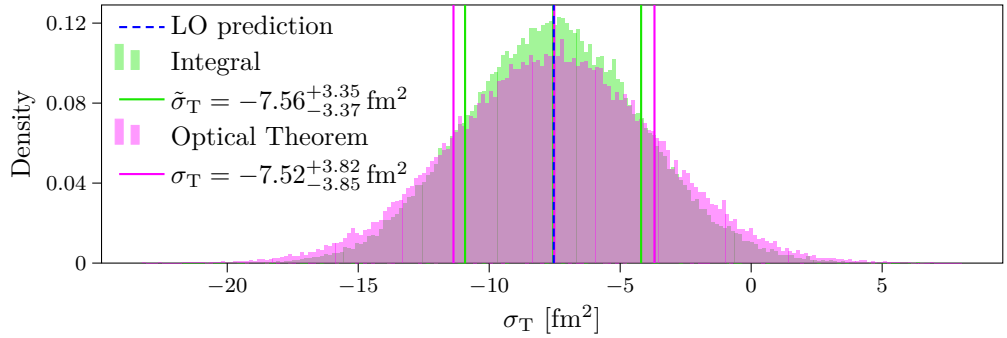

(b) From Saclay amplitudes

Figure C.10: Same as figure 8.7 but for laboratory kinetic energy $T_{\mathrm{lab}} = 25\,\mathrm{MeV}$.

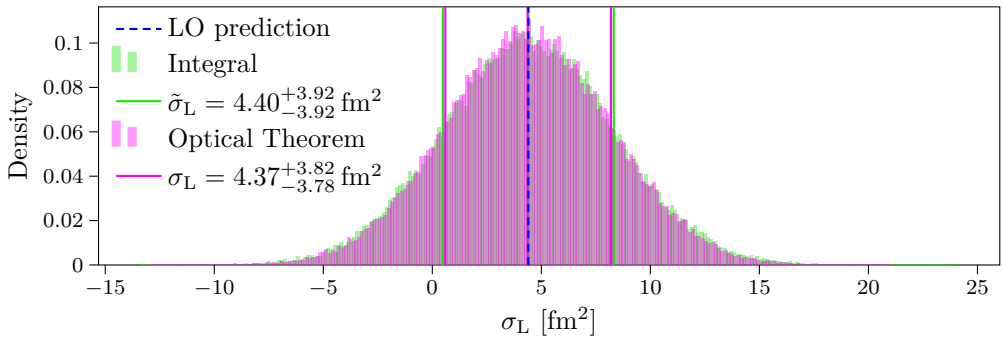

(a) From helicity amplitudes

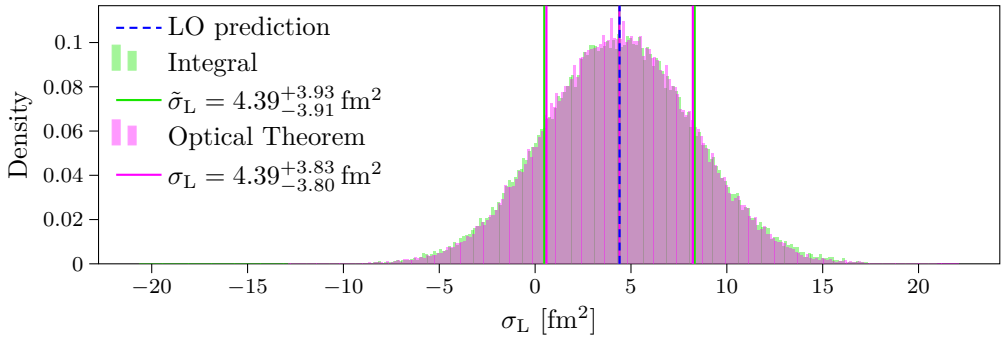

(b) From Saclay amplitudes

Figure C.11: Same as figure 8.8 but for laboratory kinetic energy $T_{\mathrm{lab}} = 25\,\mathrm{MeV}$.

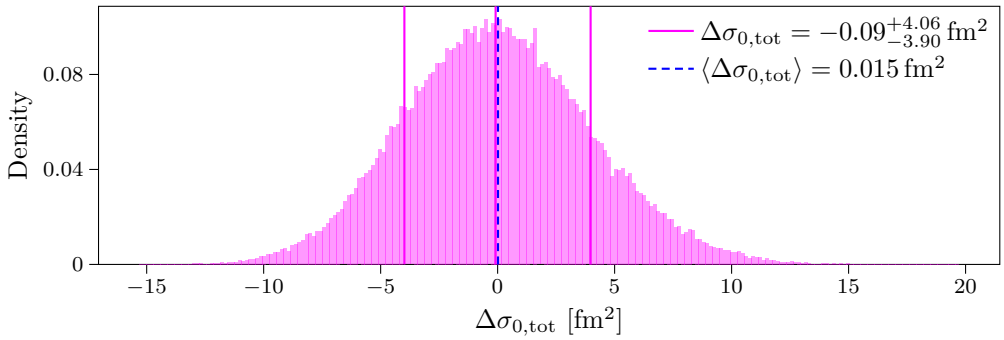

(a) From helicity amplitudes

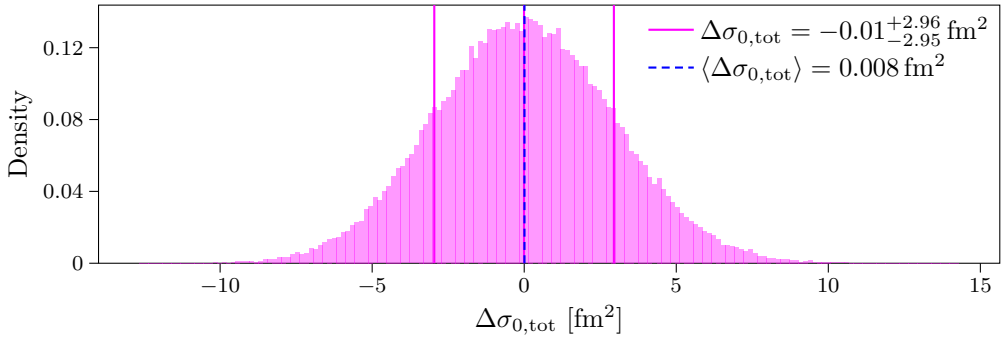

(b) From Saclay amplitudes

Figure C.12: Same as figure 8.9 but for laboratory kinetic energy $T_{\mathrm{lab}} = 25\,\mathrm{MeV}$.

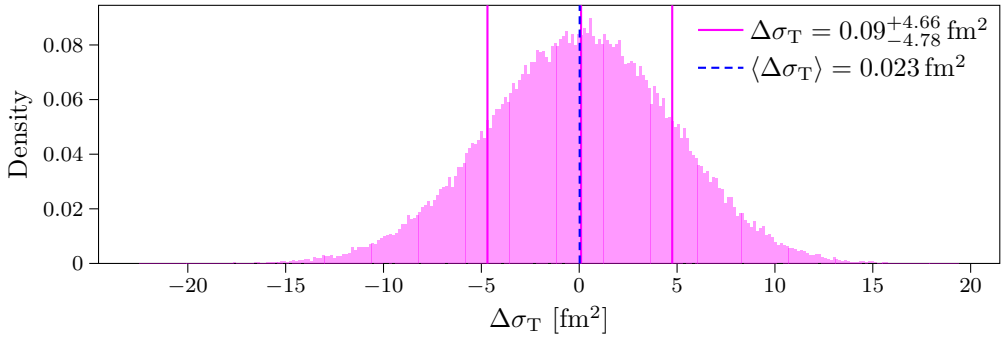

(a) From helicity amplitudes

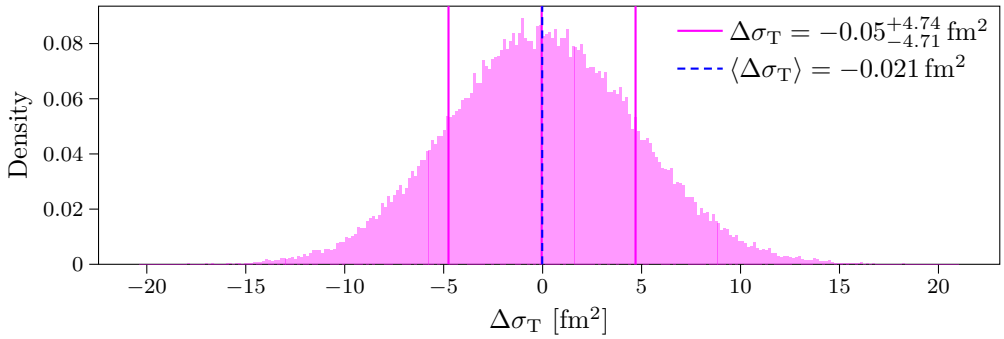

(b) From Saclay amplitudes

Figure C.13: Same as figure 8.10 but for laboratory kinetic energy $T_{\text{lab}} = 25\,\text{MeV}$.

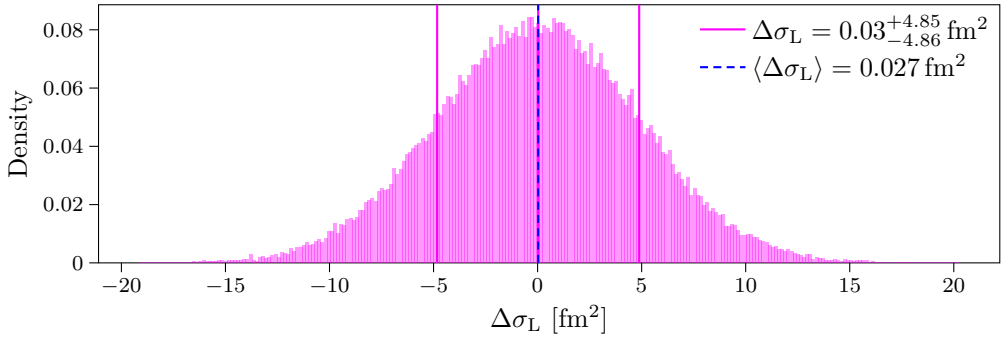

(a) From helicity amplitudes

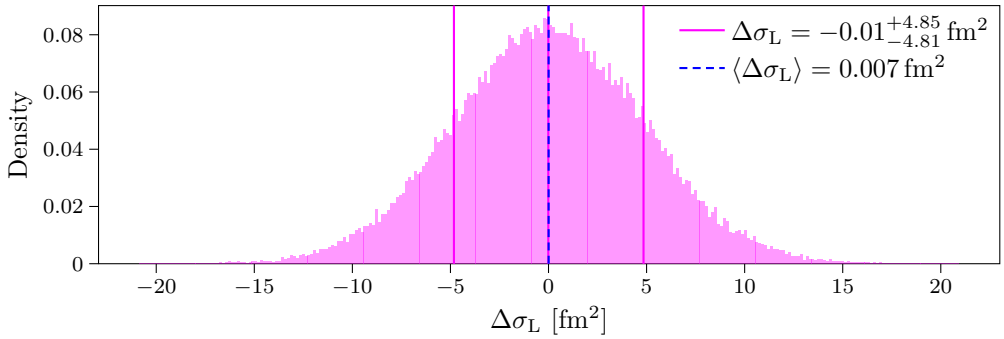

(b) From Saclay amplitudes

Figure C.14: Same as figure 8.11 but for laboratory kinetic energy $T_{\text{lab}} = 25\,\text{MeV}$.

DEPARTMENT OF SOME SUBJECT OR TECHNOLOGY
CHALMERS UNIVERSITY OF TECHNOLOGY
Gothenburg, Sweden
www.chalmers.se

CHALMERS
UNIVERSITY OF TECHNOLOGY